Contact-mediated nucleation during the crystallization of organic melt emulsions

Zur Erlangung des akademischen Grades einer

DOKTORIN DER INGENIEURWISSENSCHAFTEN
(Dr.-Ing.)

von der KIT-Fakultät für Chemieingenieurwesen und Verfahrenstechnik des
Karlsruher Instituts für Technologie (KIT)

genehmigte

DISSERTATION

von

M.Sc. Gina Patricia Kaysan

Tag der mündlichen Prüfung:	14.02.2025
Erstgutachter:	Prof. Dr.-Ing. Matthias Kind
Zweitgutachterin:	apl. Prof. Dr. Gisela Guthausen

"Jede Berührung hinterlässt eine
Spur."
— Henri-Frédéric Amiel

Abstract

The main focus of this work is the energy- and time-efficient design of the manufacturing process of suspensions with particles in the micrometer range. The classic manufacturing process for these suspensions is the resource-intensive wet grinding process. A more cost-effective alternative to this is melt emulsification. In this process, coarse particles are melted, emulsified and then converted into smaller particles by cooling them to temperatures well below their melting point. However, incomplete droplet crystallization often occurs, which promotes colloidal processes during storage and transport of the dispersion. These instability mechanisms can compromise product performance.

The present work starts here and aims to develop a concept with which a complete droplet crystallization in the manufacturing process can be guaranteed and thus the fluctuations in product quality can be minimized.

There are several methods for triggering the crystallization of droplets: For example, the addition of suitable surfactants and the addition of external substances can promote crystallization. While the crystallization efficiency with regard to the solid content of the droplets could be improved with the methods mentioned, the supercooling required for droplet nucleation could not be significantly reduced. A new and promising approach to increasing the efficiency of the melt emulsion process is contact-mediated nucleation (CMN).

CMN describes the crystallization of supercooled droplets through brief contact with an already crystallized droplet (i.e. a particle). CMN already occurs at significantly lower supercooling temperatures, and therefore higher temperatures, than primary nucleation. The targeted use of CMN offers the possibility of energy savings, shorter process times and thus contributes to a more sustainable manufacturing process. Although CMN has already been described in the literature, no systematic investigation of the mechanism has yet been reported. In particular, the influence of flow on CMN has not been considered. This is the focus of the present work.

To comprehensively characterize the CMN in terms of nucleation efficiency, several aspects must be considered:

- The knowledge about coalescence processes of liquid droplets described in the literature makes it clear how important it is to investigate the influence of the flow field. The flow present in the process influences the relative velocity between particle and droplet and thus has an effect on the contact force, the contact time and the collision frequency.
- Assuming that the coalescence theory is transferable to the CMN, parameters such as the composition of the continuous and dispersed phases should also influence the CMN.

The present work consists of three main sections, which deal with the specific investigation of the flow effects on the CMN in different experimental setups and scales:

The first step in characterizing the CMN in terms of its applicability in industrial crystallization processes is to investigate the role of surfactants and flow dynamics on a very basic level. To minimize the complexity and possible external influencing factors at the beginning, the investigations were carried out on individual droplets in a microfluidic channel.

The experiments showed that increasing the surfactant concentration in the dispersed oil phase increased the nucleation efficiency of the CMN. In contrast, increasing the surfactant concentration in the aqueous continuous phase resulted in a decrease in nucleation efficiency. In addition, higher relative velocities between the collision partners (droplets and particles) were associated with a higher probability of nucleation. These results illustrate the importance of flow dynamics for CMN. Further investigations should therefore be carried out under flow conditions similar to industrial conditions.

In addition, the influence of the charge of the surfactant molecules on the CMN in the microfluidic structure was demonstrated. Compared to nonionic surfactants, the use of charged, ionic emulsifiers resulted in higher contact times and contact forces being required to trigger CMN. This is consistent with the expectation that the charge introduced at the interface should increase the repulsive forces between the two reactants. All other things being equal, this should lead to lower nucleation efficiencies.

In the second step, the findings observed on individual droplets were transferred to a droplet collective in a laminar flow field. For this purpose, two temperature-controlled shear cells in the design of a Taylor-Couette reactor were developed and each integrated into a nuclear magnetic resonance spectrometer. This enabled the targeted application of a laminar shear field to the droplet collective and thus the directed investigation of the influencing factors. The aim was not to investigate the rheology of the emulsion but to describe the influence of the flow on a tempered emulsion with a semi-crystalline dispersion phase in a temperature range in which no spontaneous nucleation took place.

The results showed that increasing the shear rate in the laminar range initially promoted CMN. However, after reaching a maximum nucleation rate, further increases in shear rate led to a decline. The shear rate at which the maximum nucleation rate occurred depended on the proportion of dispersed phase present in the emulsion. Lower dispersed phase content required higher shear rates to reach the maximum nucleation rate. Additionally, increasing the emulsifier concentration in the continuous phase enhanced the nucleation rate. Doubling the aqueous surfactant concentration increased the nucleation rate by 30% to 400%, depending on the shear rate.

In the last step of the transfer to the controlled use of CMN on an industrial scale, the effects of transient and turbulent flow on the crystallization dynamics in oil-in-water emulsions were investigated. These experiments were carried out in a stirred tank equipped with an ultrasonic probe to detect the crystallization progress of the dispersed phase.

By providing a particle fraction, the nucleation rate of the CMN could be determined, excluding influences from spontaneous or shear-induced nucleation. A second order kinetics approach described the nucleation kinetics of the dispersed phase at low supercooling, assuming CMN as the sole nucleation mechanism. At higher supercooling ($\Delta T > 14$ K), no existing model could describe the evolution of the solid fraction due to the simultaneous occurrence of multiple nucleation mechanisms.

In addition to homogeneous primary nucleation caused by supercooling, shear-induced nucleation and secondary crystallization by CMN were also identified to take place in the stirred vessel. The proposed Weibull model demonstrated superior fitting performance ($R^2 > 0.95$) across all experiments compared to existing literature models.

For the first time, this study showed that increasing the mean energy dissipation (up to $\bar{\epsilon} = 0.37\,\mathrm{W\,kg^{-1}}$) and the micelle concentration in the aqueous phase (up to $\tilde{c}^{aq}_{\mathrm{TW20}} = 24\,\mathrm{mol\,m^{-3}}$, corresponding to 407 cmc) led to accelerated nucleation kinetics. As a result, the process times until complete crystallization of the dispersed phase could be shortened. The nucleation efficiency declined despite the increased collision frequency at higher energy input.

Shear-induced nucleation, which occurred particularly during the early stages of crystallization with large droplets and high shear, was shown to be an essential mechanism for generating particles in addition to primary nucleation. The generated particles acted as collision partners for the CMN in later stages of the process.

For the experimental setups in this work, it was demonstrated that the nucleation rate was comparable across laminar, transient, and turbulent flow regimes. Thus, scale transfer for investigating CMN is feasible if comparable shear rates are maintained. This enables the study of processes on an industrial scale in laboratory experiments.

In summary, this study offers valuable insights for the industrial production of suspensions. In particular, the results highlight the advantages of an increased input of mechanical energy to shorten the cooling phase and reduce the cooling capacity in suspension production processes. The integration of these findings into industrial practice promises a more efficient and reliable droplet crystallization of melt emulsions. Future research can build on these findings to develop advanced crystallization control strategies with the potential to transform production processes across industries.

Kurzfassung

Im Hauptfokus der Arbeit liegt die energie- und zeiteffizientere Gestaltung des Herstellungsprozess von Suspensionen mit Partikeln im Mikrometerbereich. Klassisches Herstellverfahren dieser Suspensionen sind ressourcenintensive Nassmahlverfahren. Eine kostengünstigere Alternative hierzu ist das Schmelzemulgieren. In diesem Prozess werden grobe Partikel aufgeschmolzen, emulgiert und dann durch Abkühlen auf Temperaturen weit unter ihrem Schmelzpunkt in kleinere Partikel als zuvor umgewandelt. Dabei kann die Partikelgrößenverteilung eingestellt werden. Jedoch kommt es häufig zu einer unvollständigen Tropfenkristallisation, was das Auftreten von kolloidalen Prozessen während der Lagerung und des Transports der Dispersion begünstigt. Diese Instabilitätsmechanismen können zum Verlust der Anwendungseigenschaften führen. Die vorliegende Arbeit setzt hier an und hat zum Ziel, ein Konzept zu entwickeln, mit dem eine vollständige Tropfenkristallisation im Herstellungsprozess gewährleistet werden kann, um so Schwankungen der Produktqualität zu minimieren.

Es gibt mehrere Methoden, die Kristallisation der Tropfen auszulösen: Zum Beispiel kann der Zusatz von geeigneten Tensiden und die Zugabe externer Substanzen die Kristallisation begünstigen. Während die Kristallisationseffizienz in Bezug auf den Feststoffanteil der Tropfen mit den genannten Methoden verbessert werden konnte, konnte die für die Tropfenkeimbildung erforderliche Unterkühlung nicht wesentlich verringert werden. Ein neuer und vielversprechender Ansatz zur Effizienzsteigerung des Schmelzemulsionsprozesses ist die kontaktinduzierte Keimbildung (engl.: contact-mediated nucleation, kurz: CMN). Dieser Mechanismus beschreibt die Kristallisation unterkühlter Tropfen durch kurzzeitigen Kontakt mit einem bereits kristallisierten Tropfen (d. h. einem Partikel). CMN tritt bereits bei deutlich niedrigeren Unterkühlungen, und damit höheren Temperaturen, als die primäre Keimbildung auf. Der gezielte Einsatz von CMN bietet damit die Möglichkeit zur Energieeinsparung, zu kürzeren Prozesszeiten und trägt somit zu einem nachhaltigeren Herstellungsprozess bei. Obwohl CMN bereits in der Literatur beschrieben wurde, gibt es keine systematische Untersuchung des Mechanismus. Im Speziellen wurde der Einfluss der Strömung auf die CMN nicht betrachtet. Dies ist Schwerpunkt der vorliegenden Arbeit.

Um die CMN im Hinblick auf die Keimbildungseffizienz umfassend zu charakterisieren, müssen mehrere Aspekte berücksichtigt werden:

- Das in der Literature beschriebene Wissen über Koaleszenzprozesse von Flüssigkeitstropfen macht deutlich wie wichtig es ist, den Einfluss des Strömungsfelds zu untersuchen. Die im Prozess vorliegende Strömung beeinflusst die Relativgeschwindigkeit zwischen Partikel und Tropfen und hat somit einen Effekt auf die Kontaktkraft, die Kontaktzeit und die Kollisionsfrequenz.

- Unter der Voraussetzung, dass die Koaleszenztheorie auf die CMN übertragbar ist, sollten auch Parameter wie die Zusammensetzung der kontinuierlichen und dispergierten Phasen die CMN beeinflussen.

Die vorliegende Arbeit besteht aus drei Hauptabschnitten, die sich mit der gezielten Untersuchung der Strömungseffekte auf die CMN in unterschiedlichen Versuchsanordnungen und Maßstäben beschäftigen:

Der erste Schritt zur Charakterisierung der CMN hinsichtlich ihrer Einsatzfähigkeit in industriellen Kristallisationsprozessen ist die Untersuchung der Rolle der Tenside und die der Strömungsdynamik. Um zu Beginn die Komplexität und die möglichen weiteren externen Einflussfaktoren zu minimieren, werden die Untersuchungen an Einzeltropfen in einem Mikrofluidikkanal durchgeführt.

Die Versuche zeigten, dass eine Erhöhung der Tensidkonzentration in der dispergierten Ölphase die Keimbildungseffizienz der CMN steigert. Die Erhöhung der Tensidkonzentration in der wässrigen kontinuierlichen Phase führte hingegen zu einer Verringerung der Keimbildungseffizienz. Darüber hinaus konnten höhere Relativgeschwindigkeiten zwischen den Kollisionspartnern (Tropfen und Partikel) mit höheren Keimbildungswahrscheinlichkeiten in Verbindung gebracht werden. Diese Ergebnisse verdeutlichen die Bedeutung der Strömungsdynamik für die CMN. Weitere Untersuchungen sollten daher unter Strömungsbedingungen durchgeführt werden, die den industriellen Bedingungen ähneln.

Zudem konnte der Einfluss der Ladung der Tensidmoleküle auf die CMN im Mikrofluidikaufbau nachgewiesen werden. Der Einsatz geladener, ionischer Emulgatoren hatte, im Vergleich zu nichtionischen Tensiden, zur Folge, dass höhere Kontaktzeiten und Kontaktkräfte benötigt wurden um CMN auszulösen. Dies stimmt mit der Erwartung überein, da die eingebrachte Ladung an der Grenzfläche die abstoßenden Kräfte zwischen den beiden Reaktionspartner erhöhen sollte. Bei sonst gleich bleibenden Bedingungen, sollte dies zu geringeren Nukleationseffizienzen führen.

Im zweiten Schritt wurden die an Einzeltropfen beobachteten Erkenntnisse auf ein Tropfenkollektiv im laminaren Strömungsfeld übertragen. Hierfür wurden zwei temperierbare Scherzellen in der Bauart eines Taylor-Couette Reaktors entwickelt und in jeweils ein Kernspinresonanz-Spektrometer integriert. Dies ermöglichte die gezielte Applikation eines laminaren Scherfelds auf das Tropfkollektiv und so die gerichtete Untersuchung der Einflussfakotren. Ziel war dabei nicht die rheologische Untersuchung der Emulsion, sondern die Beschreibung des Einflusses der Strömung auf eine tempertierte Emulsion mit teilkristalliner Dispersphase in einem Temperaturbereich, in dem keine spontane Keimbildung stattfand.

Die Ergebnisse zeigten, dass eine Erhöhung der Schergeschwindigkeit im laminaren Bereich anfänglich die CMN fördert. Nach Erreichen einer maximalen

Keimbildungseffizienz durch CMN führte eine weitere Steigerung der Schergeschwindigkeit zu einer Absenkung der Keimbildungsrate. Die Schergeschwindigkeit, bei der die maximale Keimbildungsrate auftrat, war dabei abhängig davon, welcher Dispersphasenanteil in der Emulsion vorhanden war. Ein geringerer Dispersphasenanteil erforderte eine höhere Schergeschwindigkeit, um die maximale Keimbildungsrate zu erreichen.

Auch konnte eine Steigerung der Keimbildungsrate durch eine Erhöhung der Emulgatorkonzentration in der kontinuierlichen Phase erzielt werden. Eine Verdopplung der wässrigen Tensidkonzentration konnte die Keimbildungsrate, in Abhängigkeit der Schergeschwindigkeit, um 30 - 400% steigern.

Im letzten Schritt des Transfers zum kontrollierten Einsatz der CMN im industriellen Maßstab, wurden die Auswirkungen transienter und turbulenter Strömung auf die Kristallisationsdynamik in n-Hexadekan-in-Wasser-Emulsionen untersucht. Diese Versuche wurden in einem Rührkessel durchgeführt, der mit einer Ultraschallsonde zur Detektion des Kristallisationsfortschritts der Dispersphase ausgestattet war.

Durch Vorgabe einer Partikelfraktion konnte die Keimbildungsrate der CMN unter Ausschluss von Einflüssen durch spontane oder scherinduzierte Nukleation bestimmt werden. Eine Kinetikansatz 2. Ordnung konnte die Kristallisationskinetik bei geringen Unterkühlungen beschreiben, sofern ausschließlich CMN auftrat.

Bei höheren Unterkühlungen ($\Delta T > 14$ K) konnte kein in der Literatur beschriebenes Modell gefunden werden, welches den zeitlichen Verlauf des Dispersphasenfeststoffanteils beschreiben konnte. Dies lag am gleichzeitigen Auftreten verschiedener Nukleationsmechanismen. Neben der homogenen primären Nukleation, die durch die Unterkühlung hervorgerufen wird, konnten auch scherinduzierte Nukleation und sekundäre Kristallisation durch CMN identifiziert werden. Das vorgeschlagene Weibull-Modell zeigte, im Vergleich zu bestehenden Literaturmodellen, eine überlegene Anpassungsleistung ($R^2 > 0{,}95$) über alle Experimente hinweg.

Erstmalig konnte gezeigt werden, dass die Erhöhung der mittleren Energiedissipation (bis zu $\bar{\epsilon} = 0{,}37\,\mathrm{W\,kg^{-1}}$) und der Mizellenkonzentration in der wässrigen Phase (bis zu $\tilde{c}_{\mathrm{TW20}} = 24\,\mathrm{mol\,m^{-3}}$, entsprechend 407 cmc) zu einer beschleunigten Kristallisationskinetik führten. Dadurch konnten die Prozesszeiten bis zur vollständigen Kristallisation der dispergierten Phase verkürzt werden. Trotz der erhöhten Kollisionsfrequenz bei höherer Energieeinbringung nahm die Kollisionseffizienz ab.

Die scherinduzierte Nukleation, die besonders zu Beginn der Kristallisation bei großen Tropfen und hoher Scherung auftrat, erwies sich neben der primären Nukleation als wesentlicher Mechanismus zur Erzeugung von Partikeln. Die generierten Partikel dienten im weiteren Prozessverlauf als Kollisionspartner für die CMN.

Für die Versuchsaufbauten in dieser Arbeit konnte eine Vergleichbarkeit der Keimbildungsrate in laminaren, instationären und turbulenten Strömungsregimen gezeigt werden. Somit ist eine Maßstabsübertragung für die Untersuchung der CMN möglich, wenn vergleichbare Scherraten vorherrschen. Damit ist es möglich, die Prozesse im industriellen Maßstab in Laborexperimenten zu untersuchen.

Zusammenfassend liefert diese Studie wertvolle Erkenntnisse für die industrielle Herstellung von Suspensionen. Insbesondere zeigen die Ergebnisse die Vorteile einer erhöhten Einbringung mechanischer Energie zur Verkürzung der Kühlphase und Verringerung der Kühlleistung in Herstellungsprozessen von Suspensionen. Die Integration dieser Erkenntnisse in der industriellen Praxis verspricht eine effizientere und zuverlässigere Kristallisation von Schmelzemulsionen. Künftige Forschungsarbeiten können auf diesen Erkenntnissen aufbauen, um fortschrittliche Strategien zur Steuerung der Kristallisation zu entwickeln, die das Potential haben, Produktionsverfahren branchenübergreifend zu verändern.

Acknowledgment

I extend my heartfelt thanks to everyone who supported me during my time at the Institute for Thermal Process Engineering:

Prof. Dr.-Ing. Matthias Kind — thank you for your exceptional guidance and constant support; your insights were invaluable to this work.

Apl. Prof. Dr. Gisela Guthausen — thank you for your extraordinary support throughout my master's and doctoral studies; the NMR results in this thesis would not have been possible without your collaboration.

To my colleagues — **Christoph**, **David**, **Nicolas**, **Hendrik**, and **Daniel** — thank you for the coffee breaks (and ice creams), your attentive ears, and your unwavering support. I am also grateful to **Monika** and **Oliver** for your motivating conversations during the months we shared an office. Special thanks to **Konrad** for your essential support with the simulations.

To the members of the mechanical and electrical workshops, especially **Max** and **Sabrina** — thank you for your constructive collaboration and reliable support.

To my students — **Sophia**, **Philipp**, **Richy**, **Laurids**, **Thomas**, **Tibor**, **Kasia**, **Anisa**, **Theresa**, **Alex**, **Martin**, **Raphael**, **Chunyang**, **Konstantinos**, **Zeynep**, **Marla**, **Judith**, **Linda**, **Tianzhao**, and **Timur** — your dedication and hard work significantly strengthened the quality of the results; working with you was a joy.

Prof. Dr.-Ing. Heike Petra Karbstein and **Jasmin** of the Institute for Food Engineering — thank you for your productive collaboration on our joint project.

I also gratefully acknowledge funding from the **Arbeitsgemeinschaft industrieller Forschungsvereinigungen (AiF)**. To the project steering committee — especially **ppa. Dr. Holger Klyszcz-Nasko** and **Dr.-Ing. Hans Breisig** — thank you for your support.

Dr. Thomas Oerther and **Dr. Klaus Zick** from the micro-imaging group at Bruker — thank you for your swift and comprehensive assistance with all RheoNMR questions and equipment.

The **KHYS Travel Grant** — thank you for your support in funding my research stay at the University of Strathclyde in Glasgow, UK. **Prof. Dr. Jan Sefcik** — thank you for welcoming me into your group for four months and for your exceptional guidance and support. **Laura**, **Andrew**, and all CMAC colleagues — thank you for making my time in Glasgow unforgettable.

Jule and **Chris** — thank you for your unwavering support since day one of my studies. A chance encounter became a unique friendship I treasure; I could not imagine better friends by my side.

Kirsten and **Eva** — thank you for standing by me since my bachelor's thesis and for your steady encouragement and support over the years — and, I hope, for many more to come as close friends.

My husband **Till** — thank you for your constant support, for your patience through my many discussions, and for your endless daily encouragement.

My family — my parents, **Regine** and **Thomas**; my brother, **Leon**; my grandfather, **Rolf**; and my grandmothers, **Nonna** and **Rosel** — thank you for your unwavering support, for countless rounds of proofreading, and for listening to my practice talks.

This thesis would not have been possible without the contributions of all these people — and many others not named here. Thank you.

Contents

Abstract . . . . **iii**

Kurzfassung . . . . **ix**

Acknowledgment . . . . **xv**

Acronyms and symbols . . . . **xxi**

1 Crystallization in Emulsions **1**
- 1.1 Crystallization of melt emulsions 1
- 1.2 Theoretical background of crystallization 3
- 1.3 Multi-phase dispersed systems 7
- 1.4 Challenges and aims of this work 10

2 Contact-Mediated Nucleation **15**
- 2.1 General description of CMN 15
- 2.2 Impact of CMN on emulsion crystallization 17
- 2.3 Models used to describe droplet crystallization in stirred emulsions 20
- 2.4 Experimental plan 25

3 Microfluidics **29**
- 3.1 Working hypothesis 29
- 3.2 Experimental approach and measurement system 31
  - 3.2.1 Experimental setup 31
  - 3.2.2 Experimental procedure 32
  - 3.2.3 Flow in microfluidic channels 36
- 3.3 Transfer of coalescence theory to CMN 39

3.4 Surfactant distribution in emulsions 42
3.5 Dependency of CMN on surfactant concentration and surfactant charge 46
    3.5.1 Surfactants initially dissolved in continuous phase 50
    3.5.2 Surfactants initially dissolved in dispersed phase 56
3.6 Dependency of CMN on contact force 60
    3.6.1 Empty channel 61
    3.6.2 Solid particle in channel 63
    3.6.3 Moving droplets 64
    3.6.4 Differential pressure during droplet crystallization 66
3.7 Conclusion 71

4 RheoNMR 73
4.1 Working hypothesis 73
4.2 Materials and methods 75
    4.2.1 Emulsion preparation 76
    4.2.2 Measurement setup 77
    4.2.3 Flow variables in the TCR 83
4.3 Results and discussion 87
    4.3.1 Primary nucleation kinetics 88
    4.3.2 Impact of shear on efficiency of CMN 91
    4.3.3 Impact of collision frequency on CMN 95
    4.3.4 Impact of surfactant concentration on CMN 98
4.4 Conclusion 101

5 Stirred Vessel 103
5.1 Working hypothesis 103
5.2 Materials and methods 104
    5.2.1 Experimental setup and material system 104
    5.2.2 Ultrasonic measurements of the solid fraction of the dispersed phase 108
    5.2.3 Flow and mixing characteristics in stirred vessels 111
    5.2.4 Droplet deformation in Stirred Vessels 114
5.3 CMN in the industry-like stirred tank 118
    5.3.1 CMN without primary nucleation 118

5.3.2 Coupling of CMN and primary nucleation 122
5.4 Conclusion 135

6 Summary and Outlook 137

A Appendix 141
A.1 General parameters and assumptions used for the calculations. . 142
A.1.1 Measurements of the density and the viscosity 144
A.1.2 Determination of the interfacial tension 146
A.1.3 Solubility of n-hexadecane in water 148
A.2 Nuclear Magnetic Resonance 151
A.2.1 Basics of NMR 151
A.2.2 Concentration measurements of TW20 in water 153
A.2.3 Additional information for RheoNMR measurements . . 154
A.3 Derivation of the fitting models for $\xi(t)$ 157
A.3.1 1Exp model for a given droplet size 157
A.3.2 1Exp for droplet size distributions 158
A.4 Microfluidics 160
A.4.1 Experimental raw data 160
A.4.2 Impact of relative velocity on induction time 163
A.4.3 Flow regime in microfluidic channel 164
A.4.4 Description of droplet hugging particle 164
A.4.5 Numeric Flow Simulations 165
A.5 Ultrasonic measurements in the stirred vessel 171
A.5.1 Determination of the speed of sound 171
A.5.2 Calculation of the solid fraction of the dispersed phase . 173
A.5.3 Optimization of measurement setting 175
A.6 Emulsion I and II 177
A.7 Surfactant information 178

List of Figures 181

List of Tables 185

List of Publications 187
Journal articles 187

Conference contributions 188

Bibliography **191**

Acronyms and symbols

Acronyms

1Exp	one exponential
ANC	active nucleation center
BSA	bovine serum albumin
CFD	computational fluid dynamics
cmc	critical micelle concentration
CMN	contact-mediated nucleation
CNT	classical nucleation theory
CTAB	Cetyltrimethylammonium bromide
DLVO	Derjaguin-Landau-Verwey-Overbeek
DSD	droplet size distribution
HSP	Hansen solubility parameter
NMR	nuclear magnetic resonance
O/W	oil-in-water
OSF	oscillating structural and depletion forces
ppm	parts per million

rpm	rounds per minute
SAXS	small-angle X-Ray scattering
SDS	sodium dodecyl sulfate
TCR	Taylor-Couette reator
TW20	Tween®20
TW60	Tween®60
TW80	Tween®80
vol	volume
W/O	water-in-oil
wt	weight

Constants

g	gravitational acceleration: 9.81 m s^{-2}
i	$\sqrt{-1}$
k_B	Boltzmann constant: $1.380649 \cdot 10^{-23}$ J K^{-1}
N_A	Avogadro number: $6.022 \cdot 10^{23}$ mol^{-1}
π	$3.14159\ldots$

Latin symbols and variables

a	number
A	area (m^2)
A_wave	amplitude of ultransonic wave (W^{-2})

$\boldsymbol{b}$	size classes (-)
$\tilde{c}$	molar concentration (mol m^{-3})
$\boldsymbol{D}$	diffusion coefficient (m^2 s^{-1})
$\boldsymbol{d}$	depth (m)
$\boldsymbol{d}_{\mathrm{h}}$	hydraulic diameter (m)
$\boldsymbol{e}$	dimensionless interaction energy (J/J)
$\boldsymbol{E}$	interaction energy (J)
$\boldsymbol{F}$	force (N)
$\boldsymbol{f}$	friction factor (-)
$\boldsymbol{F}_{1/2}$	fitting parameters (*var.*)
$\boldsymbol{f}_{\mathrm{coll}}$	collision frequency (s^{-1})
$\boldsymbol{G}$	Gibbs free energy (J)
$\boldsymbol{GCI}$	grid convergence index (-)
$\boldsymbol{h}_{\mathrm{coll}}$	collision rate (m^{-3} s^{-1})
$\boldsymbol{h}_{\mathrm{d,d}}$	dimensionless distance between to droplets (m/m)
$\boldsymbol{h}_{\mathrm{f}}$	film thickness between particle and wall (m)
$\boldsymbol{H}$	height (m)
$\boldsymbol{H}_{\mathbf{m}}$	melting enthalpy (J mol^{-1})
ΔH_{f}	enthalpy of fusion (J mol^{-1})
$\boldsymbol{I}$	acoustic impedance (N s m^{-3})
$\boldsymbol{Imag}$	imagninary part of a number
$\boldsymbol{j}$	accumulation frequency (s^{-1})

J	nucleation rate (m^{-3} s^{-1})
k	kinetic constant (s^{-1})
K	distribution coefficient (mol/mol)
L	length (m)
m	mass (kg)
M	module (Pa)
$\tilde{M}$	molar mass (kg mol^{-1})
n	volume-based number density (m^{-3})
N	stirring speed (s^{-1})
p	pressure (Pa)
Δp	differential pressure (Pa)
P	probability (-)
P_{W}	power (W)
q_3	volume-weighted size distribution (μm^{-1})
Q_3	volume-weighted size distribution (-)
r	radius (m)
r_{i}	outer radius of inner cylinder (m)
r_{o}	inner radius of outer cylinder (m)
R	radial positions (m)
R^2	coefficient of determination
R_2	transversal relaxation rate (s^{-1})
R_{a}	absolute roughness (μm)

$Real$	real part of a number
R_{Han}	Hansen solubility distance ($MPa^{1/2}$)
s	distance (m)
t	time (s)
t^*	transit time (s)
$\bar{t}$	mean time (s)
T	temperature (K)
T_2	transversal relaxation time (s)
ΔT	supercooling (K)
u	velocity ($m\ s^{-1}$)
$\bar{u}$	mean velocity ($m\ s^{-1}$)
Δu	relative velocity ($m\ s^{-1}$)
U	perimeter (m)
v	speed of sound ($m\ s^{-1}$)
V	volume (m^3)
$\dot{V}$	volumetric flow ($m^3\ h^{-1}$)
W	width (m)
x	droplet/particle diameter (m)
$x_{3,2}$	Sauter diameter (m)
$x_{50,3}$	volume-based mean diameter (m)
z	distance traveled by ultrasonic wave (m)
Z	Zeldovich factor (-)

Greek symbols and variables

α	shape parameter of the Weibull model (-)
α_{wave}	attenuation constant (m^{-1})
β	collision kernel ($m^3\ s^{-1}$)
χ	factor of heterogeneity (-)
δ_{c}	chemical shift (ppm)
$\delta_{\mathrm{Han,d}}$	Hansen solubility parameter describing dispersion forces ($MPa^{1/2}$)
$\delta_{\mathrm{Han,h}}$	Hansen solubility parameter describing hydrogen bonding interactions ($MPa^{1/2}$)
$\delta_{\mathrm{Han,p}}$	Hansen solubility parameter describing dipole-dipole interactions ($MPa^{1/2}$)
$\dot{\gamma}$	shear rate (s^{-1})
ϵ	energy dissipation ($W\ kg^{-1}$)
$\bar{\epsilon}$	mean energy dissipation ($W\ kg^{-1}$)
η	dynamic viscosity ($N\ s\ m^{-2}$)
γ	interfacial tension ($N\ m^{-1}$)
$\boldsymbol{\Gamma}$	surface loading ($mol\ m^{-2}$)
κ	compressibility (Pa^{-1})
λ_{CMN}	nucleation efficiency (-)
λ_{turb}	Kolmogorov vortices (m)
λ_{wave}	wavelength (m)

μ	chemical potential (J mol^{-1})
ν	kinematic viscosity (m^{2} s^{-1})
$\boldsymbol{\Phi}$	volumetric fraction (m^{3}/m^{3})
$\boldsymbol{\Pi}$	disjoining pressure (Pa)
ρ	density (kg m^{-3})
σ	span of a distribution (*var.*)
τ	shear stress (Pa)
τ_{η}	Kolmogorov time (s)
ϑ	temperature (°C)
φ	correction factor for pipe friction coefficient in channels with non-circular cross-sections (-)
ξ	solid fraction (-)

Dimensionless numbers

$\mathbf{Ca}$	Capillary number (Equation 5.12)
$\mathbf{Fr}$	Froude number (Equation 5.6)
$\mathbf{Ne}$	Newton number (Equation 5.4)
$\mathbf{Oh}$	Ohnesorge number (Equation 5.15)
$\mathbf{Re}$	Reynolds number (Equations 3.4, 4.3 and 5.5)
$\mathbf{We}$	Weber number (Equation 5.14)

Subscripts

0	initial
2000	after 2000 s
5000	after 5000 s
1p	one particle
2p	two particles
al	aluminum
aq	aqueous
body	body
bridge	liquid bridge between droplet and particle
c	chemical
ca	capillary
cap	cap
channel	channel
clust	cluster
CMN	contact-mediated nucleation
coll	collision
comp	compression
conti	continuous
crit	critical
cryst	crystal

cs	cross-sectional
cyl	cylinder
d	droplet
def	deformation
disp	dispersed
dj	disjoining
ec	empty channel
el	electrostatic
ela	elasticity
em	emulsion
exp	experiment
f	fluid
flow	flow
gap	gap
H2O	water
het	heterogeneous
hex	n-hexadecane
hom	homogeneous
i	inner
if	surface/interface
imp	impurities
ind	induction

int	integral
ip	impulse
l	liquid
lam	laminar
loc	local
m	melting
mag	magnitude
max	maximal
mic	micelle
min	minimal
nuc	nucleation
o	outer
osc	oscillatory
prim	primary
prob	probe
refl	reflected
s	solid
sm	small molecule
st	stirrer/impeller
surf	surfactant
surface	surface
tip	tip

total	total
turb	turbulent
V	volume
VdW	van-der-Waal
ves	vessel
w	wetted
WB	Weibull model
x, y, z	direction in a Cartesian coordinate system

1 Crystallization in Emulsions

This chapter introduces the fundamental concepts of crystallization and nucleation in general and in regard to emulsions. It provides an overview of models assessing nucleation rates in quiescent emulsions and explains collision effects in emulsions.

An emulsion is defined as a system comprising two inherently immiscible liquid phases. The dispersed phase is finely distributed in the form of droplets within the continuous phase, and these droplets are stabilized by a surfactant. Complete crystallization of the dispersed phase converts an emulsion into a suspension. In this work, all dispersions with purely liquid or partially crystalline dispersed phases are called emulsions. This terminology emphasizes the continuing potential of these dispersions for further crystallization processes.

1.1 Crystallization of melt emulsions

Emulsions with crystalline dispersed phases (i.e., suspensions) are widely used in industrial processes. They play a significant role in the fields of food, cosmetics (Müller et al. (2007)), pharmaceuticals (for example as solid-liquid nanoparticles) (Almeida and Souto (2007), Pardeike et al. (2009)), petroleum as well as metal processing, as they are used as lubricants (an overview can be found in Försters and von Rybinsky (1998), Hong et al. (2023)). In recent years, they have also been used as phase change materials for intermediate thermal energy storage (Delgado et al. (2012), Müller (2000)).

Suspensions with small particles in the range of a few micrometers are often prepared by time- and energy-intensive wet milling processes. A more cost-effective process is melt emulsification (Figure 1.1), in which coarse particles are melted by heating, then emulsified, and then converted into smaller particles by cooling them far below the melting point (Köhler and Schuchmann (2012)).

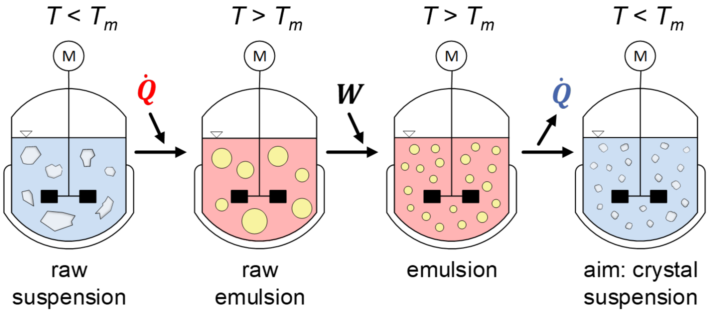

Figure 1.1: Schematic illustration of the melt emulsification process with the corresponding temperatures T to the melt temperature of the dispersed phase T_m.

In the first step, the coarsely dispersed solid phase and the continuous phase (raw suspension) are heated above the melting temperature T_m of the dispersed phase. Consequently, the solid dispersed phase is transformed into a dispersed liquid phase (melt) and further emulsified by common emulsification methods and stabilized using surface-active substances (surfactants). The desired properties of the melt emulsion, such as droplet size distribution, are adjusted during this process. One advantage of incorporating the phase transition into the liquid phase instead of the direct grinding of the dispersion phase of the initial suspension is the lower energy consumption for adjusting the particle size and new possibilities for product formulation (Köhler and Schuchmann (2012)). For instance, active ingredients can be uniformly incorporated in the liquid state and subsequently encapsulated within the solidified particle. This is particularly significant for applications in the pharmaceutical industry or in the increasingly popular sector of functional foods (Weiss et al. (2008), Dickinson (2015), Cheon et al. (2023)).

To utilize the aforementioned advantages of the process, it is crucial to convert the finely dispersed droplets back into the solid, often crystalline state (crystal suspension) during the final cooling step. This final step is crucial for achieving the desired product properties. Incomplete or uncontrolled crystallization can lead to loss of quality or instability of the product (Figure 1.2) (Mehnert and Mäder (2012)).

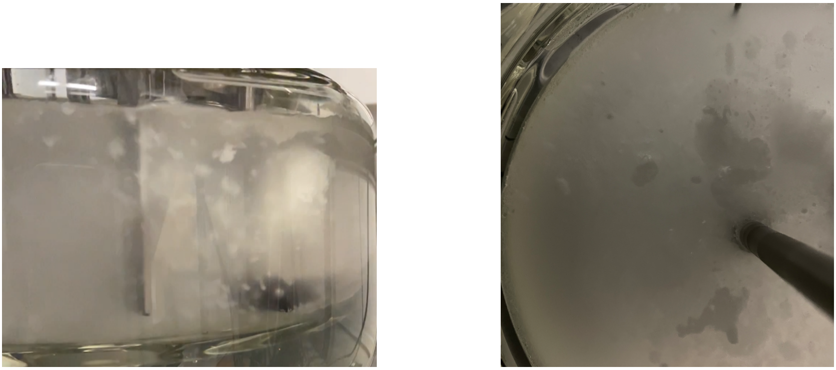
(a) Side view.

(b) Top view.

Figure 1.2: Images of dispersions where instability mechanisms such as post-crystallization aggregation of the solid particles or pre-crystallization coalescence of the liquid droplets happened. The emulsion is broken and has lost its applicability.

1.2 Theoretical background of crystallization

The Classical Nucleation Theory (CNT), formulated by Volmer and Weber (1926), Zeldovich (1992), Becker and Döring (1935), states that crystal nuclei form spontaneously in a homogeneous phase through random molecular collisions. These collisions lead to transiently stable, homogeneous, and spherical molecular aggregates with defined radii, known as clusters. When a cluster reaches a critical radius r_{crit}, attachment and detachment probabilities of further molecules become equal. Beyond r_{crit}, crystal growth occurs as the attachment of additional nuclei becomes energetically more favorable.

The free enthalpy ΔG required to form a cluster is the sum of the free volume enthalpy due to the phase transition ΔG_{V} and the free surface enthalpy ΔG_{if}. ΔG_{if} must be spent to create a new interface between the liquid and solid phases (Figure 1.3) (Mullin (2002), Mersmann (2001)). The critical free enthalpy

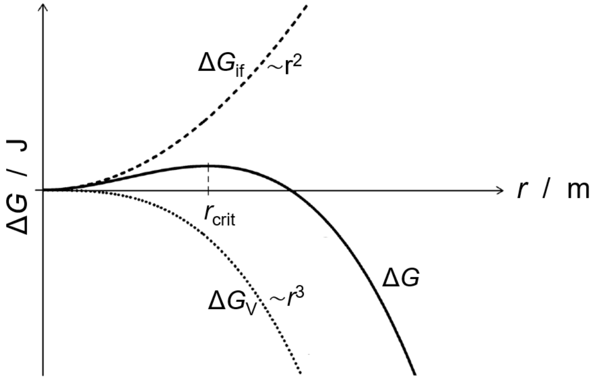

Figure 1.3: Schematic illustration of the free enthalpy ΔG as a function of the cluster radius r_{clust}. The critical radius r_{crit} and the corresponding critical free enthalpy are labeled. The dashed line represents the exemplary course of the surface free enthalpy ΔG_{if} and the dotted line, the course of the volume free enthalpy ΔG_{v}.

ΔG_{crit} required to form a critical spherical nucleus can be determined by

$$\Delta G_{\mathrm{crit}} = \chi \cdot 16\pi \frac{\gamma_{\mathrm{sl}}^3}{3(\Delta\mu)^2} \left(\frac{\tilde{M}_{\mathrm{cryst}}}{\rho_{\mathrm{cryst}}} \right)^2 . \tag{1.1}$$

γ_{sl} corresponds to the interfacial tension between the solid and liquid phases, $\tilde{M}_{\mathrm{cryst}}$ represents the molar mass of the crystalline phase, ρ_{cryst} denotes the density of the crystalline phase, and $\Delta\mu$ represents the difference of the chemical potentials of the liquid μ_l and solid μ_s phase ($\Delta\mu = \mu_\mathrm{l} - \mu_\mathrm{s}$).

The factor of heterogeneity χ extends CNT for heterogeneous nucleation. χ corresponds to the volume ratio of a dome-shaped nucleus on a substrate to a solid sphere of the same radius. χ can assume values between 0 (indicating that the nucleus has no catalytic effect on the substrate) and 1 (indicating complete wetting) (Volmer and Weber (1926), Mullin (2002)).

For melts, an approximation of the chemical potential $\Delta\mu$ by Clausius-Clapeyron is permissible:

$$\Delta\mu(T) = \frac{\Delta H_\mathrm{m}(T_\mathrm{m} - T)}{T_\mathrm{m}}. \tag{1.2}$$

ΔH_m corresponds to the melting enthalpy. The difference between melting temperature T_m and temperature T is the supercooling ΔT. A detailed derivation of Equation 1.2 can be found in Kashchiev (2000).

In the context of this study, cooling crystallization was employed. In this process, the unstable state is achieved by lowering the temperature below the melting temperature of the dispersed phase T_m. The difference between T_m and the temperature where nucleation occurs is denoted as supercooling ΔT, representing the driving force behind crystallization.

The crystallization process unfolds into two consecutive steps. The initial step is nucleation, followed by crystal growth. When crystals are already in the solution, further crystal nuclei are formed, or crystal growth occurs (e.g., Kind (2003)). Given the small volume of the droplets in this study, crystal growth is negligible at the applied subcooling because the droplets solidify in < 1 s after nucleation. Consequently, the rate-determining step is nucleation. In literature, primary and secondary nucleation mechanisms are distinguished, with primary nucleation further categorized into homogeneous and heterogeneous nucleation (Figure 1.4). Primary homogeneous nucleation describes the kind of nucleation when no impurities are present in the melt or solution.

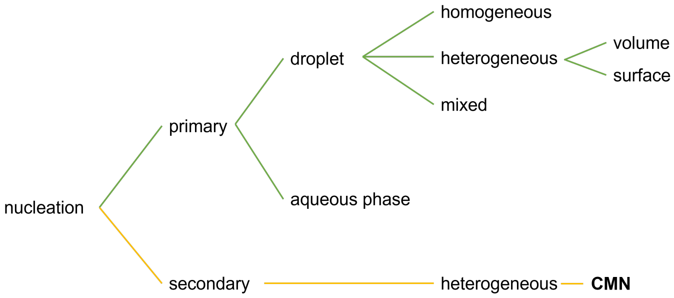

Figure 1.4: Types of nucleation and nucleation mechanisms in melt emulsions.

The nucleation occurs solely via supersaturation (e.g., Hartel (2001)). If the liquid phase encounters impurities, so-called active nucleation centers (ANC) like dust particles, crystals, oil droplets, air bubbles, inverted micelles, or the container surface, nucleation may take place at a higher absolute temperature or supersaturation than anticipated for homogeneous nucleation. This mechanism is called primary heterogeneous nucleation (Walstra (2003)). The ANCs have a different chemical structure from the medium to be crystallized. Heterogeneous nucleation can further be subdivided, taking the location of nucleation into account: Nucleation can occur on the surface, for example, due to surfactants. This effect is called *template effect* (Palanuwech and Coupland (2003), Awad and Sato (2002)). It can also happen in the droplet volume due to impurities dissolved in the dispersed phase. Importantly, both primary homogeneous and primary heterogeneous nucleation can coincide within the same droplet ensemble, contributing to the complexity of the nucleation process in mixed systems.

Secondary heterogeneous nucleation occurs when crystals are already present in a supersaturated solution. The seed crystals' chemical structure is that of the dispersed phase. Thus, contact-mediated nucleation (CMN) is a form of secondary nucleation.

According to the heterogeneous nucleation theory, the formation of stable nuclei is thermodynamically more favorable due to the additional surface than in the pure liquid phase. A lower critical free energy ΔG_{crit} is required to form stable nuclei, leading to a reduced need for supercooling compared to homogeneous nucleation (e.g., McClements (2012)).

In line with CNT, the nucleation rate J can be described as the pace at which critical clusters (i.e., nuclei) form. This is contingent upon the likelihood of a critical cluster being present in the supercooled liquid (thermodynamics) and the subsequent attachment of another molecule to it (kinetics) (Sear (2007)).

$$\begin{aligned} J(T) = j \cdot Z \cdot n_{\mathrm{crit}} = j \cdot Z \cdot n_0 \cdot exp\Big(- \frac{\Delta G_{\mathrm{crit}}}{k_{\mathrm{B}} \cdot T}\Big) \\ = B(T) \cdot exp\Big(- \frac{\Delta G_{\mathrm{crit}}}{k_{\mathrm{B}} T}\Big). \end{aligned} \tag{1.3}$$

The molecular accumulation is dictated by the accumulation frequency j, and n_{crit} describes the number density of critical nuclei. n_{crit} is derived from the number density of potential nucleation centers n_0 and the likelihood of the presence of critical clusters (expressed as an exponential term). The probability of an energy state (in this case, ΔG_{crit}) can be elucidated using the Boltzmann distribution.

Z is known as the Zeldovich factor or disequilibrium factor. With the help of Z, the absence of a stationary cluster distribution due to nucleation is considered (Sear (2007)).

1.3 Multi-phase dispersed systems

Depending on the nature of the dispersed and continuous phase, an emulsion is classified as either an oil-in-water emulsion (O/W) if the dispersed phase is oil or a water-in-oil emulsion (W/O) if the dispersed phase is water. Emulsions are thermodynamically unstable and, without stabilization, separate to minimize free energy. Without stabilization, such as when mechanical energy input ceases, the emulsion undergoes creaming, aggregation, phase inversion, coalescence, and Ostwald ripening, separating into an aqueous and an oily phase.

A stabilized emulsion is achieved by adding surface-active substances known as surfactants or emulsifiers. Surfactants have a molecular structure with both lipophilic and hydrophilic groups. When they are introduced into an aqueous phase with dispersed oil droplets, the surfactant molecules quickly migrate to the oil-water interface and adsorb to it. This adsorbed layer lowers the interfacial tension, facilitates emulsification and helps to stabilize the emulsion against destabilization processes. As soon as the entire interface is covered with surfactant molecules, further surfactant molecules remain as single molecules in the continuous phase until the critical micelle concentration cmc is reached.

At surfactant concentrations in the aqueous phase that exceed the cmc, individual molecules begin to cluster, minimizing their contact area with water by orienting their hydrophobic tails inward. Above the cmc, the concentration of single molecules in solution $\tilde{c}^{aq}_{\mathrm{sm}}$ remains constant at the cmc value. Any further added molecules will be used to form micelles. Micelles act as reservoirs for these additional molecules, allowing a dynamic exchange in which individual molecules continuously move in and out of micelles. This exchange process and the presence of surfactant molecules adsorbed at interfaces facilitate the efficient diffusion of individual molecules to new or unoccupied interfaces. The time required for surfactant molecules to cover newly formed interfaces depends on their diffusion coefficient in the continuous phase and their concentration.

The structure, size, and number of surfactant molecules in micelles depend on the size and molecular structure of the surfactant itself. Specifically, the molar mass and hydrophobicity of the lipophilic portion play a significant role in determining the cmc in the aqueous phase. Additionally, the cmc exhibits a temperature dependence that differs between ionic and nonionic surfactants (e.g., Kim and Lim (2004)). Once the cmc is reached, further addition of surfactant molecules only marginally reduces the interfacial tension (Bąk and Podgórska (2016)).

When the concentration of surfactant molecules dissolved in the emulsion $\tilde{c}_{\mathrm{em}}$ surpasses the cmc, surfactant molecules exist in multiple forms (schematically illustrated in Figure 1.5): (A) as single molecules dissolved in the continuous phase, (B) as micelles in the continuous phase, and (C) adsorbed at the droplet interface. Additionally, in emulsions with dispersed phases, nanodroplets of the dispersed phase may become solubilized within micelles (D). For emulsions with (partially) crystalline dispersed phases, it should be noted that NMR diffusion, relaxation, and spectroscopy studies have shown that fewer surfactant molecules are found at solid-liquid interfaces (E) compared to liquid-liquid interfaces (Kaysan et al. (2022a)). In a static scenario, the concentration of micelles in the aqueous phase $\tilde{c}^{aq}_{\mathrm{mic}}$ can be calculated as the difference between the total added surfactant concentration $\tilde{c}_{\mathrm{em}}$, the concentration of molecules adsorbed at the interface $\tilde{c}_{\mathrm{if}}$ and the concentration of single molecules in solution $\tilde{c}^{aq}_{\mathrm{sm}}$:

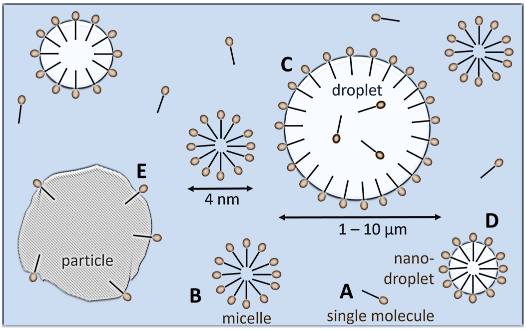

Figure 1.5: Illustration of surfactant species appearing in emulsions with a (semi) crystalline dispersed phase. Note the different sizes of micelles/nanodroplets and droplets. A: single molecule, B: micelle, C: surfactant at the liquid-liquid interface, D: nanodroplet, E: surfactant at the solid-liquid interface.

$$\tilde{c}^{aq}_{\mathrm{mic}} = \tilde{c}_{\mathrm{em}} - \tilde{c}^{aq}_{\mathrm{sm}} - \tilde{c}_{\mathrm{if}}\,. \tag{1.4}$$

The amount of surfactant required to cover one square meter of the oil-water interface is represented by the molar surface loading Γ_{if}, specific to each surfactant. Based on Γ_{if} and the surface area of all droplets (= the dispersed phase) A_{disp}, the concentration of surfactant molecules adsorbed at the interface $\tilde{c}_{\mathrm{if}}$ can be determined:

$$\tilde{c}_{\mathrm{if}} = \Gamma_{\mathrm{if}} \cdot A_{\mathrm{disp}}. \tag{1.5}$$

1.4 Challenges and aims of this work

In addition to well-known parameters from bulk crystallization, such as the material system, cooling profile, and mechanical stress, additional peculiarities must be considered in the crystallization of droplets (Povey (2001)):

- Fragmenting the dispersed phase creates many individual droplets, each nucleating independently.
- Crystallization involves nucleation and the subsequent nucleus growth into a crystal. Unlike bulk crystallization, the crystallization of droplets is significantly dominated by nucleation, as the time required for crystal growth is negligible due to the small volumes and high subcooling (Kashchiev et al. (1994)).
- Dispersing the melt greatly increases interfacial area, making interfacial phenomena and impurity effects more pronounced. For example, nucleation in the dispersed phase can be favored by self-crystallization or certain structural elements of the surfactant (Skoda and van den Tempel (1963)).
- Surfactants enhance the solubility of the dispersed phase in the continuous phase. Consequently, phenomena such as Ostwald ripening or crystallization of the dispersed phase outside the droplets are intensified (Davey et al. (1997), Povey (2001)).

- In emulsified products, there is a distribution of droplet sizes. Depending on the application, emulsions exhibit various time scales on which different types of nucleation dominate (McClements (2012)).
- Nucleation in bulk is favored by active nucleation centers (ANC; e.g., foreign substances, dust, surfaces of walls and fixtures, etc.). The proportion of ANC per droplet is reduced and varies individually by dividing the melt into many individual droplets. This is reflected in significantly higher supercooling of the droplets (Günther et al. (2010)).
- Due to Brownian motion flow, collisions occur between already solidified droplets (particles) and liquid droplets, facilitating their crystallization (McClements et al. (1990)).

The overlapping of all these aspects, combined with the stochastic nature of nucleation, often results in liquid droplets and solid particles existing side by side over a wide temperature range and an extended period during and after the cooling step.

As the previous listing illustrates, there is extensive knowledge in the literature about the qualitative processes and influences in the crystallization of dispersed systems, particularly in the field of food physics and colloid chemistry (see, for example, Kloek et al. (2000), Katsuragi et al. (2001), Shinohara et al. (2008), McClements et al. (1994), Davey et al. (1996)). However, these studies mostly characterized resting samples in milliliter volumes with droplet sizes in the nano- and micrometer range, focusing on individual, isolated influencing factors such as droplet size distribution or surfactant.

In common melt emulsification processes, such as stirred tanks with simple agitators, rotor-stator machines, or high-pressure homogenizers (Köhler and Schuchmann (2012)), larger volumes are involved, and the flow in the vessel can impact the contact of the droplet and the particle. Moreover, mutual interactions of various influencing factors are highly probable regarding emulsion crystallization. The lack of kinetic data, especially under stirred conditions where multiple factors overlap, is a key reason why crystallization design still relies on empirical trial-and-error.

This work investigates melt-emulsion crystallization in stirred systems to obtain an in-depth process understanding. In particular, the impact of stirring, namely shear, must be considered: As the droplets and particles in the system move, they can collide and interact. Different outcomes of such a contact are possible (Figure 1.6). Two (supercooled) droplets may either undergo coalescence (A) after the collision or stay separated (B). According to Chesters (1991), this depends, amongst other factors, on the surfactant concentration. Two solid particles (C) are likely to rebound after contact if the adhesion force is not strong enough or if the contact areas are too small. There is also the possibility that the two solid particles aggregate (D). For the collision of semisolid droplets, it is assumed that crystals at the droplet's surface can penetrate the liquid film between the two reaction partners and lead to complete (E) or partial (F) coalescence. This depends on the strength of the solid network (Boode and Walstra (1993)). Finally, a supercooled droplet may contact a solid particle.

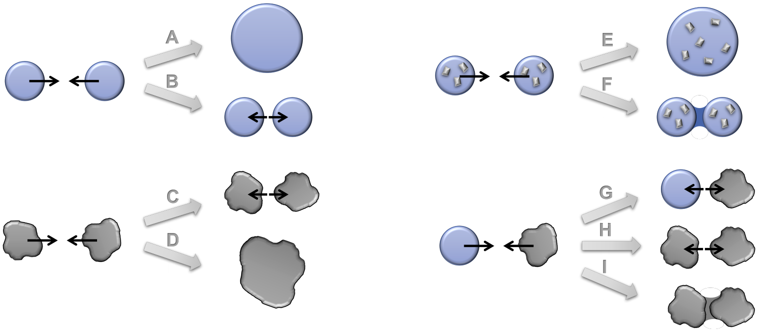

Figure 1.6: Possible outcomes of the collisions in an emulsion with a (semi-)crystalline dispersed phase. The collision of two liquid droplets can lead to coalescence (A) or separation (B). Similarly, the collision of two particles could result in the separation (C) or the aggregation (D). The collision of semi-solid droplets can result in either coalescence (E) or partial coalescence (F). The contact of a supercooled droplet with a particle may lead to separation without (G) or with (H) nucleation, or to aggregation (I).

This kind of contact is the focus of this work. Three outcomes of this contact are possible: The two reaction partners separate after the collision, either without (G) or with (H) nucleation in the supercooled droplet. Still, a liquid bridge could be formed, and no separation, but, besides crystallization, aggregation is taking place (I) (e.g., Kaysan et al. (2020, 2021, 2023b)).

Various methods exist to induce droplet crystallization, such as selecting surfactants or introducing other substances (e.g., Spiegel (2019), Kaysan et al. (2022b)). These methods have already shown promising results in increasing the productivity of the solid fraction of the dispersed phase. However, the required supercooling has seen only a marginal reduction. A new, highly promising strategy to enhance the melt emulsion process is contact-mediated nucleation (CMN). CMN refers to the crystallization of a supercooled droplet triggered by brief contact with a pre-existing crystallized droplet (i.e., a particle). This approach holds great potential for significantly improving industrial processes.

Different aspects must be considered to characterize CMN as a function of nucleation efficiency. Firstly, the relative droplet/particle velocity plays an important role, as the contact force that occurs is strongly dependent on this. For comparable coalescence processes of two liquid droplets, it is already known that contact force, contact time, and collision frequency are important parameters. The listed parameters are influenced by the external flow field. Moreover, parameters like the composition of the continuous and dispersed phases affect this secondary nucleation mechanism.

This work aims not only for faster process times but also for higher product quality. This also increases the solid fraction of the dispersed phase. To gain a deeper understanding of the crystallization processes in melt emulsions used in industrial applications, a systematic investigation of CMN is crucial. This includes a comprehensive parameter study of potential influencing factors, such as surfactant concentration on isolated droplets. Subsequently, the study of CMN in a well-defined flow is necessary to demonstrate the applicability of the findings from single droplets to droplet ensembles. Finally, the results need to be extrapolated to a scenario with a more complex flow. With the knowledge gained from this research, the findings can be scaled up for use in large-scale industrial processes, highlighting the potential impact and relevance of this work.

2 Contact-Mediated Nucleation

This chapter outlines the background of CMN and gives a detailed literature review of the state-of-the-art results and models found for CMN so far.

2.1 General description of CMN

Contact-mediated nucleation (CMN) in the context of emulsion crystallization is a secondary nucleation mechanism initiated by the interaction between a liquid, subcooled droplet, and a preexisting crystallized droplet (i.e., particle). Due to this contact, molecules from the liquid droplet attach to the crystal surface of the crystallized droplet, a process referred to as seeding or nucleation. This leads to crystal growth, resulting in the complete crystallization of the liquid phase of the droplet.

Time-resolved microscopic observation of CMN reveals three distinct stages (Figure 2.1): The droplet moves toward the particle at a temperature below the melting point but above the temperature of spontaneous nucleation. Upon contact, crystals appear and rapidly grow through the droplet until it is fully solidified. Thus, CMN can only occur when contact between a subcooled droplet and a solid particle exists. Particle collisions involving droplets, particles, molecules, etc., necessitate relative motion between them. Such motion may arise from Brownian motion (perikinetic), externally imposed shear (orthokinetic), or velocity differences caused by size- or density-driven settling (Figure 2.2) (Friberg et al. (2004)). The collision rate emerges from the combined influence of these factors. The presence of different densities, droplet

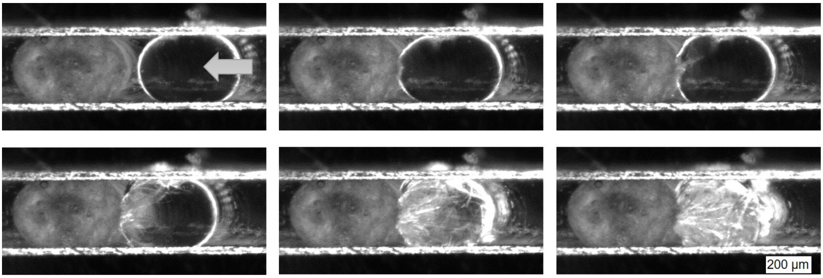

Figure 2.1: Time-resolved images illustrating the CMN. The time between each picture is 0.3 s. The liquid droplet approaches the solid particle. After the contact, CMN takes place. Adapted from Kaysan et al. (2021), CC BY 4.0

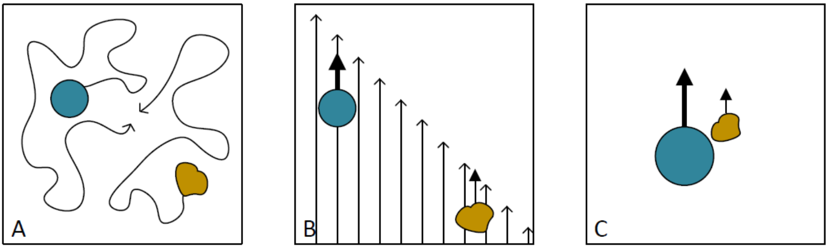

Figure 2.2: Mechanisms of collision between droplets (blue) and particles (brown): (A) perikinetic, (B) orthokinetic, and (C) differential motion (according to Friberg et al. (2004)).

sizes and swarming effects in real melt emulsions leads to additional complexity. Generally, perikinetic effects are less significant for particle sizes above 1 μm when compared to orthokinetic collisions (Levich (1962)). The theoretical description of collision kinetics, starting with the fundamental work of Smoluchowski (1918), was treated in further work for different scenarios (for example, laminar or turbulent flow) (Chesters (1991), Liao and Lucas (2010)) and can be transferred to droplet-particle systems in good approximation (Povey (2001)).

2.2 Impact of CMN on emulsion crystallization

The literature describes different investigations of CMN, which mainly differ in applied shear (unstirred, stirred, or controlled) and in cooling protocols.

- van Boekel and Walstra (1981): Orthokinetic coalescence in a liquid paraffin oil emulsion was investigated. The study emphasized that the duration of encounters was more relevant than the absolute number of encounters. Transferring to this work would mean that contact time is more relevant than the number of contacts.
- McClements et al. (1990): N-hexadecane- and n-octadecane-in-water emulsions with 16.2 wt% oil and 2 wt% TW20 were studied (sauter diameter $x_{3,2} = 0.36 \pm 0.01\,\mu$m). Experiments were performed at 6 °C ($\Delta T = 12.6$ K) in small, assumably unstirred glass cuvettes. A mixture of solid particles and liquid droplets (50:50) led to the crystallization of the subcooled droplets. Crystallization proceeded faster when a single oil was used than when a mixture of oils was present.
- Dickinson et al. (1993): A 20 vol% n-hexadecane-in-water emulsion with 2.5 wt% TW20 was studied ($x_{3,2} = 0.32 — 0.37\,\mu$m). Experiments were done at 4 or 6 °C ($\Delta T = 14.6 — 12.6$ K). An increased aqueous surfactant concentration led to an increased nucleation rate in emulsions with a 50:50 mixture of subcooled droplets and solid particles. Complete droplet crystallization was achieved after 500 h. An increase in the aqueous TW20 concentration was found to accelerate the CMN. Crystallization was faster with TW20 than with sodium dodecyl sulfate (SDS).
- McClements et al. (1994): An n-hexadecane-in-water emulsion stabilized with 3 wt% TW20 was investigated using nuclear magnetic resonance (NMR). Experiments were performed at 6 or 8 °C ($\Delta T = 12.6 — 10.6$ K) with a 50:50 mixture of subcooled liquid and solidified droplets. On the contrary to the mixture, the presence of only subcooled droplets led to no

crystallization. Additionally, the rate of crystallization decreased as mean droplet size increased ($x_{50,3} = 0.5 — 3.5\ \mu$m) but was independent of dispersed-phase volume fraction (Φ_{disp} = 20 — 40%)

- McClements and Dungan (1997): A 30 wt% n-hexadecane-in-water emulsion ($x_{3,2} = 0.34\ \mu$m) was studied by means of NMR. The emulsion was stabilized by TW20. Experiments were performed at 6 °C ($\Delta T = 12.6$ K). There was an increase in the solid fraction when solid particles and subcooled droplets (50:50 mixture) of the same material were present. Complete crystallization of the dispersed phase was found after 175 h, and no change was measurable in the droplet size distribution (DSD) before and after the experiments. The rate of induced nucleation increased with the aqueous surfactant concentration.

- Hindle et al. (2000): A quiescent 25.8 vol% n-hexadecane-in-water emulsion ($x_{3,2} = 0.043 — 0.14\ \mu$m) was investigated. The emulsion was stabilized by TW20 (3.6 vol%). Experiments were performed at 6 °C. A mixture of particles and subcooled droplets led to complete crystallization after 15 days, with some collisions resulting in coalescence.

- Vanapalli and Coupland (2001): A quiescent n-hexadecane-in-water emulsion with 20 wt% n-hexadecane and 2 wt% Tween®20 (TW20) was studied. The droplet size distribution had a median diameter of $x_{50,3}$ = 0.3 μm. The experiments were done at 6 °C ($\Delta T = 12.6$ K) in a concentric cylinder rheometer, with shear rates ranging from 0 to 200 s^{-1}. The crystallization rate of emulsified n-hexadecane was independent of the applied shear rate. The authors mentioned that the chosen shear rates might have been too low to generate a detectable change in the collision rate.

- Hindle et al. (2002): A 20.8 vol% West African cocoa butter oil-in-water emulsion stabilized with 0.8 vol% TW20 was investigated when being either quiescent or stirred at 250 rpm and a temperature of 15 °C

($\Delta T \approx 6.3$ K). It was found that the application of shear led to an increase in the nucleation kinetics.

- Povey et al. (2009): Ultrasonic measurement was employed. The type of surfactant significantly influenced the nucleation rate. The emulsion was gently stirred with a magnetic flea, with no controlled stirring rates.
- Abramov et al. (2017): The study focused on an n-hexadecane-in-water emulsion. Shear rates varied between 50 and 1250 s^{-1}. A rotational rheometer was used, and no crystallization was observed during cooling. Crystallization was not directly measured; changes in dynamic viscosity were noted.

The literature provides several reasons to explain the increase in the solid fraction of the dispersed phase during the simultaneous presence of solid particles and liquid droplets.

The difference in the chemical potential of the solid and liquid dispersed phase is meant to act as a driving force for the solubilization of the liquid dispersed phase in the continuous phase by surfactants (Callen (1985)). On the contrary, McClements and Dungan (1997) commented that this process, similar to Ostwald ripening, should lead to a change of DSD as a function of time, which they did not observe. They postulated that the increase of the solid fraction in the dispersed phase is due to CMN. Dickinson et al. (1993) postulated that CMN happens as a crystal of the solid particle penetrates the liquid interface and consequently induces crystal growth. They stated that CMN is enhanced by forming surfactant bridges between the particle and the droplet and found increasing nucleation rates with increasing aqueous surfactant concentration. Hindle et al. (2000) also tried to explain CMN due to forming a surfactant bridge between the colliding reaction partners, which could also explain their slight change in DSD. Dickinson et al. (1993) found that increasing the surfactant concentration increased nucleation efficiency.

Also, the Derjaguin-Landau-Verwey-Overbeek (DLVO) theory must be considered when describing the approach and contact of two collision partners

(Verwey (1947), Derjaguin and Landau (1993)). The DLVO theory provides a theoretical framework addressing the stability of colloidal systems. It focuses on the interplay of attractive and repulsive forces, such as steric, electrostatic, or van der Waals interactions, between the dispersed particles/droplets.

Dimitrova and Leal-Calderon (1999) found that the forces between droplets in emulsions stabilized with TW20 are only described by the DLVO theory as long as $\tilde{c}^{aq} \leq 50\ cmc$. They hypothesized that micelles accumulated at the interface of the droplets, which increased the repulsive forces. They also found that the addition of β-casein and bovine serum albumin (BSA) resulted in forces that were not consistent with DLVO theory and postulated depletion attraction as the reason for the deviation from DLVO theory for β-casein and steric repulsion for BSA.

In this work, it is assumed that, in analogy with the coalescence theory (Chesters (1991)), the nucleation efficiency of CMN P_{CMN} is mainly influenced by three flow factors: The contact force F_{coll}, the contact time t_{coll} as well as the collision frequency f_{coll}. Besides being a function of the shear rate, F_{coll} and t_{coll} additionally depend on further flow factors. These further flow factors are, for example, the surfactant concentration, the type of surfactant, especially the charge of the head groups, and the surfactant distribution between the dispersed and the aqueous phase. Further factors influencing the CMN can be the type of oil or the composition of the water phase.

2.3 Models used to describe droplet crystallization in stirred emulsions

To date, no model describes emulsion crystallization in stirred vessels; therefore, a comprehensive model incorporating primary, shear-induced, and contact-mediated nucleation is required.

The initial model for describing the time dependence of the solid fraction of the dispersed phase ξ was introduced by Turnbull (1950, 1952), Turnbull and Cormia (1961). Subsequent work by Dickinson et al. (1993, 1996), along with McClements et al. (1993b,a), McClements (1994), McClements et al. (1990), validated the applicability of this model for O/W emulsions.

For emulsions, ξ is the ratio of the volume-based number density of crystallized droplets n_s to the total number density of droplets and particles ($n_\mathrm{s} + n_\mathrm{l}$):

$$\xi = \frac{n_\mathrm{s}}{n_\mathrm{s} + n_\mathrm{l}}. \tag{2.1}$$

For monodisperse particles and droplets, n_s can be calculated as

$$n_\mathrm{s} = \xi \cdot \frac{\Phi_\mathrm{disp}}{\frac{\pi}{6}\, x_\mathrm{s}^3}, \tag{2.2}$$

and, similarly, n_l is determined by

$$n_\mathrm{l} = 1 - \xi \frac{\Phi_\mathrm{disp}}{\frac{\pi}{6}\, x_\mathrm{l}^3}. \tag{2.3}$$

Φ_disp represents the volumetric fraction of the dispersed phase, x_l and x_s display the droplet and particle diameter, respectively.

The primary nucleation rate J_prim in emulsions at a constant subcooling can be determined based on modeling $d\xi/dt$ (Equation 2.4 and 2.5). Assuming exclusively primary homogeneous nucleation, or a single primary heterogeneous mechanism, J_prim is time-independent and similar in all droplets (J_prim = const.). Thus, $d\xi/dt$ can be described by an exponential decay with a kinetic constant for primary nucleation k_prim (Equation 2.4). The derivation can be found in Chapter A.3.1 and A.3.2.

$$\frac{d\xi}{dt} = k_\mathrm{prim} \cdot (1 - \xi). \tag{2.4}$$

k_{prim} can be expressed as a function of J_{prim} (Hindle et al. (2000)). In cases where homogeneous nucleation occurs inside the volume of the droplet, k_{prim} is proportional to the droplets' volume V_{d} and is given by:

$$k_{\mathrm{prim}} = J_{\mathrm{prim}} \cdot V_{\mathrm{d}} = J_{\mathrm{prim}} \cdot x_{\mathrm{l/s}}^{3} \cdot \frac{\pi}{6}. \tag{2.5}$$

Solving the differential Equation (2.4) with the initial condition that at the time of the beginning of the experiments t_0 no solid droplets are present $(\xi(t_0) = 0)$ yields:

$$\xi(t) = 1 - \exp(-k_{\mathrm{prim}} \cdot t). \tag{2.6}$$

This model, known as the 1Exp model, does not account for emulsions with a DSD. As most emulsions have a span of droplet sizes, the nucleation volume (here: droplet volume) is subject to distributions, and each droplet size class experiences a dynamic nucleation rate due to different induction times (time until nucleation happens). Therefore, it is essential to consider DSD in the context of emulsion crystallization (Equation 2.7) (Perepezko et al. (2002)):

$$\xi(t) = 1 - \int_{0}^{\infty} q_{3,0}(x) \cdot \exp(-k_{\mathrm{prim}} \cdot t) \, \mathrm{d}x. \tag{2.7}$$

$q_{3,0}(x)$ denotes the volumetric number-density distribution of droplet diameter at the commencement of crystallization. Given that larger droplets crystallize at lower subcooling than smaller ones, the density distribution of liquid droplets changes as crystallization progresses (Equation (2.8)):

$$\xi(t) = 1 - \int_{0}^{\infty} \Big(\Big(1 - \xi(t_0)\Big) \cdot q_{3,\mathrm{t},0}(x) \; \exp\Big(-J_{\mathrm{prim}} \; V_{\mathrm{nuc}}(x) \; (t - t_0)\Big) \Big) \mathrm{d}x. \tag{2.8}$$

When assuming homogeneous nucleation, V_{nuc} equals the droplets' volume V_{d}. This assumption is valid as the influence of contamination in the droplets, acting as active nucleation centers, can be neglected for droplets consisting of alkanes with purities > 99% (Montenegro and Landfester (2003)).

Hindle et al. (2000) suggest that, when a purity of > 99% is not guaranteed, or ANCs are added, an acceleration of the droplet crystallization due to the number of catalytic impurities a_{imp} must be considered:

$$\xi(t) = \xi_{\max} \cdot \frac{J_{\mathrm{prim},0} \cdot V_{\mathrm{d}} \cdot t}{1 + J_{\mathrm{prim},0} \cdot V_{\mathrm{d}} \cdot t}. \tag{2.9}$$

The term $\xi_{\max}$ (Equation 2.10) represents the maximum solid fraction, and $J_{\mathrm{prim},0}$ signifies the initial nucleation rate:

$$\xi_{\max} = 1 - \exp(-V_{\mathrm{d}} \cdot n_{\mathrm{imp}}). \tag{2.10}$$

In contrast to the nucleation kinetics for primary nucleation, the nucleation kinetic for CMN is expressed by Dickinson et al. (1996) (Equation 2.11):

$$\frac{\partial \xi}{\partial t} = -k_{\mathrm{CMN}} \cdot \xi \cdot (1 - \xi). \tag{2.11}$$

k_{CMN} denotes the kinetic constant for CMN, analogous to k_{prim}.

For the evaluation of the CMN, the following considerations are imperative: A CMN event requires a collision between a particle and a liquid droplet coupled with a successful inoculation process (Hindle et al. (2000)). Because CMN does not occur every time a particle collides with a liquid droplet, the inoculation efficiency is defined, derived from coalescence theory as per Chesters (1991). The inoculation efficiency is influenced by three factors: The collision rate h_{coll}, the contact force F_{coll}, and the contact time t_{coll}.

The overall nucleation rate J_{CMN} should thus be a function of these three factors:

$$J_{\mathrm{CMN}} = f(h_{\mathrm{coll}}, F_{\mathrm{coll}}, t_{\mathrm{coll}}). \tag{2.12}$$

The collision rate h_{coll}

h_{coll} depends on the collision kernel $\beta_{\mathrm{l,s}}$ and on n_{l} and n_{s}. Therefore, it is a function of x_{l} and x_{s}:

$$h_{\mathrm{coll}}(x_{\mathrm{s}}, x_{\mathrm{l}}) = n_{\mathrm{s}} n_{\mathrm{l}} \beta_{\mathrm{l,s}}. \tag{2.13}$$

$\beta_{\mathrm{l,s}}$ is computed based on the flow regime. For a laminar flow, the collision kernel is defined as (Friedlander (2000)):

$$\beta_{\mathrm{lam,l,s}} = \frac{4}{3}\, \dot{\gamma}_{\mathrm{mean}} \left(\frac{x_{\mathrm{l}}}{2} + \frac{x_{\mathrm{s}}}{2} \right)^3 . \tag{2.14}$$

$\dot{\gamma}_{\mathrm{mean}}$ represents the average shear rate.

In the case of turbulent flow, the collision kernel is expressed as (Kruis and Kusters (1997)):

$$\beta_{\mathrm{turb,l,s}} = 1.3 \sqrt{\frac{\varepsilon}{\nu}} \left(\frac{x_{\mathrm{l}}}{2} + \frac{x_{\mathrm{s}}}{2} \right)^3 . \tag{2.15}$$

ε displays the local rate of energy dissipation and ν the kinematic viscosity.

The contact time t_{coll}

The contact time of two colliding droplets (t_{coll}) is described by Levich (1962) as:

$$t_{\mathrm{coll}} \propto \frac{(x_{\mathrm{l}} + x_{\mathrm{s}})^{2/3}}{\epsilon^{1/3}}. \tag{2.16}$$

and by Chesters (1991) as

$$t_{\mathrm{coll}} \propto \left(\frac{\epsilon}{\nu} \right)^{-1/2} . \tag{2.17}$$

For laminar flows or local calculations in small areas of turbulent flows, ϵ is commonly defined as (Schlichting and Gersten (2000))

$$\epsilon = \frac{\eta}{\rho}\left(\frac{du}{ds}\right)^2, \tag{2.18}$$

with ρ as the fluid density, u the streamwise velocity and y the distance from the wall. For laminar flow, $\frac{du}{ds}$ equals to the shear rate $\dot{\gamma}$ ($\rightarrow \epsilon \propto \dot{\gamma}$). Consequently, there is an inverse proportionality of t_{coll} to both, ϵ and $\dot{\gamma}$.

The contact force F_{coll}

An increase in shear rate results in enhanced droplet collisions and a reduction in contact duration (Vanapalli and Coupland (2001)). Coulaloglou and Tavlarides (1977), Hasseine et al. (2005) describes the force with which two droplets collide:

$$F_{\mathrm{coll}} \propto \rho_{\mathrm{conti}} \overline{u}^2 \left(\frac{x_{\mathrm{s}} x_{\mathrm{l}}}{x_{\mathrm{s}} + x_{\mathrm{l}}}\right)^2. \tag{2.19}$$

Here, the mean relative velocity of the droplets $\overline{u}$ is proportional to ϵ, x_{l} and x_{s}:

$$\overline{u}^2 \propto \epsilon^{2/3} \cdot (x_{\mathrm{s}} + x_{\mathrm{l}})^{2/3}. \tag{2.20}$$

This leads to a proportional relationship of F_{coll} with ϵ and $\dot{\gamma}$. Liao and Lucas (2010) provide an overview of the approaches describing the processes behind the coalescence found in the literature so far.

2.4 Experimental plan

The literature review and overview of modeling approaches highlight a significant need to enhance the understanding of the CMN and its influencing factors in stirred systems. In addition to the system's shear or movement/stirring, the surfactant concentration and type of surfactant play a crucial role. This is derived from the consideration that the collision force imposed by external flow and contact events are influenced by the flow between the two approaching droplets/particles, for example in the drainage film (Chesters (1991)). This "internal flow" is defined by the deformation of the approaching liquid-liquid interfaces. Given enough time, this process may also involve the rupture of the film and the contacting of the colliding reaction partners. All aforementioned parameters are influenced by the surfactant charge and aqueous concentration (e.g., Narayan et al. (2020), Chesters and Bazhlekov (2000)).

The following experimental plan was drawn up to ensure a structured and, as far as possible, isolated investigation of all the influencing parameters on CMN mentioned above (Figure 2.3). As a first step, microfluidic experiments on isolated droplets in the nanoliter scale ($V_\mathrm{d} \approx 25$ nL) were done to gain an understanding of the influence of the internal flow parameters on the contact time and the necessary contact force for inducing CMN. In the second step, the insights gained at the microscopic level were transferred to the milliliter scale (concerning emulsion volume). In addition to assessing the impact of aqueous surfactant concentration on the CMN, the study also explores the influence of laminar flow on the efficiency of CMN. Ultimately, these findings will be tested in a further up-scaled setup: A 1 L stirred tank. This enables the investigation of CMN in a more industry-like setup with more complex flow regimes.

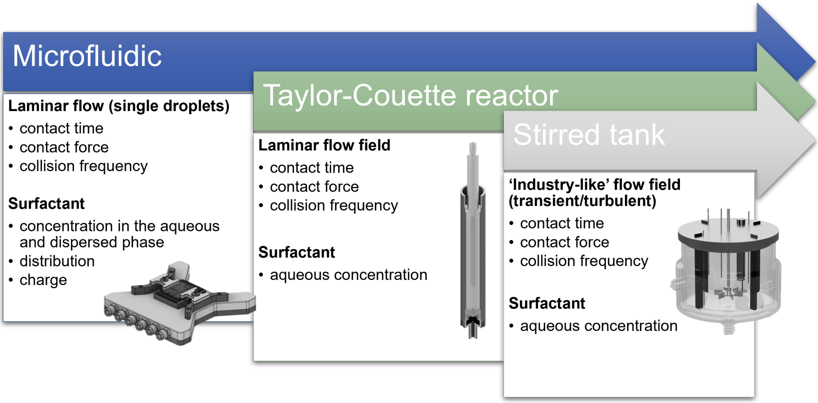

Figure 2.3: Outline of the experimental plan. The microfluidic experiments aimed to generate a general understanding of the parameters influencing CMN. Their impact will then be investigated in, at first, laminar and, finally, a more complex flow in a stirred vessel.

3 Principal understanding of CMN: A microfluidic approach

Parts of this chapter are published in the following peer-reviewed publications:

Kaysan, G.; Rica, A.; Guthausen, G.; Kind, M. Contact-Mediated Nucleation of Subcooled Droplets in Melt Emulsions: A Microfluidic Approach. Crystals 2021, 11, 1471, doi:10.3390/cryst11121471.

Kaysan, G.; Hirsch, T.; Dubil, K.; Kind, M. A Microfluidic Approach to Investigate the Contact Force Needed for Successful Contact-Mediated Nucleation; Colloids Interfaces 2023, 7, 12, doi: 10.3390/colloids7010012.

3.1 Working hypothesis

The impact of surfactant concentration needs to be studied in microfluidics concerning the continuous and dispersed phases as well as the charge of the surfactant (Figure 3.1). The disjoining pressure Π_{dj} of the two reaction partners, namely the supercooled droplet and the solid particle, is a function of the van-der-Waals attractive forces Π_{VdW}, the repulsive electrostatic and oscillatory forces Π_{el} and Π_{osc} and other forces Π_{i} that might influence the approach of the two reaction partners:

$$\Pi_{\mathrm{dj}} = \Pi_{\mathrm{VdW}} + \Pi_{\mathrm{el}} + \Pi_{\mathrm{osc}} + \sum \Pi_{i}. \tag{3.1}$$

Π_i will not be further discussed in this thesis. An example for Π_i would be a steric hindrance of molecules. Equation 3.1 leads to the following working hypothesis:

An increase in surfactant charge and an increase in micelle concentration within the continuous phase lead to longer contact times needed for nucleation, making CMN less probable (in a given time window). Critical relative velocities, above which CMN occurs, will increase as either Π_{el} or Π_{osc} will increase.

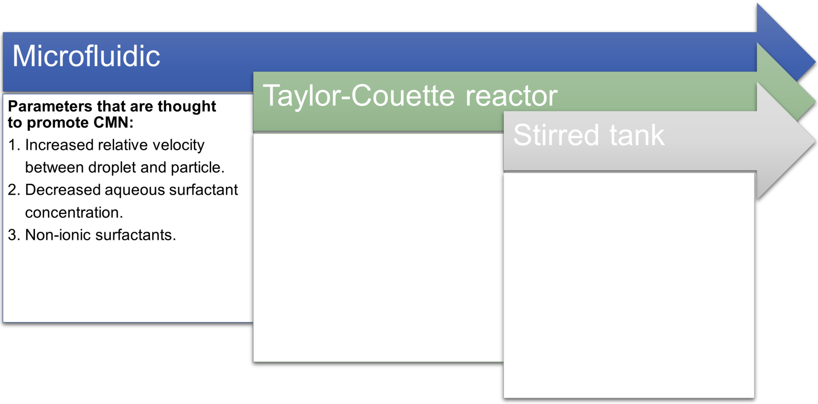

Parameters that are thought to promote CMN:

1. Increased relative velocity between droplet and particle.
2. Decreased aqueous surfactant concentration.
3. Non-ionic surfactants.

Figure 3.1: Expected influencing parameters on CMN that will be evaluated in the microfluidic setup.

3.2 Experimental approach and measurement system

3.2.1 Experimental setup

The microfluidic chip represents the setup's centerpiece. It was made out of a transparent polycarbonate plate (thickness 2 mm) with numerous microchannels cut into it. The channels were 300 μm $^{+10}_{-52}$ μm wide and 200 μm ± 20 μm deep. In addition, a channel for a temperature sensor was drilled into the chip's side. The channels' distinctive rectangular cross-sectional area was realized by thermal bonding of a thin 250 μm thick polycarbonate foil on top of the chip (Figure 3.2). As a dispersed phase, n-hexadecane ($C_{16}H_{34}$, Hexadecane ReagentPlus®, Sigma-Aldrich, Schnelldorf, Germany, purity: 99%) was used, and the continuous phase was ultrapure water (OmniTap®, stakpure GmbH, Niederahr, Germany; electrical conductivity 0.057 µS cm^{-1}). Five different surfactants were used to stabilize the droplets and to investigate the impact of surfactant concentration and charge on the inoculation efficiency of CMN (Table A.9 and Table A.10).

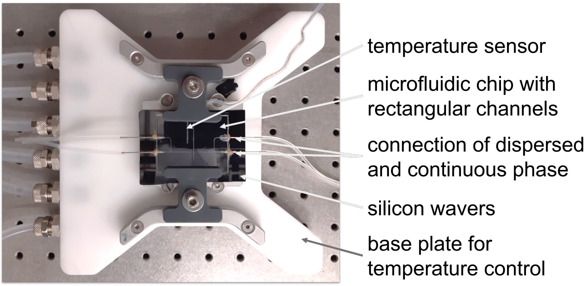

Figure 3.2: Detailed presentation of the centerpiece of the microfluidic experiment - the microfluidic chip with the tempering plate.

The channel walls were hydrophilized to ensure that n-hexadecane did not wet the walls (Selzer et al. (2018)). The alteration in the hydrophobicity of the channel walls induces a chemical change, leading to the formation of lipophilic droplets that remain unattached to the channel walls. Consequently, these droplets do not fully occupy the channel but nearly extend across its width and height. The ends of the drops are rounded and known as caps (Musterd et al. (2015)).

The microfluidic chip was mounted on top of a water-tempered aluminum cooling block with two temperature zones that could be regulated separately. A temperature sensor (Pt 100, ES Electronic Sensor GmbH, Heilbronn, Germany) was used to detect the temperature of the microfluidic chip at the area of the contact experiment. A high-speed camera (sCMOS pco.edge 5.5®, Excelitas PCO GmbH, Kelheim, Germany) was linked to a stereo microscope (SZ61, OLYMPUS EUROPA® SE & Co. KG, Hamburg, Germany) with an integrated polarization filter to follow crystallization processes. To assist the polarization filter in revealing crystalline formations, two silicon wafers were put directly in the back of the microfluidic chip. A low-pressure injection pump (Nemesys, CETONI GmbH, Korbußen, Germany) was used to adjust the volumetric flow rates of the continuous and dispersed phases. A BASE120 base module was used to link the syringe pump system to the computer (Figure 3.3). The melting temperature of n-hexadecane was determined by bulk phase experiments in the microfluidic chip as $\vartheta_{\mathrm{m,hex}}$ = 18.6 ± 0.2 °C. In literature, $\vartheta_{\mathrm{m,hex}}$ ranges from 16.7 to 20.0 °C (McClements et al. (1993b), Vélez et al. (2003), G.L. Zou et al. (2004), González et al. (2008), Zhang et al. (2010)). ϑ_m is used to calculate the supercooling ΔT by

$$\Delta T = \vartheta_m - \vartheta. \tag{3.2}$$

3.2.2 Experimental procedure

The microfluidic T-junction enabled the reproducible creation of well-defined droplet sizes (Figure 3.4). The specified volume flows for the droplet formation

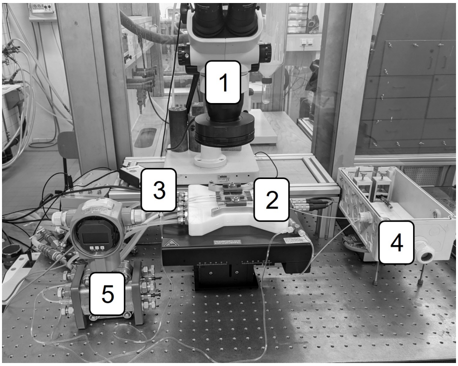

Figure 3.3: Experimental setup: (1) stereo microscope with polarization filter and high-speed camera, (2) microfluidic chip positioned on the tempering unit, (3) coolant inlets and outlets, (4) syringe pump, and (5) differential pressure sensor. This sensor was only integrated for experiments described in Chapter 3.6. Reproduced from Kaysan et al. (2023b), CC BY 4.0.

were as follows: $\dot{V}_{\mathrm{disp}} = 15\ \mu\mathrm{L\ h}^{-1}$ and $\dot{V}_{\mathrm{conti}} = 250\mu\mathrm{L\ h}^{-1}$. These flow rates ensured a separation between individual droplets of at least 1.5 cm and a good reproducibility of the droplets' size.

The two immiscible liquids (here: n-hexadecane and water) create an interface at the T-junction of the inlet channels from the dispersed or continuous phase (Figure 3.4). A detailed description of the mechanisms behind the droplet formation can be found in Garstecki et al. (2006). The volume of a droplet in a rectangular channel was approximated according to Musterd et al. (2015).

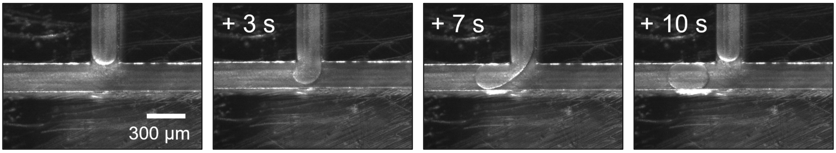

Figure 3.4: Presentation of the droplet formation at T-junction. The time shown in the pictures refers to the time difference from the first picture. The dispersed phase comes from the top; the continuous phase flows from right to left. Adapted from Kaysan et al. (2021), CC BY 4.0.

The droplet must be crystallized to investigate the contact between a supercooled droplet and a solid particle. Therefore, the temperature profile of the microfluidic channel during the collision followed a specified routine (Figure 3.5 and 3.6).

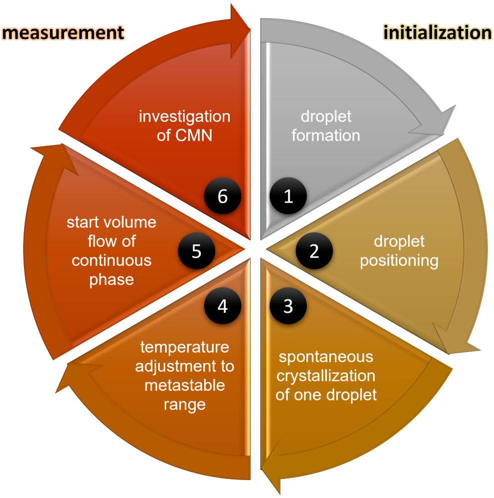

Figure 3.5: General procedure to investigate CMN in microfluidic setup.

Initialization:

Droplets were generated at the T-junction to begin the experiment (1). Once droplets were found in the total length of the channel (2), one side of the chip was cooled to roughly $\vartheta_{\text{prim}} = 11$ °C ($\Delta T_1 = 7.6$ K) to force spontaneous droplet crystallization (3). As a result of crystallization, the solid particle became firmly attached to the channel walls and did not move. To ensure a homogeneous temperature profile at the cold side of the chip, pictures were taken with a thermal imaging camera (FLIR E5-XT, FLIR Systems, Wilsonville, Oregon, USA) (Figure 3.7). As there is a gap filled with air between the two aluminum

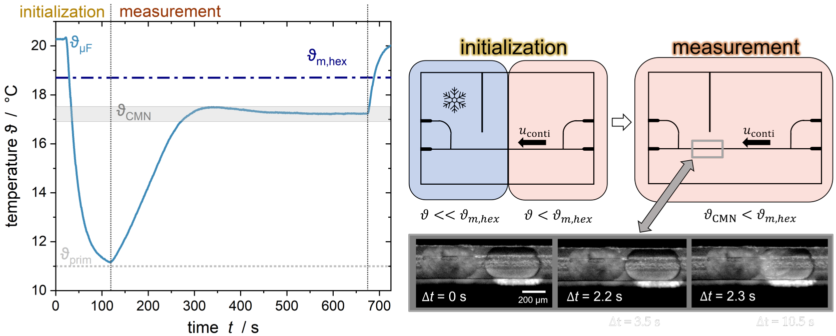

(a) Temperature profile.

(b) Illustration of experiments.

Figure 3.6: Temperature profile during initialization and observation of droplets crystallization in the microfluidic setup. Adapted from Kaysan et al. (2021), CC BY 4.0.

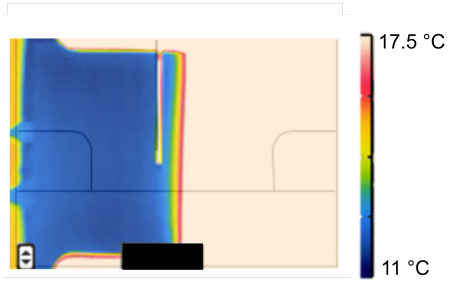
[redacted]

Figure 3.7: Temperature distribution in the microfluidic chip. The left part was cooled to 12°C (ΔT = 6.6 K) and the right to 17.5°C (ΔT = 1.1 K).

plates where the silicon wafers are mounted on top (Figure 3.7, red region), good isolation of the two plates is achieved.

Measurement:
To start the experiments, both plates were tempered at ϑ_{CMN} = 16.9 - 17.5 °C (ΔT_2 = 1.7 - 1.1 K) to avoid nucleation by other mechanisms than CMN (4). This chosen supercooling is in the metastable region of n-hexadecane and therefore below $\vartheta_{\mathrm{m,hex}}$. As a consequence, frozen particles did not thaw. The volumetric flow of the continuous phase was started, and consequently,

the liquid droplet proceeded to the solid particle (5). The continuous phase flow rates ranged from 15 to 400 μL h^{-1}. The aqueous phase could pass by the spherical particle in the corners of the channel (rectangular cross-section). This experimental design allowed for the controlled interaction of two collision partners.

A high-speed camera enabled the time-resolved observation of the nucleation events and the contact evolution (for example, the relative velocities of the droplet and particle Δu and wetting history) (6).

The camera tracked all collisions with frame rates between 10 and 100 frames per second. The distance traveled by the supercooled liquid droplet during a particular time defined the relative velocity Δu, because the solid particle had a fixed location (Figure 2.1).

3.2.3 Flow in microfluidic channels

Based on the hydraulic diameter d_h Kandlikar and Grande (2003) introduced a classification system to categorize various types of channels. According to their classification, a channel is considered a microchannel when 10 μm $< d_\mathrm{h} \leqq$ 200 μm and a minichannel when 200 μm $< d_\mathrm{h} \leqq$ 3 mm.

The flow characteristics in mini- and microchannels are predominantly influenced by wall roughness (Figure 3.8) and pressure (Kandlikar et al. (2006)). Consequently, the minichannel structure was optically investigated by a digital microscope (VHX-700, Keyence, Osaka, Japan). The assessment of the arithmetical mean height of the roughness in a channel yielded an absolute roughness value of $R_\mathrm{a} = 4.2$ μm $\pm$ 1.5 μm, averaged across 11 datasets covering the entire channel width and length. More considerable variations in roughness were observed mainly along the channel width, which can be attributed to the milling process.

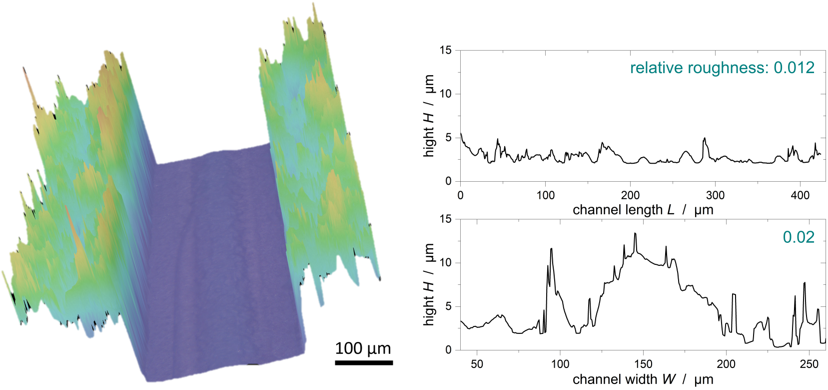

(a) 3D representation of the microfluidic channel.

(b) Roughness profile along channel length (top) and width (bottom).

Figure 3.8: Roughness within the microfluidic channel as observed by optical microscopy. Adapted from Kaysan (2023), CC BY 4.0.

In a laminar pipe flow, pressure loss is proportional to fluid velocity. Consequently, the pressure drop Δp can be calculated as:

$$\Delta p = f \cdot \frac{L}{d_\mathrm{h}} \cdot \frac{\rho \cdot u^2}{2} = \varphi \frac{64}{Re} \cdot \frac{L}{d_\mathrm{h}} \cdot \frac{\rho \cdot u^2}{2} = \varphi \frac{32 \cdot \eta \cdot u \cdot L}{d_\mathrm{h}^2}. \tag{3.3}$$

L represents the channel length and d_h the hydraulic diameter of the pipe. The friction factor f is influenced by the Reynolds number (Reynolds (1883)), flow properties, channel geometry, and wall roughness (Kandlikar et al. (2006)). For noncircular channel cross-sections and laminar flow, the pipe friction coefficient is given by the correction factor φ, which depends on the geometry of the channel. By Kast et al. (2010), the parameters are the following, specific for the channel dimensions of a channel width of $\approx 300\ \mu$m and a channel depth of $\approx 200\ \mu$m. With these, φ is determined to 0.92.

The Reynolds number in pipe flows is defined as

$$Re = \frac{u \cdot \rho \cdot d_\mathrm{h}}{\eta}. \tag{3.4}$$

η is the dynamic viscosity of the fluid. The hydraulic diameter d_{h} of a rectangular channel is calculated as

$$d_{\mathrm{h}} = \frac{4A_{\mathrm{channel}}}{U_{\mathrm{w}}}. \tag{3.5}$$

A_{channel} represents the cross-sectional area of the flow channel, and U_{w} is the wetted perimeter (Kandlikar et al. (2006)).

In conventional pipes, wall roughness has a negligible impact on pressure drop in a laminar flow. However, in microfluidic systems, wall roughness may impede a significant portion of the flow channel (Kandlikar et al. (2006)). As the scale decreases, length-related effects, such as the in-flow behavior at the inlet and thus the length until a stationary flow is formed, increase significance (Kockmann (2008)). Chan and Horn (1985) investigated films of liquids between molecularly smooth plates at nanometer-scale distances. They concluded that conventional Navier-Stokes equations remain valid down to a distance of 50 nm. However, when the film thickness is less than ten molecular layers (molecular size: water $\approx$ 0.2 nm, n-hexadecane $\approx$ 1.9 nm (Hanwell et al. (2012))), the liquid can no longer be considered as a continuum (Chan and Horn (1985)). Since the channel is wider and deeper than 50 nm, a continuum-mechanical behavior can be assumed for the fluid flows.

Qu et al. (2006) and Xu et al. (2000) numerically and experimentally investigated flow development and pressure loss in micro- and minichannels. Their findings revealed that conventional Navier-Stokes equations are applicable for predicting microfluidic flow behavior. Re numbers in mini- and microchannels are notably lower than those in commercial pipe systems, owing to smaller d_{h} and u. This implies that frictional forces dominate while inertial forces are comparatively weak. However, it is crucial to note that the critical Reynolds number Re_{crit} governing the transition from laminar to turbulent flow must be adjusted for microfluidics. The transition to turbulent flow starts below Re_{crit} for classical pipe flow (Re_{crit} = 2300 - 10,000). This is caused in particular by the surface roughness, which becomes more important as d_{h} decreases (Kandlikar et al.

(2006)). For d_h in the range of 30 to 344 μm, the transition occurs at Re_crit = 300 - 900 (Mohiuddin Mala and Li (1999)), to be compared to d_h = 240 μm in this study. Taking into account the impact of wall roughness on Re_crit, with the relative roughness of the channel used here (Figure 3.8, relative roughness $\approx$ 0.02), $Re_\mathrm{crit} \approx 1800$ is estimated. Thus, the experiments carried out in this work show a purely laminar flow (Table A.6).

The friction factors in microfluidics for fully developed flows are consistent with those predicted by the conventional theory (Mirmanto (2017)). They were independent of whether the flow was laminar or turbulent. This fact is confirmed by the results of Ghajar et al. (2010) in a comprehensive review. In addition, Ghajar et al. (2010) found that the relative roughness of the microfluidic channels plays an important role. Steinke and Kandlikar (2006) compared the friction factors given in the literature with the theoretical values. They found close agreement between the theoretical and experimental data. The discrepancies were attributed to inaccuracies due to irregularities in the channel dimensions. Thus, in this work, it is assumed that all common equations of classical hydrodynamics apply to the experimental setup used here.

3.3 Transfer of coalescence theory to CMN

In the case of coalescence, a phenomenon between liquid droplets or gaseous bubbles, no phase transformation occurs in either of the contacting partners. An interesting difference in CMN results from the state of aggregation, as one of the two contacting units is already crystallized while the other is present as a supercooled liquid droplet. This results in a generalized assumption for CMN: the interface of the liquid droplet exhibits a spectrum of states ranging from mobile to rigid, depending on the concentration of interfacial surfactants. In contrast, it is assumed that the interface of the crystallized particle remains rigid.

According to Shinnar and Church (1960), coalescence requires that the interstitial film falls below a critical thickness. Below this threshold, the van der Waals attraction between two approaching droplets outweighs all repulsive forces. Various mechanisms are available to counteract film thinning in the material system of an n-hexadecane-water emulsion stabilized by TW20. These are explained in more detail below.

The DLVO theory (Verwey (1947), Derjaguin and Landau (1993)) constitutes a theoretical framework for illustrating the stability of colloidal systems, such as emulsions, by considering attractive and repulsive forces. For stability factors of more than 1, repulsion predominates in the interaction between suspended particles (Fuchs (1934)). Electrostatic repulsion among colloids mandates surfaces that are endowed with identical charges. Consequently, an increased charge with the same polarity among colloids can counteract film thinning. Dimitrova and Leal-Calderon (1999) undertook force measurements among ferrofluidic suspension droplets within an aqueous solution stabilized with TW20. Increasing the aqueous surfactant concentration correspondingly escalated the electrostatic repulsion. At lower aqueous surfactant concentrations, their observations aligned with the DLVO theory. However, at higher aqueous surfactant concentrations, the measured repulsive forces exhibited higher values at shorter distances than those predicted by the DLVO theory. To explain these discrepancies, the authors proposed a steric component in the repulsive force attributed to the presence of TW20 micelles between the droplets.

The influence of micelles in the continuous phase on colloid interaction is attributed to oscillating structural and depletion forces (OSF) (Israelachvili (2011)). These forces manifest in the interstitial film when the film thickness diminishes, owing to the presence of minute dissolved entities, such as micelles, in the film liquid.

Taking into consideration the OSF, Basheva et al. (2007) derived a nonlinear relationship linking the diameter of spherical micelles d_{mic}, the volume fraction of these micelles ϕ_{mic}, the separation distance between two colliding droplets

$s_{\mathrm{d,d}}$, and the interaction energy E between said droplets. This approach estimates emulsion stability depending on the number of micelles within the solution.

The total dimensionless interaction energy e_{total} was calculated as the sum of the oscillatory component e_{osc} and the Van der Waals interaction e_{VdW}. Comprehensive equations are available in Basheva et al. (2007). Figure 3.9 presents insights into the potential impact of micelles in the aqueous phase, demonstrating their capacity to impede CMN by amplifying repulsion ($e_{\mathrm{total}} > 0$). The parameters used for the computation can be found in Table 3.1. Assuming that TW20 micelles are non-deformable, solid spheres, the appearance of micelles in the aqueous phase does not necessarily lead to a repulsion. Still, with increasing the aqueous micellular concentration, repulsion becomes increasingly pronounced (Figure 3.9).

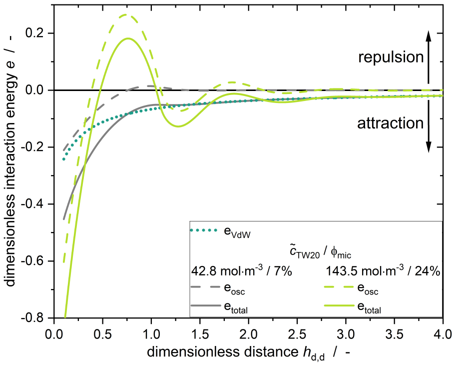

Figure 3.9: Simulated interaction energies for two spherical droplets with the dimensionless distance $h_{\mathrm{d,d}} = s_{\mathrm{d,d}}/x_{\mathrm{mic}}$: The dimensionless oscillatory interaction energy e_{osc}, the dimensionless Van-der-Waals interaction energy e_{VdW} and the sum of both, the dimensionless total interaction energy e_{total}. For the simulations, the assumption is made that the micelles are hard, non-deformable spheres. The dedimensioning of the absolute interaction energy e was carried out using the following relationship: $E(s_{\mathrm{d,d}}, \phi_{\mathrm{mic}}) = k_{\mathrm{B}}T\frac{r_{\mathrm{d}}}{x_{\mathrm{mic}}} \cdot e(h_{\mathrm{d,d}}, \phi_{\mathrm{mic}})$. The simulation was done according to Basheva et al. (2007) and Trokhymchuk et al. (2001) (Kaysan et al. (2021)).

Table 3.1: The parameters for calculation of the total interaction energy E.

Parameter	Value	Reference
TW20 micelle diameter	7.2×10^{-9} m	Basheva et al. (2007)
Droplet radius in the microfluidic chip	3×10^{-4} m	own measurement
Temperature	290.35 K	own measurement
Length of surfactants brush layer	1.2×10^{-9} m	determined with AVOGADRO (Hanwell et al. (2012))
Hamaker constant	4×10^{-21} J	Basheva et al. (2007)

The calculations show that an increase in the aqueous surfactant concentration should increase the time needed for nucleation or, if OSF is strong enough, completely prevent CMN. They also show that micelles in the aqueous phase are crucial for stabilizing the emulsion.

3.4 Surfactant distribution in emulsions

The degree to which the droplet and particle surfaces are coated with surfactant may impact the CMN. The effect of the interfacial energy on coalescence has been explored previously (e.g., Schroën et al. (2020)). Because coalescence and CMN are similar, the coverage of the particles' and droplets' surfaces should also be important for CMN. Moreover, micelles may affect the inoculation of the supercooled droplet by CMN. Besides the surfactant concentration at the interface, the surfactant distribution between the dispersed oil and aqueous continuous phases must be studied.

NMR measurements were performed on a 400 MHz spectrometer (Avance Neo, Bruker BioSpin GmbH, probe: DiffBB) to investigate whether surfactant diffusion takes place from the water to the oil phase, which is driven by concentration gradients due to distinct chemical potentials. Surfactant concentrations of up to $\tilde{c}^{aq}_{\mathrm{TW20}}$ = 180 mol m^{-3} were used. N-hexadecane was added to the continuous phase in two distinct mass ratios: 50:50 and 80:20 (water:n-hexadecane). After adding n-hexadecane, the samples were mixed for 2 min with a stir bar at 700 rpm and room temperature.

Droplets ranging in size from 10 to 500 μm were created. The samples were stored for one week. Phase separation occurred within that time frame, leading to three distinct phases. At the top, large n-hexadecane droplets were observed. The intermediate phase consisted of smaller n-hexadecane droplets, whereas water was at the bottom of the tube. The surfactant distribution between these phases could not be investigated visually. Still, it can be assumed that micelles are present in the phases and all liquid-liquid interfaces are fully covered with surfactant molecules. After one week, the aqueous phase was carefully separated with a syringe to measure the surfactant solution. ^{1}H NMR spectroscopy was used to investigate the samples (Figure 3.10). Samples with known surfactant concentrations were measured to conclude the actual surfactant concentrations from the NMR measurements. The calibration establishes a correlation between the integral area of the TW20 peak A_{TW20} at a chemical shift of $\delta_{\mathrm{c}} = 3.67$ ppm and the aqueous surfactant concentration. To ensure the comparability of all samples and to compensate for the influence of different numbers of scans during the measurements, A_{TW20} was normalized to the integral area of the water peak A_{H2O} at $\delta_{\mathrm{c}} = 4.87$ ppm (Figure A.8). Up to a concentration of $\tilde{c}^{aq}_{\mathrm{TW20}}(t = 0)$ = 90 mol m^{-3}, the measurement results after 7 days agreed well with the initial concentrations. Consequently, no quantifiable amounts of surfactants were dissolved in the n-hexadecane phase up to the prescribed concentration. This confirms the expectation that the diffusion of surfactants had no significant influence within the experimental time frame of the microfluidic experiments ($\tilde{c}^{aq}_{\mathrm{TW20}}(t = 0)$ < 50 mol m^{-3}). Diffusion of the surfactant would be possible due to concentration gradients and, thus, chemical

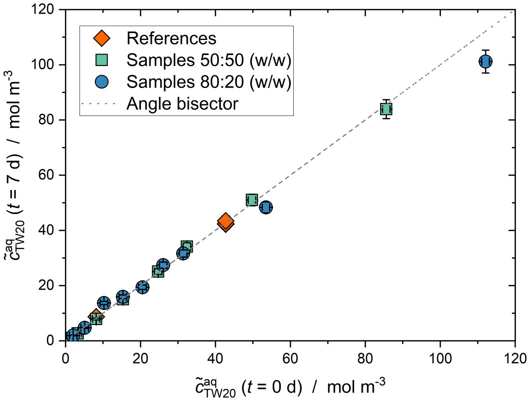

Figure 3.10: TW20 concentration in water measured by NMR spectra $\tilde{c}^{aq}_{\text{TW20}}(t = 7\ d)$ as a function of the concentration of the weighed-in components $\tilde{c}^{aq}_{\text{TW20}}(t = 0)$ of samples having a 50:50 or 80:20 mass ratio of the continuous phase to the scattered phase (n-hexadecane). Also, reference samples of TW20 in ultrapure water at specific concentrations are shown (red). The samples were measured at 20 °C (Kaysan et al. (2021)). The spectrometer's relative measurement error was 2%.

potential differences between the continuous and the dispersed phase had no significant influence.

When comparing the results of the tests in which either a 50:50 or an 80:20 mass ratio of water to n-hexadecane was used, it becomes clear that there is no difference in the aqueous surfactant concentration after 7 days. Thus, the ratio between water and n-hexadecane did not influence the surfactant distribution. The results apply to the microfluidic experiments and also to the emulsions used in the experimental setups described in the following chapters (Chapter 4 and 5).

A possible cause for the lower $\tilde{c}^{aq}_{\text{TW20}}$ after 7 days of storage, when exceeding $\tilde{c}^{aq}_{\text{TW20}}(t = 0)$ = 90 mol m^{-3}, is the diffusion of surfactants from the aqueous phase into the oil phase. The surfactant molecules aim to distribute between the oil and water phases to balance the chemical potential in both phases. This ensures a stabilization of the emulsion.

Additionally, long-term studies were carried out over 43 days to corroborate the findings of the slow equilibrium adjustment of the surfactant concentration between the continuous and dispersed phases and to determine the distribution coefficient K_{TW20} of TW20 between water and n-hexadecane. K_{TW20} is defined as

$$K_{\mathrm{TW20}} = \frac{\tilde{c}_{\mathrm{TW20}}^{hex}}{\tilde{c}_{\mathrm{TW20}}^{conti}} \tag{3.6}$$

K_{TW20} was determined via NMR-spectroscopy on a 300 MHz spectrometer (nanobay, Bruker BioSpin GmbH, Germany, probe: BBFo). The sample comprised two distinct phases: pure n-hexadecane and water with an initial total surfactant concentration of 16.6 mol m^{-3}. Both phase volumes were 300 μL. The sample was placed in the sensitive region of the NMR probe, allowing just the water phase to contribute to the NMR signal. To minimize overlapping and the impact of the water peak on the interesting TW20 peak, the CH_2 signal was chosen for the time-dependent measurement of the surfactant concentration. The initial area of the CH_2 peak was assumed to correspond to the initial surfactant concentration of 16.6 mol m^{-3}. Consequently, the integral CH_2 signal reflects the aqueous surfactant concentration as a function of time (Figure 3.11). When the experimental data was modeled using a monoexponential decay (Figure 3.11), the equilibrium concentration of $\tilde{c}_{\mathrm{TW20}}^{aq}(t \rightarrow \infty)$ = 13.6 mol m^{-3} was obtained. Using mass balance calculations of the two-phase system observed, the value of $\tilde{c}_{\mathrm{TW20}}^{hex}(t \rightarrow \infty)$ for the extrapolated equilibrium state was estimated as 3.0 mol m^{-3}. At an initial aqueous surfactant concentration of $\tilde{c}_{\mathrm{TW20}}^{aq}(t = 0)$ = 16.6 mol m^{-3}, identical amounts of water and n-hexadecane, and an interfacial area of roughly 13.2 mm^2, the distribution coefficient (Equation 3.6) was determined to be K_{TW20} = 0.22.

The surfactant concentration at the oil-water interface was too low to be detectable by spectroscopic measurements. Pendant drop measurements must be used to determine the surfactant concentration at the interface (Chapter A.1.2).

These findings indicate that, for the microfluidic experiments performed, with around 10 minutes in duration, changes in the surfactant concentrations in the

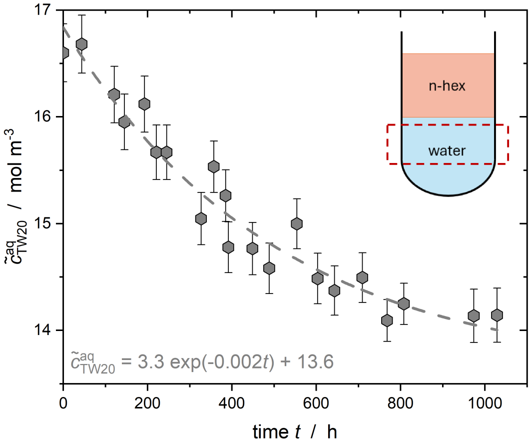

Figure 3.11: NMR spectroscopy-based time-resolved observations of the concentration of Tween®20 in the continuous water phase for up to 43 days. For the experiment, an n-hexadecane phase was layered on top of a water phase (see graphical illustration). The volume ratio of the two phases was 50:50, and the liquid-liquid interface was 13.2 mm^2 (Kaysan et al. (2021)). The initial aqueous surfactant concentration was $\tilde{c}^{aq}_{\mathrm{TW20}}$ = 16.6 mol m^{-3}. The calculated exponential decay curve is depicted as a dashed line.

continuous or dispersed phase can generally be neglected. However, when working with emulsions aged over days or weeks, it is important to ensure that samples have a comparable age. This consistency helps to avoid variability in surfactant distribution, which could otherwise influence CMN.

3.5 Dependency of CMN on surfactant concentration and surfactant charge

Microfluidics allow direct observation of crystallization in single droplets, making them ideal for probing CMN, specifically the induction time for nucleation t_{ind} and the minimal force required for CMN $F_{\mathrm{CMN,min}}$.

However, there are limitations to the comparison with experiments on larger scales. The flow conditions in minichannels differ from those in the large-scale production and crystallization of melt emulsions. The different flow patterns can result in non-comparable conditions regarding the concentration of micelles and single molecules in the interstitial space between the droplets and particles. If comparable conditions are assumed, the factors investigated in the microfluidic chip represent a minimum estimate that must be exceeded in stirred systems to trigger CMN (Table 3.2).

Table 3.2: The characteristics of the factors that determine the effectiveness of CMN in agitated systems are compared with the parameters studied in the microfluidic system.

Parameters influencing CMN in stirred systems (Chesters (1991))	Parameters investigated in minichannel	Condition for CMN
Contact force F_{coll}	$F_{\mathrm{CMN,min}}$	$F_{\mathrm{coll}} \geq F_{\mathrm{CMN,min}}$
Contact time t_{coll}	t_{ind}	$t_{\mathrm{coll}} \geq t_{\mathrm{ind}}$

As previously stated, the surfactant concentrations in the water and oil phases and at the separating interface can impact t_{ind} and $F_{\mathrm{CMN,min}}$ needed for CMN. This could be attributed to longer film-draining periods (time needed for the outflow of the gusset liquid) or surfactant rearrangement at the interface when the two collision partners approach each other.

Throughout microfluidic experiments of roughly 10 min, the specific interfacial energy depends on the surfactant distribution between the continuous and dispersed phase (Chapter A.1.2). For the investigation of the impact of surfactant concentration and surfactant charge on the efficiency of CMN, different concentrations of the nonionic surfactants Polysorbate 20 (TW20), Polysorbate 60 (TW60) and Polysorbate 80 (TW80), as well as the ionic surfactants sodium dodecyl sulfate (SDS) and Cetyltrimethylammonium bromide (CTAB), were dissolved in the dispersed and continuous phases. $F_{\mathrm{CMN,min}}$ required for crystallization may be influenced by the number of micelles or single molecules per unit volume in the continuous phase, the specific interfacial energy as well as the charge of the surfactant. All parameters would increase the disjoining pressure Π_{dj} (Equation 3.1).

Given that $F_{\mathrm{CMN,min}}$ could not be measured directly, the relative velocity between the supercooled droplet and the crystalline particle is used as a parameter representative for the evaluation of CMN. It is shown later that $F_{\mathrm{CMN,min}}$ and the critical relative velocity needed for CMN Δu_{crit} correlate with each other (Chapter 3.6). Because the continuous phase continually pushes the liquid droplet towards the solid particle, the contact time in the microfluidic chip is not restricted. This is not comparable to conditions in 'real' flows (e.g., a stirred vessel).

The surfactant distribution between the continuous and dispersed phase or the interface cannot be determined inside the microfluidic system and was therefore estimated empirically: TW20 mass transport to the water-n-hexadecane interface was studied using a diffusion-controlled model. This approach can be used according to Jin et al. (2004) because the droplets had an average size larger than 10 μm (assumption: TW20 is a highly surface-active species).

The calculations revealed that the maximum surface loading Γ_{max} is reached in less than three seconds for all aqueous surfactant concentrations higher than cmc. $\Gamma_{\mathrm{max}} = 3.62 \times 10^{-6}$ mol m^{-2} was used (Staszak (2016)), as well as a TW20 molecular diffusion coefficient in water of $D^{aq}_{\mathrm{TW20}} = 2.1 \times 10^{-10}$ m^2 s^{-1} (Kaysan et al. (2022a)). Γ_{max} was calculated according to Bąk and Podgórska (2016), assuming a surfactant monolayer exhibiting a maximum coverage of the liquid-liquid interface and a zero surface pressure. Adsorption and desorption activities from the interface into the n-hexadecane droplet phase may be neglected within the experimental time range (Figure 3.11).

When TW20 was initially dissolved in n-hexadecane, measurements of the specific interfacial energy revealed fast adsorption to the interface, followed by desorption from the interface to the continuous phase. After about 50 min, a constant Γ_{if} was measured (Figure A.5). It is assumed that in the time frame of the microfluidic experiments (5 to 10 mins after interface formation), no or very few micelles are formed in the continuous phase before the contact of the droplet and particle occurs. This statement will be tested later.

The diffusion coefficient of TW20 in n-hexadecane was determined as $D_{\mathrm{TW20}}^{hex} = 2.0 \times 10^{-10}\,\mathrm{m^2\,s^{-1}}$ for surfactant concentrations ranging from 0.2 to 360 mol m^{-3} by NMR diffusion measurements (Kaysan et al. (2022a)). Thus, D_{TW20}^{hex} equals D_{TW20}^{aq}. Unlike the diffusion measurements of TW20 in water, only one diffusion coefficient was found for all studied TW20 concentrations in n-hexadecane. This shows no agglomerates, so-called *inverse micelles*, of TW20 are present in n-hexadecane within the lower detection limit.

Assuming that comparable mechanisms occur during CMN and coalescence, the following steps have to take place for inoculation of the supercooled droplet by the solid particle (Figure 3.12).

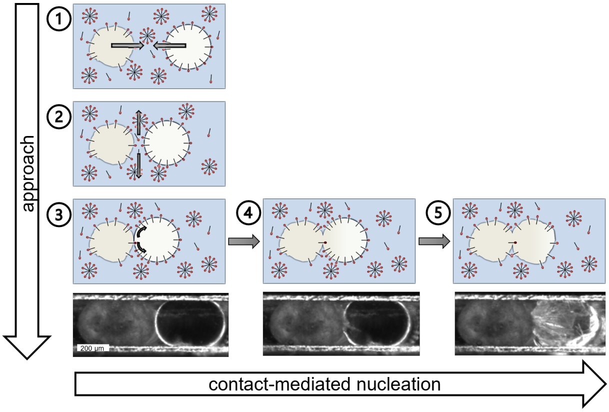

Figure 3.12: Single steps that need to happen to successfully inoculate the supercooled, liquid droplet by the solid particle of the same material.

1. Approach of the supercooled droplet and the particle.
2. Outflow of the gusset fluid: solvent and the contained surfactant molecules.
3. Reorganization of the surfactant molecules at the liquid-liquid interface of the droplet. This results in a potential contact point becoming free of surfactant.
4. Nucleation of the supercooled droplet.
5. Crystal growth throughout the droplet. The individual crystal nuclei form at the contact point and grow through the droplet until complete crystallization.

The subsequent discussion will present the experimental outcomes when the surfactant was initially dissolved in the aqueous phase, followed by the results when the surfactant was initially dissolved in the oily phase (droplet). A key aspect of this research is exploring the impact of nonionic and ionic surfactants and the surfactant concentration, which will be thoroughly examined.

3.5.1 Surfactants initially dissolved in continuous phase

Figure 3.13 shows the results for nonionic (TW20 (red), TW60 (yellow), and TW80 (green); Table A.11) and ionic (SDS (blue), CTAB (purple); Table A.12) surfactants. The critical relative velocity Δu_{crit} is defined as the relative velocity between particle and droplet which was minimally needed to observe nucleation within the experimentally evaluated 60 s after contact. Data points are shown for $\Delta u_{\mathrm{crit}} < 10^{-6}$ m s^{-1} refer to experiments where all collisions led to nucleation. On the contrary, $\Delta u_{\mathrm{crit}} > 2 \times 10^{3}$ m s^{-1} means that within the viable volumetric flows in the setup, no velocity was found where nucleation happened within the first 60 s after the initial contact of droplet and particle.

For better comparison between the various experiments, all measured induction times for one concentration (Chapter A.4.1) of the same surfactant were averaged and are presented as the mean induction time $\bar{t}_{\mathrm{ind}}$. $\bar{t}_{\mathrm{ind}} > 60$ s indicated that no nucleation took place within the experimental time frame. Higher Δu_{crit} and longer mean induction times $\bar{t}_{\mathrm{ind}}$ were required for inducing nucleation at concentrations exceeding cmc compared to those below cmc. This trend is visible for all three surfactants shown here. This confirms the hypothesis that OSF increases and thus also Π_{dj} increases with increasing aqueous surfactant concentrations. As soon as the cmc was exceeded, Δu_{crit} increased with increasing $\tilde{c}^{aq}$. For $\tilde{c}^{aq}/cmc \approx 10^2$, no further CMN was detectable within the experimental time of 60 s. The sane findings can be seen when considering $\bar{t}_{\mathrm{ind}}$.

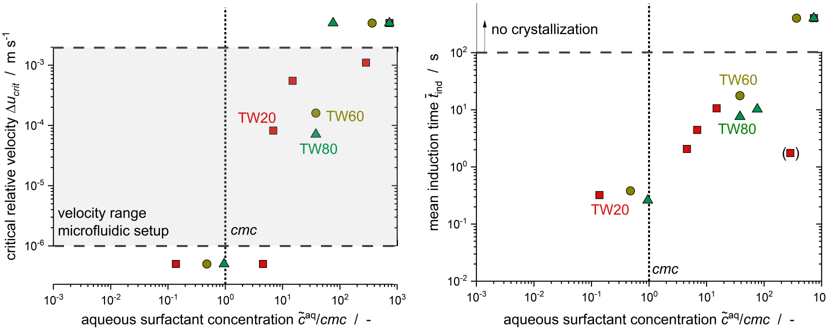

(a) Minimum contact force, here represented by critical relative velocity Δu_{crit} between droplet and particle.

(b) Mean induction times $\bar{t}_{\mathrm{ind}}$ needed for CMN.

Figure 3.13: Impact of surfactant concentration added to the continuous aqueous phase and surfactant charge on the CMN. Due to the different cmc, a comparison was made based on $\tilde{c}^{aq}/cmc$.

Typically, the liquid droplet enveloped the particle before nucleation commenced at concentrations above cmc (Figure A.18), leading to an increase in its interfacial area. It can be assumed that an increasing surfactant concentration in the continuous phase leads to a faster filling of a newly formed liquid-liquid droplet interface. This hinders the CMN by preventing direct contact between crystalline structures and supercooled liquid in the droplet. Conversely, inoculation occurs at lower surfactant concentrations. This is because less free surfactant is available and the new interface cannot be covered quickly enough. As a result, an increase in the aqueous surfactant concentration leads to both longer induction times and increasing critical relative velocities.

Results obtained on ionic surfactants showed a noticeable contrast compared to nonionic surfactants, necessitating both higher critical relative velocities and extended contact times (Figure 3.14). The additional molecular-level repulsion introduced by an electrical charge resulted in longer contact times, as requiring a higher applied force to overcome these supplementary repulsive forces (Equation 3.1).

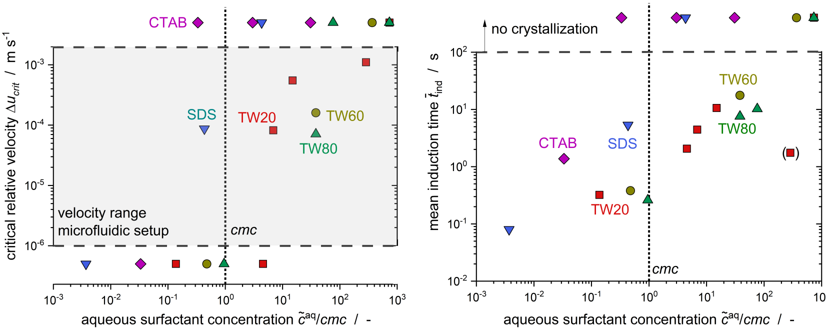

(a) Minimum contact force, here represented by critical relative velocity Δu_{crit} between droplet and particle.

(b) Mean induction times $\bar{t}_{\mathrm{ind}}$ needed for CMN.

Figure 3.14: Impact of nonionic surfactant concentration added to the continuous aqueous phase and surfactant charge on the CMN.

When the experimental concentration of aqueous TW20 exceeded cmc, it led to the presence of micelles in the continuous phase with a micellular volume fraction Φ_{mic} exceeding 0.1% (calculated according to Basheva et al. (2007), related to the volume of the continuous phase). As a result of this micelle formation, the induction time increased by at least a factor of 10 compared to scenarios in which most of the surfactants were present as isolated molecules in the continuous phase (Figure 3.16).

Without any surfactant, the induction time typically ranges from 0.1 s to 0.4 s (Figure A.11). This observation underscores the hindering effect on crystallization posed by surfactants, especially micelles, in the aqueous phase.

Following the approach outlined by Chen et al. (1984), Mackay and Mason (1963), Hodgson and Woods (1969), theoretical coalescence times were calculated for two n-hexadecane droplets suspended in water in the absence of any surfactant. Under such conditions, the theoretical coalescence times varied, ranging from 0.3 s to 1.1 s. These calculations were done at room temperature, with properties such as emulsion viscosity η = 30.3 mPa s, the density of n-hexadecane ρ_{hex} = 773.6 kg m^{-3}, density of water ρ_{H2O} = 998.21 kg m^{-3}, liquid-liquid interfacial tension without surfactant γ_{ll} = 47 mN m^{-1}, and x_{l} = 368 μm. Experimental observations (Taboada et al. (2020)) revealed coalescence times ranging from 10 s to more than 30 min in experiments with various surfactants in single droplet setups with water as continuous phase. Similarly, for nonionic surfactants, Leister and Karbstein (2021) reported coalescence times spanning from 5 s to around 100 s.

These experimental findings closely correspond to the theoretical coalescence times. Consequently, it is reasonable to anticipate that induction times would fall within a similar range when the surfactant is dissolved in water (Figure 3.13 (b)). Moreover, the theoretical coalescence time without any surfactant (calculated as 0.3 — 1.1 s) aligns with the range of experimental induction times. Dudek et al. (2020) previously documented increasing mean coalescence times and the expanding range of coalescence times with increasing surfactant concentrations. Consequently, it can be inferred that mechanisms hindering coalescence impede crystallization, particularly with the increasing surfactant concentration in the continuous phase.

The results shown in Figure 3.13 indicate that higher relative velocities and, consequently, larger contact forces are necessary to facilitate crystallization as the surfactant concentration in the continuous aqueous phase increases. For aqueous surfactant concentrations of TW20 exceeding approximately 23 mol m^{-3} (with an aqueous micellar volume fraction of around 3.8%, equivalent to $\tilde{c}^{aq}_{\mathrm{TW20}}/cmc \approx 400$), an oscillatory, repulsive force generated by micelles is to be expected, as suggested by calculations based on Basheva et al. (2007) (Figure 3.9). Combining this repulsive force with the attractive Van der Waals forces can produce an energy barrier that must be overcome by the contact force for crystallization to occur. Taking into account this combination of forces, an energy barrier would theoretically be built for $\tilde{c}^{aq}_{\mathrm{TW20}}/cmc >\approx 1500$. Thus, crystallization should occur even at low contact forces (i.e., low relative velocities).

In addition to the volume fraction of micelles, the stability of these micelles can also play a role. Christov et al. (2010) found in atomic force microscopy measurements that, for example, TW20 micelles are significantly less stable under hydrodynamic shear than micelles from other surfactants like Brij 35. These micelles tend to dissolve into single molecules even under relatively mild forces. As a possible result, this could increase the induction time as the micelles are destroyed first, and the newly formed, additional surfactant molecules must leave the gusset liquid. This could increase the contact force needed for CMN and hence in Δu_{crit}.

For some experiments, the liquid droplet spread around the solid particle before nucleation (= *hugging*). This leads to an increased liquid-liquid interface. Consequently, the newly formed single surfactant molecules can occupy these newly formed interfaces. This phenomenon of the liquid droplet *hugging* the solid particle, was only observed when the surfactants were dissolved in the aqueous phase and became more dominant with increasing relative velocities. Depending on the concentration of freely available single molecules, this newly formed interface may not be occupied quickly enough, allowing nucleation to occur. Relative velocities also influence the nucleation process, likely due to increased contact forces and the detachment of the surfactant from the droplet/-particle surfaces due to elevated shear forces at larger velocities, resulting in an unoccupied interface.

With all that in mind, the efficiency P_{CMN} of CMN should decrease with increasing surfactant concentrations in the continuous phase. Here, P_{CMN} is calculated as the number of experiments that led to nucleation compared to an overall number of experiments. At a constant $\tilde{c}^{aq}/cmc$, there should be a lower P_{CMN} for the ionic than for the nonionic surfactants (Figure 3.15) For all nonionic surfactants, the likelihood of crystallization decreased with increasing $\tilde{c}^{aq}/cmc$, also for $\tilde{c}^{aq}/cmc > 1$. This states that micelles within the continuous phase hinder nucleation, as the highest crystallization probability was achieved at $\tilde{c}^{aq}/cmc < 1$. Experiments without surfactant were performed to validate this hypothesis, resulting in crystallization in every experiment. This affirms that micelles and increasing monomer concentrations in the continuous phase can attenuate or prevent CMN (Figure A.11). These observations closely align with the findings of Bera et al. (2021), who did not observe coalescence when the surfactant concentration exceeded cmc. The difference lies in the fact that,

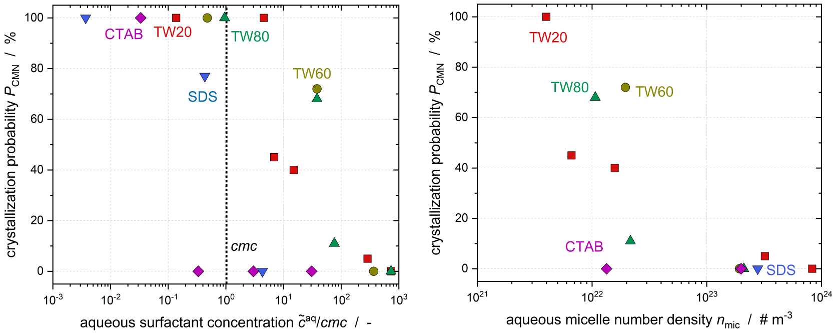

(a) Probability of CMN P_{CMN} as a function of $\tilde{c}^{aq}/cmc$.

(b) Probability of CMN P_{CMN} as a function of the number density of micelles in the aqueous phase n_{mic}.

Figure 3.15: P_{CMN} is shown to be a function of $\tilde{c}^{aq}/cmc$ and the charge of the surfactants' head groups (nonionic vs. ionic).

for the nonionic surfactants tested, a surfactant concentration of approximately $\tilde{c}^{aq}/cmc$ = 800 was needed to entirely exclude CMN within the measurement time for the nonionic surfactants.

Above cmc, this approach does not necessarily represent the micelle concentrations in the continuous phase. To evaluate the influence of the micelles, the measurements above cmc were plotted against the calculated number denisty of micelles in the continuous phase n_{mic} (Figure 3.15 b). In contrast to nonionic surfactants, the experiments with ionic surfactants showed a different behavior: Comparing the results at a given n_{mic}, fewer nucleation processes occurred for the ionic surfactants. This indicates that the electrostatic repulsion of the charged surfactant molecules reduced P_{CMN}.

Another possible reason for limited nucleation is the absence of a monolayer at the liquid-liquid interface and the presence of a multilayer or even micelles attached to the interface. This additional shield may also hinder CMN completely or reduce P_{CMN}.

3.5.2 Surfactants initially dissolved in dispersed phase

In experiments where the surfactant was initially added solely to the dispersed phase, all contacts led to nucleation, regardless of the surfactant concentration (Figure 3.16 (a)). All measured induction times were below one second (Chapter A.4.1). Additionally, the formation of liquid bridges between the liquid droplet and the solid particle was observed during some experiments (Figure 3.17). The formation of liquid bridges was never observed when the surfactants were initially dissolved in the continuous phase. In industrial processes, it is imperative to avoid the aggregation of the dispersed phase post-collision. Therefore, it is essential to minimize the formation of liquid bridges. Excessive formation of liquid bridges can shorten product shelf life or induce

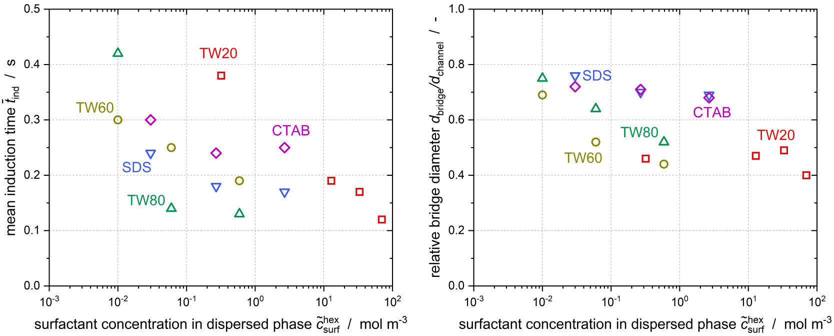

(a) Induction time needed for CMN.

(b) Thickness of liquid bridge.

Figure 3.16: Impact of dissolving the surfactant in the dispersed phase (= lower interfacial tension, less aqueous micelles).

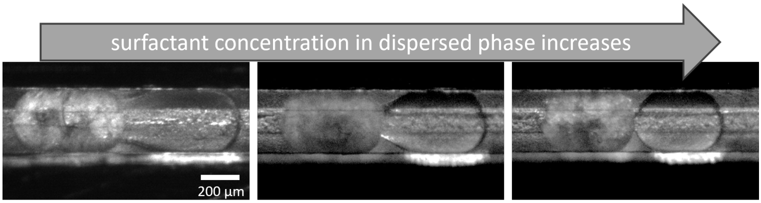

Figure 3.17: The bridge diameter decreases with increasing surfactant concentration in the dispersed phase. From right to left, $\tilde{c}^{hex}_{\mathrm{TW20}}$ is the following: 33.2 mol m^{-3}, 12.9 mol m^{-3} and 0.3 mol m^{-3}
.

alterations in product properties. In the given setup, it was not possible to investigate the separation after the collision (compare Figure 1.6).

Nonpolar substances are attracted to each other in an aqueous environment due to hydrophobic interactions, but the exact mechanism remains incompletely understood (e.g., Hammer et al. (2010)). The hydrophobic attraction has been observed at various distances, from 100 to 6500 Å (Krawczyk et al. (1991), Opawale and Burgess (1998)) and even up to around 3.5 mm for superhydrophobic surfaces (Singh et al. (2006)). However, micelles in the continuous phase appear to attenuate hydrophobic interactions between n-hexadecane particles and droplets more strongly than surfactants at the interface. Hydrophobic interactions, such as the formation of liquid bridges, occur only when there are no micelles or very few single molecules in the continuous phase.

The size of the liquid bridge formed between the droplet and the particle varied in response to the surfactant concentration in the dispersed phase no matter which kind of surfactant was used (Figure 3.16 (b)). Therefore, it can be assumed that dissolving the surfactant in the dispersed phase restricts the wetting of the crystalline surface.

Increasing surfactant concentration in the dispersed phase reduced the liquid bridge diameter in the context of two coalescing droplets (Nowak et al. (2016)). This can be attributed to the surfactant's impact on specific interfacial energies, necessitating smaller driving forces for coalescence and, thus, for CMN in these experiments. During CMN, there's presumably a gradient of specific interfacial energy on the droplet surface due to surfactants' movement at the interface, leading to the development of Marangoni flow (Scriven and Sterling (1960)). This flow facilitates a homogeneous surfactant distribution at the interface.

The promotion of small liquid bridges at higher surfactant concentrations results from two factors:

1. With more surfactants in the dispersed phase, diffusion-limited transport to the interface occurs more rapidly.
2. The larger surfactant concentration at the interface creates a more pronounced gradient on the surface, thus strengthening Marangoni flow. Larger surfactant concentrations also enable faster "refilling" of the interface when there's a concentration gradient of surfactant molecules between the continuous and dispersed phases, leading to the desorption of surfactant molecules from the interface into the continuous phase.

Chesters (1991) posits that coalescence is favored in scenarios where the dispersed phase has lower viscosities. As the addition of surfactant increases the viscosity (Figure A.2), this may also contribute to forming larger liquid bridges at lower surfactant concentrations. Smaller or absent liquid bridges are preferable for industrial processes to prevent partial coalescence, coalescence, or agglomeration and maintain product quality.

Two mechanisms could have an impact on the separation of the collision partners and on P_{CMN}: The rupture of the liquid film is mainly affected by the aqueous surfactant, whereas the stabilization of the interface after local gradients were induced should be faster when the surfactant is dissolved in the dispersed phase due to shorter travel distances (Krawczyk et al. (1991)). Surfactants dissolved in the continuous phase can delay film rupture because the surfactants migrate from the film perimeter to the film center, where the lowest surfactant concentration occurs during the approach of a droplet and a particle. Compared to surfactants in the continuous phase, surfactants dissolved in the oil phase must travel shorter distances and should be more effective in equalizing local specific interfacial energy gradients. According to Bancroft's rule (Bancroft (1913)), for a stable n-hexadecane-in-water emulsion, the surfactant needs to be dissolved in the aqueous phase. Consequently, the effect of the aqueous surfactant molecules should be the dominant mechanism for hindering CMN.

To determine this predominant impact on CMN, the equilibrium distribution for TW20 between the two phases was investigated ($\tilde{c}^{aq}_{\mathrm{TW20}} = 13.6$ mol m^{-3}, $\tilde{c}^{hex}_{\mathrm{TW20}} = 3$ mol m^{-3}). The phase composition was determined using data from long-term spectroscopic measurements (Figure 3.11). If the influence of the micelles in the continuous phase is dominant, crystallization should not occur. If, on the other hand, the surfactant plays a greater role in the dispersed phase and at the interface, crystallization should occur in all collisions. In none of the experiments with TW20 concentrations displaying an equilibrium concentration between the dispersed and continuous phases, CMN was detectable within 60 s. This emphasizes that the micelle concentration in the continuous phase is crucial for the efficiency of the CMN and must be considered in the following investigations.

3.6 Dependency of CMN on contact force

To validate that Δu reflects the contact force indirectly, a differential pressure sensor (Deltabar S PMD70, Endress + Hauser, Reinach, Switzerland) was integrated into the microfluidic setup (Figure 3.18). With this addition, the minimal contact force needed for CMN $F_{\mathrm{CMN,min}}$ can be estimated. The differential pressure sensor sends an analog output current signal to the signal converter (General Industrial Controls Private Limited, Pune, Maharashtra, India), which converts the current into a voltage signal. This signal is transmitted to the computer via an analog-to-digital converter (Measurement Computing Corporation, Norton, MA, USA). The data is analyzed using the DAQamiTM v4.2.1 software (Measurement Computing, Norton, MA, USA).

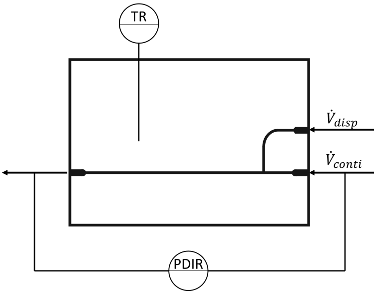

Figure 3.18: Integration of the pressure sensor in the microfluidic setup. The locations marked as $\dot{V}_{\mathrm{disp}}$ and $\dot{V}_{\mathrm{conti}}$ indicate the points where the dispersed and continuous phases were introduced into the microfluidic chip. The channel through which the dispersed phase entered the system could be sealed to enhance the precision of the Δp measurements. The dispersed phase forms droplets at the T-junction, where the two streams intersect (Figure 3.4). Adapted from Kaysan et al. (2023b), CC BY 4.0.

To ensure accuracy, the sensor underwent calibration, establishing a linear relationship between the voltage output signal and the actual differential pressure. Subsequently, the signal data were smoothed utilizing OriginPro 2021 (OriginLab, Northampton, MA, USA) employing a *floating average* method, which involved averaging ten data points via sliding average. Compensation measurements were carried out without the polycarbonate chip to consider all external factors that could influence the measurements. This made it possible to isolate and quantify the effects caused by valves, connectors and hose connections. Thus, it was possible to focus exclusively on the pressure drop within the primary channel. It is important to note that these corrections were consistently applied to all data presented in this chapter.

To determine if $F_{\mathrm{CMN,min}}$ increases with increasing aqueous surfactant concentration same as the relative velocity, possible influences of the 'empty' channel (filled with water only), solid particles as well as moving droplets are evaluated at first.

3.6.1 Empty channel

The study examined the water flow through a vacant rectangular channel to check the incorporation of the differential pressure sensor and to generate a baseline of the pressure drop for all further experiments (Figure 3.19). With increased temperature, the pressure drop across the channel diminished at all continuous phase velocities. According to McComas (1967), the inlet length L_{in} for laminar flow can be calculated with

$$L_{\mathrm{in}} = f \cdot d_{\mathrm{h}} \cdot Re. \tag{3.7}$$

Equation 3.7 leads to $L_{\mathrm{in}} = 5$ mm. Consequently, run-in effects can be neglected when evaluating the experiments.

There is a notable concurrence between the outcomes of the experimental and numerical investigations, validating the numerical simulations. To assess the accuracy of the experimental data, a comparative analysis was performed against information provided in existing literature (Figure 3.20).

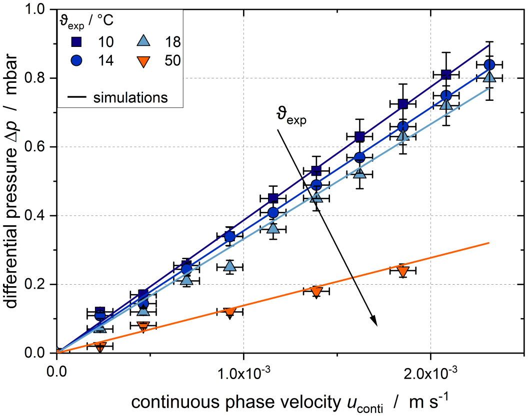

Figure 3.19: Experimental and simulated differential pressure values obtained for the rectangular microfluidic channel with pure water at temperatures ϑ_{exp} ranging from 10 to 50 °C (Kaysan et al. (2023b)).

The friction factor f can be determined from Equation 3.8, considering the calculation of the pressure drop in a straight pipe section:

$$f = \Delta p \cdot \frac{d_{\text{h}}}{L} \cdot \frac{2}{\rho u^2}. \tag{3.8}$$

In the laminar flow regime for a relative roughness smaller than 0.05, Moody (1944) posited that the friction factor f (Equation 3.8) is independent of the relative roughness. Hence, the description should follow $f = 64/Re$ in the laminar region. However, taking into account the different channel geometry (rectangular cross-section instead of circular), it is suggested that $f = 0.92 \times 64/Re$ corresponds to the experimental findings (Kast et al. (2010)). In the context of mini- and microchannels, however, the channel geometry is not the only influencing factor, as various authors have pointed out that increasing relative roughness leads to an increased friction factor even in laminar flow. This is due to significant changes in the free cross-sectional area of the channel (Ghajar et al. (2010), Moody (1944), Krishnamoorthy and Ghajar (2007), Tam et al. (2011), Gloss and Herwig (2009)). These roughness effects could explain the

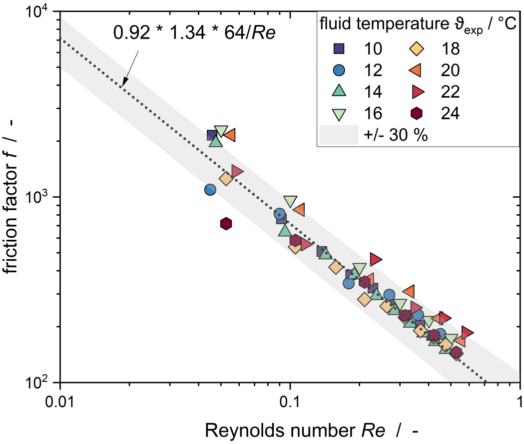

Figure 3.20: The Moody diagram illustrates the relationship between the friction factor f and the Reynolds number Re. The friction factor was computed using Equation 3.8, and Re was determined according to Equation 3.4. The shaded area denotes the range within $\pm$ 30% of the fitted data points (dotted line): $Re = 0.92 \times 1.34 \times 64/Re$, where 0.92 serves as the correction factor for employing a rectangular channel instead of a round cross-section (Kast et al. (2010)). The additional correction factor of 1.34 accounts for the channel's roughness (Kaysan et al. (2023b)).

deviation of the experimentally determined friction factor from the theoretical friction factor. Therefore, an additional correction parameter was introduced to fit the model to the experimental data points. The fit (Figure 3.20) resulted in the expression $f = 0.92 \times 1.34 \times 64/Re$. Since this formula satisfactorily reproduces the data with a coefficient of determination R^2 of more than 0.98, it can be assumed that inertia effects can be neglected.

The results demonstrate that the experimental setup is generally suitable for ascertaining the pressure drop in the microfluidic channel.

3.6.2 Solid particle in channel

The introduction of a solid particle into the channel will be addressed to evaluate its impact on Δp.

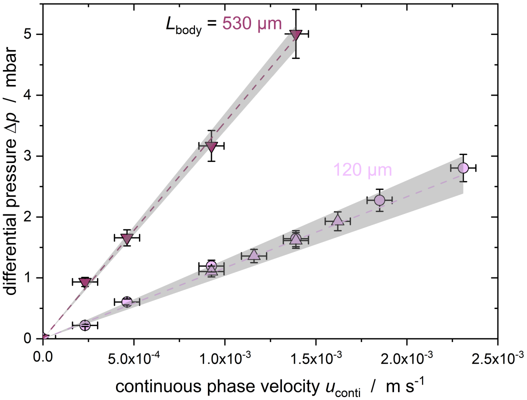

Figure 3.21: The experimental outcomes of Δp along the microfluidic channel with one particle in the channel. The impact of the continuous phase flow was already considered and only the impact of the particle on Δp is shown. The shaded regions denote the 95% confidence intervals derived from linear fits (dashed lines).

As expected, with an increase of the droplet length, Δp increased at all u_{conti} tested. This is due to diminishing the free cross-sectional area (Chapter A.4.5.2).

3.6.3 Moving droplets

Assessing the contact force required for CMN involves an experimental exploration of how the movement of liquid droplets within the channel influences Δp (Figure 3.22). Numerous studies have delved into the effects of moving droplets on Δp and have consistently reported an increase in Δp upon the introduction of moving droplets into the microfluidic channel in comparison to an empty channel (Baroud et al. (2010), Adzima and Velankar (2006)). At a constant velocity of the continuous phase u_{conti}, it becomes evident that Δp increases linearly with the total length (body + caps) of the droplet within the channel. This observation underscores that moving droplets influence the overall pressure drop, a phenomenon documented in prior literature (Baroud et al. (2010),

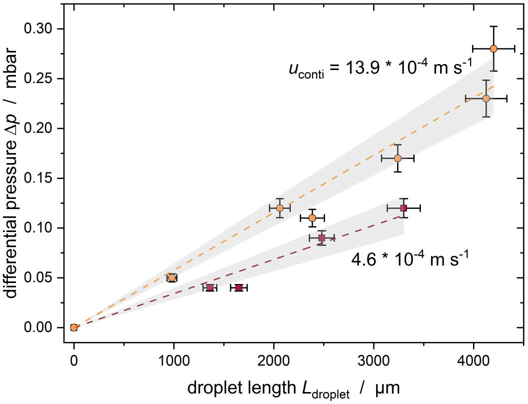

Figure 3.22: The experimental outcomes of Δp along the microfluidic channel with one droplet in the channel under two distinct velocities of the continuous phase u_{conti}. The impact of the continuous phase flow was already considered and only the impact is the droplets on Δp is shown. The shaded regions denote the 95% confidence intervals derived from linear fits (dashed lines). Apdapted from (Kaysan et al. (2023b)), CC BY 4.0.

Adzima and Velankar (2006)). The explanation for this outcome is that the liquid droplets moved slightly slower than the set velocity of the continuous phase. As per Jousse et al. (2005), the disparity between the continuous phase's and droplet's velocity should not exceed 6%. In the experiments in this work, the droplets exhibited a velocity 1–10% slower than the continuous phase, aligning well with what's reported by Jousse et al. (2005). While there is a notable discrepancy in the magnitude of impact on Δp between moving droplets and solid particles (compare Figure A.21), it is imperative to account for the influence of moving droplets on the overall Δp when performing the final assessment of CMN and calculating the force required to initiate crystallization.

3.6.4 Differential pressure during droplet crystallization

With the knowledge gained about the effects of droplets and particles on the total pressure loss, the pressure loss curves recorded during the investigation of the CMN can now be interpreted. Figure 3.23 presents an illustrative Δp measurement during an experimental CMN procedure. During the experimental investigation of CMN, different phases of Δp in dependence on the experimental time t can be identified:

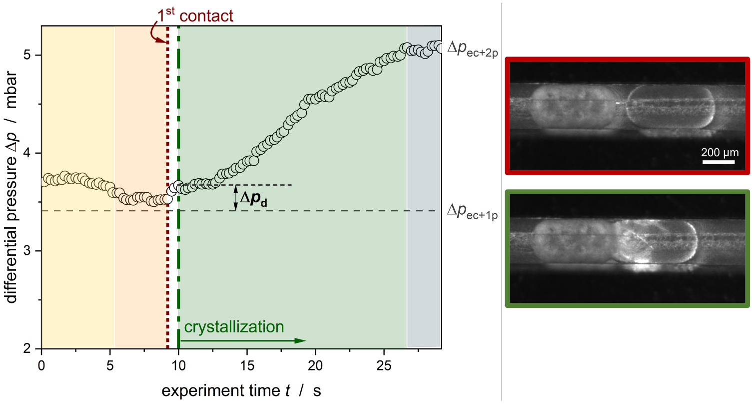

Figure 3.23: The provided data exemplifies the pressure drop as a function of time during the stages of CMN in the microfluidic setup: the droplet formation at the T-junction (depicted in yellow), the subsequent droplet movement along the channel (depicted in orange), and critical events such as the initial contact between the particle and droplet, as well as the crystallization of the droplet (depicted in green). After the complete crystallization of the droplet, the pressure drop stayed constant (shown in dark blue). $\Delta p_{\mathrm{ec+1p}}$ and $\Delta p_{\mathrm{ec+2p}}$ correspond to the measured differential pressures when either one or two solid particles were integrated in the channel and surrounded by the continuous phase. The microscopic images showcase the droplets advancing toward the solid particle (outlined in a red frame) and the subsequent crystallization of the droplet upon contact with the solid particle (outlined in a green frame) (Kaysan et al. (2023b)).

- $t < 0$: At this stage, a single solid particle is present within the channel. The corresponding $\Delta p_{\mathrm{ec+1p}}$ combines the pressure loss attributed to the fluid flow of the continuous phase around the particle and the empty channel.

- Yellow region: In addition to the solid particle, a liquid droplet forms at the T-junction of the channel and is introduced into the main channel.

- Orange region: The liquid droplet formation is complete, and the droplet advances towards the solid particle along the rectangular channel. As the previous results indicated, the moving droplet leads to an additional pressure loss, resulting in $\Delta p > \Delta p_{\mathrm{ec+1p}}$ within this region. The initial contact between the liquid and the solid particles marks the end of this phase.

- The time elapsed between the first observable contact and the visible onset of crystallization is termed the induction time. It characterizes the duration required for the successful inoculation of the supercooled liquid droplet. As demonstrated in Chapter 3.5, the induction time depends on the aqueous surfactant concentration and the relative velocity between the two colliding partners (Kaysan et al. (2021), Figure A.17). Furthermore, nucleation is possible because the solid particle appears to only have partial interfacial coverage with surfactant molecules, in contrast to the fully covered interface of liquid droplets (Kaysan et al. (2022a)). The mobility of surfactant molecules on the droplet's interface allows for molecular contact between these two partners.

- Green region: Following the initiation of crystallization, crystal strands extend through the supercooled droplet until it is entirely crystallized. The growth rate heavily depends on the degree of supercooling (in this case, $\Delta T \approx 1.1$ K). As the temperature decreases, the growth rate increases. In addition to the deformation of the liquid portion of the droplet, as it is displaced towards the particle, the elevation of Δp can also be attributed to the altered elasticity of the droplet as it solidifies.

- Upon the complete crystallization of the droplet, Δp remains constant, as indicated by $\Delta p_{\mathrm{ec+2p}}$ (empty channel + two solid particles).

Assuming that the deformation of the droplet after contact with the particle is negligible, the pressure difference Δp_{d} between $\Delta p_{\mathrm{ec+1p}}$ and the start of crystallization can be used to estimate the force F_{nuc} required for successful inoculation after contact:

$$F_{\mathrm{nuc}} = \Delta p_{\mathrm{d}} \cdot A_{\mathrm{channel}}. \tag{3.9}$$

Here, A_{channel} denotes the cross-sectional area of the channel, which is $A_{\mathrm{channel}} = 6 \times 10^{-8}$ m^2. The examination of Δp_{d} needed for nucleation was performed as a function of the TW20 concentration in the continuous phase at different u_{crit} (Figure 3.24).

At a constant relative velocity of the droplet and the particle Δu, Figure 3.24 indicates that Δp_{d} increases with increasing surfactant concentration, as F_{nuc} increases (compare Equation 3.9). The velocity of the continuous phase is in a linear relationship with Δu since it is comparable to the velocity of the liquid droplet in this setup. In the case of the two lower surfactant concentrations in the continuous phase (without (w/o) TW20 and 4 cmc), the induction time t_{ind} was $<<$ 1 s for $u_{\mathrm{conti}} > 4.6 \times 10^{-4}$ m s^{-1}, rendering it impossible to determine Δp_{d}. However, all of these collisions led to nucleation of the supercooled droplet, indicating the exceedance of F_{nuc}.

In addition to F_{nuc}, also the force attributable to the impulse of the decelerating droplet F_{ip} must be considered:

$$F_{\mathrm{ip}} = m_{\mathrm{d}} \cdot \frac{du_{\mathrm{d}}}{dt}. \tag{3.10}$$

Here, m_{d} represents the mass of the droplets, with values ranging from 1.2×10^{-8} to 3.4×10^{-8} kg, based on the minimal and maximal droplet volumes. A maximal deceleration time of 0.01 s was assumed, as this aligns with the

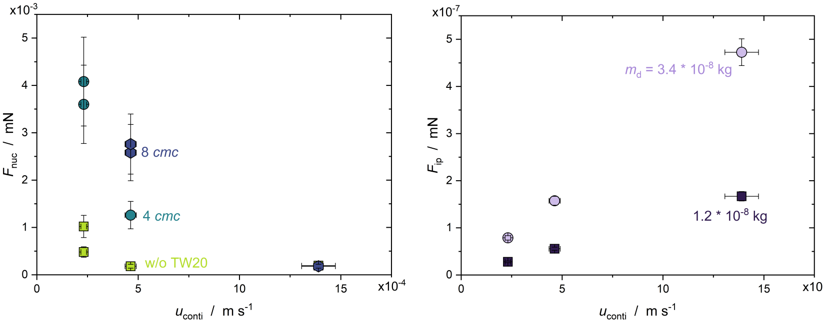

(a) Calculated force needed for nucleation.

(b) Calculated force due to the deceleration of the droplet for three aqueous surfactant concentrations. A deceleration time of 100 ms was assumed for the calculation.

Figure 3.24: Calculated forces F_{nuc} and F_{ip} (Kaysan et al. (2023b)).

highest possible camera resolution. This underscores that the estimation of F_{ip} is limited, as the time required for droplet deceleration cannot be precisely determined. Nevertheless, higher droplet velocities would inevitably lead to an increase of F_{ip}. Hence, the calculated F_{ip} represents a minimal estimate (Figure 3.24).

To determine the overall minimum force required for CMN $F_{\text{CMN,min}}$, the sum of both forces has to be calculated (Equation 3.11). The summation of the two forces is valid under the assumption that there is no temporal decoupling of F_{ip} and F_{nuc}. Since F_{ip} is lower than F_{nuc} by a factor of 10^{-3} to 10^{-4} in the investigated velocity range of the continuous phase, the influence of F_{ip} on $F_{\text{CMN,min}}$ can be neglected in these experiments.

$$F_{\text{CMN,min}} = F_{\text{nuc}} + F_{\text{ip}}. \tag{3.11}$$

With increasing u_{conti}, F_{nuc} decreases and F_{ip} increases (Figure 3.24). This could lead to the conclusion that with increasing Δu, the additional force needed for CMN is decreasing as F_{ip} is increasing. This fits well to the decrease of the induction time with increasing Δu (Figure A.17). However, it is important to note that the estimation of F_{ip} is subject to potential errors due to experimental constraints, such as the temporal resolution of the camera or the deformation of the droplet. For comparison of the impact of micelles, $F_{\mathrm{CMN,min}}$ is only evaluated for one constant Δu (Figure 3.25).

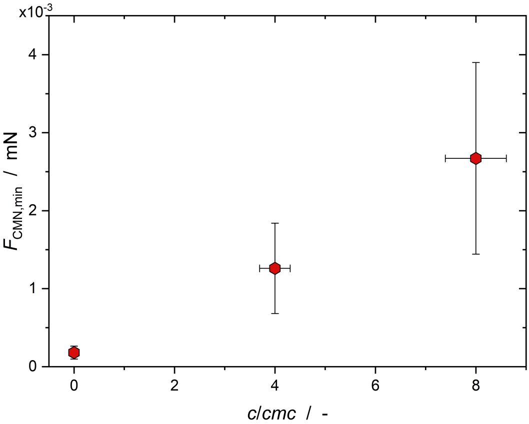

Figure 3.25: Calculated $F_{\mathrm{CMN,min}}$ according to Equation 3.11 at a constant velocity of the continuous phase of u_{conti} = 4.9 × 10^{-4} m s^{-1}.

The escalation of $F_{\mathrm{CMN,min}}$ with increasing surfactant concentration can be elucidated by the rise in the aqueous number of micelles. This aligns with findings from previous studies by Dudek et al. (2020), who observed longer mean coalescence times with increased $\tilde{c}^{aq}_{\mathrm{TW20}}$ and the results presented in Chapter 3.5.1. Notably, for $\tilde{c}^{aq}_{\mathrm{TW20}}$ = 0.41 mol m^{-3} (8 cmc), no crystallization was detectable for $u_{\mathrm{conti}} < 4.6 \times 10^{-4}$ m s^{-1}, which can also be attributed to a large number of micelles preventing contact between the two colliding partners. Before nucleation, the droplet enclosed the particle and was finely emulsified into smaller droplets (Figure A.18).

3.7 Conclusion

This study presents a comprehensive analysis of the factors influencing crystallization in microfluidic systems, specifically focusing on the crystallization of single droplets in a microfluidic channel. Through rigorous experimental and theoretical exploration, several key insights have emerged, which contribute to the fundamental understanding of microfluidic processes and have significant practical implications for the design and optimization of industrial crystallization systems.

Firstly, the impact of surfactant concentration on CMN of single droplets was substantiated. It was shown that both the location of surfactant dissolution and its concentration crucially affect the efficiency of CMN. Surprisingly, higher surfactant concentrations in the dispersed oil phase promoted nucleation more effectively than in the continuous phase.

Moreover, the study highlighted the role of relative velocity between droplets and particles in determining the likelihood of nucleation. Faster relative velocities were associated with increased nucleation probabilities, underscoring the importance of flow dynamics in microfluidic settings. These insights are particularly valuable for optimizing processes such as manufacturing pharmaceuticals and fine chemicals, where crystallization outcomes affect the efficacy and purity of the final products.

Furthermore, investigating the effects of physical parameters such as pressure drop and particle presence within microfluidic channels provided novel understandings of fluid dynamics at the microscale. The detailed characterization of pressure losses due to various channel and flow conditions contributes to a better predictive capability for designing more efficient microfluidic devices less prone to operational issues like clogging and uneven flow distribution.

Combining experimental data and numerical simulations offered a powerful approach to unraveling the complex interactions between physical forces and chemical properties in microfluidic environments. This dual approach validated the experimental observations and strengthened the theoretical foundations of droplet behavior and nucleation in confined geometries. At the same time, the CFD simulations gave the first indications that there is a difference in the flow in the minichannel compared to industry-like droplet-particle contacts (Chapter A.4.5.2).

In conclusion, this research advances the understanding of the intricate dynamics of droplet crystallization in microfluidic systems. The findings deepen the understanding of phase transition phenomena at the microscale and provide actionable insights for designing and optimizing technologies reliant on precise crystallization control. The following studies will explore the implications of these findings, potentially leading to novel approaches to controlling crystallization in various industrial and research applications.

4 CMN under laminar shear flow

Parts of this chapter are published in the following peer-reviewed papers:

Kaysan, G.; Spiegel, B.; Guthausen, G.; Kind, M. Influence of Shear Flow on the Crystallization of Organic Melt Emulsions – A Rheo-Nuclear Magnetic Resonance Investigation. Chem. Eng. Technol. 2020, 43, 1699, doi:10.1002/ceat.202000193.

Kaysan, G.; Schork, N.; Herberger, S.; Guthausen, G.; Kind, M. Contact-mediated nucleation in melt emulsions investigated by Rheo-NMR. Magn Reson Chem 2021, 60, 615, doi:10.1002/mrc.5228.

4.1 Working hypothesis

As seen in the microfluidic experiments described in the previous chapter, surfactant concentration impacts CMN. Since the crystallization of melt emulsions is industrially carried out in stirred processes, the flow and the resulting shear must be investigated as a further influencing factor. In addition, the results from the microfluidic experiments on the individual droplets must be transferred to a droplet collective with a droplet size distribution. The first step is to investigate the transfer of the results to a laminar flow.

A Taylor-Couette reactor (TCR) is particularly suitable for this purpose (Figure 4.1). The TCR can be used to have a constant shear rate across the gap so that shear distributions can be excluded in the first step. The experiments were performed inside an NMR spectrometer. This enabled the inline and non-invasive investigation of the emulsion's crystallization at a constant, adjustable temperature.

Liquids generally exhibit a low transverse relaxation rate R_2, while solids, primarily crystalline solids, usually display high R_2. Liquid state NMR spectroscopy can distinguish between the two states of aggregation (liquid and solid) allowing the quantification of the fraction of solidified droplets during crystallization to be assessed in situ.

Experiments are carried out in two different TCR setups:

- TCR with inner rotating cylinder: This setup allows the integration into the 200 MHz spectrometer, enabling the determination of the velocity profile in the slit. However, the spectral resolution of the individual peaks is limited.
- TCR with outer rotating cylinder: To investigate the influence of lower dispersed phase concentrations and the influence of the surfactant in the laminar shear field, a different TCR was integrated into the 300 MHz spectrometer.

In analogy to the coalescence theory according to Chesters (1991), an increase in shear rate leads to an increasing collision frequency, a higher contact force and a shorter contact time. Consequently, more than an increase in the shear rate is needed to guarantee that the efficiency of the CMN will also increase. Efficiency refers to the number of collisions that lead to CMN. The following hypothesis can be derived: **An increase in the shear rate initially leads to an increase in the efficiency of the CMN. However, if the shear rate is increased further, the short contact time limits the CMN and the seeding efficiency decreases.**

Regarding the effect of the surfactant concentration in the aqueous continuous phase, the results obtained from the microfluidic experiments (Chapter 3) conflict with results discussed by McClements and Dungan (1997) and Dickinson et al. (1993). In contrast to the experiments on the isolated droplets in the minichannel in this work, they found that an acceleration of the CMN was achieved by increasing the surfactant concentration in the continuous phase for quiescent emulsions. Since the flow in the microfluidic channel is more restricted than in industrial stirred tanks, it is assumed that comparable to the literature data, **an increase in the number of micelles in the continuous phase leads to a rise in J_{CMN}.**

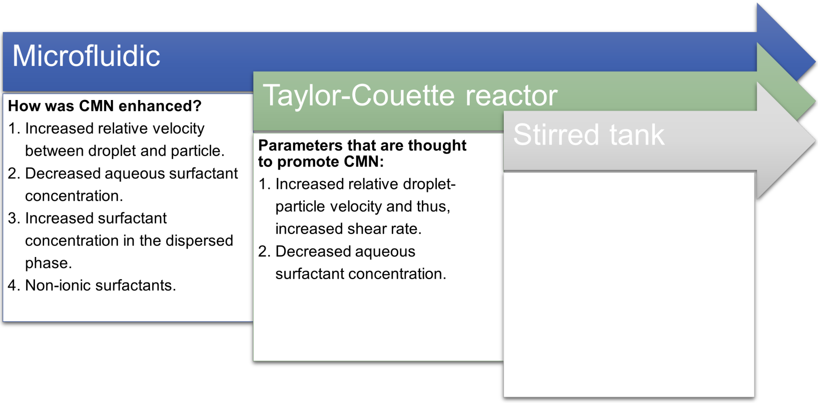

How was CMN enhanced?

1. Increased relative velocity between droplet and particle.
2. Decreased aqueous surfactant concentration.
3. Increased surfactant concentration in the dispersed phase.
4. Non-ionic surfactants.

Parameters that are thought to promote CMN:

1. Increased relative droplet-particle velocity and thus, increased shear rate.
2. Decreased aqueous surfactant concentration.

Figure 4.1: Expected influencing parameters on CMN will be evaluated in the two TCR setups. These parameters are derived from the findings of the performed microfluidic experiments.

4.2 Materials and methods

To test the hypothesis of a nonlinear relationship between shear rate and CMN efficiency, the following requirements must be met:

- The presence of defined reproducible flow conditions.
- Measurement technology for determining the solids content of moving dispersions.
- No coalescence or break-up of the droplets due to the external flow field.
- Avoidance of superimposed primary nucleation.

To meet the requirements, a Taylor-Couette geometry was selected enabling the application of laminar flow. This geometry was integrated into an NMR spectrometer leading to an experimental setup where the solid fraction of the dispersed phase of the emulsion can be detected inline and non-invasive. The setup is in analogy to Vanapalli and Coupland (2001).

4.2.1 Emulsion preparation

A 50 mL stock emulsion was prepared. It consisted of 20 wt% n-hexadecane as the dispersed phase ($C_{16}H_{34}$, Hexadecane ReagentPlus®, Sigma-Aldrich™, purity: 99%), 2 wt% TW20 (Merck, Darmstadt, Germany) as surfactant and 78 wt% D_2O (Deutero®, purity: 99.9%). The components were emulsified at room temperature for 5 min at 20,000 rpm (13.3 m s^{-1} tangential speed) in a gear rim dispersing machine (IKA® T25 digital). A new stock was created weekly to avoid long-term impacts such as coalescence or agglomeration. D_2O was used to minimize the effect of the water peak in the ^1H NMR spectrum.

The droplet size distribution (DSD) was measured using a Mastersizer 3000E (Malvern Panalytical GmbH, Kassel, Germany). The stock emulsion's DSD was modeled using a logarithmic normal distribution (droplet mean diameter $x_{50,3}$ = 2.8 μm, distribution width σ = 1.2 μm, span: 0.9 to 10.2 μm, Figure 4.2 (a)). To ensure repeatability, the stock was gently shaken before obtaining samples for the measurements.

To investigate the effects of micelle concentration in the continuous phase and dispersed phase fraction on the efficiency of CMN, emulsions with a dispersed phase fraction of 5 wt% were prepared as described above. These were stabilized with either 1 or 2 wt% TW20. The preparation as well as the DSD was the same for the emulsions with 20 wt% n-hexadecane as the dispersed phase.

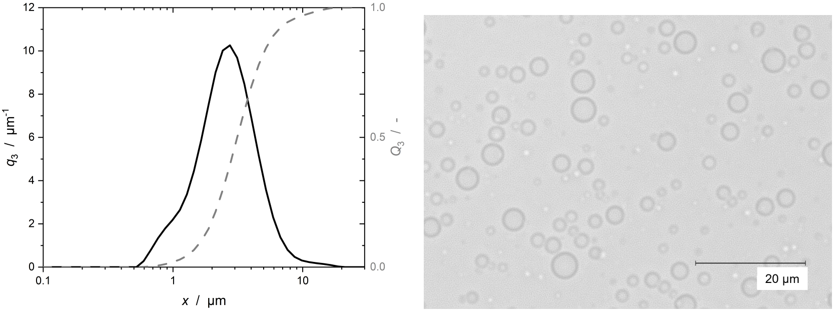

(a) DSD of an n-hexadecane-in-water emulsion stabilized with TW20.

(b) Microscopic image of an n-hexadecane-in-water emulsions.

Figure 4.2: Characteristics of a typical n-hexadecane-in-water emulsion used in this work. The emulsion contained 20 wt% n-hexadecane and was stabilized with 2 wt% TW20.

4.2.2 Measurement setup

Two different set-ups of TCR were built to estimate the influence of shear flow as well as the impact of the surfactant concentration on the crystallization of the dispersed phase: A) An inner rotating TCR was integrated into a 200 MHz NMR spectrometer with limited spectral resolution (larger diameter of sample), whereas B) an outer rotating TCR was constructed in combination with a 300 MHz NMR spectrometer (higher spectral resolution also to investigate lower dispersed phase fractions and different surfactant concentrations).

4.2.2.1 TCR with inner rotating cylinder

The experiments were performed in a Taylor-Couette Rheo-NMR reactor (Figure 4.3), similar to the one constructed by Nikolaeva et al. (2020). The TCR consists of a spinning inner cylinder attached to a shaft and powered from the top by an external motor. This inner cylinder is inserted into the stationary outer cylinder, creating a gap in which the fluid (emulsion) is subjected to a well-defined shear stress via inner cylinder rotation. The outer cylinder is attached to a base section from below via a support rod, which allows the TCR to be tempered. The cell's outer cylinder is 3D printed from GreenTEC (FD3D GmbH, Lauterach, Austria). This substance is a blend of a polylactic acid copolyester with additions. All other components were made of polyether ether ketone (Eisen-Schmitt, Karlsruhe, Germany).

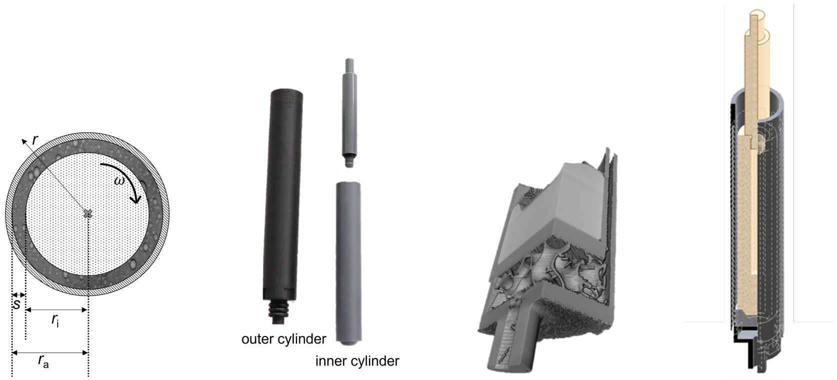

(a) Axial section of the TCR.

(b) Outer and inner cylinder of the TCR.

(c) μCT image of the 3D printed outer cylinder.

(d) Graphical illustration of the TCR.

Figure 4.3: Details of the TCR setup used in the 200 MHz spectrometer. Panels (c) and (d) reproduced from Kaysan et al. (2022c), CC BY 4.0.

The outer cylinder has an inner diameter of 18.2 mm. The ability to control the temperature in the sample volume is provided via gas passages in the outer cylinder's wall. The thickness of the wall between the gap and the channels was

0.6 mm. The inner cylinder's outer diameter $2r_\mathrm{i}$ was 16 mm, resulting in a gap width of 1.1 mm. The TCR is linked to a separate Rheo-NMR setup (Bruker BioSpin, Ettlingen, Germany). This configuration, which comprises a bottom and a top portion, allows for rotation frequencies of up to 10 Hz.

A hole was milled into the inner cylinder which was filled with methanol during the experiments. By that, the temperature can be assessed during the experiments due to the temperature-dependent chemical shift of the two methanol peaks (Ammann et al. (1982)).

Experimental procedure

Before starting each experiment, the TCR gap was filled with 5 mL of an n-hexadecane-in-water emulsion (Chapter 4.2.1) externally to the spectrometer. Subsequently, the filled TCR was connected to the Bruker Rheo-NMR shaft with the engine and integrated into the spectrometer. To ensure precise temperature control, the bottom part of the TCR was coupled with the external temperature control system. This consisted of a BVT 3000 (Bruker, Billerica, Massachusetts, USA) connected to an external nitrogen tank and with the temperature sensor close to the TCR in the spectrometer. Thus, CMN could be investigated under controllable temperature conditions.

To initiate the experiment, an emulsion with a solid fraction of the dispersed phase between 10 and 15 wt% was prepared through spontaneous, primary crystallization at a supercooling of ΔT_prim = 14.6 K. The supercooling was then reduced to ΔT_CMN = 3.1 K ($\pm$ 0.5 K) and maintained constant throughout the experiment. Under this reduced supercooling temperature, no further spontaneous crystallization occurred, and solid particles remained frozen (metastable range of the n-hexadecane droplets/particles). Following the attainment of the target temperature for CMN ΔT_CMN, a waiting period of 3.5 minutes was incorporated to ensure temperature uniformity and reliability. This waiting interval ensures consistent temperature conditions throughout the experiment, using the thermal properties of GreenTEC (Table A.3) and the mixing characteristics of the probe upon rotation initiation. The equilibration of this waiting time was further verified by monitoring methanol in the gap to calculate temperature and rotational profiles. The experiments' duration was set to 40 min after the beginning of the rotation (Figure 4.4). Only liquid n-hexadecane is detectable in the NMR measurements here, as the spin-spin relaxation (T_2 relaxation, with $T_2 = 1/R_2$) of crystalline n-hexadecane is too short. Consequently, crystalline n-hexadecane remains invisible in the liquid's ^{1}H peaks of the CH_2 and CH_3 peak (Figure 4.5). Thus, the signal detected is directly proportional to the number of ^{1}H spins in the liquid droplets of the emulsion within the field of view of the spectrometer. The presence of solidified droplets is determined by the reduction of this NMR signal (Figure 4.5). The fraction of solidified droplets at a specific time $\xi(t)$ is defined as the ratio of crystallized droplets at that time to the total number of droplets at the beginning of the experiment (Equation 2.1). Assuming a given monomodal droplet size distribution, the

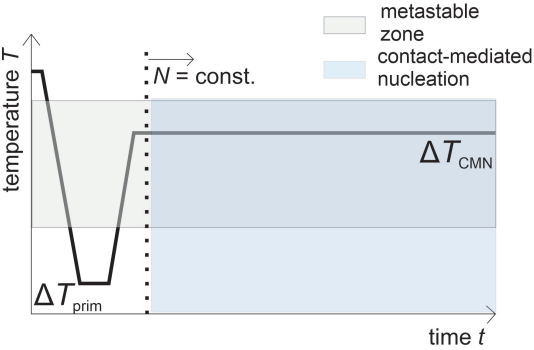

Figure 4.4: The schematically depicted standardized temperature profile was employed throughout all experiments. The gray zone signifies the metastable range, where primary nucleation is not anticipated. The blue interval represents the sustained temperature and rotational speed phase, during which contact-mediated nucleation phenomena were expected and measured (Kaysan et al. (2022c)).

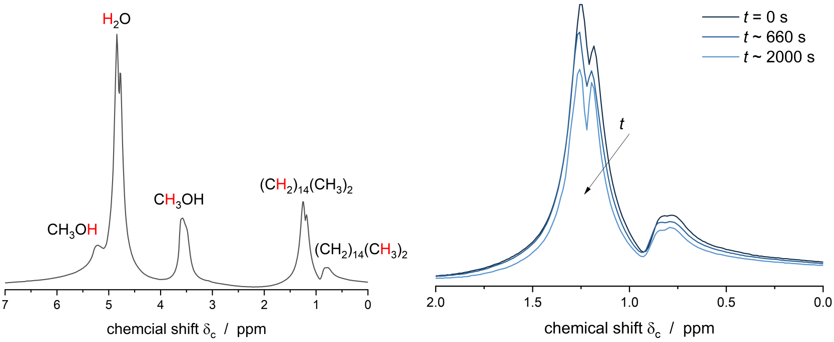

(a) ^{1}H spectrum. **(b)** Time-dependent decrease of the liquid ^{1}H signal.

Figure 4.5: (a) ^{1}H spectrum of an n-hexadecane-in-water emulsion (Φ_{disp} = 0.26), measured in a 20 mm birdcage resonator. The emulsion was stabilized with 2 wt% TW20. The spectrum reveals peaks related to the emulsion, predominantly residual H_2O (at δ_c = 4.6 ppm), and the aliphatic peaks of n-hexadecane (at δ_c = 1.26 and 0.78 ppm). Methanol peaks, utilized for temperature calibration following Ammann et al. (1982), are also visible at δ_c = 3.5 and 5.2 ppm (Kaysan et al. (2022c)). (b) NMR signal of n-hexadecane (liquid) over time during the ongoing crystallization of the droplets (Kaysan et al. (2022c)).

number density of liquid droplets is directly proportional to the integral area A_{int} of the corresponding peaks in the ^{1}H spectra (Figure 4.5):

$$\xi(t) = \frac{A_{\text{int}}(t)}{A_{\text{int}}(t_0)}. \tag{4.1}$$

The upper and lower integration limits were set to 0.6 and 1.4 ppm, respectively. The chemical shift difference between the two methanol peaks (CH_3 and OH) reflects the temperature inside the inner cylinder, which can be calculated according to Ammann et al. (1982) (Figure A.9 (a)). The peaks corresponding to TW20 are obscured by methanol and n-hexadecane signal contributions.

4.2.2.2 TCR with outer rotating cylinder

To also investigate the impact of the aqueous surfactant concentration as well as the fraction of the dispersed phase on the CMN, a TCR with an outer rotating cylinder was constructed according to Nikolaeva et al. (2020) and Kaysan et al. (2020) (Figure 4.6). Another experimental setup was needed as the spectral resolution of the 200 MHz spectrometer was insufficient to investigate the impact of shear in an emulsion with only 5 wt% n-hexadecane. The outer rotating cylinder also ensured a laminar flow profile in the gap (see Chapter 4.2.3).

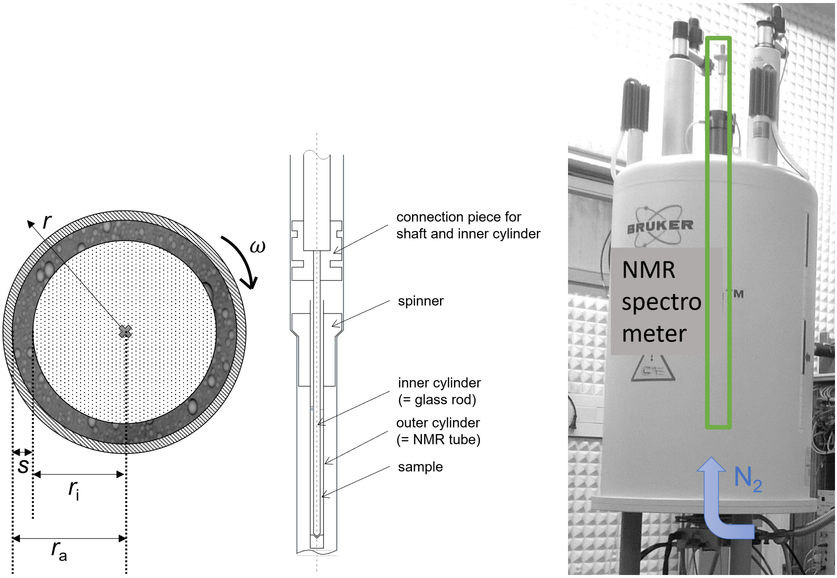

(a) Axial section of the TCR. **(b)** Schematic drawing of the TCR. **(c)** TCR integration in NMR spectrometer.

Figure 4.6: Setup of the Taylor-Couette cell in the 300 MHz spectrometer with outer moving cylinder.

A sample volume of 300 μL was introduced into the slit between the inner (r_i = 1.15 mm) and the outer cylinder (r_o = 2.0 mm), resulting in a sample height of 3.6 cm. Cole (1976) found that from a gap height of $40 \cdot s_\mathrm{gap}$ on (in this case 3.4 cm), the gap can be assumed to be an infinitely long cylinder, and thus, vertical flows can be neglected. Comparable to the experimental setup described in Section 4.2.2.1, the sample was then cooled to ΔT_prim = 14.6 K to produce a solid fraction of the dispersed phase of $\xi(t_0) \approx 0.1 - 0.15$ (Figure 4.4). All experiments were performed at ΔT_CMN = 7.8 K, where no further spontaneous nucleation occurred. The spinning of the NMR tube (outer cylinder) was started after 2 mins to guarantee that the sample was able to adjust to the newly set temperature (compare Figure 4.4). The PFG-NMR measurements' pulse-frequency details are shown in Table A.5. The temperature calibration according to Ammann et al. (1982) is presented in Figure A.9 (b).

4.2.3 Flow variables in the TCR

The geometry and rotational speeds of the two cylinders in TCRs give rise to various flow patterns (for an overview see, e.g., Cross and Greenside (2012), Czarny et al. (2002), Andereck et al. (1986)). Taylor-Couette instabilities typically arise when there is a decreasing pressure gradient with an increasing radius, occurring notably when the inner cylinder rotates and the outer remains stationary. According to Andereck et al. (1986), the sole rotation of the outer cylinder results in laminar Couette flow as the only flow form. This is characterized by a shear flow with an almost linear radial velocity profile between the two cylinders.

This study utilized Magnetic Resonance Imaging (MRI) to examine the flow field within the TCR gap, mainly when the inner cylinder was in motion. This analysis forms a critical basis for understanding the effects on crystallization efficiency. The theoretical mean magnitude velocity $u_\mathrm{xy,mag,mean}$ was defined by considering the surface velocity of the inner cylinder as the maximal velocity and assuming a gradual decrease in velocity across the gap to the outer cylinder. A no-slip condition, a thin gap, and Newtonian flow behavior were also assumed. This is following Hollingsworth and Johns (2004), given a dispersed phase fraction of 20 wt%. Rheological measurements confirmed the Newtonian behavior of the emulsion (Appendix A.3).

Experimental determination of the mean magnitude velocity involved segmenting MR images of the TCR gap filled with liquid emulsion (ΔT = 2.5 K ± 0.5 K, no crystallization) into concentric rings. The calculated magnitude velocities $u_{\mathrm{xy,mag}}(x, y)$ in each one-pixel-wide ring were averaged over the angle to obtain $u_{\mathrm{xy,mag}}$ as a function of the radius employing a similar data quantification method as described in Schork et al. (2019), Schuhmann et al. (2019) (Figure 4.7 (a)). This approach ensures good numerical stability of the velocity data up to a rotational frequency of 5 Hz. Before this, MRI was examined to exclude any angular dependence of $u_{\mathrm{xy,mag}}(r)$. $u_{\mathrm{xy,mag}}(r)$ represents the magnitude velocity at a radial position r, distinct from the velocity component along a constant radius. The mean magnitude velocity $u_{\mathrm{xy,mag,mean}}$ was then determined by volume-averaging all velocities in the gap (Figure 4.7 (b)).

Given that the experiments were done with liquid emulsion at a supercooling where no crystallization occurred, any viscosity influences can be disregarded during an experiment at a constant shear rate. Rheological measurements showed that the dynamic viscosity of the liquid emulsion remained constant at approximately 3.9 mPa s (at $\vartheta = 15.5$°C) for shear rates between 5 and 1000 s^{-1} (Appendix A.3). Thus, the viscosity of the liquid emulsion should remain unchanged throughout the experiments. Linear velocity profiles were observed for $u_{\mathrm{xy,mag}}$ across the gap (Figure 4.7 (a)). The onset of a nonlinear profile at 10 Hz may be attributed to the transition from laminar Couette flow to laminar Taylor eddy flow. Attempts to detect Taylor eddies through u_{z} measurements at a speed of 10 Hz proved challenging in terms of triggering the measurements.

There is no conclusive evidence of wall slip at higher rotational speeds, as increasing shear rates could lead to wobbling and weak movements of the

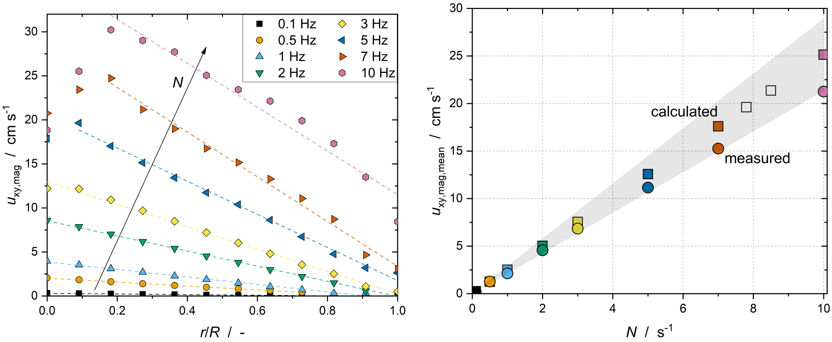

(a) Velocity across the normalized gap size (r/R) filled with the liquid emulsion at various rotational speeds. The dashed lines represent linear fits to the data with an accuracy of $R^2 > 0.95$.

(b) Mean magnitude velocity ($u_{\mathrm{xy,mag,mean}}$) obtained from theoretical calculations (squares) and experimentally determined mean magnitude velocities (circles) as a function of rotational frequency N. The shaded gray area represents a 15% error margin of a linear fit to the calculated $u_{\mathrm{xy,mag,mean}}$. The theoretical values were computed using linear interpolation of the circumferential velocity of the inner cylinder to the velocity at the outer cylinder ($u_{\mathrm{xy,mag,mean}} = 0$).

Figure 4.7: Description and validation of the velocity distribution in the gap of the TCR with inner rotating cylinder (Kaysan et al. (2022c)).

inner cylinder in the guidance. These movements impact data acquisition and processing, making experimental observations not completely aligned with theoretical expectations. Consequently, measurement errors must be considered together with the impact of the complex rheological behavior of the emulsions.

There is a good agreement between experimental and theoretical results with a maximum deviation of 15%. The absolute deviation increases with rising rotation speed, potentially attributed to factors such as using the ring method in averaging experimental data, fluctuations in the rotational speed, or assumptions made for theoretical calculations (e.g., linear profile across the gap and non-slip condition). This ensures a well-known flow field (Figure 4.7 (b)).

Hanlon et al. (1998b,a) detected a linear velocity profile for a Newtonian fluid under laminar Couette flow. Additionally, Gottwald et al. (2003) and Callaghan (2006) observed a linear velocity profile for laminar Couette flow, showcasing the suitability of NMR and MRI in determining flow profiles in small gaps. Gabriele et al. (2009) found no evidence of wall slip for dairy emulsions. Moreover, they noted an increase in nonlinearity of the velocity profile along the gap with higher shear rates. In worm-like micellular systems, a nonlinear shear profile across the gap was measured due to shear banding, independent of the shear rate (Al-kaby et al. (2018), Brown and Callaghan (2011), Brox et al. (2016)). Taylor vortex flow could also be observed with MRI, as shown by Seymour et al. (1999) and Vallatos et al. (2012). At a rotational frequency of 10 Hz, these findings align well with the results presented here that the flow pattern differs from strictly laminar flow in the gap. Thus, the results at 10 Hz cannot be compared to the rest of the data set.

To compare the findings of CMN in the TCR with conclusions in a stirred vessel (Section 5.3.1), the applied shear rate must be known. According to Hollingsworth and Johns (2004), local shear rates in a TCR can be calculated with

$$\dot{\gamma}(r) = r \frac{\partial\left(\frac{u(r)}{r}\right)}{\partial r}. \tag{4.2}$$

For the inner rotating cylinder, $u(r) = u_{\mathrm{xy,mag}}(r)$ is used for the calculation of $\dot{\gamma}(r)$.

At rotational speeds below 10 Hz, the shear rate demonstrates no radial dependence, while the velocity exhibits a linear dependency along the gap. Thus, a single value characterizes the shear per rotation speed.

Various characteristic numbers exist in the literature to describe flow within the TCR. Reynolds numbers, for instance, are employed to characterize flow regimes. The Reynolds number for the TCR was calculated as

$$Re_{\mathrm{TCR}} = \frac{u \cdot s_{\mathrm{gap}}}{\nu_{\mathrm{em}}}. \tag{4.3}$$

For the inner rotating cylinder, $u = u_{\mathrm{xy,mag,mean}}$ is used to calculate Re_{TCR}. The critical Reynolds number (Re_{crit}) delineates the shift from laminar Couette flow to laminar Taylor eddy flow. Additional critical Reynolds numbers are established for the transition from eddy flow to wave flow ($Re^{'}_{\mathrm{crit}} = 1.05 - 10^3 \cdot Re_{\mathrm{crit}}$), contingent on the size of the cylinders and the gap width (Prima and Swinney (1985), Kataoka (1986), Cole (1976)).

Furthermore, flow maps offer an approach to approximate the flow regime by considering the geometry and angular velocity (Andereck et al. (1986)). Re_{crit} was computed for the transition from laminar Couette to laminar Taylor eddy flow using Equation 4.4, following Esser and Grossmann (1996).

$$Re_{\mathrm{crit}} = \frac{1}{0.1556^2} \cdot \frac{(1+\frac{r_{\mathrm{i}}}{r_{\mathrm{o}}})^2}{2\frac{r_{\mathrm{i}}}{r_{\mathrm{o}}} \cdot \sqrt{(1-\frac{r_{\mathrm{i}}}{r_{\mathrm{o}}})(3+\frac{r_{\mathrm{i}}}{r_{\mathrm{o}}})}}. \tag{4.4}$$

According to Cole (1976), the aspect ratio of the cylinder length and the gap width gives information about whether there is vertical mixing in the gap. There is no vertical mixing for $L_{\mathrm{cyl}}/s_{\mathrm{gap}} > 40$. Thus, the critical Reynolds number for the transition to laminar vortices would solely depend on $\frac{r_{\mathrm{i}}}{r_{\mathrm{o}}}$.

The setup with the inner rotating cylinder shows $L_{\mathrm{cyl}}/s_{\mathrm{gap}} = 77$. Thus, Equation 4.4 can be used to examine the transition of the flow field. For the specific experimental configuration of the inner rotating cylinder, Re_{crit} is determined to be 121, corresponding to a rotation frequency of the inner cylinder of 17.6 Hz ($\dot{\gamma} \approx 800$ s^{-1}). This is above the maximal 10 Hz that was used in the following experiments and consequently, the flow regime should be a laminar Couette flow. However, as instabilities in the flow field were seen by the MRI measurements, the evaluation and interpretation of the experiments will only be made up to a rotational frequency of 7 Hz.

4.3 Results and discussion

The production and storage of industrial melt emulsions are highly influenced by the crystallization behaviors dictated by nucleation processes. These processes can dramatically affect the stability, texture, and quality of the final products, underscoring the significance and impact of this research. This chapter delves into the complex kinetics of nucleation, focusing on both primary nucleation and CMN, which often occur simultaneously in industrial processes but under different conditions and influencing factors.

The first subsection addresses primary nucleation kinetics, exploring the spontaneous formation of new crystalline phases from a supercooled melt without the influence of pre-existing crystal structures. Following the analysis of primary nucleation, how shear rates affect the efficiency of contact-mediated nucleation will be examined. This discussion explores the kinetic factors that govern CMN, mainly how external flow conditions influence the nucleation process. The present data will show the relationship between shear rates and solid fraction transformation over time, highlighting the practical implications for industrial crystallization processes.

The applied shear rate impacts the collision frequency, so this will be explored, detailing how changes in dispersed phase concentration affect collision rates and, consequently, nucleation rates. By comparing different experimental setups, it is discussed how varying the dispersed phase concentration can be used to control and optimize nucleation in emulsions.

Finally, the role of surfactant concentration on the efficiency of CMN is explored. The discussion will explore how micelle dynamics, surfactant concentrations, and interfacial properties affect nucleation. This section aims to link changes in chemical composition with nucleation behavior modifications, providing a comprehensive overview of how surfactants can be engineered to enhance or control nucleation in industrial applications.

4.3.1 Primary nucleation kinetics

To understand and improve the production and storage process of industrial melt emulsions primary nucleation must be considered, since in industrial processes, crystallization by primary nucleation and CMN occur side by side. The primary nucleation rate J_{prim} was determined by fitting the 1-exponential model according to Equation 2.8 to the experimental data at varying supercooling (Figure 4.8 (a)). This fit led to J_{prim} (Figure 4.8 (b)), which can also be used to determine the interfacial tension at the solid-liquid interface γ_{sl} (Figure 4.8 (c)). To calculate k_{prim}, a total droplet volume of $4.9 \cdot 10^{-8}$ m^3 was used (Figure 4.8 (d)).

The experiments were done in a 400 MHz NMR spectrometer. The setup was similar to the experiments in the TCR with the outer rotating cylinder, except that the emulsion sample was placed in a 5 mm NMR tube. Following the classical nucleation theory (see, for example, Mullin (2002)), the nucleation rate can be determined by

$$J_{\mathrm{prim}} = J_{\mathrm{prim,max}} \cdot \exp\left(- \underbrace{\frac{16\pi \cdot \gamma_{\mathrm{sl}}^3 \cdot \tilde{M}_{\mathrm{cryst}}^2 \cdot T_{\mathrm{m}}^2}{3 \cdot k_{\mathrm{B}} \cdot \Delta H_{\mathrm{f}}^2 \cdot \rho_{\mathrm{cryst}}^2}}_{\substack{thermodynamic \\ nucleation \\ parameter}} \cdot \frac{1}{\Delta T^2 \cdot T} \right). \tag{4.5}$$

$J_{\mathrm{prim,max}}$ represents the theoretical, maximal nucleation rate for a critical free enthalpy $\Delta G_{\mathrm{crit}} \to 0$ ($\widehat{=}$ kinetic nucleation parameter). γ_{sl} the interfacial tension of the solid-liquid interface, ν_m the molar volume of the crystallizing melt and ΔH_f the enthalpy of fusion.

γ_{sl} can be determined by rearranging Equation 4.5 and fitting it to the experimental data (Figure 4.8 (c)). This lead to $J_{\mathrm{prim,max}} = 1.3 \cdot 10^{39}$ m^{-3}s^{-1} and $\gamma_{\mathrm{sl}} = 10.8 \pm 0.2$ mN m^{-1}. Herhold et al. (1999) determined $\gamma_{\mathrm{sl}} = 9.9 \pm 0.2$ mN m^{-1} for an n-hexadecane-in-water emulsion stabilized with SDS and a cosurfactant. Spiegel (2019) calculated γ_{sl} between 9.4 and 9.7 mN m^{-1} for an n-hexadecane-in-water emulsion stabilized with TW20. Their values are in good agreement with these findings. The thermodynamic nucleation parameter (Equation 4.5) was determined as $3.8 \cdot 10^6$ K^3.

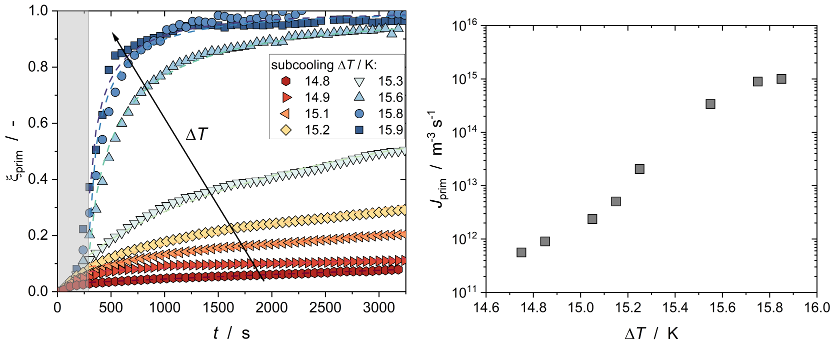

(a) Time-resolved solid fraction of n-hexadecane for different supercooling. The grey area represents the time when the temperature was not yet fully homogeneous throughout the complete sample volume.

(b) Primary nucleation rate as a function of supercooling.

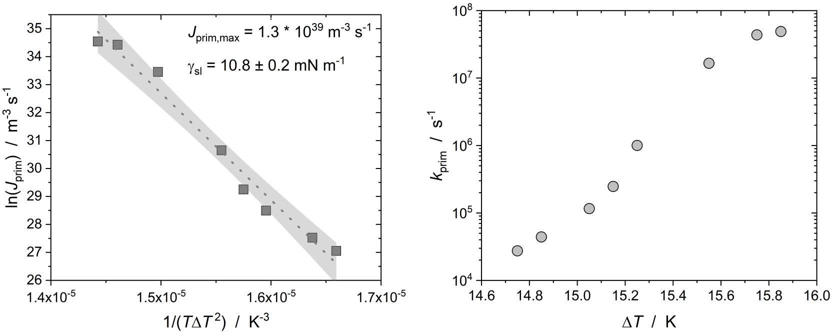

(c) Determination of the interfacial tension second order kinetic factor from the time-resolved data of the solid fraction of the dispersed phase.

(d) Primary nucleation frequency. The total droplet volume was used to calculate k_{prim} according to Equation 2.6.

Figure 4.8: Findings for primary nucleation in the dispersed phase of an n-hexadecane-in-water emulsion stabilized with TW20. The measurements were done via NMR spectroscopy.

The primary nucleation rate J_{prim} was found to be in the range of $5.6 \cdot 10^{11}$ and $1 \cdot 10^{15}$ m^{-3} s^{-1} for supercoolings between ΔT = 14.8 — 15.9 K. These determined J_{prim} will be used as a baseline for future experiments, especially for those where primary nucleation and CMN occur at the same time (Chapter 5.3.2).

4.3.2 Impact of shear on efficiency of CMN

The proportion of n-hexadecane droplets solidified as a result of contact-mediated nucleation ξ_{CMN} was measured as a function of time (Figure 4.9 (a)). ξ_{CMN} was shown to be dependent on N and, hence, on $\dot{\gamma}_{\mathrm{mean}}$. Equation 2.11 was used to get the effective collision's kinetic factor k_{CMN} (Figure 4.9 (b)). All data sets were smoothed using a five-point moving average. A distinction can be made between experiments taking the involved crystallization mechanisms into account:

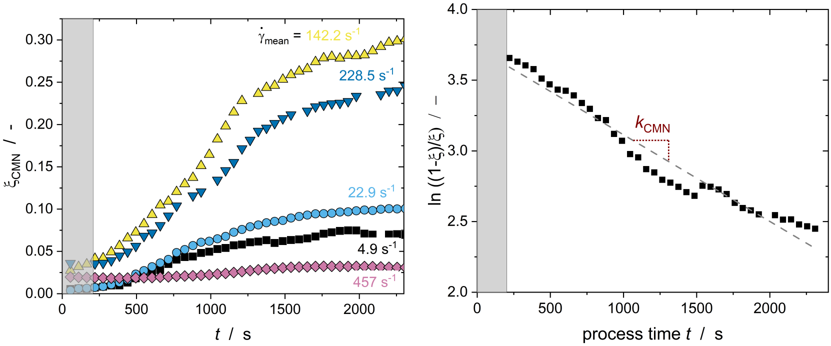

(a) Time-resolved solid fraction of n-hexadecane for different shear rates. With increasing the shear rate up to 142.2 s^{-1}, an increase in the time-dependent solid fraction can be noticed, followed by a decrease.

(b) Example of the determination of the second-order kinetic constant k_{CMN} from the time-resolved data of the solid fraction of the dispersed phase ($\dot{\gamma}_{\mathrm{mean}}$ = 4.9 s^{-1}).

Figure 4.9: Impact of shear on CMN in laminar Couette flow. The gray region indicates that temperature homogeneity was not yet given and thus was not analyzed. The experiments were performed using the TCR with an inner rotating cylinder at 200 MHz (Kaysan et al. (2022c)).

- Superposition of primary (due to supercooling) and secondary (due to CMN/shear) nucleation in a flow field (Povey et al. (2009), Abramov et al. (2017)),

- pure secondary nucleation in a flow field (Vanapalli and Coupland (2001)), and
- secondary nucleation without external flow, i.e., only Brownian motion (Dickinson et al. (1993), McClements et al. (1990), McClements and Dungan (1997)).

Mudge and Mazzanti (2009) reported that increased shear rates did not always result in higher solid fat levels of cacao butter but can also inhibit crystallization. The latter is also evident in the data provided here, as $\xi_{\mathrm{CMN}}(t_{2300\mathrm{s}})$ increases to around 29% at a rotational frequency of 3 Hz and subsequently falls as a function of the mean shear rate (Figure 4.9).

The impact of shear on k_{CMN} is described in Figure 4.10. There wasn't a linear relationship between k_{CMN} and $\dot{\gamma}_{\mathrm{mean}}$ found, but the formation of a maximum in the range of $\dot{\gamma}_{\mathrm{mean}} \approx 170$ s^{-1}. For laminar Couette flow with shear rates up to $\dot{\gamma}_{\mathrm{mean}} = 296$ s^{-1}, a linear relationship between k_{CMN} and $\dot{\gamma}_{\mathrm{mean}}$ was pointed out by Kaysan et al. (2020). One of $3{\cdot}10^5$ theoretically calculated collisions resulted in the nucleation in a liquid droplet by a crystalline particle. Dickinson

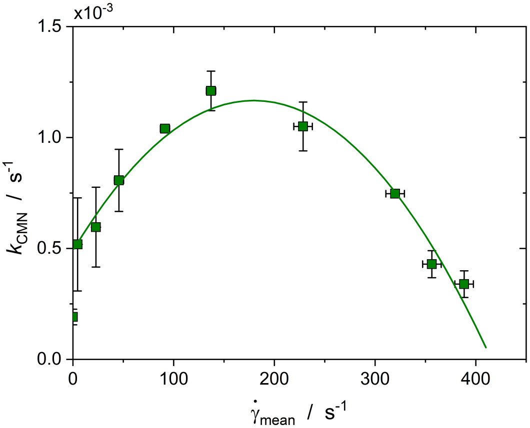

Figure 4.10: The kinetic factor k_{CMN} as a function of shear rate. The line is a guide to the eye.

et al. (1993) stated that one out of every 10^7 collisions resulted in nucleation. In this work, one out of $1.5{\cdot}10^2$ to one out of $1.3{\cdot}10^8$ collisions led to CMN, depending on the collision partners' sizes and mean shear rate. Smaller shear rates and, consequently, reduced relative velocities and decreasing droplet sizes result in a higher CMN efficiency.

Due to certain similarities between coalescence and CMN, the interpretations of the results are based on the coalescence theory according to Chesters (1991). Thus, the underlying mechanisms of coalescence will be used to describe and discuss the efficiency of CMN in the following.

Distinguishing coalescence from CMN involves two key differences: (1) The interface of the liquid droplet can be either mobile or immobile, whereas the interface of the crystalline droplet is presumed to be permanently immobile. (2) Upon contact with particles, the interface of the liquid droplet can deform, whereas the particle is non-deformable.

In general, for coalescence to happen, the distance between the surfaces of the supercooled droplet and the crystalline particle must be less than the critical film thickness for nucleation (Liao and Lucas (2010)). Multiple models can be used to characterize the collision efficiency of two droplets (Liao and Lucas (2010)):

- Two physical models:
  - The energy model (Howarth (1967), Sovová (1981)) and
  - the film drainage model (Chesters (1991), Jeffreys and Davies (1971), Davis et al. (1989), Mackay and Mason (1963), Sagert and Quinn (1976))
- One empirical approach:
  - The critical velocity model (Lehr and Mewes (2001), Lehr et al. (2002))

Applying these models to CMN, the energy model would predict nucleation for relative velocities exceeding a critical relative velocity. However, this approach fails to explain the observed decline in secondary nucleation efficiency with increasing flow velocity.

In film-drainage models, coalescence occurs when the contact time t_{coll} exceeds the thin-film drainage time. The latter decreases with increasing driving force and increases with viscosity and film size (e.g., Chesters (1991), Mackay and Mason (1963), Chappelear (1961)). In turbulent flow, t_{coll} is commonly taken to scale with the Kolmogorov time, $\tau_{\eta} = (\nu/\epsilon)^{1/2}$, and thus decreases with increasing energy dissipation rate ϵ (Levich (1962)).

Studies in microfluidic devices (e.g., Krebs et al. (2012) and Zhou et al. (2016)) show that, under laminar flow, lower droplet velocities yield longer contact times. By contrast, increasing the approach velocity raises the hydrodynamic contact force and generally shortens thin-film drainage and coalescence/induction times up to a critical velocity, beyond which contact times may become too short and bounce can occur. Accordingly, both very low and very high velocities can reduce collision/coalescence (and CMN) efficiencies, consistent with the trends reported here.

The critical velocity model (considering also data from Doubliez (1991) and Duineveld (1994)) introduces a contact force dependency, suggesting that CMN should be sensitive to collision strength, favoring soft collisions. The qualitative statements obtained with the critical velocity model are in line with the results obtained in this work.

Given these results, the maximum of the kinetic factor k_{CMN} as a function of the shear rate $\dot{\gamma}_{\mathrm{mean}}$ should be caused by high collision numbers. This results in high solid fractions. At higher shear rates, k_{CMN} is probably limited by the short contact time of the collision between droplets and particles.

4.3.3 Impact of collision frequency on CMN

To analyze the possible effects of shear that are assimilated in the previously shown experiments (collision rate, contact time, contact force), now the impact of the collision rate h_{coll} is investigated isolated from the impact of contact time and contact force. h_{coll} is defined as the volume-specific number of collisions between droplets and particles per time.

As an increasing shear rate leads to an increasing number of possible collisions (an increase of h_{coll}), experiments are performed with an emulsion with a dispersed phase fraction of 5 wt% n-hexadecane ($\Phi_{\mathrm{disp}} = 0.06$). This emulsion contains a lower absolute number of droplets compared to an emulsion with 20 wt% n-hexadecane ($\Phi_{\mathrm{disp}} = 0.26$). Both emulsions showed a similar droplet size distribution. At a constant shear rate, the effect of h_{coll} on the CMN can be investigated (Figure 4.11 and Figure 4.12). At a constant shear rate and

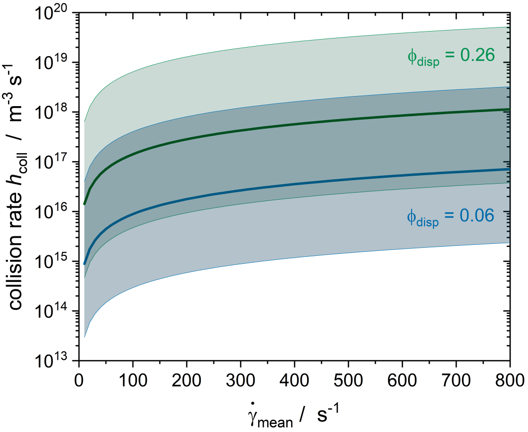

Figure 4.11: Comparison of the collision rates for emulsions with either $\Phi_{\mathrm{disp}} = 0.06$ (blue) or $\Phi_{\mathrm{disp}} = 0.26$ (green) for a solid fraction of the dispersed phase of $\xi_{\mathrm{hex}} = 0.2$. The solid line represents h_{coll} when assuming the collision of droplets and particles with $x_{50,3}$. In contrast, the lighter area represents all possible collisions, such as the smallest (bottom) or largest (top) droplets/particles with each other.

solid fraction of the dispersed phase, h_{coll} is about 16 times smaller when using only $\Phi_{\mathrm{disp}} = 0.06$ instead of $\Phi_{\mathrm{disp}} = 0.26$, as the total number of droplets is reduced.

When decreasing the dispersed phase fraction from $\Phi_{\mathrm{disp}} = 0.26$ to $\Phi_{\mathrm{disp}} = 0.06$ at a constant surfactant concentration, the maximum of k_{CMN} is shifted to higher shear rates (Figure 4.12 (a)). According to Liao and Lucas (2010), the coalescence rate can theoretically be described as the product of the collision rate and the coalescence efficacy. Similarly, for CMN, the following applies:

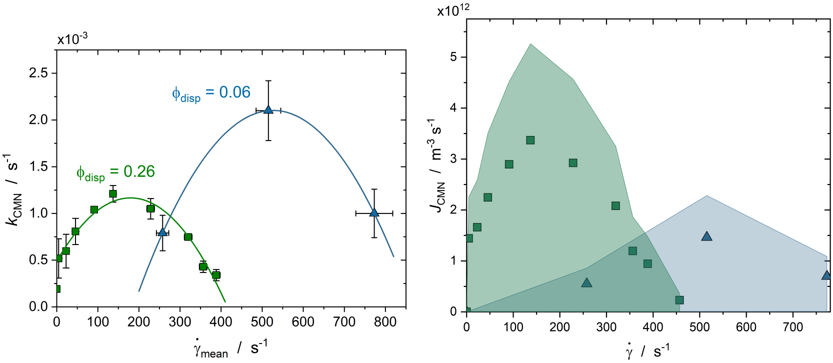

(a) Comparison of the kinetic factor of CMN for two different dispersed phase fractions Φ_{disp} at a range of shear rates. The data points are fitted by a second-order function as a guide to the eye.

(b) Calculated nucleation rate for CMN J_{CMN} for $\Phi_{\mathrm{disp}} = 0.26$ (green) and 0.06 (blue) (Equation 4.6). The shown data points are calculated for $\xi = 0.2$. The highlighted areas represent the range of J_{CMN} during the crystallization of the dispersed phase ($J_{\mathrm{CMN,max}}$ for $\xi = 0.5$).

Figure 4.12: Impact of h_{coll} on the CMN.

$$J_{\mathrm{CMN}} = \lambda_{\mathrm{CMN}} \cdot h_{\mathrm{coll}}. \tag{4.6}$$

No theoretical equation to calculate λ_{CMN} was found in the literature. Therefore k_{CMN} will be used for the estimation: The mean collision rate $\bar{h}_{\mathrm{coll}}$ can be calculated according to Equation 4.7. The basic assumption is that the two particle classes, liquid and solid, have the same density and constant droplet size. In addition, a constant number of droplets and particles is assumed (no agglomeration) and a size-independent, time-constant nucleation efficiency λ_{CMN}.

$$\begin{aligned}\bar{h}_{\mathrm{coll}} &= \frac{\beta_{\mathrm{lam,l,s}} \cdot n_{\mathrm{total}}^2}{\xi - \xi_0} \int_{\xi_0}^{\xi} \xi(1-\xi)d\xi \\ &= \frac{\beta_{\mathrm{lam,l,s}} \cdot n_{\mathrm{total}}^2}{\xi - \xi_0} \left[\left(\frac{\xi^2}{2} - \frac{\xi^3}{3} \right) - \left(\frac{\xi_0^2}{2} - \frac{\xi_0^3}{3} \right) \right]. \end{aligned} \tag{4.7}$$

Using a population balance of the dispersion with J_{CMN} (Equation 4.6) as the so-called aggregation rate, the change in particle number density n_{s} with time can be calculated with

$$\begin{aligned}\frac{\partial n_{\mathrm{s}}}{\partial t} &= J_{\mathrm{CMN}}(\lambda_{\mathrm{CMN}}, \beta_{\mathrm{l,s}}, x, \xi) \\ &= \lambda_{\mathrm{CMN}} \cdot \beta_{\mathrm{l,s}}(x) \cdot n_{\mathrm{total}}^2 \cdot \xi(1-\xi) = \frac{\partial \xi}{\partial t} \cdot n_{\mathrm{total}}. \end{aligned} \tag{4.8}$$

Comparing Equation 4.8 with Equation 2.11 finally leads to

$$k_{\mathrm{CMN}} = \lambda_{\mathrm{CMN}} \cdot \beta_{\mathrm{l,s}} \cdot (n_{\mathrm{s}} + n_{\mathrm{l}}). \tag{4.9}$$

Rearranging Equation 4.9 enables the determination of λ_{CMN} and finally also the calculation of J_{CMN} according to Equation 4.6 (Figure 4.12 (b)).

Figure 4.12 (b) shows that to achieve the maximum of J_{CMN} for the emulsion with lower dispersed phase fraction, higher shear rates are needed than compared to an emulsion with $\Phi_{\mathrm{disp}} = 0.26$. This indicates that the number of collisions is of great importance for the final solid content of the dispersion. Consequently, the impact of shear cannot be neglected when investigating the crystallization of emulsion droplets in a stirred system.

4.3.4 Impact of surfactant concentration on CMN

To also investigate the impact of the aqueous micelle numbers on the efficiency of CMN in laminar flow, the surfactant concentration was decreased at a constant number of droplets (Figure 4.13). According to the results found for the microfluidic experiments, a decrease in the aqueous surfactant concentration should lead to an increase in the efficiency of CMN. This would be visible in an increase of J_{CMN} and λ_{CMN} as the induction time and minimum contact force needed for successful CMN are shortened/decreased. Different from the microfluidic results, a decrease in the aqueous surfactant concentration led to a reduction of k_{CMN} and thus a decrease of the efficiency of CMN at a given shear rate and $\Phi_{\mathrm{disp}} = 0.06$. The different flow conditions and geometrical constraints in the TCR and the microfluidic setup might explain this. Using computational fluid dynamic (CFD) simulations to investigate the flow in the

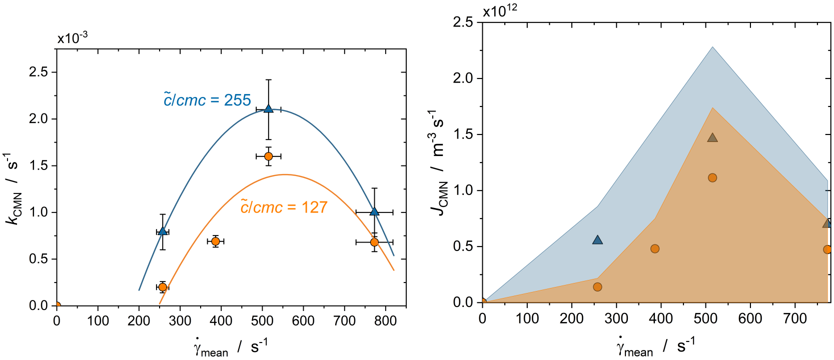

(a) Comparison of the kinetic factor of CMN for two different surfactant concentrations at a range of shear rates. The data points are fitted by a second-order function as a guide to the eye.

(b) Calculated nucleation rate for CMN J_{CMN}. The represented data points are calculated for $\xi = 0.2$. The highlighted areas represent the range of J_{CMN} during the crystallization of the dispersed phase ($J_{\mathrm{CMN,max}}$ for $\xi = 0.5$).

Figure 4.13: Impact of surfactant concentration on CMN.

minichannel, Kaysan et al. (2023b) revealed that circular flow conditions occur between the two approaching reaction partners.[1] (Figure 4.14).

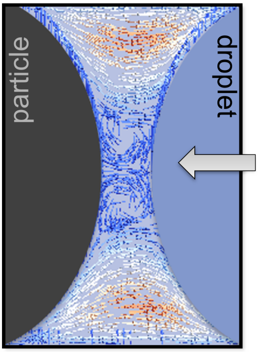

Figure 4.14: Simulations of the fluid flow between two objects in a minichannel. For the simulations, two non-deformable, static particles were assumed.

In the confined microchannel geometry, recirculating flow near the droplet–particle gap can hinder convective removal of surfactant and micelles from the thin film. As a result, residual surfactant (as monomers or micelles) may persist in the gap. Consistent with this picture, increasing surfactant concentration in the microfluidic setup led to longer induction times and a higher contact force needed for CMN. At higher relative velocities, the simulated vortices became stronger, further promoting retention in the gap. These confined-flow conditions are not directly comparable to the laminar collision environment in the TCR, where collisions are not spatially confined and such recirculations between colliding droplets/particles are not expected.

In line with the TCR results, an acceleration of nucleation with increasing surfactant concentration was observed by McClements et al. (1994) and corroborated by Dickinson et al. (1993) for n-hexadecane emulsions stabilized by

---

[1] For the CFD simulations, two immobile particles were assumed to investigate the flow between the two reaction partners, compare Section A.4.5

various surfactants. Their experiments used small emulsion volumes in cuvettes and ultrasonic measurements of solids content. Notably, there was no steric hindrance caused by micelles, and the movement of droplets within the emulsions was considered. Regardless of the chemical nature of the surfactant, the presence of seed crystals, i. e. particles, led to a substantial increase in the nucleation rate.

Dickinson et al. (1993) reported an increase of k_{CMN} with rising surfactant concentration, regardless of surfactant type, in quiescent emulsions. Using a second-order kinetic model at $\Delta T = 12.6$ K, k_{CMN} rose from $1.7 \cdot 10^{-6}$ s^{-1} at $\tilde{c}^{aq}_{\mathrm{TW20}} = 6$ mol m^{-3} to $5.2 \cdot 10^{-6}$ s^{-1} at $\tilde{c}^{aq}_{\mathrm{TW20}} = 18$ mol m^{-3} (this work: $k_{\mathrm{CMN}} \approx 2 {\cdot} 10^{-3}$ s^{-1}). The lower values in Dickinson et al. (1993) are consistent with their quiescent conditions and smaller droplets ($x_{3,2}$ = 0.37 μm vs. $x_{3,2} \approx$ 2.4 μm here), which reduce the collision frequency h_{coll} and thus k_{CMN}.

McClements and Dungan (1997) likewise observed higher k_{CMN} with increasing aqueous TW20 concentration in n-hexadecane-in-water emulsions (30 wt% n-hexadecane, $\Delta T = 12.6$ K), from $2.2 \cdot 10^{-6}$ s^{-1} at $\tilde{c}^{aq}_{\mathrm{TW20}} = 2$ mol m^{-3} to $5.8 \cdot 10^{-6}$ s^{-1} at $\tilde{c}^{aq}_{\mathrm{TW20}} = 14$ mol m^{-3}. They attributed the increase to changes in interfacial properties and droplet–droplet interactions (reduced interfacial tension, template effects, and depletion flocculation).

For the emulsions studied here, nucleation acceleration due to a further decrease in interfacial tension is unlikely: the surfactant concentration was well above the *cmc*, so additional interfacial tension reduction is minimal (Bąk and Podgórska (2016)). The template effect (promotion of nucleation by similarity between the surfactant tail and the dispersed phase) can be excluded for TW20 with n-hexadecane due to their dissimilar hydrophobic structures (Elfgen et al. (2017), Spiegel (2019)).

Depletion flocculation, as discussed by McClements and Dungan (1997), typically requires non-adsorbing polymer coils in the continuous phase; since no polymer was present in the systems studied here, classical polymer-induced depletion is not expected to contribute.

Kaysan et al. (2022a) investigated the interfacial occupancy of liquid and solid droplets and established that there are fewer TW20 molecules on the surface of a crystalline n-hexadecane droplet compared to a liquid droplet. As crystallization progresses, TW20 molecules desorb from the interface. The small-angle X-Ray scattering (SAXS) measurements revealed that n-hexadecane molecules were trapped in the center of TW20 micelles. Although these nanodroplets occupy a small volume, they possess a considerable surface area and are present in significant numbers. When these small droplets undergo crystallization, they substantially contribute to CMN by increasing the collision frequency. The experiments in this study achieved the supercooling of $\Delta T \succcurlyeq 13$ K required for homogeneous nucleation in nanodroplets with a diameter of x = 10 nm (El Rhafiki et al. (2011)).

4.4 Conclusion

In this chapter, the nucleation kinetics of CMN of n-hexadecane-in-water emulsions were explored in two different TCR setups. The findings obtained emphasized the significant role of CMN in the crystallization of melt emulsions in a shear field.

The analysis started by exploring primary nucleation as a baseline for all the following experiments, focusing on the spontaneous generation of new crystalline structures from a supercooled melt emulsion. Considering the droplet size distribution, the experimental data were fitted using the one exponential fit according to Perepezko et al. (2002). This quantitative approach helps to understand the thermodynamic and kinetic parameters controlling nucleation rates. Both parameters were in the range of what is reported in the literature.

The chapter then delves into how shear rates influence CMN, with a detailed discussion on how external flow conditions and collision frequency affect nucleation processes. It presents experimental data showing the relationship between shear rates and the transformation of solid fractions over time, highlighting the practical implications for industrial crystallization. Notably, it is observed that increased shear rates do not always enhance crystallization; instead, they can inhibit it due to changes in collision dynamics.

Further, the effect of varying the number density of droplets in emulsions on nucleation rates is evaluated. The findings indicate that adjusting the number of droplets can significantly influence nucleation efficiency, offering a method to control and optimize nucleation processes in industrial applications.

Lastly, the influence of surfactant concentration on CMN is investigated. It discusses how changes in micelle dynamics, surfactant concentrations, and interfacial properties can alter nucleation behavior. The results suggest that surfactants can be engineered to enhance or control nucleation effectively, linking chemical composition changes with nucleation behavior modifications. An increase in the aqueous surfactant concentration led to a faster crystallization of the dispersed phase of the emulsion.

The chapter provides a comprehensive overview of how various factors, such as shear rates, dispersed phase concentration, and surfactant levels, influence nucleation kinetics in industrial melt emulsion systems. It lays a theoretical and experimental foundation for optimizing these processes to improve the texture, stability, and quality of the final products.

5 CMN in industry-like flow pattern

Parts of this chapter are published in the following peer-reviewed paper:

Kaysan, G.; Elminger, L.; Kind, M. Increasing the Efficiency of Emulsion Crystallization in Stirred Vessels by Targeted Application of Shear and Surfactant. *Colloids Interfaces*, 7(4):68, 2023. doi:10.3390/colloids7040068.

5.1 Working hypothesis

The primary focus of this chapter is to explore the potential to enhance the crystallization of melt emulsions in a more industrial-relevant environment compared to those previously studied. A stirred vessel equipped with an ultrasonic probe was chosen as an experimental setup. This study will primarily assess the effects of increased energy input on the crystallization dynamics (Figure 5.1). Based on earlier findings, the following hypothesis is stated:

A higher nucleation rate of the dispersed phase can be achieved by adjusting the shear rate and increasing the surfactant concentration in the aqueous phase. Since a stirred vessel exhibits a range of shear rates, the impact of shear might be weaker than in the TCR experiments.

This research initially evaluates crystallization of n-hexadecane-in-water emulsions in conditions that mimic those in industrial melt emulsion production, integrating observed nucleation mechanisms. The results of this study are expected to offer crucial insights, facilitating the more precise application of shear and surfactants in industrial settings. Adopting such a strategic approach could lead to more sustainable manufacturing practices by minimizing energy usage and reducing overall process duration.

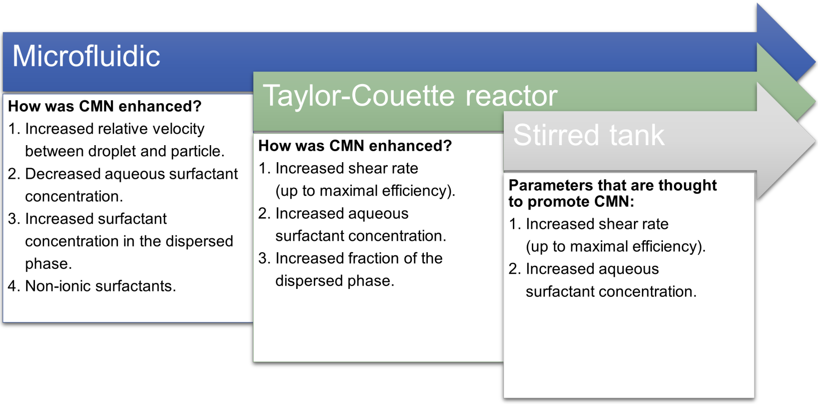

How was CMN enhanced?

1. Increased relative velocity between droplet and particle.
2. Decreased aqueous surfactant concentration.
3. Increased surfactant concentration in the dispersed phase.
4. Non-ionic surfactants.

How was CMN enhanced?

1. Increased shear rate (up to maximal efficiency).
2. Increased aqueous surfactant concentration.
3. Increased fraction of the dispersed phase.

Parameters that are thought to promote CMN:

1. Increased shear rate (up to maximal efficiency).
2. Increased aqueous surfactant concentration.

Figure 5.1: Expected influencing parameters on CMN that will be evaluated in the stirred vessel. These parameters are derived from the findings of the performed microfluidic and TCR experiments.

5.2 Materials and methods

5.2.1 Experimental setup and material system

The experiments were done in a double-jacket stirred vessel made of borosilicate glass with a working volume of one liter (Figure 5.2, Table 5.1). The vessel was equipped with a six-bladed impeller (engine: Hei-TORQUE Expert 100, Heidolph Instruments GmbH, Schwabach, Germany), four baffles to prevent the formation of a vortex flow as well as four temperature sensors (Pt100, ES Electronic Sensor GmbH, Heilbronn, Germany) to detect any temperature inhomogeneities (Figure 5.2). The temperature is recorded every 10 s (software: DAQami, Version 4.2.1 Measurement Computing GmbH, Bietigheim-Bissingen, Germany). The temperature in the vessel is adjusted by two external thermostats (Lauda Eco RE 1050 G (temperature constancy of ± 0.02 K) and Lauda Eco E 10, Lauda, Lauda-Königshofen, Germany). A 35 wt% ethylene glycol-water mixture is used as a tempering medium, flowing through the double jacket of the tank. The vessel was insulated with the elastomer foam ArmaFlex to minimize heat loss flows to the environment.

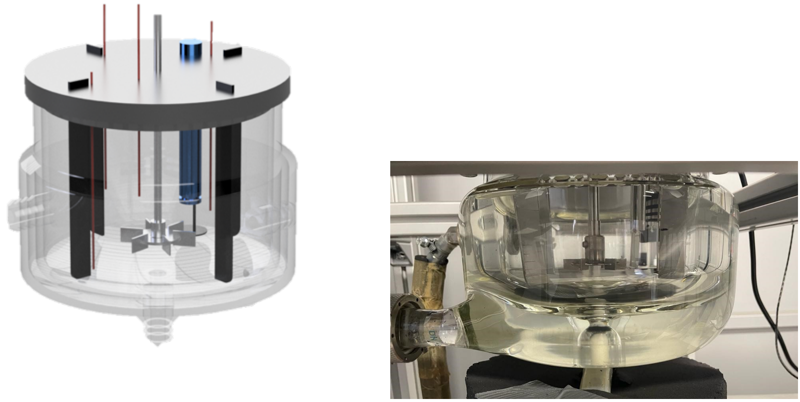

(a) CAD drawing of the used stirred vessel, equipped with the ultrasonic probe (Kaysan et al. (2023a)).

(b) Photo of the experimental setup of the stirred vessel. Besides the ultrasonic probe, also the 6-bladed impeller is visible.

Figure 5.2: Stirred vessel — Drawing and photo of the experimental setup.

In this study, the solid fraction of the dispersed phase was quantified using an ultrasound echoscope (GS200, GAMPT mbH, Merseburg, Germany) equipped with a 2 MHz ultrasound probe (GAMPT mbH, Merseburg, Germany). This probe functioned as transmitter and receiver of ultrasonic signals. Known for its high axial resolution and low signal attenuation, the probe was strategically

Table 5.1: Dimensions of the stirred vessel and the stirring element with specifications according to Deutsches Institution fuer Normung (1992).

	DIN 28131	**Value**
diameter vessel d_{ves} / mm	—	150
diameter impeller d_{st} / mm	$\approx(0.3 \text{ to } 0.4) \cdot d_{\mathrm{ves}}$	50 (= 0.33 $\cdot d_{\mathrm{ves}}$)
width of impeller blades	$\approx 0.25 \cdot d_{\mathrm{st}}$	12 (= 0.24 $\cdot d_{\mathrm{st}}$)
height of impeller blades	$\approx 0.2 \cdot d_{\mathrm{st}}$	10 (= 0.2 $\cdot d_{\mathrm{st}}$)
distance of impeller to tank bottom	$\approx 1 \cdot d_{\mathrm{st}}$	28 (= 0.56 $\cdot d_{\mathrm{st}}$)
width of baffles	$\approx 0.1 \cdot d_{\mathrm{ves}}$	15 (= 0.1 $\cdot d_{\mathrm{ves}}$)
tank wall spacing of baffle	$\approx 0.02 \cdot d_{\mathrm{ves}}$	3 (= 0.02 $\cdot d_{\mathrm{ves}}$)
number of impeller blades	≥ 6	6
number of baffles	≥ 2	4

positioned at the same height as the impeller blades to minimize the deposition of solid droplets, which often accumulate in stagnant flow regions. An aluminum plate (20 mm × 20 mm × 3 mm) was placed 20 mm from the probe to reflect the ultrasound for measurement purposes. To counteract sound signal propagation losses, both emitted and received signals were amplified by 5 dB. The recorded signals were then analyzed using a Matlab script (Version 2021b, MathWorks, Inc., Natick, MA, USA) to calculate the speed of sound v every 10 seconds. The parameters used for the measurement were chosen after a study of the parameters' impact on the quality of the speed of sound calculation (Appendix A.5.3).

In the experiments, an n-hexadecane-in-water emulsion was utilized, comprising the volumetric fraction of the dispersed phase of $\Phi_{\mathrm{disp}} = 0.06$ (Hexadecane ReagentPlus®, Sigma-Aldrich, St. Louis, MO, USA; purity: 99%) and varying concentrations of Tween®20 (TW20, Sigma-Aldrich, St. Louis, MO, USA) as the surfactant. The continuous phase was demineralized water (OmniaTap, stakpure GmbH, Niederahr, Germany; electrical conductivity: 0.057 μS cm^{-1}).

For the preparation of the emulsions, a premix of the continuous phase and the surfactant was generated using a magnetic stir bar (RCT basic, IKA Werke, Staufen im Breisgau, Germany) at 700 rpm and room temperature for 1 min. Subsequently, n-hexadecane was added. Two emulsions were produced: Emulsion I was prepared with a gear-rim dispersing machine (IKA® T25 digital, ULTRA-TURRAX®, Staufen im Breisgau, Germany) at 20,000 rpm (13.3 m s^{-1} tangential speed) for 5 min at room temperature, while Emulsion II was prepared using an inclined blade impeller (four blades, impeller diameter 59 mm) at 2,000 rpm (6.18 m s^{-1} tangential speed) for 10 min at room temperature.

The DSD of the emulsions (Figure 5.3) was determined using a Mastersizer 3000E (Malvern Panalytical, Malvern, UK), with a reflection index of 1.433 and an adsorption index of 0.05 set for the measurements. The spherical form of the droplets was confirmed by microscopic examinations (digital microscope VHX-7000, Keyence, Osaka, Japan) (Figure 5.4). TW20 concentrations between 4 and 24 mol m^{-3} were investigated (Table A.8).

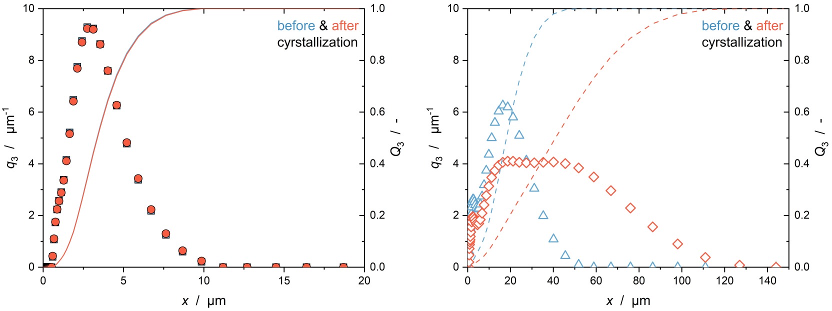

(a) Emulsion I

(b) Emulsion II.

Figure 5.3: DSD for Emulsion I (q_3: full symbols, Q_3: continuous line) and Emulsion II (q_3: empty symbols, Q_3: dashed line) before (blue) and after (red) the first crystallization cycle. Please note the different scales of the *x*-axis.

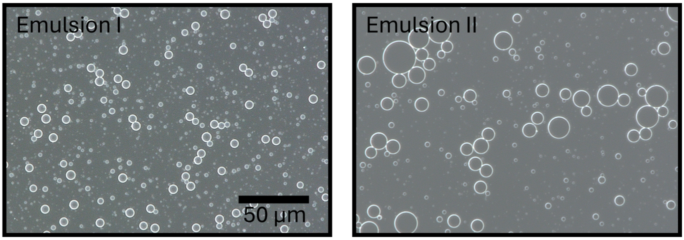

Figure 5.4: Microscopic images of Emulsion I (left) and Emulsion II (right). Adapted from Kaysan et al. (2023a), CC BY 4.0.

5.2.2 Ultrasonic measurements of the solid fraction of the dispersed phase

Using the known distance s_{pr} between the probe and reflector plate, as well as the measured transit time t^* of the ultrasonic signal, the speed of sound v can be calculated (Equation 5.1). t^* represents the time between the transmitting signal and the first response signal (Figure 5.5).

$$v = \frac{2 \cdot s_{\mathrm{pr}}}{t^*}. \tag{5.1}$$

In combination with the Urick equation (Urick (1947)) [1] and the knowledge of the speed of sound of an emulsion with only liquid droplets $v_{\mathrm{l}}(T)$ and the corresponding suspension with only crystalline particles $v_{\mathrm{s}}(T)$, $\xi(T)$ can be determined. The solid fraction of the dispersed phase can be calculated at every temperature $\xi(T)$ (Equation 5.2, Figure 5.6).

$$\xi(T) = \frac{n_{\mathrm{s}}}{n_{\mathrm{l}} + n_{\mathrm{s}}} = \frac{v^{-2}(T) - v_{\mathrm{l}}^{-2}(T)}{v_{\mathrm{s}}^{-2}(T) - v_{\mathrm{l}}^{-2}(T)}. \tag{5.2}$$

---

[1] The derivation of Urick's equation can be found in Appendix A.5.2.

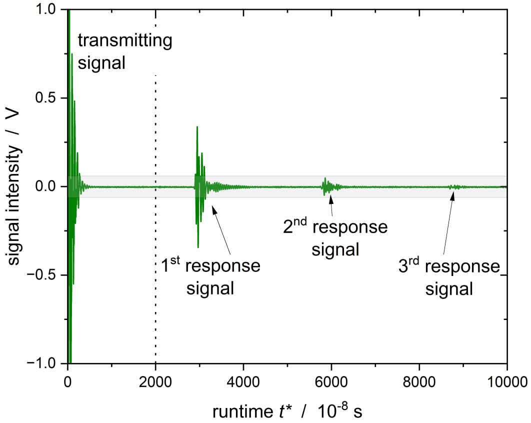

Figure 5.5: Transmitted as well as three response signals of the ultrasonic probe. The dashed line indicates from which runtime on the Mathlab script will look for the first response signal. The grey region shows the minimal intensity of the response signal needed to be detected as the signal. Everything in the grey area is determined as noise.

Equation 5.2 is applicable under the condition of no sound signal scattering at the phase boundary. The ultrasonic signal has a wavelength ranging from 690 μm to 728 μm, significantly larger than the diameters of the droplets in the two emulsions. Therefore, scattering can be effectively ruled out.

During each measurement, the ultrasonic signal traverses the emulsion between the probe and the reflector plate. The emulsion flow in the vessel leads to a variation in the number of droplets between the probe and the reflector plate. Consequently, the measured sound velocities exhibit statistical changes in the number of particles in the measured emulsion volume, introducing fluctuations in the calculated solids content of the dispersed phase. This is why the graphs depicting the solids content were smoothed using the moving average method applied over 15 data points (OriginPro 2021b, OriginLab Corp., Northampton, MA, USA). Equation 5.2 highlights the necessity of calculating ξ as a function of the average vessel temperature $\bar{\vartheta}$, considering the temperature-dependent nature of $v_{\mathrm{l/s}}$. To address this, the cooling and heating curves (Figure 5.6) were modeled using a single exponential decay function in Origin 2023. This

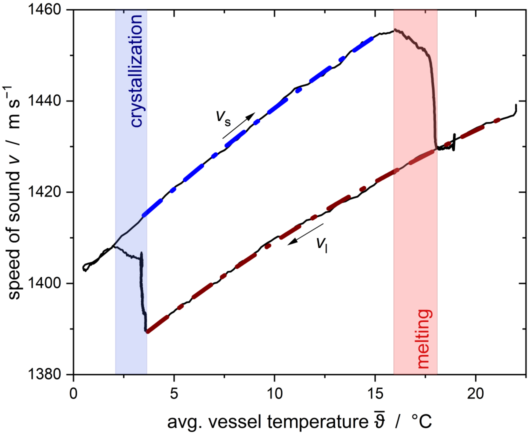

Figure 5.6: Hysteresis diagram of a time-resolved crystallization and thawing process of the dispersed phase of an n-hexadecane-in-water emulsion. The dashed lines represent Equation 5.3 fitted to the data points of either an emulsion with liquid droplets only (red) or a suspension with only solid particles (blue). Adapted from Kaysan et al. (2023a), CC BY 4.0.

analysis incorporated two fitting parameters, F_1 and F_2, along with the offset $v_{\mathrm{l,s,0}}$:

$$v_{\mathrm{l/s}} = v_{\mathrm{l/s,0}} + F_1 \cdot exp(-\bar{\vartheta}/F_2). \tag{5.3}$$

The observed data indicate that the speed of sound initially reduces with a decrease in temperature. However, upon the onset of crystallization within the dispersed phase, there is a notable increase in the speed of sound until all droplets have solidified. Further cooling results in a decline in the speed of sound, albeit at a different level than observed initially. Conversely, as the temperature rises, an increase in the speed of sound is observed until the point at which the particles begin to melt. At the onset of melting, the speed of sound decreases, reverting to the levels characteristic of an emulsion composed entirely of liquid droplets. A consistent speed of sound before and after crystallization suggests that the droplet size distribution within the emulsion remains unchanged.

The temperature hysteresis was measured for every experiment to ensure the correct determination of the solid fraction of the dispersed phase, as ξ is strongly impacted by the level of $v_{\mathrm{l/s}}$.

5.2.3 Flow and mixing characteristics in stirred vessels

To determine the flow regime in stirred systems, the total volume must be considered as there is a spatial variation of the local energy dissipation ϵ_{loc} (Laufhuette and Mersmann (1985)). As the most critical processes of the micro-mixing occur close to the impeller, the flow field is determined at this location. A dimensional analysis by Zlokarnik (1999) showed that the process of stirring can be described by three dimensionless numbers, which consider the following: The gravitational acceleration g, the density ρ and viscosity η of the fluid, the rotational speed N_{st}, the diameter of the impeller d_{st}, and the power input by the impeller $P_{\mathrm{W,st}}$. The three dimensionless numbers are

- the Newton Number Ne

$$Ne = \frac{P_{\mathrm{W,st}}}{\rho \cdot N_{\mathrm{st}}^3 \cdot d_{\mathrm{st}}^5} = \frac{\text{resistance force}}{\text{inertia force}}, \tag{5.4}$$

- the Reynolds Number of the impeller Re_{st}

$$Re_{\mathrm{st}} = \frac{\rho \cdot N_{\mathrm{st}} \cdot d_{\mathrm{st}}^2}{\eta} = \frac{\text{inertial forces}}{\text{viscous forces}}, \tag{5.5}$$

- and the Froude Number of the impeller Fr_{st}

$$Fr_{\mathrm{st}} = \frac{N_{\mathrm{st}}^2 \cdot d_{\mathrm{st}}}{g} = \frac{\text{flow inertia}}{\text{external field/gravity forces}}. \tag{5.6}$$

The $Ne - Re$ diagram can be used to estimate the flow field within the stirred vessel. For a vessel equipped with a six-bladed disk impeller (also called a Rushton turbine) and four baffles, Rushton et al. (1950) determined the following performance characteristic (Figure 5.7). Fr_{st} is neglected since no vortex is formed when using baffles and the density difference between dispersed and continuous phase is assumed to be neglectable. Concerning Re_{st}, the flow in the stirred vessel can be classified into three regions:

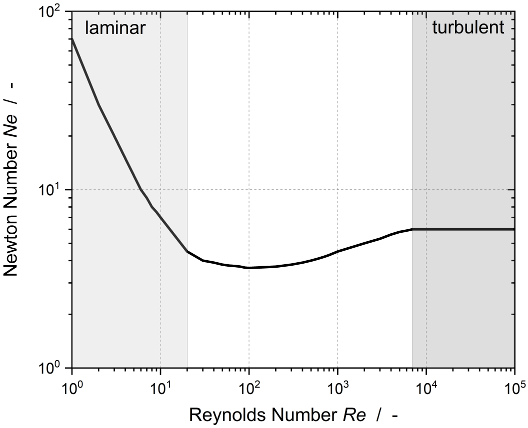

Figure 5.7: Performance characteristic for a stirred vessel equipped with a Rushton turbine and four baffles according to Rushton et al. (1950).

- A creeping, largely laminar flow up to $Re_{\mathrm{st}} \approx 20$ with a low mixing quality.
- A transitional region for $20 < Re_{\mathrm{st}} < 7 \cdot 10^3$ with damped turbulence and areas with minimal mass transfer and consequently limited mixing.
- A full turbulent flow within the vessel for $Re_{\mathrm{st}} > 7 \cdot 10^3$ ($Ne \approx$ const.) with an optimal mixing.

Especially for multi-component systems, the capability of the impeller to mix the surrounding volume must be considered. A homogeneous temperature and concentration profile is essential for the determination of the crystallization kinetics in the stirred vessel. The quantification of the mixing quality can be made using the mixing time characteristic, which defines the relationship between the dimensionless mixing time $N_{\mathrm{st}} \cdot \Theta$ and Re_{st} (Zlokarnik and Judat (1967), Moo–Young et al. (1972), Zlokarnik (1999)). $N_{\mathrm{st}} \cdot \Theta$ indicates the efficiency and effectiveness of the mixing process in stirred tanks or vessels at a given Re_{st}. Thus, the relationship quantifies how long it takes to achieve a homogeneous mixture at given operational parameters like the impeller speed and fluid properties. For $Re_{\mathrm{st}} > 10^4$, $N_{\mathrm{st}} \cdot \Theta$ stays approximately constant when using a 6-bladed disk impeller (Zlokarnik (1999)).

The energy cascade illustrates the dissipation of kinetic energy in a stirred vessel. Turbulence is generated by the motion of the impeller, forming vortices whose sizes depend on the impeller geometry and operating conditions. In some cases, such as for Rushton turbines, the vortex diameter has been empirically observed to be approximately half the impeller blade height (Schäfer et al. (1997), Zhou and Kresta (1996)). Transferred to this work, this leads to a size of the large vortices of 5 mm.

In contrast, diffusive micro-mixing refers to the mixing of components at the molecular level and occurs in parallel with macro-mixing over time. According to Kolmogorov's turbulence theory (Kolmogorov (1991)), the macro-vortices generated by an impeller break down into smaller vortices in a cascade, transferring kinetic energy progressively from larger to smaller eddies. This cascade continues until the kinetic energy dissipates into heat due to frictional forces at the smallest scales, where the local Reynolds number equals one. The smallest vortices, at the micro-scale of turbulence, are referred to as Kolmogorov vortices, and their size λ_{turb} can be estimated using Equation 5.7 (Kolmogorov (1956, 1991)):

$$\lambda_{\mathrm{turb}} = \left(\frac{\nu^3}{\bar{\epsilon}}\right)^{\frac{1}{4}}. \tag{5.7}$$

$\bar{\epsilon}$ represents the averaged mass-related energy dissipation in the stirred vessel and can be calculated as

$$\bar{\epsilon} = \frac{P_{\mathrm{W,st}}}{V \cdot \rho} = \frac{Ne \cdot d_{\mathrm{st}}^5 \cdot N_{\mathrm{st}}^3}{V}. \tag{5.8}$$

There is a great range of levels of energy dissipation in the vessel. The highest energy input can be found close to the impeller tip, which results in the local energy dissipation ϵ_{loc} in this region being $\epsilon_{\mathrm{loc}} > 10 \cdot \bar{\epsilon}$. In contrast, regions far from the impeller can show $\epsilon_{\mathrm{loc}} < 1 \cdot \bar{\epsilon}$ (Geisler (1991)).

The local shear rate close to the impeller tip can be calculated according to Schlichting and Gersten (2000) as

$$\dot{\gamma}_{\mathrm{tip}} = \frac{u_{\mathrm{tip}}^2}{2 \cdot \nu}, \tag{5.9}$$

with

$$u_{\mathrm{tip}} = \pi \cdot d_{\mathrm{st}} \cdot N_{\mathrm{st}}. \tag{5.10}$$

5.2.4 Droplet deformation in Stirred Vessels

As the droplet size influences the CMN, it is crucial to determine the impact of the shear field on possible droplet breakups, leading to a change in DSD.

Droplet disruption occurs when the local deformation forces exceed the droplet capillary pressure p_{ca} (Taylor (1934)), and the deformation time t_{def} surpasses a critical threshold (Walstra (1993)). The droplet capillary pressure is defined by the Young-Laplace equation:

$$p_{\mathrm{ca}} = \frac{4\gamma_{\mathrm{ll}}}{x}. \tag{5.11}$$

The impact of deformation forces on dispersed droplets is contingent upon the prevailing flow regime. Specifically, viscous forces are pivotal in laminar flow, causing shear and elongational stresses on the droplet surface (Walstra (1983)). In turbulent flow, viscous and inertial forces contribute to droplet deformation and breakup (Kolmogorov (1956)).

Laminar flow

Within laminar flow, inertial and viscous forces predominantly induce shear and elongational stresses on the droplet surface. Shear stresses arise from velocity gradients perpendicular to the flow direction, while elongational stresses correspond to velocity changes aligned with the flow direction. These stress components may occur in regions far from the impeller tip within a stirred vessel. The calculation of shear and elongational stresses is feasible. The Capillary number Ca represents the ratio between viscosity forces and surface tensions at the liquid-liquid interfaces and can be calculated as

$$Ca = \frac{\tau_{\mathrm{def}} \cdot x}{2 \cdot \gamma_{\mathrm{ll}}}. \tag{5.12}$$

τ_{def} represents the deformation stress. When a critical Ca is exceeded, droplet breakup happens. The value of Ca_{crit} depends on the type of flow, the stress mechanism, and the viscosity ratio $\eta_{\mathrm{conti}}/\eta_{\mathrm{disp}}$ between the continuous and dispersed phases (Grace (1982), Bentley and Leal (1986)).

In regions dominated by shear flow, Ca_{crit} reaches a minimum for $0.1 < \eta_{\mathrm{conti}}/\eta_{\mathrm{disp}} < 1$ (Grace (1982)). For $1 < \eta_{\mathrm{conti}}/\eta_{\mathrm{disp}} < 4$, Ca_{crit} increases strongly and for $\eta_{\mathrm{conti}}/\eta_{\mathrm{disp}} > 4$, breakup is not observed in simple shear up to very large Ca. In low-viscosity droplets, internal flow leads to droplet rotation while maintaining orientation. The addition of surfactants allows droplet breakup even at high viscosity ratios ($\eta_{\mathrm{conti}}/\eta_{\mathrm{disp}} > 4$) under shear flow conditions. Varying surfactant concentrations at the interface and the associated gradients result in non-constant forces acting on the droplet surface, preventing rotation (Walstra (1993)).

In elongational flows, droplets do not rotate, and even high-viscosity droplets can undergo breakup if sufficiently deformed over an extended period. However, elongational flows are often transient, limiting the deformation duration.

For more complex flow conditions, Ca_{crit} lies between the two extreme cases of laminar shear flow and laminar elongational flow (Walstra (1993), Walstra and Smulders (1998)). In literature, different fracture mechanisms are generally described for simple laminar flows, e.g., Janssen and Meijer (1993), Janssen et al. (1994), Briscoe et al. (1999), Risso (2000). According to Janssen et al. (1994) or Briscoe et al. (1999), deformed droplets are significantly more stable at low viscosity ratios than at high viscosity ratios.

The duration of exceeding Ca_{crit} does also play a role for a possible droplet breakup. In laminar flow, this time can be estimated according to Walstra and Smulders (1998):

$$t_{\mathrm{def}} \approx \frac{\eta_{\mathrm{d}}}{\tau_{\mathrm{def}}}. \tag{5.13}$$

In Equation 5.13, the assumption is made that the deforming viscous stress dominates the capillary restoring stress. As droplet size increases, the eddies that couple most strongly to the droplet are of comparable size; the larger these flow structures are, the more kinetic energy they carry and the stronger the inertial stresses they impose. Consequently, larger droplets typically deform (and break) faster, whereas smaller droplets, which interact with less energetic eddies, require proportionally longer exposure times or multiple encounters to accumulate sufficient deformation. The same qualitative trend holds for droplets with greater stability (higher interfacial tension), which require longer effective deformation times.

Whether deformation occurs in the inertial or the dissipation range is set by the droplet size relative to the Kolmogorov length. Droplets larger than this length are predominantly stressed by inertial-range eddies, while droplets comparable to or smaller than this length experience essentially viscous, dissipation-range strains. Comprehensive overviews are given in Stone (1994), Walstra and Smulders (1998).

Turbulent flow

The fundamental understanding of deformation and droplet breakage due to turbulent velocity fluctuations owes significantly to the seminal works of Hinze (1955) and Kolmogorov (1958). According to Hinze (1955), droplets experience predominantly viscous (locally linear) deformation only when their diameter is comparable to or smaller than the Kolmogorov length of the turbulence. As the Reynolds number increases, this length scale shrinks, so for a given droplet size inertial stresses become increasingly dominant.

The Kolmogorov-Hinze framework (Hinze (1955), Kolmogorov (1958)), which builds on the principles of local isotropic turbulence, highlights that turbulent pressure fluctuations or velocity differentials across the droplet diameter are critical for droplet breakage. Larger turbulence structures primarily transport droplets without deforming them, while smaller vortices often lack sufficient energy for breakup. This view is supported by Batchelor (1952), Hinze (1955), Kresta and Brodkey (2003).

To describe droplet breakup in turbulent flows, viscous and inertial stresses must be considered. The dominant mechanism depends on the droplet size relative to the turbulence scale λ_{turb}, as outlined by Kolmogorov (1956). The Weber number We and the Ohnesorge number Oh are pivotal in describing droplet deformation, where We quantifies the balance between disruptive hydrodynamic forces and stabilizing surface tension forces:

$$We_{\mathrm{imp}} = \frac{N_{\mathrm{st}}^2 \cdot x_{\mathrm{imp}}^3 \cdot \rho_{\mathrm{conti}}}{\gamma_{\mathrm{ll}}}. \tag{5.14}$$

Conversely, the Oh number relates viscous forces to inertial and surface tension forces:

$$Oh = \frac{\eta_{\mathrm{disp}}}{\sqrt{\rho_{\mathrm{disp}} \cdot \gamma_{\mathrm{ll}} \cdot x_{\mathrm{d}}}}. \tag{5.15}$$

For low viscosity scenarios ($\eta_{\text{disp}} < 10$ mPa s), interfacial forces dominate, with the maximum droplet diameter estimated by:

$$x_{\mathrm{d,max}} \approx \epsilon^{-\frac{2}{5}} \cdot \rho_{\text{conti}}^{-\frac{3}{5}} \cdot \gamma_{\text{ll}}^{\frac{3}{5}} \, . \tag{5.16}$$

For smaller droplets within turbulent eddies, deformation is influenced by shear stress, with $x_{\mathrm{d,max}}$ approximated by:

$$x_{\mathrm{d,max}} \approx \frac{\gamma_{\text{ll}}}{\eta_{\text{conti}}} \left(\frac{\nu_{\mathrm{conti}}}{\epsilon} \right)^{0.5} \, . \tag{5.17}$$

The concept of local isotropy proposed by Hinze (1955), further elaborated by Kolmogorov (1958, 1991), remains relevant even in the non-isotropic flows typical of stirred environments. This confirms the applicability of these dynamics under high Reynolds number conditions, where droplets are smaller than the macro-scale turbulence.

5.3 CMN in the industry-like stirred tank

5.3.1 CMN without primary nucleation

Like the TCR experiments, CMN was investigated at a temperature where primary nucleation was absent (ϑ = 15.5 °C, ΔT = 3.1 K). Unlike the TCR experiments, the initial solid fraction was prepared externally: A defined amount of suspension was first crystallized externally in an ice bath before being added to the tempered emulsion, resulting in an initial solid fraction of the dispersed phase of approximately $\xi_0 = 0.14$.

Four different rotational speeds ranging from 50 rpm to 200 rpm were tested. The DSD was measured at depths of 15 cm, 30 cm and 45 cm below the surface to prevent separation during the experiments. Creaming was observed at speeds up to 50 rpm; therefore, only speeds above 100 rpm were considered. The DSD remained constant during the experiments and even post-thawing, confirming that CMN did not result in irreversible aggregate formation, a finding consistent with the TCR measurements.

Different from the TCR, there is not only one constant shear rate for every rotational speed of the impeller in the stirred vessel. For the energy dissipation, Geisler (1991) found that ϵ_{max} close to a 6-balded disk impeller can be up to $30 \cdot \bar{\epsilon}$, whereas regions far away from the impeller show local energy dissipation rates smaller than $0.2 \ \cdot \bar{\epsilon}$. There are also various equations on how to calculate the maximum and average apparent shear rate in a stirred vessel (Table 5.2), leading to a wide distribution of theoretically calculated shear rates in the vessel (Figure 5.8 (a)).

Table 5.2: Overview of various equations for calculating mean and maximum apparent shear rate in turbulent stirred tanks.

Equation	Reference
$\dot{\gamma}_{\mathrm{mean}} = 4.2 N_{\mathrm{st}} \left(\frac{d_{\mathrm{st}}}{d_{\mathrm{ves}}}\right)^{0.3} \frac{d_{\mathrm{st}}}{W_{\mathrm{st}}}$	Bowen (Jr), R. L. (1986)
$\dot{\gamma}_{\mathrm{mean}} = \left(\frac{P_{\mathrm{st}}}{V \cdot \eta_{\mathrm{em}}}\right)^{0.5}$	Henzler and Kauling (1985)
$\dot{\gamma}_{\mathrm{mean}} = 33.1 \cdot N_{\mathrm{st}}^{1.4}$	Sánchez Pérez et al. (2006) with data from Kelly and Gigas (2003)
$\dot{\gamma}_{\mathrm{max}} = 9.7 N_{\mathrm{st}} \left(\frac{d_{\mathrm{st}}}{d_{\mathrm{ves}}}\right)^{0.3} \frac{d_{\mathrm{st}}}{W_{\mathrm{st}}}$	Bowen (Jr), R. L. (1986)
$\dot{\gamma}_{\mathrm{max}} = 3.3 N_{\mathrm{st}}^{1.5} d_{\mathrm{st}} \left(\frac{\rho}{\eta}\right)^{0.5}$	Robertson and Ulbrecht (1987)

In addition to the distribution of energy dissipation, it must be considered that droplets/particles tend to reside longer in areas with low fluid velocities, i.e., low local shear rates, and are exposed to maximum shear rates only briefly. Without numerical simulation of the fluid flow within the stirred vessel, comparing the mean shear rate to that in the TCR is not viable.

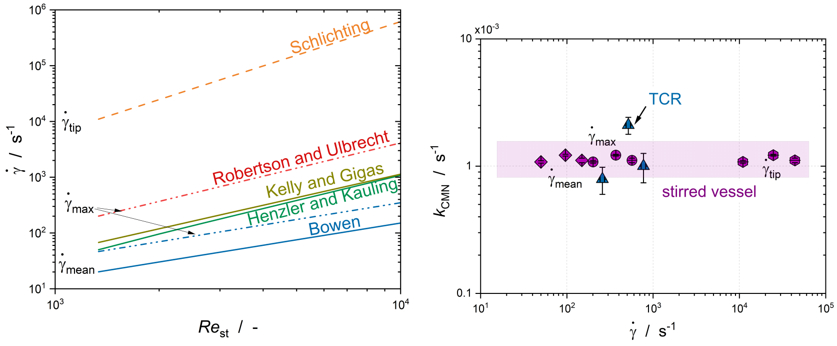

(a) Calculated mean, max, and tip shear rates in the vessel according to Schlichting and Gersten (2000), Robertson and Ulbrecht (1987), Kelly and Gigas (2003), Henzler and Kauling (1985), Bowen (Jr), R. L. (1986).

(b) k_{CMN} shown for the different calculated shear rates according to Henzler and Kauling (1985) ($\dot{\gamma}_{\mathrm{mean}}$), Robertson and Ulbrecht (1987) ($\dot{\gamma}_{\mathrm{max}}$) and Schlichting and Gersten (2000) ($\dot{\gamma}_{\mathrm{tip}}$). The data is compared to results from the TCR experiments. The purple area indicates the possible range for all equations presented in Table 5.2.

Figure 5.8: Theoretically calculated shear rates in the stirred vessel and the corresponding k_{CMN} determined for a constant supercooling of ΔT = 3.1 K to exclude spontaneous nucleation. As surfactant, TW20 with $\tilde{c}_{\mathrm{TW20}}/cmc = 270$ ($\tilde{c}_{\mathrm{TW20}}$ = 16 mol m^{-3}) was used (compared to $\tilde{c}_{\mathrm{TW20}}/cmc = 255$ in the TCR experiments shown here).

The efficiency of the CMN was investigated by determining k_{CMN} according to Equation 2.11 (Figure 5.8 (b)). It was observed that crystallization of the dispersed phase occurs only when solid particles were introduced into the supercooled emulsion at a supercooling level precluding spontaneous crystallization ($k_{\mathrm{CMN}} > 0$), indicating CMN in industry-like stirred vessels.

Comparative analysis with k_{CMN} from the TCR experiments showed similar results in stirred vessels, with no apparent dependence of k_{CMN} on the shear rate. This suggests that CMN efficiency may not be significantly influenced by shear within the stirred vessel since the contact time at high shear rates is limited. However, given the wide distribution of energy dissipation within the stirred vessel, the displayed $\dot{\gamma}_{\mathrm{tip}}$ (Equation 5.9, Schlichting and Gersten (2000)) represents only the maximum shear rate in a small volume near the impeller's tip.

To evaluate the efficiency of CMN in the stirred vessel, J_{CMN} and λ_{CMN} were calculated (Equation 4.6 and 4.9, Figure 5.9). J_{CMN} represents the maximum nucleation rate detectable in the system, assuming $\xi_{\mathrm{hex}} = 0.5$. All J_{CMN} values determined in the TCR and the stirred vessel are within the range of those nucleation rates observed for primary nucleation at various supercoolings (gray range, data according to Figure 4.8 (b)). Given the wide range of energy dissipations in the stirred vessel (Geisler (1991)), J_{CMN} represents an average maximum nucleation rate, assuming an equal distribution of droplets throughout the vessel and constant values for h_{coll} and λ_{CMN}.

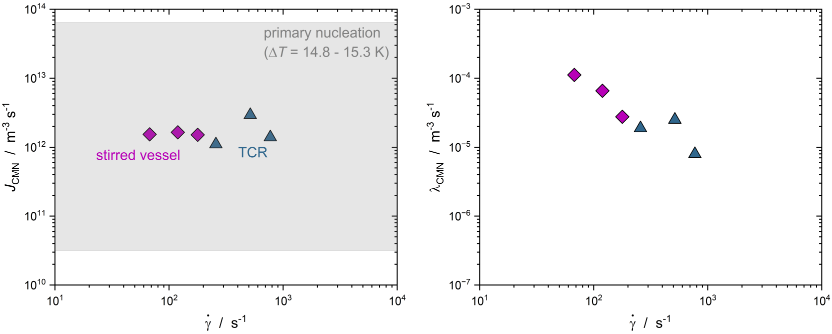

(a) Calculated J_{CMN} for a solid fraction of the dispersed phase of $\xi_{\mathrm{hex}} = 0.5$. Thus, the J_{CMN} shown represents the maximum nucleation rate. The gray area points out the range where the primary nucleation rates were found at various supercooling (compare Figure 4.8).

(b) Calculated corresponding nucleation efficiency λ_{CMN} according to Equation 4.9.

Figure 5.9: Comparison of J_{CMN} and λ_{CMN} for the crystallization experiments in the stirred vessel and the TCR. For the stirred vessel, the shear rate was calculated according to Sánchez Pérez et al. (2006).

To assess the impact of collision numbers, λ_{CMN} can be evaluated (Equation 4.6). Increasing the mean (apparent) shear rate decreases the efficiency, supporting the hypothesis that contact time is limited at higher shear rates. This correlation shows that results from the well-defined laminar flow in the TCR can be applied to stirred vessels. Thus, the surfactant concentration likely plays a crucial role, with an increase in aqueous micelle concentration potentially leading to faster nucleation in the dispersed phase.

5.3.2 Coupling of CMN and primary nucleation

When transferring the aforementioned findings to industrial-scale crystallization of the dispersed phase in n-hexadecane-in-water emulsions, the initial formation of solid particles must be considered. It has been demonstrated that the supercooling required for CMN is significantly lower than that required for primary nucleation. However, industrial melt emulsion crystallization depends not only on the crystallization temperature but also on the time required to achieve a fully crystalline dispersed phase. Thus, CMN alone cannot serve as the sole solution for industrial crystallization of melt emulsions. Nonetheless, combining primary crystallization with the targeted application of CMN can reduce both the time needed to achieve a fully crystalline dispersed phase and the required degree of supercooling.

The overlapping effects of primary and secondary nucleation mechanisms happening in a stirred vessel will be the main focus of this chapter. As primary nucleation cannot be investigated in a stirred tank decoupled from CMN or further shear-influenced crystallization processes, the primary nucleation kinetics from the NMR approach (Figure 4.8) will be taken into account.

The degree of the solid fraction of the dispersed phase of Emulsion I (compare Section 5.2.1) is recorded as a function of time (Figure 5.10). Figure 5.10 exhibits various curve shapes. Larger droplets are more likely to undergo primary nucleation due to shorter induction times, allowing the formation of growable clusters (Turnbull and Cormia (1961)). Consequently, large droplets crystallize due to homogeneous nucleation, while smaller droplets remain unchanged as stable clusters are very unlikely to form. In instances of high supercooling, an abrupt surge in solid content within the stirred tank occurs immediately after or shortly before achieving constant supercooling (after the gray region). This rapid increase is attributed to heterogeneous or homogeneous nucleation in the

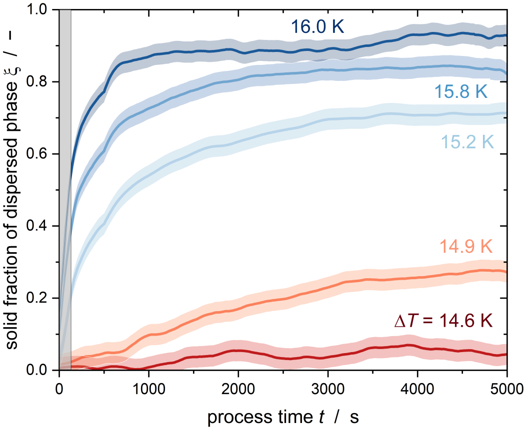

Figure 5.10: Temporal evolution of the solid fraction of the dispersed phase in Emulsion I is depicted at various supercooling ΔT. Enhanced supercooling, resulting in a lower absolute temperature, accelerates the crystallization of droplets (Emulsion I, $\bar{\epsilon}$ = 0.37 W kg^{-1} (N_{st} = 350 rpm), $\tilde{c}_{\mathrm{TW20}}$ = 16 mol m^{-3}). In this context, ξ = 0 denotes an emulsion comprising solely liquid droplets, while ξ = 1 signifies an emulsion with only solid particles as the dispersed phase, essentially forming a suspension. Reproduced from Kaysan et al. (2023a), CC BY 4.0.

large droplets of the emulsion. Primary homogeneous nucleation, is typically observed in the initial phase of a crystallization process without seed crystals (Agrawal and Paterson (2015)).

The slope of the curve diminishes after the rapid increase at $t \to 0$ s, although the solid content continues to rise subsequently. This slower increase is dominated by secondary nucleation. The collision between already solidified droplets and still-liquid supercooled droplets leads to CMN, causing the crystallization of droplets that might not crystallize through pure homogeneous nucleation at the given supercooling. Moreover, the efficiency of CMN peaks when there are equal numbers of liquid and solid droplets, corresponding to a solid fraction of $\xi_{\mathrm{hex}} = 0.5$. As the solid fraction rises, efficiency decreases due to the diminishing probability of a liquid droplet colliding with a particle.

Additionally, nucleation triggered by shearing the droplets in the flow field serves as another nucleation mechanism. Determining the occurrence of shear-induced nucleation based on tests at identical impeller speed (and identical shear rate) is challenging. If homogeneous nucleation does not occur initially due to insufficient supercooling, there is no discernible jump in the solids content. Instead, crystalline nuclei form in emulsion droplets through heterogeneous or shear-induced nucleation, evident from the constant, gradual increase in solids content. Once particles are present, CMN takes place.

Despite maintaining constant supercooling for approximately 90 min, none of the depicted curves in this study reached a solid content of $\xi_{\mathrm{hex}} = 1$, indicating that not all droplets had undergone crystallization. A potential explanation for this observation is the relatively short experimental duration. Hindle et al. (2000) achieved full crystallization in stirred n-hexadecane emulsions only after an experimental period of 16 days. The slightly positive slope of ξ_{hex} after 90 min in Figure 5.10 suggests that, with an extended experimental duration, complete crystallization of the emulsion through secondary nucleation could become feasible.

To validate the coupling of primary and flow-related nucleation, simulations of the time-dependent solid fraction of the dispersed phase are performed with the primary nucleation rate obtained previously (Section 4.3.1). These results are compared to those found for the crystallization of the dispersed phase in the stirred tank. If CMN or any shear-related nucleation triggers of the dispersed phase do not play a major role and primary nucleation dominates, the experimental results should align with the simulations (Figure 5.11). For $\Delta T > 15.8$ K, primary nucleation dominates the experiments as almost all droplets crystallize within the first 500 s at $T =$ constant. For $\Delta T < 15.8$ K, the experimental values exceed the simulated $\xi(t)$. This leads to the conclusion that either CMN or shear-induced nucleation, or a combination of both, could increase the efficacy of the process and primary nucleation does not entirely dominate the crystallization itself, as long as $\Delta T < 15.8$ K.

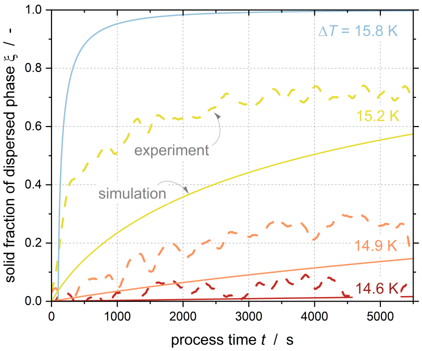

Figure 5.11: Comparison of the experimental results ($\bar{\epsilon}$ = 0.37 W kg^{-1} (N_{st} = 350 rpm), $\tilde{c}_{\mathrm{TW20}}$ = 16 mol m^{-3}) with the theoretical time-dependent solid fraction of the dispersed phase when only primary nucleation would take place.

The nucleation rate of the dispersed phase in the stirred vessel must be determined to compare the crystallization efficiencies of solely primary nucleation with the combination of primary nucleation and flow-induced nucleation. None of the proposed models (Section 2.3) was able to achieve fitting accuracy R^2 > 0.85 in modeling $\xi(t)$ for the presented crystallization experiments. Thus, a new model must be developed to describe the combination of primary and secondary nucleation mechanisms. A model featuring a time-dependent nucleation rate $J_{\mathrm{WB}}(t)$ is necessary for characterizing $\xi(t)$. To achieve this, a statistical approach was used, modifying Equation (2.6) (1Exp model) based on the Weibull probability density function, as presented in Equation (5.18).

$$\xi(t) = 1 - (1 - \xi_0) \exp\left(-\frac{k_{\mathrm{WB},0}}{\alpha} (t - t_0)^{\alpha} \right). \tag{5.18}$$

This approach is herein referred to as the Weibull model. The first fitting parameter α, referred to as the shape parameter of the Weibull model, describes the temporal evolution of the nucleation rate. For $\alpha < 1$, a decreasing nucleation rate, and for $\alpha > 1$ an increasing nucleation rate can be found. For $\alpha = 1$, the

Weibull model coincides with the 1Exp-model, featuring a constant nucleation rate (Sear (2014)). The second parameter, $k_{\mathrm{WB},0}$, represents the kinetic constant for droplet crystallization in the stirred vessel at $t = 0$ and serves as the scale parameter of the Weibull distribution. The third parameter, ξ_0, signifies the solid fraction of the dispersed phase at $t = 0$.

In analogy to Equation 2.5, $k_{\mathrm{WB},0}$ can be calculated as follows:

$$k_{\mathrm{WB},0} = J_{\mathrm{WB},0} \cdot V_{\mathrm{d}}. \tag{5.19}$$

This is possible as only primary nucleation is assumed to take place at the beginning of the experiments.

Equation (5.18) applies under the assumption that the emulsion droplets possess identical sizes. When the droplet size is distributed, a calculation analogous to Equation (2.8) should be considered.

$$\xi(t) = 1 - \int\limits_0^\infty \left(\Big(1 - \xi(t_0)\Big) \cdot q_{3,\mathrm{t},0}(x)\ \exp\left[-\frac{J_{\mathrm{WB},0}\ V_{\mathrm{d}}(x)}{\alpha}\ (t - t_0)^\alpha \right] \right) \mathrm{d}x. \tag{5.20}$$

$J_{\mathrm{WB}}(t)$ can be calculated after obtaining α and $J_{\mathrm{WB},0}$ by fitting Equation 5.20 to the experimental data.

$$J_{\mathrm{WB}}(t) = J_{\mathrm{WB},0} \cdot t^{\alpha - 1}. \tag{5.21}$$

The Weibull model is employed to elucidate the progressive solid fraction increase of emulsion droplets during their crystallization in a stirred vessel. Specifically, two distinct nucleation rates are highlighted. First, $J_{\mathrm{WB},0}$ denotes the initial nucleation rate. This rate assumes the absence of CMN due to the unavailability of solid particles that could induce nucleation. Thus, $J_{\mathrm{WB},0}$ is solely influenced by primary nucleation. Especially in stirred systems, the initial primary nucleation can also be induced due to the shear-related deformation of the droplets (i.e., shear-induced nucleation). Second, $J_{\mathrm{WB},5000}$ represents the nucleation rate at 5000 s after reaching a constant supercooling state. This work anticipates that CMN will predominantly influence the nucleation process after $\approx$2500 seconds at a constant supercooling. A comprehensive discussion elaborating on this aspect is provided in the following discussion in this chapter.

Figure 5.12 (a) points out that the single exponential model cannot describe the initial increase of the measured curves. This leads to an underestimation of the actual nucleation rate in the first part of the curve and an overestimation of J at higher process times (Figure 5.12 (b)). Therefore, the Weibull model (Equation 5.20) is used to evaluate the nucleation rates. Shear not only affects CMN.

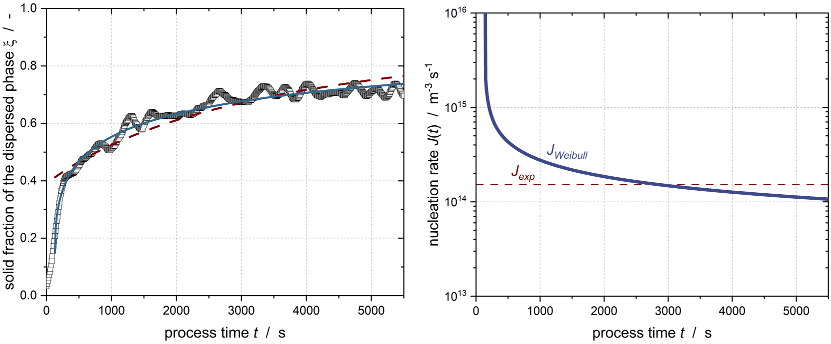

(a) 1Exp (red, dashed line) and Weibull (solid blue line) fit to one time-dependent coarse of ξ_{hex}.

(b) Time-dependent nucleation rates.

Figure 5.12: Comparison of single exponential with Weibull fit. ξ was fitted as soon as the temperature was constant (ΔT = 15.2 K).

As observed in polymer solutions by, e.g., Lagasse and Maxwell (1976) and Mykhaylyk et al. (2010), it can induce crystallization by influencing molecular structure, thereby reducing the energy barrier. While the impact of shear on droplets intensifies with increasing stirring rate, potentially expediting droplet crystallization without constraints, CMN might reach a peak at a certain shear rate, losing its efficacy in promoting the crystallization of the dispersed phase due to limited induction time. It is assumed that the influence of shear on droplets, referred to as shear-induced nucleation, is likely more pronounced at the onset of crystallization for larger droplets. Consequently, $J_{\mathrm{WB},0}$ is employed to assess the effects of shear-induced nucleation (in combination with further primary nucleation mechanisms). CMN requires pre-existing solid particles. Therefore, $J_{\mathrm{WB},5000}$ is utilized to evaluate the potential enhancement of dispersed phase crystallization through CMN.

Considering only primary homogeneous and heterogeneous nucleation in the stirred tank should result in approximately $J_{\mathrm{prim}} = 2.04 \cdot 10^{13}$ m^{-3}s^{-1} (gray line in Figure 5.13 (a)). $J_{\mathrm{WB},0}$ exhibits an upward trend with increasing stirring rate and thus a rise in mean energy dissipation (Figure 5.13 (a)). Since supercooling remains constant across all experiments, this increase indicates the impact of shear-induced nucleation, as primary homogeneous and heterogeneous nucleation is expected to be unaffected by applied shear. With escalating stirring rates, the shape parameter α decreases, resulting in an increasing disparity in nucleation rates throughout the experiment (Figure 5.13 (b)). To ensure that

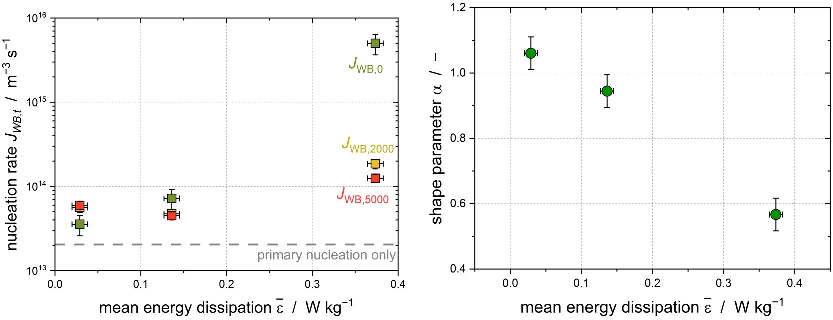

(a) Nucleation rates calculated for three different times: As soon as the constant supercooling was reached ($J_{\mathrm{WB},0}$), after 2000 s ($J_{\mathrm{WB},2000}$) and after 5000 s (($J_{\mathrm{WB},5000}$). Adapted from Kaysan et al. (2023a), CC BY 4.0.

(b) Corresponding shape parameter (Equation 5.21). Reproduced from Kaysan et al. (2023a), CC BY 4.0.

Figure 5.13: Nucleation rates at the very beginning, after 2,000 s and 5,000 s as well as the corresponding shape parameters for an n-hexadecane-in-water emulsion stabilized with TW20 (Emulsion I, $\tilde{c}_{TW20}$ = 24 mol m^{-3}) at ΔT = 15.2 ± 0.1 K.

higher energy input did not compromise temperature homogeneity, the temperature difference among the four integrated temperature sensors was compared and found to be unrelated to the stirring rate. It is reasonable to assume that CMN, in combination with primary nucleation, is predominantly at play for $t > 2000$ s, leading to $J_{\mathrm{WB},5000} = J_{\mathrm{prim}} + J_{\mathrm{CMN}}$.

This finding agrees with the previously presented results of investigating CMN decoupled from primary nucleation in the stirred tank (Section 5.3.1). For mean energy inputs up to $\bar{\epsilon} = 0.14$ W kg^{-1}, no dependency of k_{CMN} and J_{CMN} on the energy dissipation was detected.

Effect of shear-induced nucleation

To further explore the influence of shear-induced nucleation, a second emulsion (Emulsion II) with a bimodal DSD was employed (Figure 5.3). At a stirring speed of $N_{\mathrm{st}} = 350$ rpm, the turbulence scale λ_{turb} was 45 μm. This led to a theoretically calculated maximal droplet diameter of $x_{\mathrm{d,max}} \approx 6.1$ mm (Equation 5.17) using the mean energy dissipation rate $\bar{\epsilon}$. Close to the impeller, where ϵ_{max} was considered, $x_{\mathrm{d,max}} \approx 1.4$ mm was calculated (Equation 5.17). As $\eta_{\mathrm{disp}} < 10$ mPa s, also interfacial forces could dominate, leading to $x_{\mathrm{d,max}} \approx 1.1$ mm (calculated with $\bar{\epsilon}$) or close to the impeller to $x_{\mathrm{d,max}} \approx 0.1$ mm (Equation 5.16).

Considering the laminar regions far from the impeller tip, critical Capillary numbers for droplet breakup were estimated: $Ca_{\mathrm{crit,sh}} \approx 1$ for shear flow and $Ca_{\mathrm{crit,el}} \approx 0.1$ for elongated flow ($\eta_{\mathrm{disp}}/\eta_{\mathrm{conti}} \approx 3.8$) (Janssen et al. (1994), Walstra and Smulders (1998)). For $N_{\mathrm{st}} = 350$ rpm, Ca was 0.06 for Emulsion I ($x_{50,3} \approx 2.9$ μm) and 0.3 for Emulsion II ($x_{50,3} \approx 14.8$ μm), indicating no droplet breakup for Emulsion I, which can be excluded from data analysis. In contrast, Emulsion II, subject to stronger deforming forces, likely experienced droplet breakup, evidenced by changes in the DSD before and after a crystallization cycle, supporting the hypothesized effects of shear-induced nucleation (Figure 5.3).

It is therefore anticipated that larger droplets, subjected to increased deforming forces, would exhibit a noticeable increase in the nucleation rate $J_{\mathrm{WB},0}$ (Figure 5.14 (a)). Emulsion II ($x_{50,3}$ = 14.8 μm) demonstrates an escalating $J_{\mathrm{WB},0}$ with an increase in the energy dissipation rate. The crystallization of Emulsion II is instigated by the shearing of larger droplets, resulting in a noticeable surge in the nucleation rate. In contrast, for Emulsion I, where only smaller droplets are present in comparison to Emulsion II, this effect is less pronounced when elevating the energy dissipation rate from $\bar{\epsilon}$ = 0.03 W kg^{-1} to $\bar{\epsilon}$ = 0.38 W kg^{-1}. The nucleation rate of Emulsion II after 5000 s converges to approximately the same value as that of Emulsion I (Figure 5.14 (b)). Presuming that the largest droplets in Emulsion II experienced shear-induced nucleation during the initial phase (up to 2000 s) of crystallization, shear-induced nucleation seems to play a diminished role at later time points (t > 2000 s), with CMN dominating the later phase of nucleation kinetics.

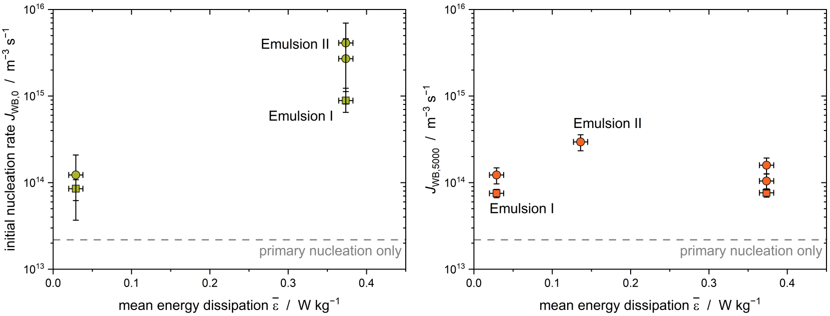

(a) Initial nucleation rate $J_{\mathrm{WB},0}$. Reproduced from Kaysan et al. (2023a), CC BY 4.0.

(b) Nucleation rate after 5000 s $J_{\mathrm{WB},5000}$. Adapted from Kaysan et al. (2023a), CC BY 4.0.

Figure 5.14: Comparison of $J_{\mathrm{WB},0}$ and $J_{\mathrm{WB},5000}$ for Emulsion I ($x_{50,3}$ = 2.9 μm, square) and Emulsion II ($x_{50,3}$ = 14.8 μm, circle) ($\bar{\epsilon}$ = 0.37 W kg^{-1}, $\tilde{c}^{aq}_{\mathrm{mic,TW20}}$ = 7.2–7.9 mol m^{-3}, ΔT = 15.2 K $\pm$ 0.1 K).

Effect of surfactant concentration

To further increase the efficiency of the process, the effect of the surfactant concentration on the nucleation rates is investigated (Figure 5.15). Following the TCR results and the literature (e.g., Dickinson et al. (1993), McClements and Dungan (1997)), increased surfactant concentration should lead to higher nucleation rates. More nano-particles should be presented at a constant stirring velocity, increasing the overall number of collisions between supercooled droplets with solid (nano-)particles. After 5000 s, an emulsion characterized by $\tilde{c}_{\mathrm{TW20}}$ = 4 mol m^{-3} exhibits a solid content of $\xi = 0.39$, while another with a higher surfactant concentration of $\tilde{c}_{\mathrm{TW20}}$ = 16 mol m^{-3} achieves a solid content of $\xi = 0.70$. This observation suggests that the crystallization process in the emulsions is expedited with an augmented surfactant concentration. However, it remains uncertain from the presented data whether additional acceleration of crystallization can be achieved by further elevating the surfactant concentration beyond $\tilde{c}_{\mathrm{TW20}}$ = 16 mol m^{-3}. It is plausible that the underlying mechanism may reach a plateau or maximum state in terms of further improvements with increased surfactant concentration.

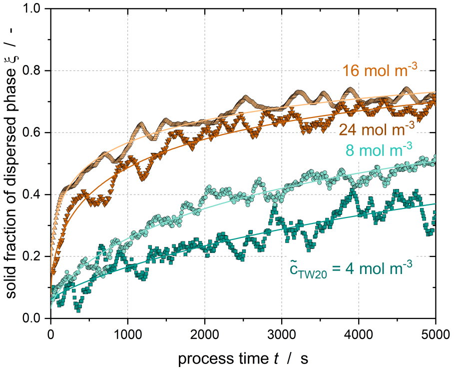

Figure 5.15: An increase in the solids content of the dispersed phase during the entire process with constant supercooling is observed at different surfactant concentrations (Emulsion I, $\bar{\epsilon}$ = 0.37 W kg^{-1}, ΔT = 15.2 K ± 0.1 K) (Kaysan et al. (2023a)).

Again, the Weibull model (Equation 5.20) was employed to fit the experimental data (depicted by the line in Figure 5.15, Figure 5.16). It is visible that an increasing surfactant concentration leads to increasing nucleation rates at every time during the experiment up to a given limit (Figure 5.16 (a)). To ensure this trend, further supercoolings were tested (Figure 5.17). The presented plots demonstrate an increase in nucleation rate with rising supercooling, aligning with the enhanced driving force for crystallization observed across various surfactant concentrations (Figure 5.17 (a) + (b)). This contrasts with findings from the microfluidic setup. Such discrepancies could stem from differences in experimental setups: In a stirred system with multiple reactants, micelles can disperse in various directions, whereas in a microfluidic channel, they may form multiple layers, increasing repulsion between reactants (Basheva et al. (2007), Trokhymchuk et al. (2001)).

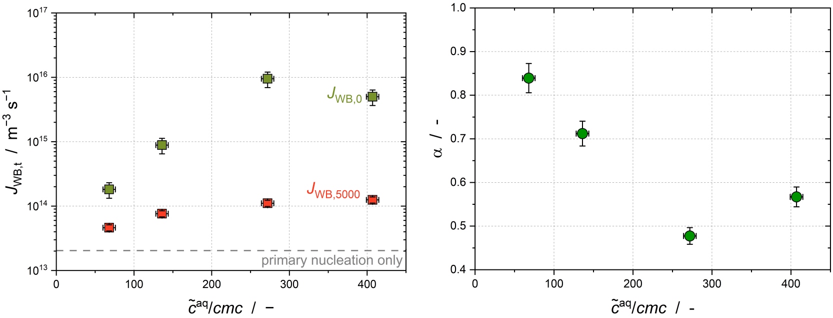

(a) Nucleation rates.

(b) Shape parameter.

Figure 5.16: Nucleation rates at the very beginning, after 2,000 s and 5,000 s as well as the corresponding shape parameters for an n-hexadecane-in-water emulsion stabilized with different TW20 concentrations at ΔT = 15.2 ± 0.1 K and $\bar{\epsilon}$ = 0.37 W kg^{-1} (Kaysan et al. (2023a)).

Furthermore, $J_{\mathrm{WB},0}$ escalates with higher surfactant concentrations, corroborating the observation in Figure 5.15 that surfactant concentration significantly

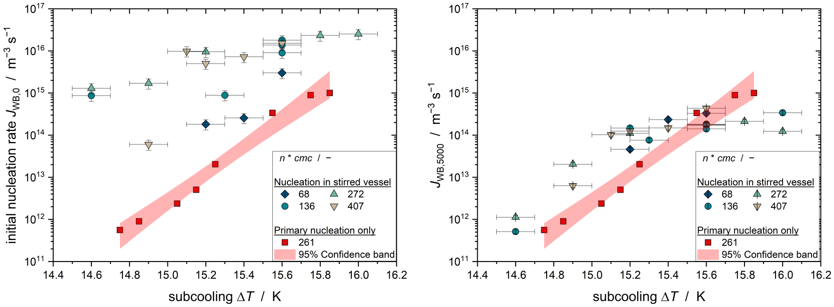

(a) Initial nucleation rate $J_{0,\mathrm{WB}}$.

(b) Nucleation rate after 5000 s $J_{\mathrm{WB},5000}$.

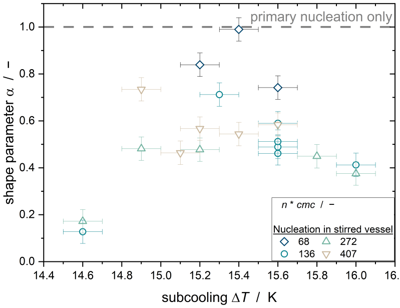

(c) Shape parameter of the Weibull fit α.

Figure 5.17: Overview about the nucleation rates and shape parameters for all tested parameters. Reproduced from Kaysan et al. (2023a), CC BY 4.0.

impacts the initial solid content increase in n-hexadecane droplets. This suggests a possible rise in surfactant presence at the liquid-liquid interface, thereby reducing the energy barrier for heterogeneous nucleation (Grange et al. (1986)).

A comparison with J_{prim} indicates that, in stirred tank experiments, $J_{\mathrm{WB},0}$ exceeds J_{prim} under all conditions, suggesting the influence of flow-mediated nucleation, including CMN and shear-induced nucleation. The discrepancy between primary nucleation and stirred tank nucleation narrows with higher supercooling, as primary nucleation becomes more prevalent at elevated supercooling levels in the emulsion droplets.

The temporal progression of nucleation rate is characterized by the shape parameter α (Figure 5.17 (c)). For all supercooling and TW20 concentrations $\alpha < 1$, indicating a decrease in nucleation rate over time. For $\tilde{c}_{\mathrm{TW20}} = 4$ mol m^{-3}, α is relatively high, suggesting a less pronounced decrease in nucleation rate at this surfactant concentration. Notably, for $\Delta T = 14.6$ K, the low α values, less than 0.2, are due to poor model fitting with low goodness of fit ($R^2 < 0.1$). This implies that second-order kinetics might be more appropriate for these experiments, especially where primary nucleation is negligible and secondary nucleation dominates at low supercooling.

$J_{\mathrm{WB,5000}}$ shows a convergence of the nucleation rate in the stirred tank to that of purely primary nucleation. Fits at varying surfactant concentrations indicate an increase in nucleation rate correlating with free surfactant concentration, supporting a micelle-mediated nucleation promotion mechanism.

Assuming J_{5000} is a combination of J_{prim} and J_{CMN}, the nucleation rate for CMN can be deduced (Figure 5.18). This result shows that J_{CMN} is comparable throughout all three experimental setups and procedures. It also shows that the isolated investigation of CMN without the impact of primary nucleation can be done, and the results are transferable to an industry-like system. For the very first time, the nucleation mechanisms in a stirred vessel have now been determined, and it was proven that contact-mediated nucleation also plays a role in the industrial production of crystalline melt emulsions. Translating these findings to the industrial production of emulsions could have substantial implications. It presents an opportunity to reevaluate the balance between power input and cooling duration, particularly in light of the observed accelerated crystallization of the dispersed phase. Increasing the energy dissipation rate ϵ might be a feasible approach to achieve thorough crystallization of the dispersed phase, especially in scenarios where further supercooling is too costly or impractical. This situation is particularly relevant in cases where tap water is used for cooling and the maximum achievable supercooling is limited by the water's temperature.

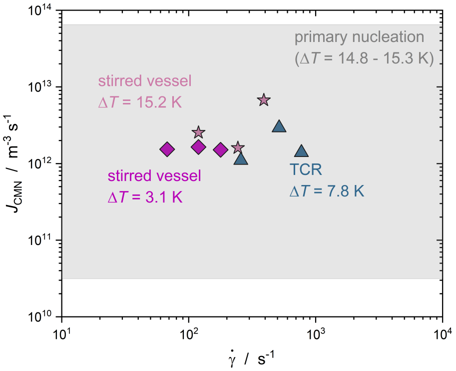

Figure 5.18: Comparison of J_{CMN} for all experimental setups (TCR (blue triangle) and stirred vessel with inoculation (only CMN, purple diamond), stirred vessel at ΔT = 15.2 K (light purple star)).

5.4 Conclusion

In this chapter, the impact of transient and turbulent flow on the crystallization dynamics of an n-hexadecane-in-water emulsion was investigated utilizing ultrasound. To align the experiments with the industrial production of melt emulsions, variations were introduced in supercooling and energy input. Classical models for crystallization kinetics were found to fit for supercooling where only CMN could occur but were inadequate for $\Delta T > 14$ K due to the simultaneous occurrence of various nucleation mechanisms. In addition to homogeneous primary nucleation resulting from applied supercooling, shear-induced nucleation, and secondary crystallization via CMN were identified. The proposed Weibull model demonstrated superior fitting performance ($R^2 > 0.95$) across all experiments compared to existing literature models (e.g., 1Exp, ...).

Notably, the study demonstrated, for the first time, that elevating mean energy dissipation (up to $\bar{\epsilon}$ = 0.37 W kg^{-1}) and micelle concentration in the continuous aqueous phase (up to $\tilde{c}_{\mathrm{TW20}}$ = 24 mol m^{-3}, equivalent to 407 cmc) resulted in significantly accelerated crystallization kinetics (up to two orders of magnitude) and consequently shorter process times until complete crystallization of the dispersed phase. Despite increased collision frequency with higher energy input, nucleation efficiency diminished. Shear-induced nucleation, especially prominent at the onset of crystallization, large droplet sizes, and high shear, emerged as a primary mechanism alongside primary homogeneous and heterogeneous nucleation, crucial for subsequent CMN in the crystallization process.

For the first time, contact-mediated nucleation was proven in a stirred vessel by recalculating the corresponding nucleation rate J_{CMN}, excluding any impacts of spontaneous or shear-induced nucleation. The comparability of J_{CMN} across various flow regimes and experimental setups was shown.

In summary, this study provides valuable insights for the industrial production of emulsions. In particular, these results lay the foundation for evaluating the potential benefits of increased energy input to counteract the prolonged cooling phase and thus optimize emulsion production processes. Transferring these findings to other oil-in-water emulsions and ultimately integrating them into industrial practice promises to yield more efficient and reliable results.

6 Summary and Outlook

Summary

This thesis has provided an in-depth analysis of the crystallization dynamics in n-hexadecane-in-water emulsions under various experimental conditions, mainly focusing on the role of contact-mediated nucleation (CMN) and its interaction with shear forces, surfactant concentration, and flow dynamics. By examining these factors across different scales and setups, from microfluidic channels to industrial-like stirred vessels, this research offers critical insights that could enhance the efficiency and control of crystallization processes in industrial settings (Figure 6.1).

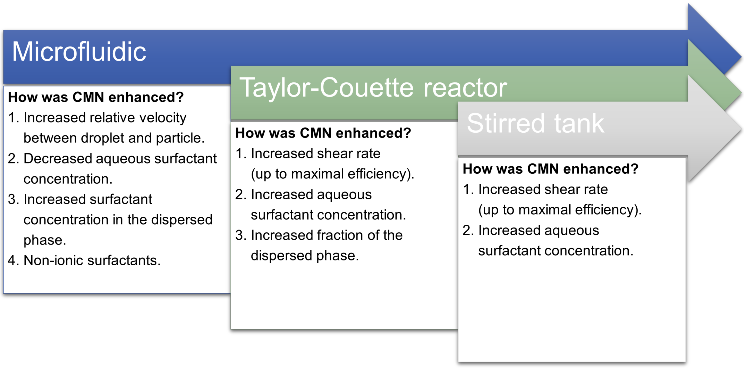

How was CMN enhanced?
1. Increased relative velocity between droplet and particle.
2. Decreased aqueous surfactant concentration.
3. Increased surfactant concentration in the dispersed phase.
4. Non-ionic surfactants.

How was CMN enhanced?
1. Increased shear rate (up to maximal efficiency).
2. Increased aqueous surfactant concentration.
3. Increased fraction of the dispersed phase.

How was CMN enhanced?
1. Increased shear rate (up to maximal efficiency).
2. Increased aqueous surfactant concentration.

Figure 6.1: Summary of the main findings in the three experimental setups.

The first experimental chapter of the experimental work hypothesized that CMN could be effectively initiated and controlled in microfluidic environments by manipulating surfactant concentration and the surfactant distribution between the continuous and dispersed phases. The findings confirmed that higher surfactant concentrations in the dispersed phase improved nucleation efficiency, while the distribution of surfactants significantly influenced the contact forces and collision dynamics necessary for CMN. This hypothesis was validated, demonstrating that microfluidic systems are a powerful tool for investigating the nuanced behaviors of CMN.

The second experimental chapter expanded on these findings by hypothesizing that shear rates within a laminar flow environment would directly influence the efficiency of CMN, potentially enhancing crystallization at optimal shear rates but inhibiting it at higher rates due to changes in collision dynamics. The experimental results supported this hypothesis, revealing a non-linear relationship between shear rate and nucleation efficiency, where an optimal shear rate maximized CMN before further increases led to reduced efficiency. This work underscores the importance of precise control over flow conditions to optimize CMN in practical applications.

Finally, the third experimental chapter explored the hypothesis that increasing the energy input and surfactant concentration in an industrial-like stirred vessel setup would accelerate crystallization processes, mainly through enhanced CMN. The research confirmed that increased energy dissipation and higher surfactant concentrations in the continuous phase significantly accelerated crystallization, supporting the hypothesis. However, it was also observed that the range of shear rates in the stirred vessel led to a more complex interaction between shear-induced nucleation and CMN, highlighting the need for careful tuning process parameters in industrial applications.

Applying these findings to other systems would require careful consideration of several factors, including phase properties, surfactant characteristics, and flow dynamics. Differences in molecular structure, polarity, and viscosity between systems may alter collision dynamics and the effectiveness of surfactants. Furthermore, the response to shear rates may vary significantly, as optimal CMN conditions in one system might translate directly to another with adjustments in flow parameters and surfactant concentrations.

Outlook

The outcomes of this thesis offer a robust foundation for future research and industrial application. Moving forward, several key areas merit further exploration:

- **Scaling to industrial applications:** The promising results from microfluidic and lab-scale experiments should be scaled up and validated in full-scale industrial processes. This includes exploring how the complex flow dynamics in large reactors influence CMN and how these insights can be applied to improve the efficiency and reliability of industrial crystallization.
- **Surfactant optimization:** There is significant potential to engineer surfactants specifically tailored to optimize CMN under various processing conditions. Future research should focus on developing surfactants that precisely control nucleation dynamics, leading to more consistent and high-quality product outcomes.
- **Advanced monitoring and control strategies:** Integrating advanced monitoring techniques, such as real-time ultrasound and NMR, into industrial processes could provide ongoing insights into crystallization dynamics, allowing for the precise control of CMN and other nucleation mechanisms in real-time.
- **Model development:** Development of more sophisticated models that can capture the complex interplay of chemical and physical factors influencing nucleation in real-time industrial scenarios would be necessary.

The use of data-driven models and combining physical models with artificial intelligence (physics-informed machine learning) would be of great interest.

- **Environmental and economic impact:** As energy efficiency and sustainability become increasingly important, future studies should assess the environmental and economic impacts of optimizing CMN in industrial processes. This includes evaluating the potential for reducing energy consumption and process times, which could significantly lower the overall carbon footprint of industrial crystallization.

In conclusion, this thesis has significantly advanced the understanding of CMN and its role in emulsion crystallization. The findings not only contribute to the academic knowledge base but also provide practical insights that could transform industrial crystallization processes, making them more efficient, sustainable, and controllable. However, further studies are recommended to assess the transferability of these findings in other substance systems. Such work could confirm the broader relevance of these findings, guiding the optimization of crystallization processes across diverse industrial applications.

A Appendix

A.1 General parameters and assumptions used for the calculations.

Table A.1: Parameters used for the calculations in this work. An emulsion and a suspension stabilized with 2 wt% TW20 ($\tilde{c}_{\mathrm{TW20}}$ = 16 mol m^{-3}) and a dispersed phase fraction of 20 wt% (Φ_{disp} = 0.26) were used for the measurements and calculations here.

Parameter	Symbol (Unit)	Water	N-hexadecane	Emulsion	Suspension
Interfacial tension	$\gamma_{\mathrm{ll/sl}}$ (mN m^{-1})	-	-	4	9.8
ϑ = 20 °C					
Density	ρ (kg m^{-3})	998.2	773.6	961.6	-
Kinematic viscosity	ν (10^{6} m^{2} s^{-1})	1.00	4.3	1.1	-
Dynamic viscosity	η (mPa s)	1.00	3.91	1.01	-
ϑ = 15 °C					
Density	ρ (kg m^{-3})	999.1	776.9	963.3	-
Kinematic viscosity	ν (10^{6} m^{2} s^{-1})	0.9	4.7	4.0	$f(\dot{\gamma})$
Dynamic viscosity	η (mPa s)	1.1	3.3	3.9	$f(\dot{\gamma})$
ϑ = 3 °C					
Density	ρ (kg m^{-3})	1000.0	-	-	-
Kinematic viscosity	ν (10^{6} m^{2} s^{-1})	0.2	-	-	$f(\dot{\gamma})$
Dynamic viscosity	η (mPa s)	4.5	15.6	5.5	$f(\dot{\gamma})$

A.1.1 Measurements of the density and the viscosity

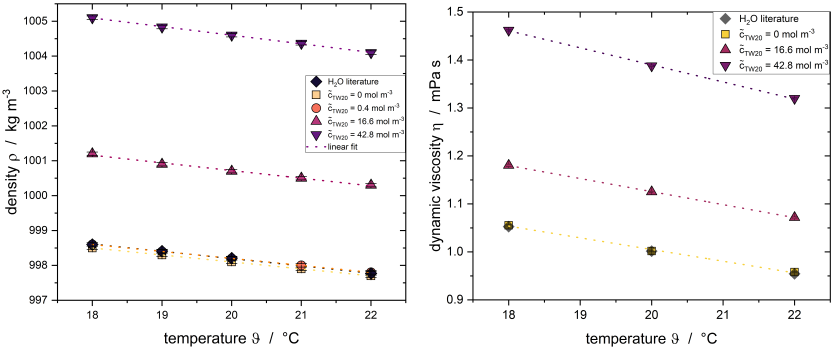

(a) Density for TW20-water mixtures. **(b)** Dynamic viscosity for TW20-water mixtures.

Figure A.1: Experimental data for the density and viscosity of binary TW20-water mixtures at various TW20 concentrations.

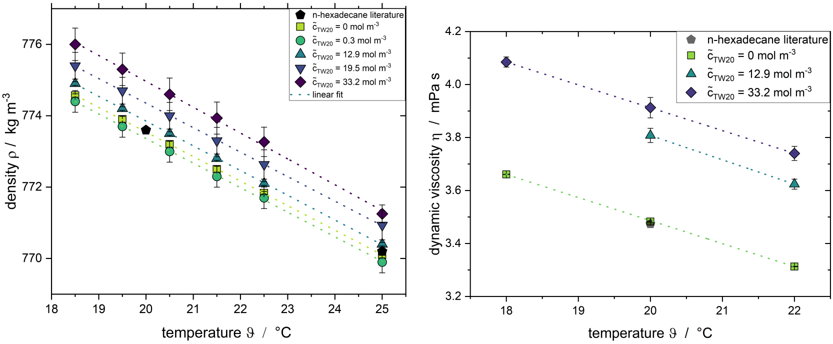

(a) Density for TW20-n-hexadecane mixtures. **(b)** Dynamic viscosity for TW20-n-hexadecane mixtures.

Figure A.2: Experimental data for the density and viscosity of binary TW20-n-hexadecane mixtures at various TW20 concentrations.

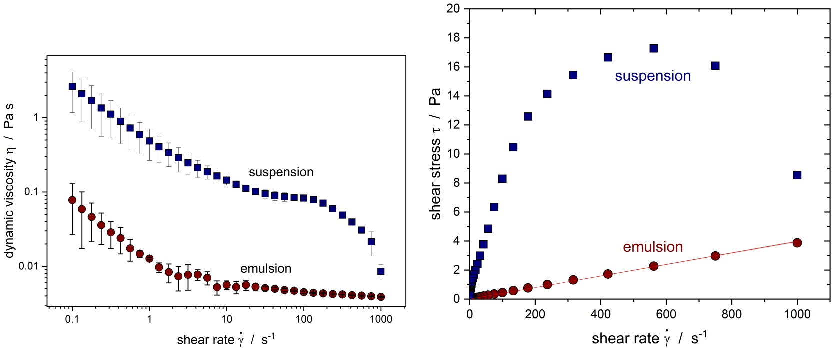

(a) Comparison between the dynamic viscosity of n-hexadecane-in-water emulsions and suspensions stabilized with 2 wt% TW20 at 15.5°C.

(b) Shear stress for an exemplary emulsion and suspension.

Figure A.3: Exemplary dynamic viscosity and shear stress of an emulsion and a suspension.

A.1.2 Determination of the interfacial tension

Dynamic measurements of the liquid–liquid interfacial tension were performed to ensure that a sufficient amount of surfactant is adsorbed at the droplet interface when a subcooled droplet collides with a pre-crystallized droplet. The measurements used the *pendant/rising drop* method on a contact-angle and contour analysis system (OCA 25, DataPhysics Instruments GmbH, Filderstadt, Germany). A cuvette containing the continuous phase was placed in the instrument; an n-hexadecane droplet ($V_\mathrm{d} = 5\ \mu$L) was dispensed at the tip of a dosing needle (Figure A.4). Because n-hexadecane is less dense than water, the configuration corresponds to a rising (inverted pendant) drop attached to the needle. The SCA22 software (DataPhysics Instruments GmbH) recorded images at fixed intervals ($\Delta t = 5$ s) and computed γ_ll from the droplet *contour* via axisymmetric drop-shape analysis (ADSA). Each measurement was stopped once a quasi-stationary value was reached (change of $\gamma_\mathrm{ll} < 0.5\ \mathrm{mN\,m^{-1}}$ per minute).

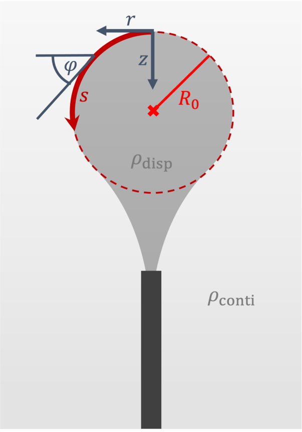

Figure A.4: Schematic of a pendant/rising droplet.

The interfacial tension γ_ll relates to the pressure jump across a curved interface via the Young–Laplace equation, $\Delta p = \gamma_\mathrm{ll}(1/R_1 + 1/R_2)$. Under gravity, the droplet is deformed by the hydrostatic pressure gradient, so the principal curvatures (and thus the contour) vary with height, yielding the characteristic pear-shaped profile. Given the density difference between the phases, the *actual* droplet dimensions (obtained from image calibration) are used in a numerical fit of the contour to the Laplace–Young shape; the fitted shape parameter then gives γ_{ll}. In practice, the evaluation employs the density difference $\Delta\rho$ and gravitational acceleration g (through the capillary constant) together with the measured contour.

$$\text{Young-Laplace equation:}\quad \Delta p = \gamma_{\mathrm{ll}}\left(\frac{1}{R_1}+\frac{1}{R_2}\right) \tag{A.1}$$

$$\text{hydrostatic pressure:}\quad \Delta p = \Delta p_0 + \Delta\rho g z \tag{A.2}$$

$$\text{equate:}\quad \Delta p_0 + \Delta\rho g z = \gamma_{\mathrm{ll}}\left(\frac{1}{R_1}+\frac{1}{R_2}\right) \tag{A.3}$$

$$\text{polar coordinate:}\quad \frac{\partial\varphi}{\partial s} = -\frac{\sin(\varphi)}{r} + \frac{2}{R_0} + \frac{(\rho_{\mathrm{conti}}-\rho_{\mathrm{disp}})gz}{\gamma_{\mathrm{ll}}} \tag{A.4}$$

$$\text{transformation:}\quad \frac{\partial r}{\partial s} = \cos(\varphi) \tag{A.5}$$

$$\frac{\partial z}{\partial s} = \sin(\varphi) \tag{A.6}$$

$$\text{boundary conditions:}\quad r(s=0) = z(s=0) = \varphi(s=0) = 0 \tag{A.7}$$

Table A.2: Interfacial tensions measured for TW20 dissolved either in the aqueous or n-hexadecane phase at the beginning of the experiment (Kaysan et al. (2021))

$\tilde{c}^{aq}_{TW20}$	$\tilde{c}^{hex}_{TW20}$	γ_{ll} (mN m^{-1})
0	0	48.6 ± 0.5
8.2	0	3.5 ± 0.3
16.6	0	2.9 ± 0.2
0	6.4	1.9 ± 0.4
0	12.9	0.9 ± 0.3

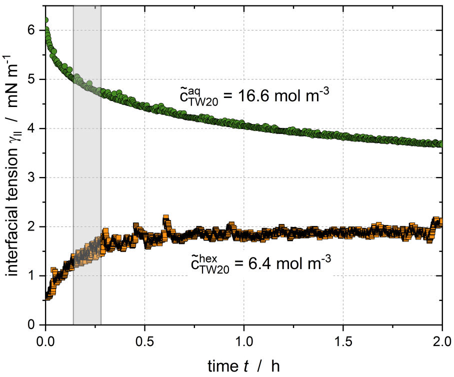

Figure A.5: Interfacial tension for n-hexadecane and water while dissolving the surfactant TW20 either in water (outer phase) or n-hexadecane (droplet) before the experiment started (Kaysan et al. (2021)).

A.1.3 Solubility of n-hexadecane in water

The Hansen Solubility Parameters (HSP) are a set of three parameters used to predict the solubility of materials, particularly in polymer science and solvent selection. They break down the total solubility parameter into three components:

- Dispersion ($\delta_{\mathrm{Han,d}}$): This parameter describes the dispersion forces (van der Waals forces) between molecules.
- Polarity ($\delta_{\mathrm{Han,p}}$): This parameter represents the dipole-dipole interactions between molecules.
- Hydrogen bonding ($\delta_{\mathrm{Han,h}}$): This parameter accounts for molecule hydrogen bonding interactions.

The solubility of a substance in a solvent can be estimated using the Hansen solubility distance R_{Han}, which is calculated as:

$$\begin{aligned} R_{\mathrm{Han}} = \Bigg(& 4(\delta_{\mathrm{Han,d1}} - \delta_{\mathrm{Han,d2}})^2 \\ & + (\delta_{\mathrm{Han,p1}} - \delta_{\mathrm{Han,p2}})^2 \\ & + (\delta_{\mathrm{Han,h1}} - \delta_{\mathrm{Han,h2}})^2 \Bigg)^{1/2} \end{aligned} \tag{A.8}$$

where $\delta_{\mathrm{Han,d1}}$, $\delta_{\mathrm{Han,p1}}$, and $\delta_{\mathrm{Han,h1}}$ are the Hansen parameters of the solvent, and $\delta_{\mathrm{Han,d2}}$, $\delta_{\mathrm{Han,p2}}$, and $\delta_{\mathrm{Han,h2}}$ are the Hansen parameters of the solute. A lower R_{Han} value indicates greater solubility, as the interactions between the solute and solvent are more similar. Conversely, a higher R_a value suggests poor solubility.

HSP are commonly used in various fields such as polymer science, coatings, adhesives, and cosmetics to select suitable solvents or predict the miscibility of materials. Thus, they can be used to estimate the solubility of n-hexadecane in water.

The parameters for water are $\delta_{\mathrm{Han,d}} = 15.5$ MPa$^{1/2}$, $\delta_{\mathrm{Han,p}} = 16.0$ MPa$^{1/2}$, and $\delta_{\mathrm{Han,h}} = 42.3$ MPa$^{1/2}$, while for n-hexadecane, they are $\delta_{\mathrm{Han,d}} = 16.3$ MPa$^{1/2}$, $\delta_{\mathrm{Han,p}} = 0.0$ MPa$^{1/2}$, and $\delta_{\mathrm{Han,h}} = 0.0$ MPa$^{1/2}$.

According to Equation A.8 the Hansen distance R_{Han} between the two substances is calculated as $R_{\mathrm{Han}} \approx 45.23$ MPa$^{1/2}$. As $R_{\mathrm{Han}} > 10$, the solubility of n-hexadecane in water is negligible (Hansen (2007)).

A.2 Nuclear Magnetic Resonance

Felix Bloch and Edward Mills Purcell and the corresponding research groups independently discovered the Nobel Prize-winning phenomenon of "nuclear magnetic resonance" in condensed matter, exemplified by substances like a droplet of water, in the year 1945. This groundbreaking discovery laid the groundwork for nuclear magnetic resonance (NMR) measurements. In contemporary contexts, NMR is prominent in diverse fields such as medicine, physics, chemistry, and materials science.

NMR encompasses various measurement methods, including spectroscopy, diffusometry, relaxometry, and imaging. This chapter provides a project-related explanation of the fundamental NMR principles relevant to this thesis's measurements. These principles are integral for understanding and executing NMR measurements in diverse applications.

A.2.1 Basics of NMR

Figure A.6 displays an illustrative example of a liquid state ^{1}H-NMR spectrum obtained from the n-hexadecane-in-water emulsion in use as well as the surfactant TW20. The sensitivity of NMR measurements is predominantly influenced by the natural isotope abundance and the observed nucleus's gyromagnetic ratio γ. In the case of ^{1}H nuclei, which are commonly analyzed in spectroscopy, the gyromagnetic ratio is notably high ($2{\cdot}\pi{\cdot}42.58$ MHz/T), resulting in sensitivity levels that are often several orders of magnitude larger than those of other heteronuclei. This characteristic enables the acquisition of meaningful spectra with a high signal-to-noise ratio, even within short measurement times of a few seconds.

The x-axis is noted in *parts per million* (ppm), increasing from right to left (Figure A.6). In particular, in Figure A.6 (a), there are four distinct peaks, with peak maxima at 0.88 ppm, 1.26 ppm, 3.67 ppm and 4.87 ppm. Using databases, the peaks can be related to the ^{1}H of specific functional groups: The ^{1}H signal

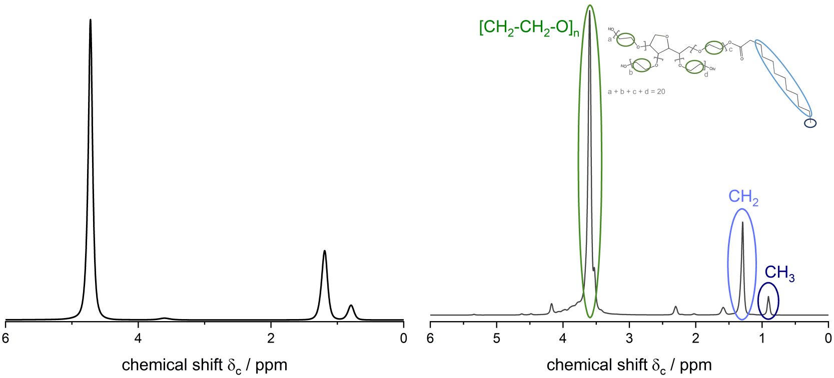

(a) N-hexadecane-in-water emulsion prepared with D_2O and TW20.

(b) Pure TW20. Reproduced from Kaysan et al. (2022a), CC BY-NC-ND 4.0. No changes were made.

Figure A.6: ^{1}H spectra of the n-hexadeacne-in-water emulsion as well as the surfactant TW20 itself.

of the CH_2 and CH_3 group of n-hexadecane and TW20 is observed at δ_c = 0.88 ppm and δ_c = 1.26 ppm. The peak at 3.67 ppm refers to the ^{1}H of the $[CH_2\text{-}CH_2\text{-}O]_n$ groups in the head of TW20. At δ_c = 4.87 ppm, the ^{1}H of water can be found. Deuterized water was used in all experiments to minimize this peak's size and avoid any overlapping with the peak at δ_c = 3.67 ppm.

Additionally, the area integrals and peak intensities vary among these peaks. The area integrals are proportional to the number of spins and can thus be used to calculate the concentration of a given substance in the liquid state. This enables the determination of the solid fraction of the dispersed phase as a function of time or temperature (Figure A.7). Consequently, the solid fraction of n-hexadecane can be calculated (Equation 4.1). The residual peak areas visible at δ_c = 0.88 ppm and 1.26 ppm belong to the corresponding ^{1}H groups of TW20 (Figure A.6 (b)).

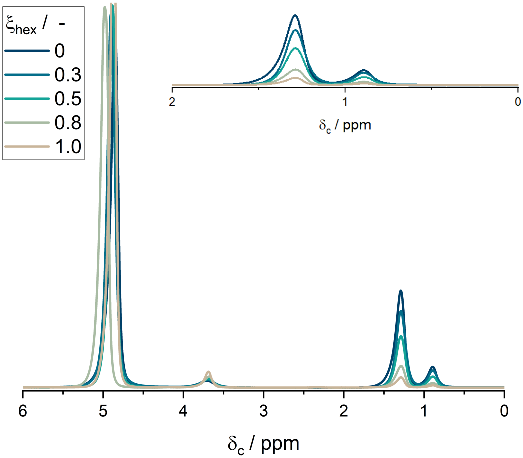

Figure A.7: Liquid state ^{1}H spectrum of an n-hexadecane-in-water emulsion stabilized with 5 wt% TW20 and 20 wt% n-hexadecane at ΔT = 15 K.

A.2.2 Concentration measurements of TW20 in water

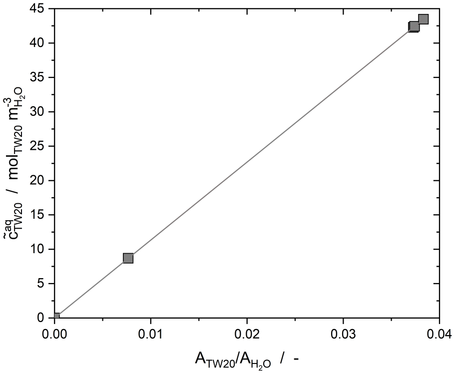

Figure A.8: Calibration for the aqueous concentration measurements of TW20.

A.2.3 Additional information for RheoNMR measurements

A.2.3.1 GreenTEC specifications

Table A.3: Overview about relevant material properties of GreenTEC at 15.5 °C used to determine the time required for temperature adaptation.

Parameter	Value
Density	$1.22\ \mathrm{g\ cm^{-3}}$
Heat capacity	$1.324\ \mathrm{J\ g^{-1}\ K^{-1}}$
Thermal conductivity	$0.251\ \mathrm{W\ m^{-1}\ K^{-1}}$

A.2.3.2 Temperature calibration

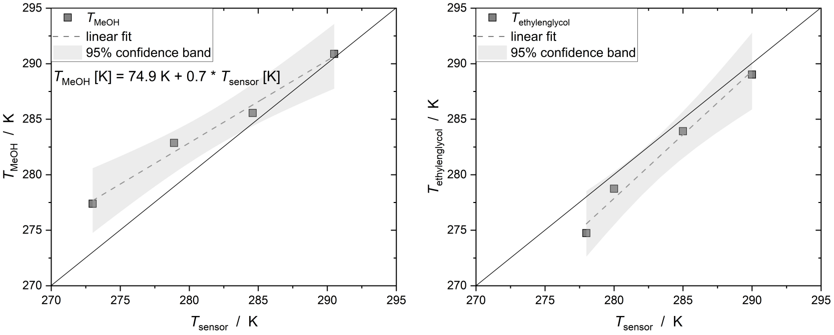

(a) Inner rotating cylinder - 200 MHz spectrometer.

(b) Outer rotating cylinder - 300 MHz spectrometer.

Figure A.9: Temperature calibration with either (a) methanol or (b) ethylenglycole.

A.2.3.3 Pulse sequences

Table A.4: Magnetic resonance imaging (MRI) settings for measuring spectral information during the rotation of the Taylor-Couette reactor's inner cylinder (TCR).

MRI parameter	Value
Pulse sequence	1D SE-CSI
Repetition time	2 s
Echo time	3 ms
Number of averages	4
Slice thickness (z-direction)	3 mm
Number of slices	1
Field of view (x-direction)	20 mm
Matrix size (x-direction	8
Spectral bandwidth (SWH)	5 kHz
Number of acquired data points	2048
Number of dummy scans	4
Measurement duration	42 s

Table A.5: NMR spectroscopy parameters for determining the time-resolved solid fraction of the dispersed phase during the rotation of the TCR's outer cylinder.

NMR parameter	Value
Pulse sequence	single pulse
Repetition time	5 s
Number of averages	4
Spectral bandwidth (SWH)	5 kHz
Receiver gain	0.5
Pre-scan delay	6.5 μs
Measurement duration	26 s

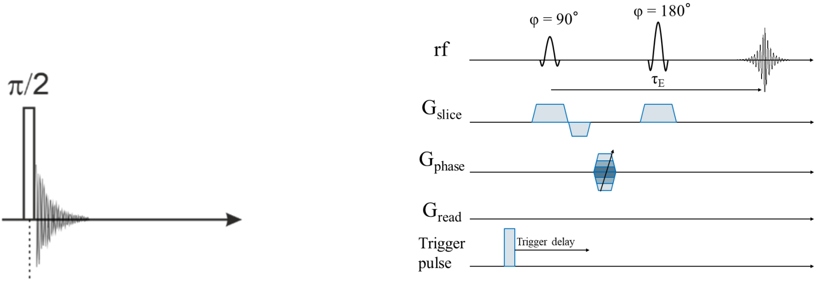

(a) Single pulse experiment: after the rf pulse, the NMR signal is acquired as the free induction decay. The spectrum itself can then be computed by fast Fourier transformation.

(b) The chemical composition of the axial slices was measured using a slice-selective spin echo-based chemical shift imaging pulse sequence. A trigger pulse from the Rheo interface reduces artifacts by activating the MRI measurement on the phase encoding stage at a well-defined position of the inner rotor.

Figure A.10: Pulse sequences for the RheoNMR measurements at 300 MHz and 200 MHz.

A.3 Derivation of the fitting models for $\xi(t)$

The derivations of the model equations used in this work are based on considering a batch-wise crystallization of the sample without inlet or outlet flows and the assumption of constant supercooling. In addition, it is assumed that the density of the liquid and solid dispersed phases is approximately the same. As a result, the proportion of the crystallized volume corresponds to the crystallized mass fraction (in each case related to the dispersed phase). Both are synonymously referred to as the solid fraction.

The liquid fraction of the dispersed phase ξ_l is more practicable for closer looking at the deviation of the single equations. The following relationship applies between the liquid and the solid fraction of the dispersed phase:

$$\xi_l(t) = 1 - \xi(t) \tag{A.9}$$

A.3.1 1Exp model for a given droplet size

The change of ξ_l with time for a given droplet size can be described with

$$\frac{d\xi_l}{dt} = -k_{\mathrm{prim}} \cdot \xi_l = -J_{\mathrm{prim}} \cdot V_{\mathrm{nuc}} \cdot \xi_l. \tag{A.10}$$

Solving the differential equation results in

$$\frac{\xi_l(t)}{\xi_l(t_0)} = exp(-k_{\mathrm{prim}}(t - t_0)) = exp(-J_{\mathrm{prim}} \cdot V_{\mathrm{nuc}}(t - t_0)). \tag{A.11}$$

With the initial values at the start of the experiment $t_0 = 0$ and $\xi_l = 1$ (all droplets are liquid) and Equation A.9, the equation for the 1Exp model is obtained:

$$\xi = 1 - exp(-k_{\mathrm{prim}} \cdot (t - t_0)) = 1 - exp(-J_{\mathrm{prim}} \cdot V_{\mathrm{nuc}} \cdot (t - t_0)). \tag{A.12}$$

A.3.2 1Exp for droplet size distributions

For primary nucleation, a droplet size distribution (DSD) can be regarded as a parallel, independent crystallization of the individual droplet size classes. For a class i, analogous to Equation A.11 with the total volume of the dispersion phase $V_{\mathrm{disp,total}}$.

$$\frac{V_{\mathrm{l,i}}(t)}{V_{\mathrm{disp,total}}} = \frac{V_{\mathrm{l,i}}(t_0)}{V_{\mathrm{disp,total}}} \cdot exp(-J_{\mathrm{prim}} \cdot V_{\mathrm{nuc,i}} \cdot (t - t_0)). \tag{A.13}$$

ξ_{l} can be estimated as the sum over all size classes b

$$\xi_{\mathrm{l}}(t) = \sum_{i=1}^{b} \frac{V_{\mathrm{l,i}}(t)}{V_{\mathrm{disp,total}}} = \sum_{i=1}^{b} \frac{V_{\mathrm{l,i}}(t_0)}{V_{\mathrm{disp,total}}} \cdot exp(-J_{\mathrm{prim}} \cdot V_{\mathrm{nuc,i}}(t - t_0)). \tag{A.14}$$

The initial discrete, volumetric distribution density (without any particles) can be written as

$$q_{3,\mathrm{t_0}}(\bar{x}_{\mathrm{i}}) \cdot \Delta x_{\mathrm{i}} = \frac{V_{\mathrm{l,i}}(t_0)}{\sum\limits_{j=1}^{b} v_{\mathrm{l,j}}(t_0)} = \frac{V_{\mathrm{l,i}}(t_0)}{V_{\mathrm{l,total}}(t_0)}. \tag{A.15}$$

Extension of Equation A.14 with the total liquid volume $V_{\mathrm{l,total}}$ and inserting Equation A.15 leads to

$$\xi_{\mathrm{l}}(t) = \sum_{i=1}^{b} \frac{V_{\mathrm{l,total}}(t_0)}{V_{\mathrm{disp,total}}} \cdot q_{3,\mathrm{t_0}}(\bar{x}_i) \cdot \Delta x_{\mathrm{i}} \cdot exp(-J_{\mathrm{prim}} \cdot V_{\mathrm{nuc,i}} \cdot (t - t_0)). \tag{A.16}$$

$V_{\mathrm{l,total}}(t_0)/V_{\mathrm{disp,total}}$ equals to $\xi_{\mathrm{l}}(t_0)$. Thus, considering Equation A.9, Equation A.16 leads to

$$\xi(t) = 1-\sum_{i=1}^{b}(1-\xi(t_0))\cdot q_{3,\mathrm{t_0}}(\bar{x}_{\mathrm{i}})\cdot\Delta x_{\mathrm{i}}\cdot exp(-J_{\mathrm{prim}}\cdot V_{\mathrm{nuc,i}}\cdot(t-t_0)). \quad \text{(A.17)}$$

The integral form is

$$\xi(t) = 1-\int_{0}^{\infty}(1-\xi(t_0))\cdot q_{3,\mathrm{t_0}}(x)\cdot exp(-J_{\mathrm{prim}}\cdot V_{\mathrm{nuc}}(x)(t-t_0))dx. \quad \text{(A.18)}$$

For t_0 = 0, Equation A.18 simplifies to

$$\xi(t) = 1-\int_{0}^{\infty} q_{3,\mathrm{t_0}}(x)\cdot exp(-J_{\mathrm{prim}}\cdot V_{\mathrm{nuc}}(x)\cdot t)dx. \quad \text{(A.19)}$$

A.4 Microfluidics

A.4.1 Experimental raw data

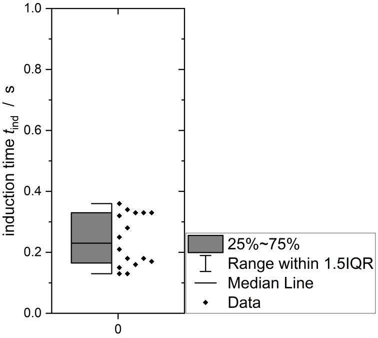

Figure A.11: Induction times without surfactant.

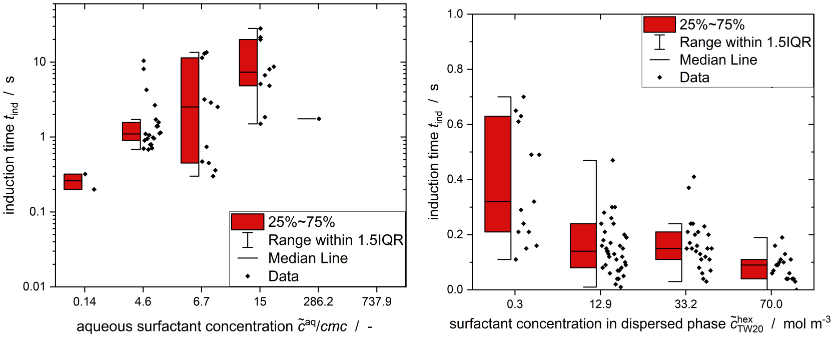

(a) In water. **(b)** In n-hexadecane.

Figure A.12: Experimental raw data for TW20.

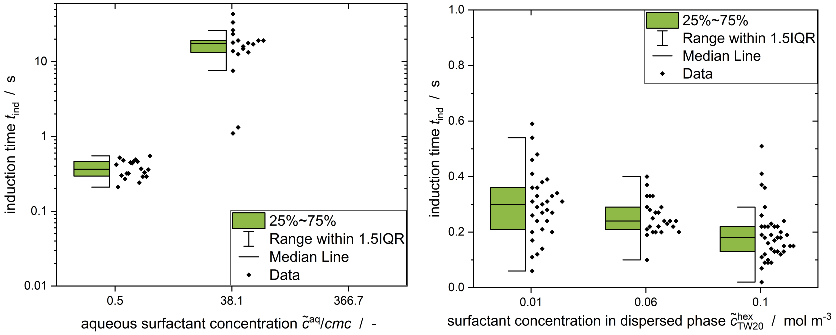

(a) In water. **(b)** In n-hexadecane.

Figure A.13: Experimental raw data for TW60.

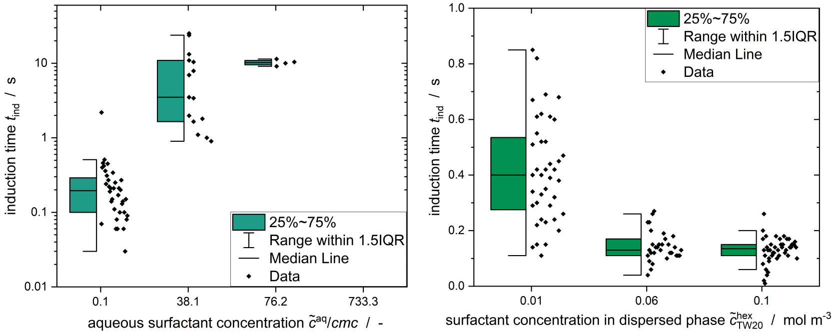

(a) In water. **(b)** In n-hexadecane.

Figure A.14: Experimental raw data for TW80.

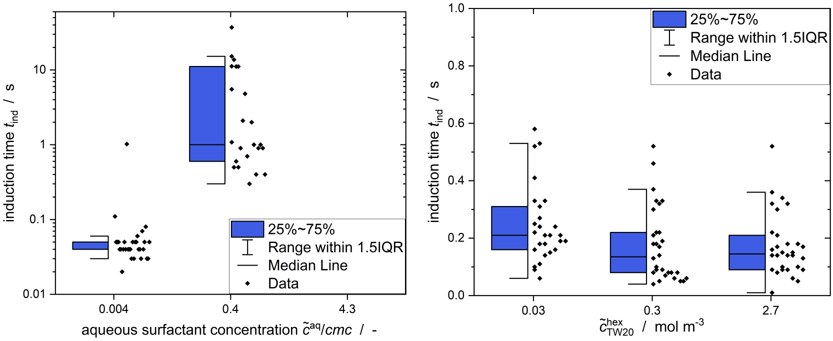

(a) In water.

(b) In n-hexadecane.

Figure A.15: Experimental raw data for SDS.

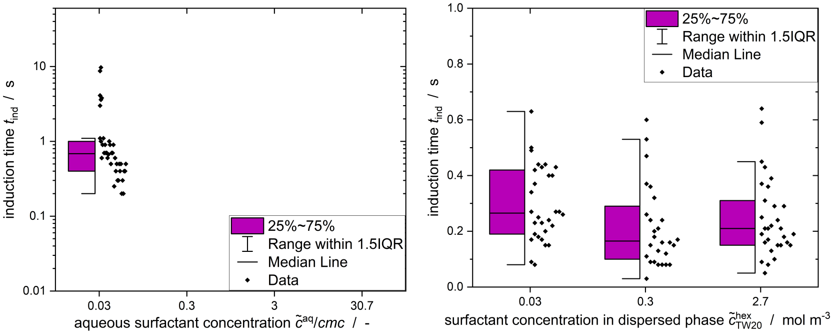

(a) In water.

(b) In n-hexadecane.

Figure A.16: Experimental raw data for CTAB.

A.4.2 Impact of relative velocity on induction time

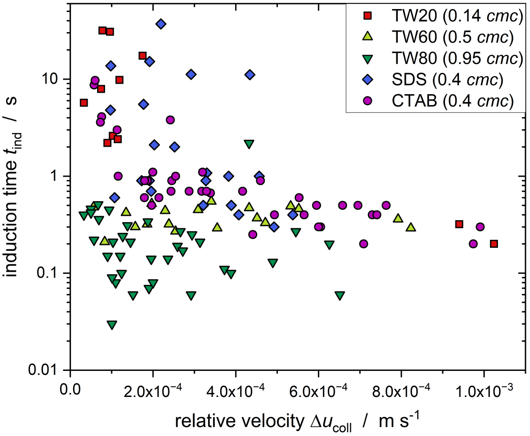

Figure A.17: As the CMN is mainly impacted by the number of micelles in the aqueous phase, surfactant concentrations below *cmc* are compared regarding the influence of the relative velocity between droplet and particle Δu_{coll}. It is visible that an increased Δu_{coll} leads to shorter induction times as the overall contact force is increased.

A.4.3 Flow regime in microfluidic channel

Table A.6: Dimensionless numbers characterizing the flow in the microfluidic channel.

Fluid velocity u_{conti} / ms^{-1}	Droplet Capillary number Ca_{d}		Reynolds number Re
	without TW20	with TW20	
$2.3 \cdot 10^{-4}$	$1.8 \cdot 10^{-5}$	$2.1 \cdot 10^{-4}$	$5.2 \cdot 10^{-2}$
$4.6 \cdot 10^{-4}$	$3.6 \cdot 10^{-5}$	$4.3 \cdot 10^{-4}$	$1.0 \cdot 10^{-1}$
$9.3 \cdot 10^{-4}$	$7.3 \cdot 10^{-5}$	$8.6 \cdot 10^{-4}$	$2.1 \cdot 10^{-1}$
$1.4 \cdot 10^{-3}$	$1.1 \cdot 10^{-4}$	$1.3 \cdot 10^{-3}$	$3.1 \cdot 10^{-1}$
$1.9 \cdot 10^{-3}$	$1.5 \cdot 10^{-4}$	$1.7 \cdot 10^{-3}$	$4.2 \cdot 10^{-1}$
$2.3 \cdot 10^{-3}$	$1.8 \cdot 10^{-4}$	$2.1 \cdot 10^{-3}$	$5.2 \cdot 10^{-1}$

A.4.4 Description of droplet hugging particle

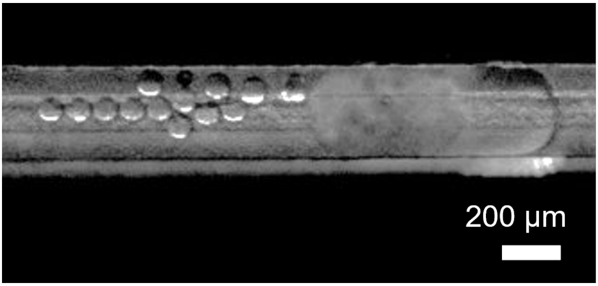

Figure A.18: The droplet is spreading around (= *hugging*) the particle solid particle without nucleation taking place. After fully surpassing the particle, the droplet is sheared into smaller droplets.

A.4.5 Numeric Flow Simulations

A.4.5.1 Setup of the CFD simulations

All computational simulations were executed utilizing the open-source software OpenFOAM (Version 6) (Weller et al. (1998)). The *simpleFoam* solver was employed to resolve the Navier-Stokes equations under the assumption of an incompressible, steady-state flow of a Newtonian fluid. For mesh generation, the SnappyHexMesh tool within the OpenFOAM software was utilized. A mapped boundary condition with varying average values was selected for the velocity at the inlet. This condition involved averaging the velocity profile over the outlet surface and then applying it at the inlet, with adjustments based on the average value. Given the channel's sufficient length to establish a fully developed flow field, a velocity gradient of 0 was imposed at the outlet. The wall of the channel and the particle were set to a fixed value of 0. A zero gradient was also chosen for the pressure at the inlet, the channel wall, and the particle. The pressure at the outlet was set to a constant value.

A grid convergence study was performed to analyze the influence of the numerical mesh on the simulation results. The grid convergence index proposed by Roache (1994) was calculated to quantify the discretization errors. It is based on the Richardson extrapolation and dependent on the order of convergence. The base cell sizes tested were 15 μm, 11.6 μm, and 9 μm (Table A.7).

Table A.7: Simulated differential pressure in the minichannel filled with water only for three different cell sizes.

Cell size / μm	Differential pressure Δp / Pa
15	44.21
11.6	44.63
9	44.94

The two corresponding grid convergence indexes *GCI* between the cell sizes of 15 and 11.6 μm $GCI_{15,11.6}$ and between the cell sizes 11.6 and 9 μm $GCI_{11.6,9}$ were the following:

$$GCI_{15,11.6} = 0.0329$$

and

$$GCI_{11.6,9} = 0.0242.$$

A base cell size of 11.6 μm was selected as a compromise between simulation duration and accuracy. The mesh underwent refinement up to three iterations, with the degree of refinement dependent on the proximity to both the particle and the channel walls. This was done to ensure the accurate resolution of gradients that develop near solid surfaces (Figure A.19).

Figure A.19: Illustration of a mesh created by *SnappyHexMesh*, employed for simulated parameter studies investigating the impact of particle shape on the total pressure drop. For accurate data, the refinement strategy varies based on the relative position of the particle and the channel walls. In this instance, the film thickness between the particle and the channel was 0. Reproduced from Kaysan et al. (2023b), CC BY 4.0.

The mesh refinement is made relative to the base grid. Specifically, cells with centers situated at a distance of 40 μm from the channel wall and 50 μm from the particle surface were refined by a factor of 2. Furthermore, cells with centers within 3 μm of the particle surface underwent threefold refinement.

A.4.5.2 Simulations of microfluidic flow in the presence of a solid particle

The simulations seek to evaluate the impact of the cap size (Figure A.20 (a)), the body length l_{body} (Figure A.20 (a)), the film thickness between the particle and the channel wall h_f (Figure A.20 (b)), and the channel corners (the region of bypass flow, Figure A.20 (b)) on Δp.

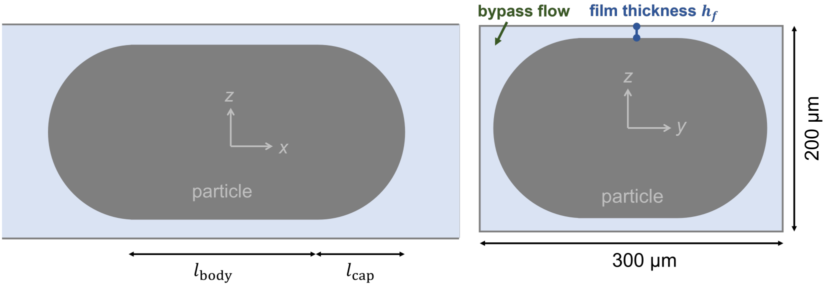

(a) The body length and the length of the caps of the particle are shown.

(b) Besides the bypass flow, the film thickness between the particle and the wall is visible.

Figure A.20: Schematic illustrations of the particle in the minichannel.

Simulations were performed for particles of various lengths to elucidate the influence of a solid particle within the microfluidic channel on Δp (Figure A.21). The geometry of the particles used in simulations was based on observations from experimental images, resulting in $l_\mathrm{caps} = 45\ \mu$m. As a first starting value, a film thickness between the droplet and the wall of h_f = 2 μm was assumed.

The results illustrate that Δp increases with the rising flow velocity of the continuous phase and with an increase in particle length. The experimental validation of these simulation results proved successful. To gain further insights into the effects of particle dimensions (Figure A.20), a parameter study was carried out (Figure A.22 (b)).

As both the l_body and l_cap parameters increased, there was a corresponding increase in Δp along the microfluidic channel. For l_body and l_cap, this trend can be attributed to the reduction in the ratio between the channel volume and the particle volume. Here, this ratio is defined as the porosity. The linear increase in Δp with increasing l_body aligns with the expectations.

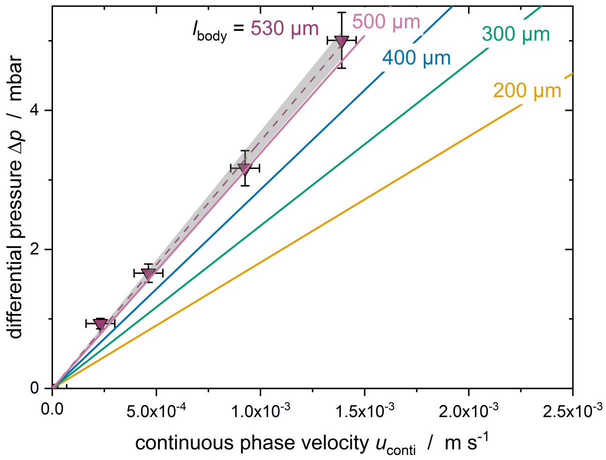

Figure A.21: Experimental data points (depicted as dots) and simulated results (represented by lines) at a temperature of ϑ_{exp} = 17.5 °C illustrate the influence of the body length l_{body}. The experimental data points were subject to linear fitting, and the shaded gray region corresponds to the 95% confidence interval (Kaysan et al. (2023b)).

When h_{f} increased, Δp along the channel decreased as A_{flow} increased. With h_{f} increasing from 0 μm to 5 μm, the relative deviation of Δp is approximately 6%. This discrepancy is smaller than the margin of error in the experimental measurements, and there is good agreement between the experimental and simulated data at a layer thickness of 2 μm (Figure A.21). Thus, it can be concluded that the layer thickness in the experiments falls within the range of 0 μm to 5 μm, when assuming a constant film thickness.

It is worth noting that the thickness of the film separating a moving droplet in a microchannel from the wall is estimated to be around 1% to 5% of the half height of the channel for Capillary numbers Ca_{d} smaller than $Ca_{\mathrm{d}} < 0.01$ (Table A.6) (Reinelt and Saffman (1985), Hazel and Heil (2002), Schwartz et al. (1986)). In this study, it is assumed that the half-height is half of d_{h}, leading to a film thickness ranging from 1.2 μm to 6 μm. This assumption aligns well with the simulations of the particle in the flow field and the corresponding experimental validation despite the initial assumption for liquid droplets, not solid particles.

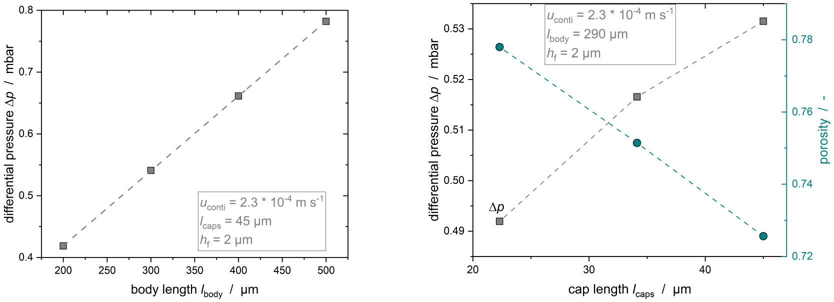

(a) Body length.

(b) Cap length.

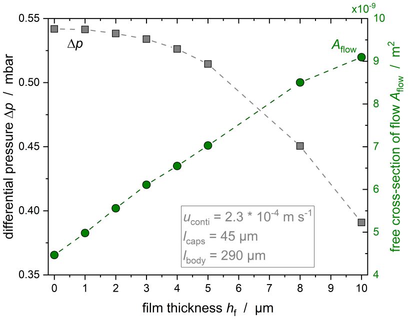

(c) Film thickness.

Figure A.22: Parameter study to determine the impact of the body length, the length of the caps as well as the film thickness between wall and particle surface (Kaysan et al. (2023b)).

Based on the simulations, Δp and u_{crit} were tracked along three lines in the minichannel to examine the individual impact of the caps and the body on Δp (Figure A.23).

The analysis shows that a significant part of Δp drops along the particle body, which underlines the significant influence of the particle on the total Δp compared to the pressure drop along the empty channel. Additionally, the pressure drop along the corners of the channel exerts a dominant effect on the overall Δp, which aligns well with the findings from a previous study Ransohoff and Radke (1988). Baroud et al. (2010) observed that the primary pressure drop for liquid droplets without surfactant occurred within the plugs (areas between

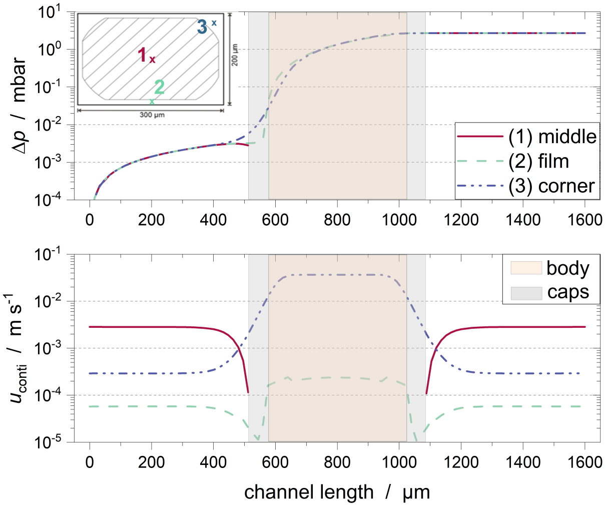

Figure A.23: The differential pressure drop Δp (top) and the velocity of the continuous phase u_{crit} (bottom) along various lines (located in the top-left corner) within the microfluidic channel at a temperature of ϑ_{exp} = 20 °C and $u_{\mathrm{conti}} = 1.4 \cdot 10^{-3}$ ms^{-1}. The orange region corresponds to the body of the particle (l_{body} = 580 μm), and the grey areas represent the two caps (l_{caps} = 45 μm) (Kaysan et al. (2023b)).

the droplets) for non-viscous droplets and along the body for viscous droplets. Furthermore, Fuerstman et al. (2007) noted that introducing an intermediate surfactant concentration (1 to 2 orders of magnitude of cmc) led to the pressure drop along a bubble primarily governed by the loss along the body length. The pressure dropped rapidly along the caps in cases with no or a high surfactant concentration.

It is important to highlight the key differences between the data found in existing literature and the results presented here. Notably, this work's investigation centered around a stationary solid particle, as opposed to the movable liquid or gaseous droplets or bubbles typically explored in literature. Moreover, the simulations and experiments presented here did not cover the presence of surfactants.

A.5 Ultrasonic measurements in the stirred vessel

A.5.1 Determination of the speed of sound

The probe's emission and reception are based on the inverse and direct piezoelectric effects Awad et al. (2012). The transducer layer contains a piezoelectric material (e.g., quartz). In the unloaded state the net polarization is zero. Applying a short voltage pulse excites a mechanical deformation and drives the crystal near its resonance, generating an ultrasonic wave (Awad et al. (2012)). The wave propagates through the medium to the reflector plate, is reflected, and returns to the transducer. Upon reception, the incoming stress induces a voltage in the piezo layer (direct effect), which is detected (McClements (1991), Awad et al. (2012)).

Physically, sound is a mechanical disturbance that propagates as a wave in an elastic medium. Pressure/density fluctuations displace particles from equilibrium and the disturbance is transferred to neighboring particles with a time delay. If particle motion is parallel to the propagation direction, the wave is longitudinal (liquids and gases); solids also support transverse waves (McClements (1991), Awad et al. (2012)). The speed of sound v is the product of wavelength λ and frequency f:

$$v = \lambda \cdot f. \tag{A.20}$$

For weakly attenuating media, v can be related to an elastic modulus M_{ela} (McClements (1991)):

$$v = \sqrt{\frac{M_{\mathrm{ela}}}{\rho}}. \tag{A.21}$$

For liquids (longitudinal waves),

$$v = \sqrt{\frac{M_{\mathrm{comp}}}{\rho}}, \tag{A.22}$$

with the compression (bulk) modulus M_{comp}, which is the reciprocal of the adiabatic compressibility κ:

$$\kappa = \frac{1}{M_{\mathrm{comp}}} = \frac{1}{\rho}\left(\frac{\partial \rho}{\partial p}\right), \tag{A.23}$$

so that

$$v(T,p) = \sqrt{\frac{1}{\kappa(T,p)\,\rho(T,p)}}. \tag{A.24}$$

The speed of sound depends on temperature and pressure. In most liquids, v decreases with increasing temperature; in water it increases up to about $74\,^{\circ}\mathrm{C}$ and then decreases (McClements (1988)). With increasing pressure, v generally increases in liquids (McClements (1991)).

During propagation in real media, attenuation arises mainly from absorption (viscous/thermal, molecular) and scattering. The amplitude of the ultrasound wave decays as

$$A_{\mathrm{wave}} = A_{\mathrm{wave},0}\,\exp(-\alpha_{\mathrm{wave}}\,z), \tag{A.25}$$

where α_{wave} is the (frequency-dependent) attenuation constant and z the propagation distance (McClements (1991, 1992), Awad et al. (2012)).

In confined or inhomogeneous systems (e.g., a dispersion in a stirred vessel), reflections and diffraction must be considered (McClements (1991)). A useful measure is the (characteristic) acoustic impedance $I = \rho\,v$. For a plane wave at normal incidence between two lossless media, here aluminum and the emulsion, with impedances I_{al} and I_{em}, the pressure-amplitude reflection coefficient is (McClements (1997), Awad et al. (2012)):

$$\frac{A_{\mathrm{wave,refl}}}{A_{\mathrm{wave},0}} = \frac{I_{\mathrm{al}} - I_{\mathrm{em}}}{I_{\mathrm{al}} + I_{\mathrm{em}}}. \tag{A.26}$$

Using typical values, $I_{\mathrm{al}} \approx 16.9 \times 10^6\ \mathrm{N\,s\,m^{-3}}$ for aluminum and, for a water-like emulsion, $I_{\mathrm{em}} \approx 1.44 \times 10^6\ \mathrm{N\,s\,m^{-3}}$ (Grimsehl (1977)), one obtains an amplitude reflection of about 84%.

A.5.2 Calculation of the solid fraction of the dispersed phase

Determining the solid content in emulsions assumes an ideal, homogeneous distribution of phases and that droplets are small compared to the acoustic wavelength, so that scattering is negligible (Urick (1947)).

In this long-wavelength limit, the speed of sound is given by

$$\frac{1}{v} = \sqrt{\kappa\,\rho} = \Big(\sum_j \kappa_j\,\xi_j\Big)^{1/2} \Big(\sum_j \rho_j\,\xi_j\Big)^{1/2}, \tag{A.27}$$

where κ and κ_j denote the adiabatic compressibility, ρ and ρ_j the density of the emulsion and phase j, and ξ_j the volume fraction of phase j.

If the continuous phase (water) does not freeze ($\vartheta > 0\,^{\circ}\mathrm{C}$), only the dispersed droplets crystallize. For an emulsion in which the dispersed phase contains a fraction ξ of crystalline droplets and a fraction $\xi_l = 1 - \xi$ of liquid droplets, the effective compressibility is

$$\kappa = \xi\,\kappa_s + (1-\xi)\,\kappa_l, \tag{A.28}$$

and similarly the density

$$\rho = \xi\,\rho_s + (1-\xi)\,\rho_l. \tag{A.29}$$

Assuming that the emulsion density is essentially the same in the two limiting states (all droplets liquid vs. all droplets solid), $\rho \simeq \rho_l \simeq \rho_s$, Equation (A.27) with Equation (A.28) yields

$$\frac{1}{v} = \sqrt{\big(\xi\,\kappa_s + (1-\xi)\,\kappa_l\big)\,\rho}\,. \tag{A.30}$$

Using

$$\frac{1}{v_l^2} = \kappa_l\,\rho, \qquad \frac{1}{v_s^2} = \kappa_s\,\rho, \tag{A.31}$$

one obtains the Urick relation

$$\frac{1}{v^2} = \xi\,\frac{1}{v_s^2} + (1-\xi)\,\frac{1}{v_l^2} \quad \Rightarrow \quad \xi = \frac{\frac{1}{v^2} - \frac{1}{v_l^2}}{\frac{1}{v_s^2} - \frac{1}{v_l^2}}. \tag{A.32}$$

The application of Equation (A.32) assumes that droplets exist either fully liquid or fully solid at the measurement timescale (no partially solid droplets), which is a standard assumption in this context (Pinfield et al. (1995)).

A.5.3 Optimization of measurement setting

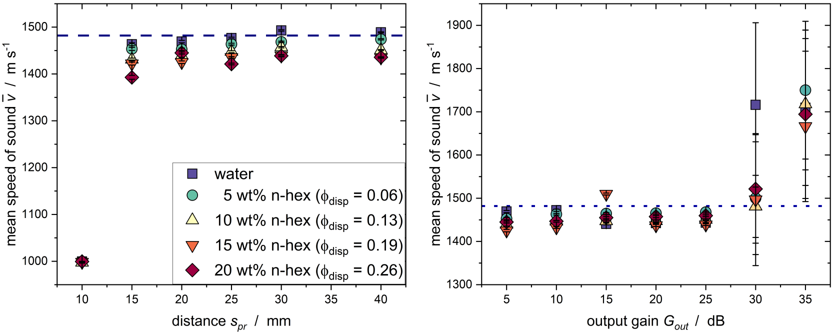

(a) Distance probe reflection plate.

(b) Gain of output signal.

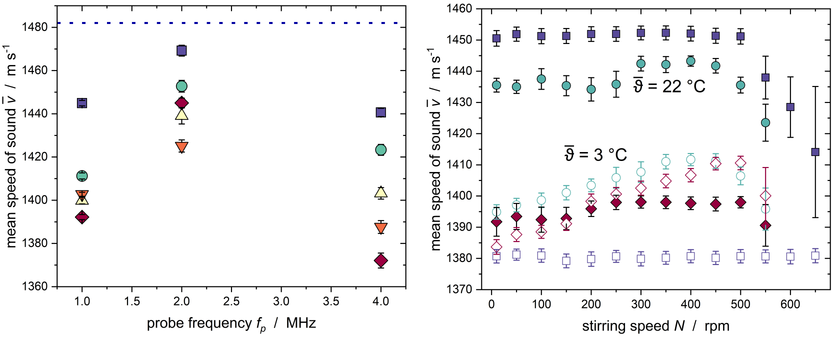

(c) Probe frequency.

(d) Stirring Speed — emulsion and suspension.

Figure A.24: Speed of sound for various measurement parameters of the ultrasound probe determined in the stirred vessel. The dashed blue line represents the speed of sound of water at $\vartheta = 20$°C.

A transmit and receive gain of 5 dB, a propagation path of 20 mm, and a 2 MHz transducer were selected because this configuration yielded the most stable signals and the closest agreement between measured transit times in water and literature values ($\upsilon \approx 1480\ \mathrm{m\,s^{-1}}$; McClements (1988, 1991)). The same settings were applied consistently to all measurements in the stirred vessel.

Transducer frequency (2 MHz). This frequency provides a practical compromise between time resolution and attenuation in liquids: absorption typically scales as f^2, while Rayleigh-limit scattering scales as f^4 (McClements (1991, 1992)). In water, the wavelength is $\lambda \approx v/f \approx 0.74\,\mathrm{mm}$; the droplet diameters used in this work (e.g., $x_{3,2}$ in the few-μm range) are orders of magnitude smaller than λ. Scattering is therefore negligible, and effective-medium relations are applicable (Urick (1947), McClements (1991)).

Propagation path (20 mm). The path length is long enough to separate the first echo clearly from the transducer ring-down (two-way time $\approx 40\,\mathrm{mm}/1480\,\mathrm{m\,s^{-1}}$ $\approx 27\,\mu$s in water), yet short enough to keep attenuation and multiple reflections moderate, enabling robust time-of-flight evaluation.

Transit and receive gain (5 dB). A low, constant electronic gain keeps the system in the linear regime (avoiding clipping and nonlinearities) while delivering sufficient signal-to-noise ratio for reproducible transit times and exponential attenuation fits, improving comparability across samples.

Empirical check. Under these conditions, the measured sound speeds in water matched the literature most closely; therefore, the configuration was retained for all emulsion measurements with varying dispersed phase content.

A.6 Emulsion I and II

Table A.8: Concentration of surfactant molecules that can be found in the complete emulsion system as well as in the micelles, calculated according to Equation 1.4 and 1.5.

Emulsion	$\tilde{c}_{\mathrm{TW20,em}}$	$\tilde{c}_{\mathrm{TW20,mic}}$	$\tilde{c}^{aq}/cmc$
I	4	3.9	68
	8	7.9	136
	16	15.9	271
	24	24	407
II	7.5	7.2	127
	15.6	15.5	264

A.7 Surfactant information

Table A.9: Chemical and trade name as well as supplier of the nonionic surfactants used in this work.

Abbreviation Trade names	TW20 Tween® 20	TW60 Tween® 60	TW80 Tween® 80
Chemical name (IUPAC)	Polyoxyethylen(20)-sorbitan-monolaurat	Polyoxyethylen(20)-sorbitan-monostearat	Polyoxyethylen(20)-sorbitan-monooleat
Supplier	Merck KGaA, Darmstadt, Germany	Merck KGaA, Darmstadt, Germany	Merck KGaA, Darmstadt, Germany

Table A.10: Chemical and trade name as well as supplier of the ionic surfactants used in this work.

Abbreviation	SDS	CTAB
Chemical name (IUPAC)	Sodium dodecyl sulfate	Cetrimonium bromide
Purity	> 99%	> 95%
Supplier	Carl Roth®, Karlsruhe, Germany	Carl Roth®, Karlsruhe, Germany

Table A.11: Relevant parameters of the nonionic surfactants.

Abbreviation	TW20	TW60	TW80
$\tilde{M}$ / g mol^{-1}	1237.54	1311.7	1310
Γ_{max} / mol m^{-2}	$3.62 \cdot 10^{-6}$	$1.24 \cdot 10^{-6}$	$2.13 \cdot 10^{-6}$
cmc / mol m^{-3}	$5.9 \cdot 10^{-2}$	$2.09 \cdot 10^{-2}$	$1.05 \cdot 10^{-2}$
HLB	16.7	14.9	15
d_{mic} / nm	5.4	4.48	4.36
$a_{\mathrm{sm,mic}}$	31	24	22
L_{tail} / C atoms	12	18	18
ϑ_{m} / °C	-32	45	-25

Table A.12: Relevant parameters of the ionic surfactants.

Abbreviation	SDS	CTAB
$\tilde{M}$ / g mol^{-1}	288.38	364.38
Γ_{max} / mol m^{-2}	$3 \cdot 10^{-6}$	$3.8 \cdot 10^{-6}$
cmc / mol m^{-3}	8.5	0.9
HLB	8.5	0.9
d_{mic} / nm	4.8	5
a_{mic}	58	81
L_{tail} / C atoms	12	16
ϑ_{m} / °C	204	250

List of Figures

1.1 Melt emulsification process. 2
1.2 Instability of dispersions. 3
1.3 Free enthalpy as a function of cluster radius. 4
1.4 Nucleation mechanisms in melt emulsions. 6
1.5 Illustration of surfactant species appearing in emulsions with a (semi) crystalline dispersed phase. 9
1.6 Contact between droplets and/or particles. 12
2.1 Time-resolved CMN in microfluidic channel. 16
2.2 Mechanisms of collision between droplets and particles. 16
2.3 Experimental plan. 27
3.1 Working hypothesis microfluidic. 30
3.2 Micorfluidic chip with the tempering plate. 31
3.3 Experimental microfluidic setup. 33
3.4 Droplet formation in microfluidic setup. 33
3.5 Microfluidic procedure to investigate CMN. 34
3.6 Temperature profile to investigate CMN in the microfluidic setup. 35
3.7 Temperature distribution in the microchip. 35
3.8 Roughness within the microfluidic channel as observed by optical microscopy. Adapted from Kaysan (2023), CC BY 4.0. . 37
3.9 Simulated interaction energies for two spherical droplets. 41
3.10 TW20 distribution between water and n-hexadecane in emulsions. 44
3.11 Long term TW20 distribution between water and n-hexadecane. . 46
3.12 Steps for successful CMN. 49
3.13 Impact of surfactant concentration added to the continuous aqueous phase and surfactant charge on the CMN. 51
3.14 Impact of nonionic surfactant concentration added to the continuous aqueous phase and surfactant charge on the CMN. 52

3.15 Probability of CMN when surfactant was initially dissolved in water. 55
3.16 Impact of dissolving the surfactant in the dispersed phase. 57
3.17 Bridge diameters in microfluidic experiments. 57
3.18 Integration of the pressure sensor in the microfluidic setup. . . . 60
3.19 Experimental and simulated differential pressure values obtained for the rectangular microfluidic channel with pure water. . 62
3.20 Moody diagram. 63
3.21 Experimental results for Δp when a solid particle is placed in the minichannel. 64
3.22 Experimental results for Δp when a liquid droplet is in the minichannel. 65
3.23 The pressure drop as a function of time during the stages of CMN in the microfluidic setup. 66
3.24 Calculated forces F_{nuc} and F_{ip} (Kaysan et al. (2023b)). 69
3.25 Calculated $F_{\mathrm{CMN,min}}$. 70
4.1 Working hypothesis TCR. 75
4.2 Characteristics of a typical n-hexadecane-in-water emulsion used in this work. 77
4.3 Details of the TCR setup used in the 200 MHz spectrometer. Panels (c) and (d) reproduced from Kaysan et al. (2022c), CC BY 4.0. 78
4.4 Temperature profile TCR. 80
4.5 ^{1}H spectrum of an n-hexadecane-in-water emulsion. 81
4.6 Setup of the Taylor-Couette cell in the 300 MHz spectrometer with outer moving cylinder. 82
4.7 Description and validation of the velocity distribution in the gap of the TCR with inner rotating cylinder (Kaysan et al. (2022c)). 85
4.8 Primary nucleation investigation. 90
4.9 Impact of shear on CMN in laminar Couette flow. 91
4.10 Kinetic factors for different shear rates in the TCR. 92
4.11 Comparison of collision rates in emulsions. 95
4.12 Impact of h_{coll} on the CMN. 96
4.13 Impact of surfactant concentration on CMN. 98
4.14 Flow simulations between two particles. 99

5.1 Working hypothesis stirred vessel. 104
5.2 Stirred vessel — Drawing and photo of the experimental setup. . 105
5.3 Droplet size distribution of the two emulsions used in the stirred vessel. 107
5.4 Microscopic images of Emulsion I (left) and Emulsion II (right). Adapted from Kaysan et al. (2023a), CC BY 4.0. 108
5.5 Ultrasonic transmitting and response signals. 109
5.6 Hysteresis diagram of a time-resolved crystallization and thawing process of the dispersed phase of an n-hexadecane-in-water emulsion. 110
5.7 Performance characteristic for a stirred vessel equipped with a Rushton turbine and four baffles according to Rushton et al. (1950). 112
5.8 Theoretically calculated shear rates in the stirred vessel and the corresponding k_{CMN} determined for a constant supercooling. 120
5.9 Comparison of J_{CMN} and λ_{CMN} for the crystallization experiments in the stirred vessel and the TCR. 121
5.10 Temporal evolution of the solid fraction of the dispersed phase in Emulsion I. 123
5.11 Comparison of experimental results with simulated data for only primary nucleation. 125
5.12 Comparison of single exponential with Weibull fit. ξ was fitted as soon as the temperature was constant (ΔT = 15.2 K). . . 127
5.13 Nucleation rates of Emulsion I as a function of energy dissipation, determined with the Weibull model. 128
5.14 Nucleation rates of Emulsion I and II as a function of energy dissipation, determined with the Weibull model. 130
5.15 Increasing solid fraction of the dispersed phase over time. 131
5.16 Nucleation rates and corresponding shape parameters at three times during the crystallization of the dispersed phase. 132
5.17 Overview about the nucleation rates and shape parameters for all tested parameters. 133
5.18 Comparison of J_{CMN} for all setups. 135
6.1 Summary of main findings. 137

A.1 Experimental data for the density and viscosity of binary TW20-water mixtures. 144
A.2 Experimental data for the density and viscosity of binary TW20-n-hexadecane mixtures. 144
A.3 Exemplary dynamic viscosity and shear stress of an emulsion and a suspension. 145
A.4 Schematic of a pendant/rising droplet. 146
A.5 Interfacial tensions for TW20. 148
A.6 ^{1}H spectra of the n-hexadeacne-in-water emulsion and pure TW20. 152
A.7 Liquid state ^{1}H spectrum of an n-hexadecane-in-water emulsion stabilized with 5 wt% TW20. 153
A.8 Concentration calibration NMR. 153
A.9 Temperature calibration for NMR measurements. 154
A.10 Pulse sequences for the RheoNMR measurements at 300 MHz and 200 MHz. 156
A.11 Induction times without surfactant. 160
A.12 Experimental raw data for TW20. 160
A.13 Experimental raw data for TW60. 161
A.14 Experimental raw data for TW80. 161
A.15 Experimental raw data for SDS. 162
A.16 Experimental raw data for CTAB. 162
A.17 Induction time as a function of relative velocity. 163
A.18 Droplet hugging particle. 164
A.19 Mesh used for simulations. 166
A.20 Schematic illustration of the particle in the minichannel. 167
A.21 Influence of droplet body length on Δp. 168
A.22 Parameter study CFD — Particle in minichannel. 169
A.23 Dependency of u_u on Δp. 170
A.24 Speed of sound for various measurement parameters of the ultrasound probe determined in the stirred vessel. 175

List of Tables

3.1 The parameters for calculation of the total interaction energy E. 42

3.2 The characteristics of the factors that determine the effectiveness of CMN in agitated systems are compared with the parameters studied in the microfluidic system. 47

5.1 Dimensions of the stirred vessel and the stirring element with specifications according to Deutsches Institution fuer Normung (1992). 106

5.2 Overview of various equations for calculating mean and maximum apparent shear rate in turbulent stirred tanks. 119

A.1 Parameters used for the calculations in this work. 143

A.2 Interfacial tensions measured for TW20 dissolved either in the aqueous or n-hexadecane phase. 148

A.3 relevant material properties of GreenTEC. 154

A.4 MRI measurement parameters. 155

A.5 NMR spectroscopy parameters. 156

A.6 Dimensionless numbers characterizing the flow in the microfluidic channel. 164

A.7 Simulated differential pressure in the minichannel filled with water only for three different cell sizes. 165

A.8 Concentration of surfactant molecules that can be found in the complete emulsion system as well as in the micelles, calculated according to Equation 1.4 and 1.5. 177

A.9 Chemical and trade name as well as supplier of the nonionic surfactants used in this work. 178

A.10 Chemical and trade name as well as supplier of the ionic surfactants used in this work. 178

A.11 Relevant parameters of the nonionic surfactants. 179

A.12 Relevant parameters of the ionic surfactants. 179

List of Publications

Journal articles

M. Hoffmann, C. Iacob, G. Kaysan, M. Simmler, H. Nirschl, G. Guthausen, and M. Wilhelm. Charge Transport and Glassy Dynamics in Blends Based on 1-Butyl-3-vinylbenzylimidazolium Bis(trifluoromethanesulfonyl)imide Ionic Liquid and the Corresponding Polymer. *Polymers*, 14(12):2423, 2022. doi: 10.3390/polym14122423.

G. Kaysan, B. Spiegel, G. Guthausen, and M. Kind. Influence of Shear Flow on the Crystallization of Organic Melt Emulsions – A Rheo–Nuclear Magnetic Resonance Investigation. *Chem. Eng. Technol.*, 43(9):1699–1705, 2020. doi: 10.1002/ceat.202000193.

G. Kaysan, A. Rica, G. Guthausen, and M. Kind. Contact-Mediated Nucleation of Subcooled Droplets in Melt Emulsions: A Microfluidic Approach. *Crystals*, 11(12):1471, 2021. doi: 10.3390/cryst11121471.

G. Kaysan, R. Kräling, M. Meier, H. Nirschl, G. Guthausen, and M. Kind. Investigation of the surfactant distribution in oil-in-water emulsions during the crystallization of the dispersed phase via nuclear magnetic resonance relaxometry and diffusometry. *Magn Reson Chem*, 60(12):1131–1147, 2022a. doi: 10.1002/mrc.5305.

G. Kaysan, J. Reiner, H. P. Karbstein, and M. Kind. Einfluss von Wachspartikeln auf die Kristallisation und die Stabilität von Schmelzemulsionen. *SOFW Journal (German version)*, 148(11):28–33, 2022b.

G. Kaysan, J. Reiner, H. P. Karbstein, and M. Kind. Impact of Wax Particles on Crystallization and Stability of Melt Emulsions. *SOFW Journal (German version)*, 148(11):26–31, 2022c.

G. Kaysan, T. Rudszuck, L. Trapp, R. Balbierer, M. Kind, and G. Guthausen. Recent applications of NMR diffusion experiments. volume 107 of *Annual Reports on NMR Spectroscopy*, pages 47–93. Elsevier, 2022d. ISBN 978-0-323-98873-5. doi: 10.1016/bs.arnmr.2022.07.003.

G. Kaysan, N. Schork, S. Herberger, G. Guthausen, and M. Kind. Contact-mediated nucleation in melt emulsions investigated by rheo-nuclear magnetic resonance. *Magn Reson Chem*, 60(7):615–627, 2022e. doi: 10.1002/mrc.5228.

G. Kaysan, L. Elmlinger, and M. Kind. Increasing the Efficiency of Emulsion Crystallization in Stirred Vessels by Targeted Application of Shear and Surfactant. *Colloids Interfaces*, 7(4):68, 2023a. ISSN 2504-5377. doi: 10.3390/colloids7040068.

G. Kaysan, T. Hirsch, K. Dubil, and M. Kind. A Microfluidic Approach to Investigate the Contact Force Needed for Successful Contact-Mediated Nucleation. *Colloids Interfaces*, 7(1):12, 2023b. ISSN 2504-5377. doi: 10.3390/colloids7010012.

Conference contributions

G. Kaysan. Influence of flow on the crystallization of organic melt emulsions: Poster, March 2019a.

G. Kaysan. Investigation of the influence of shear stress on the crystallization of organic melt emulsions via Rheo-NMR: Talk, January 2019b.

G. Kaysan. Investigation of collision-induced nucleation in the stirred tank by means of ultrasound: Talk, 2020.

G. Kaysan. Characterization of emulsifier properties during crystallization of the disperse phase of organic emulsions by NMR diffusometry and relaxometry: Talk, March 2021a.

G. Kaysan. Contact-mediated nucleation - Investigation of inoculation efficiency in the microfluidic channel: Talk, March 2021b.

G. Kaysan. Contact-mediated nucleation in melt emulsions investigated by rheo-nuclear magnetic resonance: Talk, October 2021c.

G. Kaysan. Contact-Mediated Nucleation in Emulsion Crystallization – Influence of Emulsifier Charge and Emulsifier Concentration: Talk, March 2022a.

G. Kaysan. Possibilities and limitations of secondary contact nucleation of subcooled melt emulsions: A microfluidic approach: Talk, September 2022b.

G. Kaysan. Contact-Mediated Nucleation – A Possibility to Make the Crystallization of Melt Emulsions more Efficient and Sustainable: Poster, March 2023a.

G. Kaysan. On the Control and Economic Optimization of the Crystallization of Melt Emulsions: Talk, May 2023b.

G. Kaysan. Secondary Nucleation Scale-Up for Stirred Vessels: Talk, September 2023c.

Bibliography

S. Abramov, A. Berndt, K. Georgieva, P. Ruppik, and H. P. Karbstein. Investigation of the influence of mean droplet size and shear rate on crystallization behavior of hexadecane-in-water dispersions. *Colloids Surf A Physicochem Eng Asp*, 529:513–522, 2017. doi: 10.1016/j.colsurfa.2017.06.029.

B. J. Adzima and S. S. Velankar. Pressure drops for droplet flows in microfluidic channels. *J Micromech Microeng*, 16(8):1504–1510, 2006. ISSN 0960-1317. doi: 10.1088/0960-1317/16/8/010.

S. G. Agrawal and A. H. J. Paterson. Secondary Nucleation: Mechanisms and Models. *Chem Eng Commun*, 202(5):698–706, 2015. ISSN 0098-6445. doi: 10.1080/00986445.2014.969369.

R. N. Al-kaby, J. S. Jayaratne, T. I. Brox, S. L. Codd, J. D. Seymour, and J. R. Brown. Rheo-NMR of transient and steady state shear banding under shear startup. *J Rheol*, 62(5):1125–1134, 2018. doi: 10.1122/1.5037594.

A. J. Almeida and E. Souto. Solid lipid nanoparticles as a drug delivery system for peptides and proteins. *Adv Drug Deliv Rev*, 59(6):478–490, 2007. doi: 10.1016/j.addr.2007.04.007.

C. Ammann, P. Meier, and A. E. Merbach. A Simple Multinuclear NMR Thermometer. *J Magn Reson*, 46:319–321, 1982.

C. D. Andereck, S. S. Liu, and H. L. Swinney. Flow regimes in a circular Couette system with independently rotating cylinders. *J Fluid Mech*, 164 (-1):155, 1986. doi: 10.1017/S0022112086002513.

T. Awad and K. Sato. Acceleration of crystallisation of palm kernel oil in oil-in-water emulsion by hydrophobic emulsifier additives. *Colloids Surf B Biointerfaces*, 25(1):45–53, 2002. ISSN 09277765. doi: 10.1016/S0927-7765(01)00298-3.

T. Awad, H. A. Moharram, O. E. Shaltout, D. Asker, and M. M. Youssef. Applications of ultrasound in analysis, processing and quality control of food: A review. *Food Res Int*, 48(2):410–427, 2012. doi: 10.1016/j.foodres.2012.05.004.

W. D. Bancroft. The Theory of Emulsification, V. *J Phys Chem*, 17(6):501–519, 1913. doi: 10.1021/j150141a002.

C. N. Baroud, F. Gallaire, and R. Dangla. Dynamics of microfluidic droplets. *Lab Chip*, 10(16):2032–2045, 2010. doi: 10.1039/C001191F.

E. S. Basheva, P. A. Kralchevsky, K. D. Danov, K. P. Ananthapadmanabhan, and A. Lips. The colloid structural forces as a tool for particle characterization and control of dispersion stability. *Phys Chem Chem Phys*, 9(38):5183–5198, 2007. doi: 10.1039/B705758J.

G. K. Batchelor. Diffusion in a field of homogeneous turbulence. *Math. Proc. Camb. Philos. Soc.*, 48(2):345–362, 1952. ISSN 0305-0041. doi: 10.1017/S0305004100027687.

R. Becker and W. Döring. Kinetische Behandlung der Keimbildung in übersättigten Dämpfen. *Ann. Phys. (Berl.)*, 416(8):719–752, 1935. ISSN 00033804. doi: 10.1002/andp.19354160806.

B. J. Bentley and L. G. Leal. An experimental investigation of drop deformation and breakup in steady, two-dimensional linear flows. *J. Fluid Mech.*, 167 (-1):241, 1986. doi: 10.1017/S0022112086002811.

B. Bera, R. Khazal, and K. Schroën. Coalescence Dynamics in Oil-In-Water Emulsions at Elevated Temperatures. *Sci Rep*, 10990(11), 2021. doi: 10.21203/rs.3.rs-135048/v1.

K. Boode and P. Walstra. Partial coalescence in oil-in-water emulsions 1. Nature of the aggregation. *Colloids Surf A Physicochem Eng Asp*, 81:121–137, 1993. ISSN 09277757. doi: 10.1016/0927-7757(93)80239-B.

Bowen (Jr), R. L. Unraveling the mysteries of shear-sensitive mixing systems. *Chem. Eng.*, 93(11):55–63, 1986.

B. J. Briscoe, C. J. Lawrence, and W. G. P. Mietus. A review of immiscible fluid mixing. *Adv. Colloid Interface Sci.*, 81(1):1–17, 1999. doi: 10.1016/S0001-8686(99)00002-0.

J. R. Brown and P. T. Callaghan. Changing micellar order, lever rule behavior and spatio-temporal dynamics in shear-banding at the onset of the stress plateau. *Soft Matter*, 7(21):10472, 2011. ISSN 1744-683X. doi: 10.1039/C1SM06135F.

T. I. Brox, B. Douglass, P. Galvosas, and J. R. Brown. Observations of the influence of Taylor-Couette geometry on the onset of shear-banding in surfactant wormlike micelles. *J. Rheol.*, 60(5):973–982, 2016. ISSN 0148-6055. doi: 10.1122/1.4961478.

A. Bąk and W. Podgórska. Interfacial and surface tensions of toluene/water and air/water systems with nonionic surfactants Tween 20 and Tween 80. *Colloids Surf A Physicochem Eng Asp*, 504:414–425, 2016. doi: 10.1016/j.colsurfa.2016.05.091.

P. T. Callaghan. Rheo-NMR and velocity imaging. *Curr Opin Colloid Interface Sci*, 11(1):13–18, 2006. doi: 10.1016/j.cocis.2005.10.003.

H. B. Callen. *Thermodynamics And An Introduction To Thermostatics*. John Wiley & Sons, New York, NY, USA, 1985. ISBN 978-0-471-86256-7.

D. Y. C. Chan and R. G. Horn. The drainage of thin liquid films between solid surfaces. *J. Chem. Phys.*, 83(10):5311–5324, 1985. doi: 10.1063/1.449693.

D. C. Chappelear. Models of a liquid drop approaching an interface. *J. Colloid Sci.*, 16(2):186–190, 1961. doi: 10.1016/0095-8522(61)90017-4.

J.-D. Chen, P. S. Hahn, and J. C. Slattery. Coalescence time for a small drop or bubble at a fluid-fluid interface. *AIChE J.*, 30(4):622–630, 1984. doi: 10.1002/aic.690300413.

J. Cheon, F. Haji, J. Baek, Q. Wang, and K. C. Tam. Pickering emulsions for functional food systems. *J. Agric. Food Res.*, 11:100510, March 2023. ISSN 26661543. doi: 10.1016/j.jafr.2023.100510.

A. A. Chesters. The modelling of coalescence processes in fluid-liquid dispersions: a review of current understanding. *Chem Eng Res Des*, 69(4):259–227, 1991. ISSN 02638762.

A. K. Chesters and I. B. Bazhlekov. Effect of Insoluble Surfactants on Drainage and Rupture of a Film between Drops Interacting under a Constant Force. *J. Colloid Interface Sci.*, 230(2):229–243, 2000. doi: 10.1006/jcis.2000.7074.

N. C. Christov, K. D. Danov, Y. Zeng, P. A. Kralchevsky, and R. von Klitzing. Oscillatory structural forces due to nonionic surfactant micelles: data by colloidal-probe AFM vs theory. *Langmuir*, 26(2):915–923, 2010. ISSN 0743-7463. doi: 10.1021/la902397w.

J. A. Cole. Taylor-vortex instability and annulus-length effects. *J. Fluid Mech.*, 75(1):1–15, 1976. doi: 10.1017/S0022112076000098.

C. A. Coulaloglou and L. L. Tavlarides. Description of interaction processes in agitated liquid-liquid dispersions. *Chem. Eng. Sci.*, 32(11):1289–1297, 1977. doi: 10.1016/0009-2509(77)85023-9.

M. Cross and H. Greenside. *Pattern Formation and Dynamics in Nonequilibrium Systems*. Cambridge University Press, 2012. ISBN 978-0-521-77935-7. doi: 10.1017/CBO9780511627200.

O. Czarny, E. Serre, P. Bontoux, and R. M. Lueptow. Spiral and Wavy Vortex Flows in Short Counter-Rotating Taylor-Couette Cells. *Theor Comput Fluid Dyn*, 16(1):5–15, 2002. ISSN 0935-4964. doi: 10.1007/s00162-002-0070-0.

R. J. Davey, A. M. Hilton, J. Garside, M. de La Fuente, M. Edmondson, and P. Rainsford. Crystallisation of oil-in-water emulsions. Amphiphile directed nucleation in aqueous emulsions of m-chloronitrobenzene. *J. Chem. Soc. Faraday Trans.*, 92(11):1927, 1996. ISSN 0956-5000. doi: 10.1039/FT9969201927.

R. J. Davey, A. M. Hilton, and J. Garside. Crystallization from Oil in Water Emulsions. *Chem Eng Res Des*, 75(2):245–251, 1997. ISSN 02638762. doi: 10.1205/026387697523525.

R. H. Davis, J. A. Schonberg, and J. M. Rallison. The lubrication force between two viscous drops. *Physics of Fluids A: Fluid Dynamics*, 1(1):77–81, 1989. ISSN 0899-8213. doi: 10.1063/1.857525.

M. Delgado, A. Lázaro, J. Mazo, and B. Zalba. Review on phase change material emulsions and microencapsulated phase change material slurries: Materials, heat transfer studies and applications. *Renew. Sustain. Energy Rev.*, 16(1): 253–273, 2012. ISSN 13640321. doi: 10.1016/j.rser.2011.07.152.

B. Derjaguin and L. Landau. Theory of the stability of strongly charged lyophobic sols and of the adhesion of strongly charged particles in solutions of electrolytes. *Prog. Surf. Sci.*, 43(1-4):30–59, 1993. ISSN 00796816. doi: 10.1016/0079-6816(93)90013-L.

Deutsches Institution fuer Normung. Agitators and baffles for agitator vessels; types, terms and main dimensions, sep 1992. Edition: DIN 28131 Bereichtigung 1 (2018-11) Issue: 28131.

E. Dickinson. Colloids in Food: Ingredients, Structure, and Stability. *Annu. Rev. Food Sci. Technol.*, 6(1):211–233, April 2015. ISSN 1941-1413, 1941-1421. doi: 10.1146/annurev-food-022814-015651.

E. Dickinson, F.-J. Kruizenga, M. J. W. Povey, and M. van der Molen. Crystallization in oil-in-water emulsions containing liquid and solid droplets. *Colloids Surf A Physicochem Eng Asp*, 81:273–279, 1993. doi: 10.1016/0927-7757(93)80255-D.

E. Dickinson, J. Ma, and M. J. W. Povey. Crystallization kinetics in oil-in-water emulsions containing a mixture of solid and liquid droplets. *J. Chem. Soc. Faraday Trans.*, 92(7):1213, 1996. ISSN 0956-5000. doi: 10.1039/FT9969201213.

T. D. Dimitrova and F. Leal-Calderon. Forces between Emulsion Droplets Stabilized with Tween 20 and Proteins. *Langmuir*, 15(26):8813–8821, 1999. ISSN 0743-7463. doi: 10.1021/la9904758.

L. Doubliez. The drainage and rupture of a non-foaming liquid film formed upon bubble impact with a free surface. *Int. J. Multiphase Flow*, 17(6):783–803, 1991. doi: 10.1016/0301-9322(91)90056-9.

M. Dudek, D. Fernandes, E. Helno Herø, and G. Øye. Microfluidic method for determining drop-drop coalescence and contact times in flow. *Colloids Surf A Physicochem Eng Asp*, 586:124265, 2020. doi: 10.1016/j.colsurfa.2019.124265.

P. C. Duineveld. *Bouncing and coalescence of two bubbles in water*. University of Twente, 1994.

T. El Rhafiki, T. Kousksou, A. Jamil, S. Jegadheeswaran, S. D. Pohekar, and Y. Zeraouli. Crystallization of PCMs inside an emulsion: Supercooling phenomenon. *Sol. Energy Mater. Sol. Cells*, 95(9):2588–2597, 2011. ISSN 09270248. doi: 10.1016/j.solmat.2011.03.027.

R. Elfgen, O. Hollóczki, and B. Kirchner. A Molecular Level Understanding of Template Effects in Ionic Liquids. *Acc. Chem. Res.*, 50(12):2949–2957, 2017. ISSN 0001-4842. doi: 10.1021/acs.accounts.7b00436.

A. Esser and S. Grossmann. Analytic expression for Taylor–Couette stability boundary. *Phys. Fluids*, 8(7):1814–1819, 1996. doi: 10.1063/1.868963.

S. Friberg, K. Larsson, and J. Sjöblom. *Food emulsions*, volume 132 of *Food science and technology*. Marcel Dekker, New York, 4., ed. rev. and expanded. edition, 2004. ISBN 0-8247-4696-1.

S. K. Friedlander. *Smoke, dust, and haze: Fundamentals of aerosol dynamics*. Topics in chemical engineering. Oxford Univ. Pr, New York, NY u.a., 2. ed. edition, 2000. ISBN 0-19-512999-7.

N. Fuchs. Ueber die Stabilitaet und Aufladung der Aerosole. *Z. Phys.*, 89 (11-12):736–743, 1934. ISSN 1434-6001. doi: 10.1007/BF01341386.

M. J. Fuerstman, A. Lai, M. E. Thurlow, S. S. Shevkoplyas, H. A. Stone, and George M. Whitesides. The pressure drop along rectangular microchannels containing bubbles. *Lab Chip*, 7(11):1479–1489, 2007. doi: 10.1039/b706549c.

T. Försters and W. von Rybinsky. Applications of Emulsions. In B. P. Binks, editor, *Modern Aspects of Emulsion Science*. The Royal Society of Chemistry, 1998. ISBN 978-0-85404-439-9.

D. Gabriele, M. Migliori, R. Di Sanzo, C. O. Rossi, S. A. Ruffolo, and B. de Cindio. Characterisation of dairy emulsions by NMR and rheological techniques. *Food Hydrocoll.*, 23(3):619–628, 2009. ISSN 0268005X. doi: 10.1016/j.foodhyd.2008.05.002.

P. Garstecki, M. J. Fuerstman, H. A. Stone, and G. M. Whitesides. Formation of droplets and bubbles in a microfluidic T-junction-scaling and mechanism of break-up. *Lab Chip*, 6(3):437–446, 2006. doi: 10.1039/B510841A.

R. K. Geisler. *Fluiddynamik und Leistungseintrag in turbulent gerührten Suspensionen.* Dissertation, TU Munich, Munich, 1991.

A. J. Ghajar, C. C. Tang, and W. L. Cook. Experimental Investigation of Friction Factor in the Transition Region for Water Flow in Minitubes and Microtubes. *Heat Transf. Eng.*, 31(8):646–657, 2010. ISSN 0145-7632. doi: 10.1080/01457630903466613.

G.L. Zou, Z.C. Tan, X.Z. Lan, L.X. Sun, and T. Zhang. Preparation and characterization of microencapsulated hexadecane used for thermal energy storage. *Chin. Chem. Lett*, 15(6):729–732, 2004. ISSN 1001-8417.

D. Gloss and H. Herwig. Microchannel Roughness Effects: A Close-Up View. *Heat Transf. Eng.*, 30(1-2):62–69, 2009. ISSN 0145-7632. doi: 10.1080/01457630802293415.

J. A. González, M. Zawadzki, and U. Domanska. Thermodynamics of mixtures containing polycyclic aromatic hydrocarbons. *J Mol Liq*, 143(2-3):134–140, 2008. ISSN 01677322. doi: 10.1016/j.molliq.2008.07.005.

A. Gottwald, P. Kuran, and U. Scheler. Separation of velocity distribution and diffusion using PFG NMR. *J. Magn. Reson.*, 162(2):364–370, 2003. doi: 10.1016/s1090-7807(03)00130-7.

H. P. Grace. Dispersion Phenomena in High Viscosity Immiscible Fluid Systems and Applications of Static Mixers as Dispersion Devices in such Systems. *Chem Eng Commun*, 14(3-6):225–277, 1982. ISSN 0098-6445. doi: 10.1080/00986448208911047.

G. Grange, A. Lévis, and B. Mutaftschiev. Solidification of stearic acid—water and laurone—water emulsions: Role of the droplet—medium interface on nucleation kinetics. *J. Colloid Interface Sci.*, 109(2):542–551, 1986. ISSN 00219797. doi: 10.1016/0021-9797(86)90335-8.

E. Grimsehl. *Lehrbuch der Physik: Band 1 Mechanik, Akustik, Wärmelehre*. Vieweg+Teubner Verlag, 1977. ISBN 978-3-663-05733-8.

E. Günther, T. Schmid, H. Mehling, S. Hiebler, and L. Huang. Subcooling in hexadecane emulsions. *Int J Refrig*, 33(8):1605–1611, 2010. ISSN 0140-7007. doi: 10.1016/j.ijrefrig.2010.07.022.

M. U. Hammer, T. H. Anderson, A. Chaimovich, M. S. Shell, and J. Israelachvili. The search for the hydrophobic force law. *Faraday Discuss.*, 146:299–308; discussion 367–93, 395–401, 2010. ISSN 1359-6640. doi: 10.1039/b926184b.

A. D. Hanlon, S. J. Gibbs, L. D. Hall, D. E. Haycock, W. J. Frith, and S. Ablett. Rapid MRI and velocimetry of cylindrical Couette flow. *Magn Reson Imaging*, 16(8):953–961, 1998a. ISSN 0730-725X. doi: 10.1016/s0730-725x(98)00089-7.

A. D. Hanlon, S. J. Gibbs, L. D. Hall, D. E. Haycock, W. J. Frith, S. Ablett, and C. Marriott. A concentric cylinder Couette flow system for use in magnetic resonance imaging experiments. *Meas Sci Technol*, 9(4):631–637, 1998b. ISSN 0957-0233. doi: 10.1088/0957-0233/9/4/011.

C. M. Hansen. *Hansen solubility parameters: a user's handbook*. CRC Press, Boca Raton, Florida, US, 2007. ISBN 978-0-8493-7248-3.

M. D. Hanwell, D. E. Curtis, D. C. Lonie, T. Vandermeersch, E. Zurek, and G. R. Hutchison. Avogadro: an advanced semantic chemical editor, visualization, and analysis platform. *J. Cheminform*, 4(1):17, 2012. doi: 10.1186/1758-2946-4-17.

R. W. Hartel. *Crystallization in foods*. Aspen food engineering series. Aspen Publ, Gaithersburg, Md., 2001. ISBN 0-8342-1634-5.

A. Hasseine, A.–H. Meniai, M. B. Lehocine, and H.–J. Bart. Assessment of Drop Coalescence and Breakup for Stirred Extraction Columns. *Chem Eng Technol*, 28(5):552–560, 2005. ISSN 0930-7516. doi: 10.1002/ceat.200407147.

A. L. Hazel and M. Heil. The steady propagation of a semi-infinite bubble into a tube of elliptical or rectangular cross-section. *J. Fluid Mech.*, 470:91–114, 2002. doi: 10.1017/S0022112002001830.

H. J. Henzler and J. Kauling. Scale-up of mass transfer inhighly viscous liquids. *Wurzberg, Germany. BHRA, Cranfield. p*, pages 303–312, 1985.

A. B. Herhold, D. Ertaş, A. J. Levine, and H. E. King. Impurity mediated nucleation in hexadecane-in-water emulsions. *Phys. Rev. E*, 59(6):6946–6955, 1999. doi: 10.1103/PhysRevE.59.6946.

S. A. Hindle, M. J. W. Povey, and K. Smith. Kinetics of Crystallization in n-Hexadecane and Cocoa Butter Oil-in-Water Emulsions Accounting for Droplet Collision-Mediated Nucleation. *J. Colloid Interface Sci.*, 232(2): 370–380, 2000. doi: 10.1006/jcis.2000.7174.

S. A. Hindle, M. J. W. Povey, and K. W. Smith. Characterizing cocoa butter seed crystals by the oil–in–water emulsion crystallization method. *J. Am. Oil Chem.' Soc.*, 79(10):993–1002, 2002. ISSN 1558-9331. doi: 10.1007/s11746-002-0593-4.

J. O. Hinze. Fundamentals of the hydrodynamic mechanism of splitting in dispersion processes. *AIChE J.*, 1(3):289–295, 1955. doi: 10.1002/aic.690010303.

T. D. Hodgson and D. R. Woods. The effect of surfactants on the coalescence of a drop at an interface. II. *J. Colloid Interface Sci.*, 30(4):429–446, 1969. doi: 10.1016/0021-9797(69)90414-7.

K. G. Hollingsworth and M. L. Johns. Rheo-nuclear magnetic resonance of emulsion systems. *J Rheol*, 48(4):787–803, 2004. doi: 10.1122/1.1753277.

J. Hong, Z. Wang, J. Li, Y. Xu, and H. Xin. Effect of Interface Structure and Behavior on the Fluid Flow Characteristics and Phase Interaction in the Petroleum Industry: State of the Art Review and Outlook. *Energy Fuels*, 37 (14):9914–9937, 2023. ISSN 0887-0624. doi: 10.1021/acs.energyfuels.3c00809.

W. J. Howarth. Measurement of coalescence frequency in an agitated tank. *AIChE J.*, 13(5):1007–1013, 1967. doi: 10.1002/aic.690130532.

J. N. Israelachvili. *Intermolecular and surface forces*. Academic Press, Burlington, MA, 3rd ed. edition, 2011. ISBN 978-0-12-375182-9.

J. J. M. Janssen, A. Boon, and W. G. M. Agterof. Influence of dynamic interfacial properties on droplet breakup in simple shear flow. *AIChE Journal*, 40(12): 1929–1939, 1994. ISSN 0001-1541. doi: 10.1002/aic.690401202.

J. M. H. Janssen and H. E. H. Meijer. Droplet breakup mechanisms: Stepwise equilibrium versus transient dispersion. *J. Rheol.*, 37(4):597–608, 1993. ISSN 0148-6055. doi: 10.1122/1.550385.

G. V. Jeffreys and G. A. Davies. Coalescence of Liquid Droplets and Liquid Dispersion. In *Recent Advances in Liquid–Liquid Extraction*, pages 495–584. Elsevier, 1971. doi: 10.1016/b978-0-08-015682-8.50018-3.

F. Jin, R. Balasubramaniam, and K. J. Stebe. Surfactant Adsorption to Spherical Particles: The Intrinsic Length Scale Governing the Shift from Diffusion to Kinetic-Controlled Mass Transfer. *J Adhes*, 80(9):773–796, 2004. ISSN 0021-8464. doi: 10.1080/00218460490480770.

F. Jousse, G. Lian, R. Janes, and J. Melrose. Compact model for multi-phase liquid-liquid flows in micro-fluidic devices. *Lab Chip*, 5(6):646–656, 2005. doi: 10.1039/B416666C.

S. G. Kandlikar and W. J. Grande. Evolution of Microchannel Flow Passages–Thermohydraulic Performance and Fabrication Technology. *Heat Transf. Eng.*, 24(1):3–17, 2003. ISSN 0145-7632. doi: 10.1080/01457630304040.

S. G. Kandlikar, S. Garimella, D. Li, S. Colin, and M. King, editors. *Heat Transfer and Fluid Flow in Minichannels and Microchannels*. Elsevier, London, 2006. ISBN 978-0-08-044527-4.

D. Kashchiev. *Nucleation*. Elsevier, 2000. ISBN 978-0-7506-4682-6. doi: 10.1016/B978-0-7506-4682-6.X5000-8.

D. Kashchiev, D. Clausse, and C. Jolivet-Dalmazzone. Crystallization and Critical Supercooling of Disperse Liquids. *J. Colloid Interface Sci.*, 165(1): 148–153, 1994. doi: 10.1006/jcis.1994.1215.

W. Kast, E. S. Gaddis, K.-E. Wirth, and J. Stichlmair. L1 Pressure Drop in Single Phase Flow. In VDI e.V., editor, *VDI Heat Atlas*, pages 1053–1116. Springer Berlin Heidelberg, Berlin, Heidelberg, 2010. ISBN 978-3-540-77876-9. doi: 10.1007/978-3-540-77877-6âĂŮ70.

K. Kataoka. Taylor vortices and instabilities in circular Couette flow. In N. P. Cheremisinoff, editor, *Encyclopedia of fluid mechanics: Flow phenomena and measurement*, volume 1, pages 236–274. Gulf Publishing Company, Houston, Texas, USA, 1986.

T. Katsuragi, N. Kaneko, and K. Sato. Effects of addition of hydrophobic sucrose fatty acid oligoesters on crystallization rates of n-hexadecane in oil-in-water emulsions. *Colloids Surf B Biointerfaces*, 20(3):229–237, 2001. doi: 10.1016/S0927-7765(00)00175-2.

G. Kaysan. Possibilities and limitations of secondary contact nucleation of subcooled melt emulsions: A microfluidic approach: Talk, September 2023.

G. Kaysan, B. Spiegel, G. Guthausen, and M. Kind. Influence of Shear Flow on the Crystallization of Organic Melt Emulsions – A Rheo–Nuclear Magnetic Resonance Investigation. *Chem. Eng. Technol.*, 43(9):1699–1705, 2020. doi: 10.1002/ceat.202000193.

G. Kaysan, A. Rica, G. Guthausen, and M. Kind. Contact-Mediated Nucleation of Subcooled Droplets in Melt Emulsions: A Microfluidic Approach. *Crystals*, 11(12):1471, 2021. doi: 10.3390/cryst11121471.

G. Kaysan, R. Kräling, M. Meier, H. Nirschl, G. Guthausen, and M. Kind. Investigation of the surfactant distribution in oil-in-water emulsions during the crystallization of the dispersed phase via nuclear magnetic resonance relaxometry and diffusometry. *Magn Reson Chem*, 60(12):1131–1147, 2022a. doi: 10.1002/mrc.5305.

G. Kaysan, J. Reiner, H. P. Karbstein, and M. Kind. Impact of Wax Particles on Crystallization and Stability of Melt Emulsions. *SOFW Journal (German version)*, 148(11):26–31, 2022b.

G. Kaysan, N. Schork, S. Herberger, G. Guthausen, and M. Kind. Contact-mediated nucleation in melt emulsions investigated by rheo-nuclear magnetic resonance. *Magn Reson Chem*, 60(7):615–627, 2022c. doi: 10.1002/mrc.5228.

G. Kaysan, L. Elmlinger, and M. Kind. Increasing the Efficiency of Emulsion Crystallization in Stirred Vessels by Targeted Application of Shear and Surfactant. *Colloids and Interfaces*, 7(4):68, 2023a. ISSN 2504-5377. doi: 10.3390/colloids7040068.

G. Kaysan, T. Hirsch, K. Dubil, and M. Kind. A Microfluidic Approach to Investigate the Contact Force Needed for Successful Contact-Mediated Nucleation. *Colloids and Interfaces*, 7(1):12, 2023b. ISSN 2504-5377. doi: 10.3390/colloids7010012.

W. Kelly and B. Gigas. Using CFD to predict the behavior of power law fluids near axial-flow impellers operating in the transitional flow regime. *Chem. Eng. Sci.*, 58(10):2141–2152, 2003. ISSN 00092509. doi: 10.1016/S0009-2509(03)00060-5.

H.-U. Kim and K.-H. Lim. A model on the temperature dependence of critical micelle concentration. *Colloids Surf. A Physicochem. Eng. Asp.*, 235(1-3): 121–128, March 2004. ISSN 09277757. doi: 10.1016/j.colsurfa.2003.12.019.

M. Kind. Industrielle Kristallisation. *Chem. Ing. Tech.*, 75(10):1487–1490, 2003. ISSN 0009-286X. doi: 10.1002/cite.200303292.

W. Kloek, P. Walstra, and T. van Vliet. Nucleation kinetics of emulsified triglyceride mixtures. *J. Am. Oil Chem.' Soc.*, 77(6):643–652, 2000. ISSN 0003021X. doi: 10.1007/s11746-000-0104-7.

N. Kockmann. *Transport Phenomena in Micro Process Engineering*. Springer-Verlag, Berlin-Heidelberg, 2008. ISBN 978-3-540-74616-4.

A. N. Kolmogorov. *The Break-up of Droplets in a Turbulent Stream*. Directorate of Scientific Information Services, DRB Canada, 1956.

A. N. Kolmogorov. Die Energiedissipation für lokalisotrope Turbulenz. In H. Göring, editor, *Statistische Theorie der Turbulenz*. Akademie Verlag Berlin, Berlin, 1958.

A. N. Kolmogorov. The local structure of turbulence in incompressible viscous fluid for very large Reynolds numbers. *Proceedings of the Royal Society of London. Series A: Mathematical and Physical Sciences*, 434(1890):9–13, 1991. ISSN 0962-8444. doi: 10.1098/rspa.1991.0075.

M. A. Krawczyk, D. T. Wasan, and C. Shetty. Chemical demulsification of petroleum emulsions using oil-soluble demulsifiers. *Ind. Eng. Chem. Res.*, 30(2):367–375, 1991. doi: 10.1021/ie00050a014.

T. Krebs, K. Schroen, and R. Boom. A microfluidic method to study demulsification kinetics. *Lab Chip*, 12(6):1060–1070, 2012. doi: 10.1039/c2lc20930f.

S. M. Kresta and R. S. Brodkey. Turbulence in Mixing Applications. In E. L. Paul, V. A. Atiemo–Obeng, and S. M. Kresta, editors, *Handbook of Industrial Mixing*, pages 19–87. Wiley, 2003. ISBN 978-0-471-26919-9. doi: 10.1002/0471451452.ch2.

C. Krishnamoorthy and A. J. Ghajar. Single-Phase Friction Factor in Micro-Tubes: A Critical Review of Measurement, Instrumentation and Data Reduction Techniques From 1991-2006. In *ASME 5th International Conference on Nanochannels, Microchannels, and Minichannels*, pages 813–825. ASMEDC, 2007. ISBN 0-7918-4272-X. doi: 10.1115/ICNMM2007-30022.

F. E. Kruis and K. A. Kusters. The Collision Rate Of Particles In Turbulent Flow. *Chem Eng Commun*, 158(1):201–230, 1997. ISSN 0098-6445. doi: 10.1080/00986449708936589.

K. Köhler and H. P. Schuchmann, editors. *Emulgiertechnik: Grundlagen, Verfahren und Anwendungen.* Behr, Hamburg, 3. aufl. edition, 2012. ISBN 978-3-89947-869-3.

R. R. Lagasse and B. Maxwell. An experimental study of the kinetics of polymer crystallization during shear flow. *Polym. Eng. Sci.*, 16(3):189–199, 1976. ISSN 0032-3888. doi: 10.1002/pen.760160312.

H. D. Laufhuette and A. Mersmann. Die lokale Energiedissipation im turbulent gerührten Fluid und ihre Bedeutung für die verfahrenstechnische Auslegung von Rührwerken. *Chem. Ing. Tech.*, 57(12):1104–1105, 1985. ISSN 0009-286X. doi: 10.1002/cite.330571217.

F. Lehr and D. Mewes. A transport equation for the interfacial area density applied to bubble columns. *Chem. Eng. Sci.*, 56(3):1159–1166, 2001. doi: 10.1016/S0009-2509(00)00335-3.

F. Lehr, M. Millies, and D. Mewes. Bubble-Size distributions and flow fields in bubble columns. *AIChE J.*, 48(11):2426–2443, 2002. doi: 10.1002/aic.690481103.

N. Leister and H. P. Karbstein. Influence of Hydrophilic Surfactants on the W1–W2 Coalescence in Double Emulsion Systems Investigated by Single Droplet Experiments. *Colloids Interfaces*, 5(2):21, 2021. doi: 10.3390/colloids5020021.

V. G. Levich. *Physiochemical hydrodynamics*. Prentice-hall international series in the physical and chemical engineering science. Prentice-Hall, Englewood Cliffs, N.J., 1962. ISBN 0-13-674440-0.

Y. Liao and D. Lucas. A literature review on mechanisms and models for the coalescence process of fluid particles. *Chem. Eng. Sci.*, 65(10):2851–2864, 2010. doi: 10.1016/j.ces.2010.02.020.

G. D. M. Mackay and S. G. Mason. The gravity approach and coalescence of fluid drops at liquid interfaces. *Can. J. Chem. Eng.*, 41(5):203–212, 1963. ISSN 00084034. doi: 10.1002/cjce.5450410504.

D. J. McClements. *The use of ultrasonics for characterising fats and emulsions*. PhD Thesis, University of Leeds, Leeds, 1988.

D. J. McClements. Ultrasonic characterisation of emulsions and suspensions. *Adv Colloid Interface Sci.*, 37(1-2):33–72, 1991. doi: 10.1016/0001-8686(91)80038-L.

D. J. McClements. Comparison of multiple scattering theories with experimental measurements in emulsions. *J. Acoust. Soc*, 91(2):849–853, 1992. ISSN 0001-4966. doi: 10.1121/1.402490.

D. J. McClements. Ultrasonic determination of depletion flocculation in oil-in-water emulsions containing a non-ionic surfactant. *Colloids Surf A Physicochem Eng Asp*, 90(1):25–35, 1994. ISSN 09277757. doi: 10.1016/0927-7757(94)02881-8.

D. J. McClements. Ultrasonic characterization of foods and drinks: principles, methods, and applications. *Crit. Rev. Food Sci. Nutr.*, 37(1):1–46, 1997. ISSN 1040-8398. doi: 10.1080/10408399709527766.

D. J. McClements. Crystals and crystallization in oil-in-water emulsions: Implications for emulsion-based delivery systems. *Adv. Colloid Interface Sci.*, 174:1–30, 2012. doi: 10.1016/j.cis.2012.03.002.

D. J. McClements and Stephanie R. Dungan. Effect of Colloidal Interactions on the Rate of Interdroplet Heterogeneous Nucleation in Oil-in-Water Emulsions. *J. Colloid Interface Sci.*, 186(1):17–28, 1997. doi: 10.1006/jcis.1996.4504.

D. J. McClements, E. Dickinson, S. R. Dungan, J. E. Kinsella, J. G. Ma, and M. J. W. Povey. Effect of Emulsifier Type on the Crystallization Kinetics of Oil-in-Water Emulsions Containing a Mixture of Solid and Liquid Droplets. *J. Colloid Interface Sci.*, 160(2):293–297, 1993a. doi: 10.1006/jcis.1993.1399.

D. J. McClements, Stephanie R. Dungan, J. B. German, C. Simoneau, and John E. Kinsella. Droplet Size and Emulsifier Type Affect Crystallization and Melting of Hydrocarbon-in-Water Emulsions. *J. Food Sci.*, 58(5):1148–1151, 1993b. ISSN 0022-1147. doi: 10.1111/j.1365-2621.1993.tb06135.x.

D. J. McClements, S.-W. Han, and S. R. Dungan. Interdroplet heterogeneous nucleation of supercooled liquid droplets by solid droplets in oil-in-water emulsions. *J. Am. Oil Chem.' Soc.*, 71(12):1385–1389, 1994. ISSN 0003021X. doi: 10.1007/BF02541360.

J. D. McClements, E. Dickinson, and M.J.W. Povey. Crystallization in hydrocarbon-in-water emulsions containing a mixture of solid and liquid droplets. *Chem. Phys. Lett.*, 172(6):449–452, 1990. doi: 10.1016/0009-2614(90)80137-3.

S. T. McComas. Hydrodynamic Entrance Lengths for Ducts of Arbitrary Cross Section. *J. basic eng.*, 89(4):847–850, 1967. ISSN 0021-9223. doi: 10.1115/1.3609713.

W. Mehnert and K. Mäder. Solid lipid nanoparticles. *Adv. Drug Deliv. Rev.*, 64:83–101, 2012. ISSN 0169409X. doi: 10.1016/j.addr.2012.09.021.

A. Mersmann, editor. *Crystallization technology handbook.* Dekker, New York u.a., 2. ed., rev. and expanded. edition, 2001. ISBN 978-0-8247-0528-2.

M. Mirmanto. Prediction and Measurement of Pressure Drop of Water Flowing in a Rectangular Microchannel. *Dinamika Teknik Mesin*, 3(2), 2017. ISSN 2088-088X. doi: 10.29303/d.v3i2.72.

G. Mohiuddin Mala and D. Li. Flow characteristics of water in microtubes. *Int J Heat Fluid Flow*, 20(2):142–148, 1999. doi: 10.1016/S0142-727X(98)10043-7.

R. Montenegro and K. Landfester. Metastable and Stable Morphologies during Crystallization of Alkanes in Miniemulsion Droplets. *Langmuir*, 19(15):5996–6003, 2003. ISSN 0743-7463. doi: 10.1021/la027019v.

L. F. Moody. Friction Factors for Pipe Flow. *Trans. Am. Soc. Mech. Eng.*, 66:671–681, 1944.

M. Moo–Young, K. Tichar, and F. A. L. Dullien. The blending efficiencies of some impellers in batch mixing. *AIChE Journal*, 18(1):178–182, 1972. ISSN 0001-1541. doi: 10.1002/aic.690180133.

E. M. Mudge and G. Mazzanti. Rheo-NMR Measurements of Cocoa Butter Crystallized Under Shear Flow. *Cryst. Growth Des.*, 9(7):3111–3118, 2009. ISSN 1528-7483. doi: 10.1021/cg800999y.

J. W. Mullin. *Crystallisation, 4th Edition By J. W. Mullin. 2001. Butterworth Heinemann: Oxford, UK. 600 pp. \pounds75.00. ISBN 075-064-833-3*, volume 6. American Chemical Society, 2002. doi: 10.1021/op0101005.

M. Musterd, V. van Steijn, C. R. Kleijn, and M. T. Kreutzer. Calculating the volume of elongated bubbles and droplets in microchannels from a top view image. *RSC Adv.*, 5(21):16042–16049, 2015. doi: 10.1039/C4RA15163A.

O. O. Mykhaylyk, P. Chambon, C. Impradice, J. P. A. Fairclough, N. J. Terrill, and A. J. Ryan. Control of Structural Morphology in Shear-Induced Crystallization of Polymers. *Macromolecules*, 43(5):2389–2405, 2010. ISSN 0024-9297. doi: 10.1021/ma902495z.

R. Müller. Solid lipid nanoparticles (SLN) for controlled drug delivery - a review of the state of the art. *Eur. J. Pharm. Biopharm.*, 50(1):161–177, 2000. doi: 10.1016/s0939-6411(00)00087-4.

R. H. Müller, R. D. Petersen, A. Hommoss, and J. Pardeike. Nanostructured lipid carriers (NLC) in cosmetic dermal products. *Adv. Drug Deliv. Rev.*, 59 (6):522–530, 2007. doi: 10.1016/j.addr.2007.04.012.

S. Narayan, A. E. Metaxas, R. Bachnak, T. Neumiller, and C. S. Dutcher. Zooming in on the role of surfactants in droplet coalescence at the macroscale and microscale. *Curr. Opin. Colloid Interface Sci.*, 50:101385, 2020. ISSN 13590294. doi: 10.1016/j.cocis.2020.08.010.

T. Nikolaeva, F. J. Vergeldt, R. Serial, Joshua A. Dijksman, P. Venema, A. Voda, J. van Duynhoven, and H. van As. High Field MicroMRI Velocimetric Measurement of Quantitative Local Flow Curves. *Anal. Chem.*, 92(6):4193–4200, 2020. doi: 10.1021/acs.analchem.9b03216.

E. Nowak, N. M. Kovalchuk, Z. Che, and M. J.H. Simmons. Effect of surfactant concentration and viscosity of outer phase during the coalescence of a surfactant-laden drop with a surfactant-free drop. *Colloids Surf A Physicochem Eng Asp*, 505:124–131, 2016. doi: 10.1016/j.colsurfa.2016.02.016.

F. O. Opawale and D. J. Burgess. Influence of Interfacial Properties of Lipophilic Surfactants on Water-in-Oil Emulsion Stability. *J. Colloid Interface Sci.*, 197 (1):142–150, 1998. doi: 10.1006/jcis.1997.5222.

J. Palanuwech and J. N. Coupland. Effect of surfactant type on the stability of oil-in-water emulsions to dispersed phase crystallization. *Colloids Surf A Physicochem Eng Asp*, 223(1-3):251–262, 2003. ISSN 09277757. doi: 10.1016/S0927-7757(03)00169-9.

J. Pardeike, A. Hommoss, and R. H. Müller. Lipid nanoparticles (SLN, NLC) in cosmetic and pharmaceutical dermal products. *Int. J. Pharm.*, 366(1-2): 170–184, 2009. doi: 10.1016/j.ijpharm.2008.10.003.

J. H. Perepezko, P. G. Höckel, and J. S. Paik. Initial crystallization kinetics in undercooled droplets. *Thermochim Acta*, 388(1-2):129–141, 2002. ISSN 0040-6031. doi: 10.1016/S0040-6031(02)00022-9.

V. J. Pinfield, M. J. W. Povey, and E. Dickinson. The application of modified forms of the Urick equation to the interpretation of ultrasound velocity in scattering systems. *Ultrasonics*, 33(3):243–251, 1995. ISSN 0041624X. doi: 10.1016/0041-624X(95)94558-Z.

M. J. W. Povey. Crystallization of oil-in-water emulsions. In N. Garti and K. Sato, editors, *Crystallization Processes in Fats and Lipid Systems*, pages 251–288. Marcel Dekker, 2001. ISBN 978-1-4822-7088-4.

M. J. W. Povey, T. Awad, R. Huo, and Y. Ding. Quasi-isothermal crystallisation kinetics, non-classical nucleation and surfactant-dependent crystallisation of emulsions. *Eur J Lipid Sci Technol*, 111(3):236–242, 2009. ISSN 14387697. doi: 10.1002/ejlt.200800193.

R. C. Prima and H. L. Swinney. Instabilities and transition in flow between concentric rotating cylinders. In H. L. Swinney and F. H. Busse, editors, *Hydrodynamic instabilities and the transition to turbulence*, volume 45 of *Topics in Applied Physics*, pages 139–180. Springer, Berlin and Heidelberg and New York and Tokyo, 1985. ISBN 978-3-540-13319-3. doi: 10.1007/3-540-13319-4âĂŮ16.

W. Qu, I. Mudawar, S.-Y. Lee, and S. T. Wereley. Experimental and Computational Investigation of Flow Development and Pressure Drop in a Rectangular Micro-channel. *J. Electron. Packag.*, 128(1):1, 2006. doi: 10.1115/1.2159002.

T.C Ransohoff and C.J Radke. Laminar flow of a wetting liquid along the corners of a predominantly gas-occupied noncircular pore. *J. Colloid Interface Sci.*, 121(2):392–401, 1988. doi: 10.1016/0021-9797(88)90442-0.

D. A. Reinelt and P. G. Saffman. The Penetration of a Finger into a Viscous Fluid in a Channel and Tube. *SIAM J. Sci. Comput.*, 6(3):542–561, 1985. ISSN 0196-5204. doi: 10.1137/0906038.

O. Reynolds. An experimental investigation of the circumstances which determine whether the motion of water shall be direct or sinuous, and of the law of resistance in parallel channels. *Phil. Trans. R. Soc.*, 174:935–982, 1883. ISSN 0261-0523. doi: 10.1098/rstl.1883.0029.

F. Risso. The mechanisms of deformation and breakup of drops and bubbles. *Multiph Sci Technol*, 12(1):50, 2000. ISSN 0276-1459. doi: 10.1615/Mult ScienTechn.v12.i1.10.

P. J. Roache. Perspective: A Method for Uniform Reporting of Grid Refinement Studies. *J. Fluids Eng.*, 116(3):405–413, 1994. doi: 10.1115/1.2910291.

B. Robertson and J. J. Ulbrecht. Measurment of shear rate on an agitator in a fermentation broth. *AIChE*, pages 72–81, 1987.

J. H. Rushton, E. W. Costich, and H. J. Everett. Power characteristics of mixing impellers. *Chem Eng Prog*, 46:467–476, 1950.

N. H. Sagert and M. J. Quinn. The coalescence of H2S and CO2 bubbles in water. *Can. J. Chem. Eng.*, 54(5):392–398, 1976. ISSN 00084034. doi: 10.1002/cjce.5450540503.

H. Schlichting and K. Gersten. *Boundary-Layer Theory*. Springer Berlin Heidelberg, Berlin, Heidelberg, 2000. ISBN 978-3-642-85831-4. doi: 10.1007/978-3-642-85829-1.

N. Schork, S. Schuhmann, H. Nirschl, and G. Guthausen. In situ measurement of deposit layer formation during skim milk filtration by MRI. *Magn Reson Chem*, 57(9):738–748, 2019. doi: 10.1002/mrc.4826.

K. Schroën, J. de Ruiter, and C. C. Berton-Carabin. The Importance of Interfacial Tension in Emulsification: Connecting Scaling Relations Used in Large Scale Preparation with Microfluidic Measurement Methods. *Chem. Eng.*, 4 (4):63, 2020. doi: 10.3390/chemengineering4040063.

S. Schuhmann, J. W. Simkins, N. Schork, S. L. Codd, J. D. Seymour, M. Heijnen, F. Saravia, H. Horn, H. Nirschl, and G. Guthausen. Characterization and quantification of structure and flow in multichannel polymer membranes by MRI. *J. Membr. Sci.*, 570-571:472–480, 2019. ISSN 03767388. doi: 10.1016/j.memsci.2018.10.072.

L. W. Schwartz, H. M. Princen, and A. D. Kiss. On the motion of bubbles in capillary tubes. *J. Fluid Mech.*, 172(-1):259, 1986. doi: 10.1017/S0022112086001738.

M. Schäfer, M. Höfken, and F. Durst. Detailed LDV Measurements for Visualization of the Flow Field Within a Stirred-Tank Reactor Equipped with a Rushton Turbine. *Chem Eng Res Des*, 75(8):729–736, 1997. ISSN 02638762. doi: 10.1205/026387697524399.

L. E. Scriven and C. V. Sterling. The Marangoni Effects. *Nature*, 187(4733): 186–188, 1960. doi: 10.1038/187186a0.

R. P. Sear. Nucleation: theory and applications to protein solutions and colloidal suspensions. *J. Phys. Condens. Matter*, 19(3):033101, 2007. ISSN 0953-8984. doi: 10.1088/0953-8984/19/3/033101.

R. P. Sear. Quantitative studies of crystal nucleation at constant supersaturation: experimental data and models. *Cryst Eng Comm*, 16(29):6506–6522, 2014. doi: 10.1039/C4CE00344F.

D. Selzer, B. Spiegel, and M. Kind. A Generic Polycarbonate Based Microfluidic Tool to Study Crystal Nucleation in Microdroplets. *J. Cryst. Process Technol.*, 08(01):1–17, 2018. ISSN 2161-7678. doi: 10.4236/jcpt.2018.81001.

J. D. Seymour, B. Manz, and P. T. Callaghan. Pulsed gradient spin echo nuclear magnetic resonance measurements of hydrodynamic instabilities with coherent structure: Taylor vortices. *Phys. Fluids*, 11(5):1104–1113, 1999. doi: 10.1063/1.869981.

R. Shinnar and J. M. Church. Statistical Theories of Turbulence in Predicting Particle Size in Agitated Dispersions. *Ind. Eng. Chem.*, 52(3):253–256, 1960. ISSN 0019-7866. doi: 10.1021/ie50603a036.

Y. Shinohara, T. Takamizawa, S. Ueno, K. Sato, I. Kobayashi, M. Nakajima, and Y. Amemiya. Microbeam X-ray Diffraction Analysis of Interfacial Heterogeneous Nucleation of n -Hexadecane inside Oil-in-Water Emulsion Droplets. *Cryst. Growth Des.*, 8(9):3123–3126, 2008. ISSN 1528-7483. doi: 10.1021/cg701018x.

S. Singh, J. Houston, F. van Swol, and C. J. Brinker. Superhydrophobicity: drying transition of confined water. *Nature*, 442(7102):526, 2006. doi: 10.1038/442526a.

W. Skoda and M. van den Tempel. Crystallization of emulsified triglycerides. *J. Colloid Interface Sci.*, 18(6):568–584, 1963. ISSN 0095-8522. doi: 10.1016/0095-8522(63)90049-7.

M. v. Smoluchowski. Versuch einer mathematischen Theorie der Koagulationskinetik kolloider Lösungen. *Z Phys Chem*, 92U(1), 1918. ISSN 0942-9352. doi: 10.1515/zpch-1918-9209.

H. Sovová. Breakage and coalescence of drops in a batch stirred vessel—II comparison of model and experiments. *Chem. Eng. Sci.*, 36(9):1567–1573, 1981. doi: 10.1016/0009-2509(81)85117-2.

Burkard Spiegel. *Kristallisation in Emulsionen.* Dissertation, Karlsruhe Institute of Technology, Karlsruhe, 2019.

M. Staszak. A Linear Diffusion Model of Adsorption Kinetics at Fluid/Fluid Interfaces. *J Surfactants Deterg*, 19:297–314, 2016. ISSN 1097-3958. doi: 10.1007/s11743-016-1789-8.

M. E. Steinke and S. G. Kandlikar. Single-phase liquid friction factors in microchannels. *Int. J. Therm. Sci.*, 45(11):1073–1083, 2006. ISSN 12900729. doi: 10.1016/j.ijthermalsci.2006.01.016.

H. A. Stone. Dynamics of Drop Deformation and Breakup in Viscous Fluids. *Annu. Rev. Fluid Mech.*, 26(1):65–102, 1994. ISSN 0066-4189. doi: 10.1146/annurev.fl.26.010194.000433.

J. A. Sánchez Pérez, E. M. Rodríguez Porcel, J. L. Casas López, J. M. Fernández Sevilla, and Y. Chisti. Shear rate in stirred tank and bubble column bioreactors. *Chem. Eng. J.*, 124(1-3):1–5, 2006. doi: 10.1016/j.cej.2006.07.002.

M. Taboada, N. Leister, H. Karbstein, and V. Gaukel. Influence of the Emulsifier System on Breakup and Coalescence of Oil Droplets during Atomization of Oil-In-Water Emulsions. *Chem. Eng.*, 4(3):47, 2020. doi: 10.3390/chemengineering4030047.

L. M. Tam, H. K. Tam, A. J. Ghajar, W. S. Ng, I. W. Wong, K. F. Leong, and C. K. Wu. The Effect of Inner Surface Roughness and Heating on Friction Factor in Horizontal Micro-Tubes. In *ASME-JSME-KSME 2011, Symposia – Parts A, B, C, and D*, volume 1, pages 2971–2978. ASMEDC, 2011. ISBN 978-0-7918-4440-3. doi: 10.1115/AJK2011-16027.

G. I. Taylor. The formation of emulsions in definable fields of flow. *Proc. R. Soc. Lond., Ser. A, Math. Phys. Eng. Sci.*, 146(858):501–523, 1934. ISSN 0962-8444. doi: 10.1098/rspa.1934.0169.

A. Trokhymchuk, D. Henderson, A. Nikolov, and D. T. Wasan. A Simple Calculation of Structural and Depletion Forces for Fluids/Suspensions Confined in a Film. *Langmuir*, 17(16):4940–4947, 2001. ISSN 0743-7463. doi: 10.1021/la010047d.

D. Turnbull. Formation of Crystal Nuclei in Liquid Metals. *J. Appl. Phys.*, 21 (10):1022–1028, 1950. ISSN 0021-8979. doi: 10.1063/1.1699435.

D. Turnbull. Kinetics of Solidification of Supercooled Liquid Mercury Droplets. *J. Chem. Phys.*, 20(3):411–424, 1952. ISSN 0021-9606. doi: 10.1063/1.1700435.

D. Turnbull and R. L. Cormia. Kinetics of Crystal Nucleation in Some Normal Alkane Liquids. *J. Chem. Phys.*, 34(3):820–831, 1961. ISSN 0021-9606. doi: 10.1063/1.1731681.

R. J. Urick. A Sound Velocity Method for Determining the Compressibility of Finely Divided Substances. *J. Appl. Phys.*, 18(11):983–987, 1947. ISSN 0021-8979. doi: 10.1063/1.1697584.

A. Vallatos, M. C. T. Wilson, A. F. Taylor, and M. M. Britton. Characterising stationary and translating vortex flow using magnetic resonance. *EPL*, 99(6): 68001, 2012. ISSN 0295-5075. doi: 10.1209/0295-5075/99/68001.

M.A.J.S. van Boekel and P. Walstra. Stability of oil-in-water emulsions with crystals in the disperse phase. *Colloids Surf A Physicochem Eng Asp*, 3(2): 109–118, 1981. ISSN 01666622. doi: 10.1016/0166-6622(81)80071-6.

S. A. Vanapalli and J. N. Coupland. Emulsions under shear—the formation and properties of partially coalesced lipid structures. *Food Hydrocoll.*, 15(4-6): 507–512, 2001. ISSN 0268005X. doi: 10.1016/S0268-005X(01)00057-1.

E. J. W. Verwey. Theory of the stability of lyophobic colloids. *J. Phys. Colloid Chem*, 51(3):631–636, 1947. ISSN 0092-7023. doi: 10.1021/j150453a001.

M. Volmer and A. Weber. Keimbildung in übersättigten Gebilden. *Z Phys Chem*, 119U(1):277–301, 1926. ISSN 0942-9352. doi: 10.1515/zpch-1926-11927.

G. Vélez, M. A. Fernández, J. Muñoz, P. A. Williams, and R. J. English. Role of hydrocolloids in the creaming of oil in water emulsions. *J. Agric. Food Chem.*, 51(1):265–269, 2003. doi: 10.1021/jf020664n.

P. Walstra. Formation of emulsions. In P. Becher, editor, *Encyclopedia of emulsion Technology*, pages 57–128. Marcel Dekker, New York, NY, USA, 1983.

P. Walstra. Principles of emulsion formation. *Chem. Eng. Sci.*, 48(2):333–349, 1993. doi: 10.1016/0009-2509(93)80021-H.

P. Walstra. *Physical chemistry of foods*, volume 121 of *Food Sci. Technol.* Marcel Dekker, New York, 2003. ISBN 0-8247-9355-2. Backup Publisher: ebrary, Inc.

P. Walstra and P. Smulders. Emulsion Formation. In B. P. Binks, editor, *Modern Aspects of Emulsion Science*. The Royal Society of Chemistry, 1998. ISBN 978-0-85404-439-9.

J. Weiss, E. A. Decker, D. J. McClements, K. Kristbergsson, T. Helgason, and T. Awad. Solid Lipid Nanoparticles as Delivery Systems for Bioactive Food Components. *Food Biophys*, 3(2):146–154, 2008. doi: 10.1007/s11483-008-9065-8.

H. G. Weller, G. Tabor, H. Jasak, and C. Fureby. A tensorial approach to computational continuum mechanics using object-oriented techniques. *Comput. Phys.*, 12(6):620, 1998. ISSN 08941866. doi: 10.1063/1.168744.

B. Xu, K. T. Ooti, N. T. Wong, and W. K. Choi. Experimental investigation of flow friction for liquid flow in microchannels. *Int. Commun. Heat Mass Transf.*, 27(8):1165–1176, 2000. ISSN 07351933. doi: 10.1016/S0735-1933(00)00203-7.

Y. B. Zeldovich. On the Theory of New Phase Formation. Cavitation. In G. I. Barenblatt and R. A. Sunyaev, editors, *Selected Works of Yakov Borisovich Zeldovich, Volume I*, pages 120–137. Princeton University Press, 1992. ISBN 978-1-4008-6297-9. doi: 10.1515/9781400862979.120.

P. Zhang, Z. W. Ma, and R. Z. Wang. An overview of phase change material slurries: MPCS and CHS. *Renew. Sustain. Energy Rev.*, 14(2):598–614, 2010. ISSN 13640321. doi: 10.1016/j.rser.2009.08.015.

G. Zhou and S. M. Kresta. Impact of tank geometry on the maximum turbulence energy dissipation rate for impellers. *AIChE Journal*, 42(9):2476–2490, 1996. ISSN 0001-1541. doi: 10.1002/aic.690420908.

Q. Zhou, Y. Sun, S. Yi, K. Wang, and G. Luo. Investigation of droplet coalescence in nanoparticle suspensions by a microfluidic collision experiment. *Soft Matter*, 12(6):1674–1682, 2016. ISSN 1744-683X. doi: 10.1039/C5SM02924D.

M. Zlokarnik. *Rührtechnik: Theorie und Praxis*. Chemische Technik, Verfahrenstechnik. Springer, Berlin u.a., 1999. ISBN 978-3-540-64639-6.

M. Zlokarnik and H. Judat. Rohr– und Scheibenrührer — zwei leistungsfähige Rührer zur Flüssigkeitsbegasung. *Chem. Ing. Tech.*, 39(20):1163–1168, 1967. ISSN 0009-286X. doi: 10.1002/cite.330392003.